SCUOLA DI DOTTORATO
UNIVERSITÀ DEGLI STUDI DI MILANO-BICOCCA

Department of Earth and Environmental Sciences (DISAT)

PhD program in Chemical, Geological and Environmental Sciences Cycle XXXII
Curriculum in Geological Sciences

Modelling of mechanical mixing and chemical interaction between the subducting crust and the overlying mantle at (ultra)high pressures: implications for the slab-to-mantle mass transfer

Pellegrino Luca
Registration number: 732246

Tutor: Prof. Nadia Malaspina
Co-tutor: Prof. Stefano Zanchetta
Coordinator: Maria Luce Frezzotti

ACADEMIC YEAR 2018/2019

Abstract

Orogenic garnet peridotites frequently occur in high-pressure (HP) and ultra-high pressure (UHP) metamorphic terranes. In these settings, peridotites and associated crustal rocks commonly display the same tectono-metamorphic evolution with similar peak P-T equilibrium conditions and identical retrograde P-T-path during exhumation. This testifies for a mechanical coupling at peak conditions and subsequent sharing of metamorphic evolution during exhumation.

Orogenic garnet peridotites frequently record metasomatic modifications by fluids, melts or supercritical fluids derived at HP or UHP from the subducted crust. The interaction between peridotites and crustal agents derived by the felsic portions of the subducted slab at HP-UHP has been reported in a series of natural and experimental studies. On the other and the interaction between peridotites and metasomatic carriers released by the subduction of the oceanic crust is still poorly constrained. Orogenic garnet peridotites are believed to be sampled by the subducted slab due to sinking processes triggered by density contrast between the overlying mantle and the underlying continental and/or oceanic crust. However, experimental studies and numerical models (refs.) highlight that mantle is harder than the crust suggesting that other mechanisms, e.g. deformation and weakening, other than density contrast and gravitational instabilities likely govern the material exchange between crust and mantle at HP and UHP.

To better characterise the interaction between the subducted crust and the overlying mantle at (U)HP conditions, and the mechanism controlling the sampling of ultramafic rocks into the slab, two HP terranes where garnet peridotites are associated to high-grade crustal rocks have been studied in detail: i) the Monte Duria area and ii) the Ulten Zone.

In the Monte Duria area (Adula-Cima Lunga unit, Central Alps, N Italy) garnet peridotites occur in direct contact with migmatised orthogneiss (Mt. Duria) and eclogites (Borgo). Both crustal and ultramafic rocks share a common high pressure (HP) peak at 2.8 GPa and 750 °C and post-peak static equilibration at 0.8-1.0 GPa and 850 °C.

Garnet peridotites show abundant amphibole, dolomite, phlogopite and orthopyroxene after olivine, suggesting that they experienced metasomatism by crust-derived agents enriched in SiO_2, K_2O, CO_2 and H_2O. Peridotites also display LREE fractionation (La/Nd = 2.4) related to LREE-rich amphibole and clinopyroxene grown in equilibrium with garnet, indicating that metasomatism occurred at HP conditions. At Borgo, retrogressed garnet peridotites show low strain domains characterised by garnet compositional layering, cut by a

subsequent low-pressure (LP) chlorite foliation, in direct contact with migmatised eclogites. Kfs+Pl+Qz+Cpx interstitial pocket aggregates and Cpx+Kfs thin films around symplectites after omphacite parallel to the Zo+Omp+Grt foliation in the eclogites suggest that they underwent partial melting at HP.

The contact between garnet peridotites and associated eclogites is marked by a tremolitite layer, which also occurs as layers within the peridotite lens, showing a boudinage parallel to the garnet layering of peridotites, flowing in the boudin necks. This clearly indicates that the tremolitite boudins formed when peridotites were in the garnet stability field. Tremolitites also show Phl+Tc+Chl+Tr pseudomorphs after garnet, both crystallised in a static regime postdating the boudins formation, suggesting that they derive from a garnet-bearing precursor. Tremolitites have Mg# > 0.90 and Al_2O_3 = 2.75 wt.% pointing to ultramafic compositions but also show enrichments in SiO_2, CaO, and LREE suggesting that they formed after the reaction between the eclogite-derived melt and the garnet peridotite at HP. To test this hypothesis, we performed a thermodynamic modelling at fixed P = 3 GPa and T = 750 °C to model the chemical interaction between the garnet peridotite and the eclogite-derived melt. Our results show that this interaction produces a Opx+Cpx+Grt assemblage + Amp+Phl, depending on the water activity in the melt, suggesting that tremolitites likely derive from a previous garnet websterite with amphibole and phlogopite.

In the Ulten Zone (Tonale nappe, Eastern Alps, N Italy), numerous peridotite bodies occur within high-grade crustal rocks. Peridotites show a transition from coarse protogranular spinel-lherzolites to fine-grained mylonitic garnet-amphibole peridotites. Pyroxenites veins and dikes, transposed along the peridotite foliation, show a similar evolution from coarse garnet-free websterites to fine-grained garnet + amphibole clinopyroxenites. This coupled evolution has been interpreted to reflect cooling and pressure increase of pyroxenites and host peridotites from spinel- (1200 °C, 1.3-1.6 Gpa) to garnet-facies conditions (850 °C and 2.8 Gpa) likely induced by mantle corner flow. As a consequence, garnet formed coronas around spinel and exsolved from porphyroclastic, high-T pyroxenes, and finally crystallised along the pyroxenite and peridotite foliations.

Textural evidences and crystallographic orientation data indicate that the transition from spinel- to garnet-facies conditions was assisted by intense shearing and deformation. Pyroxene porphyroclasts in garnet clinopyroxenites show well-developed CPOs, high frequencies of low-angle misorientations, and non-random distribution of the low-angle misorientation axes, indicating that pyroxene porphyroclasts primarily deform by dislocation creep.

Dislocation creep is accompanied by reaction-induced dynamic recrystallisation during the spinel to garnet phase transition, which promotes a sudden reduction of the grain size and a shift from dislocation creep in the porphyroclast to grain-size sensitive creep (GSS) in the recrystallised grains. This results in a dramatic rheological weakening of pyroxenites at HP peak conditions when pyroxenites and host peridotites were coupled with crustal rocks.

The Monte Duria area is a unique case study where we can observe eclogite-derived melts interacting with garnet peridotites at HP. The interaction between peridotites and eclogite-derived melts promotes the formation of websterites. Development of websterites, and clinopyroxenites in general, results in the formation of compositional and rheological anisotropies where deformation can be localised. Strain localisation and weakening can also occur when such anisotropies are already present in the mantle, as observed in the case of pyroxenites of Ulten zone which accommodate most of deformation during shearing and mineral phase transformations induced by mantle corner flow. In both cases strain softening of the mantle tends to reduce the rheological contrast between the subducted crust and the overlying mantle creating favourable condition for the emplacement of peridotites into the slab.

Riassunto

Peridotiti orogeniche a granato spesso affiorano all'interno di terreni metamorfici di alta e ultra-alta pressione. In questi contesti, peridotiti e rocce crostali condividono la stessa evoluzione tettono-metamorfica, dall'equilibratura in alta pressione al percorso retrogrado durante l'esumazione. Le peridotiti spesso registrano metasomatismo ad opera di fluidi, fusi o fluidi supercritici rilasciati dalla crosta in subduzione in condizioni di alta o ultra-alta pressione. L'interazione tra le peridotiti e gli agenti metasomatici rilasciati dalla crosta continentale è stata studiata ampiamente attraverso casi di studio naturali ed espermenti. D'altra parte, l'interazione tra peridotiti e gli agenti metasomatici rilasciati dalla crosta mafica è ancora poco chiara.

Si suppone che le peridotiti orogeniche possano essere campionate dallo *slab* in subduzione attraverso meccanismi che prevedono lo sprofondamente di porzioni di mantello all'interno della crosta per contrasto di densità. Tuttavia, studi sperimentali e modelli numerici hanno evidenziato che il mantello è più rigido della crosta, suggerendo che altri processi come localizzazione degli sforzi e deformazione oltre che contrasto di densità e instabilità gravitative probabilmente governano lo scambio di materiale tra il mantello e la crosta in subduzione ad alta o ultra-alta pressione.

Nell'area del Monte Duria, peridotiti a granato affiorano in contatto diretto con orthogneiss (Mt. Duria) e eclogiti migmatitiche (Borgo). Sia le peridotiti che le eclogiti registrano condizioni di picco in alta pressione a 2.8 GPa e 750 ° C e un riequilibratura statica a 1.0 GPa e 850 ° C. Le peridotiti mostrano abbondanti anfibolo, dolomite, flogopite e ortopirosseno (cresciuto a spese dell'olivina), suggerendo che le peridotiti registrano metasomatismo ad opera di agenti crostali arrichiti in SiO_2, K_2O, CO_2 e H_2O. Le peridotiti mostrano anche un frazionamento in LREE (La/Nd = 2.4) legato alla presenza di anfibolo e clinopirosseno. Questi minerali registrano condizioni di equilibrio con il granato, indicando che il metasomatismo è avvenuto in condizioni di alta pressione. Le peridotiti a granato (retrocesse a clorite) affioranti a Borgo mostrano domini a basso *strain* caratterizzati dalla presenza di un *layering* composizionale a grato trasposto da una successiva foliazione a clorite svilluppata in in condizioni di bassa pressione.

Nelle eclogiti, microstrutture di fusione come aggregati microcristallini a Kfs+Pl+Qz+Cpx e Cpx + Kfs sono allineate lungo la foliazione a Zo+Omp+Grt, indicando che le eclogiti hanno subito un evento di fusione parziale in codizioni di alta pressione.

Il contatto tra le peridotiti e le eclogiti di Borgo è contrassegnato dalla presenza di un livello di tremolitite. *Boudins* di tremolititi si ritrovano anche trasposti lungo la foliazione a granato della peridotite, indicando che il *boudinage* delle tremolititi è avvento in alta pressione. Le tremolititi mostrano aggregati a Phl+Tc+Chl+Tr interpretati come psudomorfi su granato. Tali pseudomorfi si sono sviluppati in condizioni statiche e quindi post-datano la formazione dei *boudins*, suggerendo che le tremoliti probabilmente derivano da precursori a granato. Le tremolititi mostrano Mg# > 0.90 e Al_2O_3 = 2.75 wt.% tipici di composizioni ultramafiche ma allo stesso tempo presentano arricchimenti in SiO_2, CaO, e LREE, indicando che esse rappresentano il prodotto dell'interazione in alta pressione tra le peridotiti e i fusi derivati dalle eclogiti. Per testare questa ipotesi abbiamo sviluppato un modello termodinamico a P = 3 GPa e T = 750 °C. I nostri risultati indicano che l'interazione fuso-peridotite produce una paragenesi a Opx+Cpx+Grt, suggerendo che le tremolititi rappresentano il prodotto di retrocessione di una westerite a granato.

Nella zona d'Ultimo, numerose lenti di peridotite affiorano all'interno di rocce crostali di alto grado. Le peridotiti mostrano una transizione da lherzoliti a spinello protogranulari a peridotiti milonitiche a granato e anfibolo. Le pirosseniti trasposte lungo la foliazione della peridotite mostrano un'evoluzione simile, da pirosseniti a spinello a pirosseniti a granato. Questa evoluzione riflette il passaggio da condizioni in facies a spinello (1200 °C, 1.5 Gpa) a condizioni in facies a granato (850 °C, 2.8 Gpa) indotto dal *corner flow* del mantello. Come consguenza, il granato forma corone intorno allo spinello ed essoluzioni all'interno dei porfiroclasti di pirosseno, e cristallizza lungo la foliazione delle pirosseniti e delle peridotiti

Evidenze tessiturali e dati cristallografici indicano che la transizione spinello-granato avviene in un contesto deformativo. I porfiroclasti di pirosseno mostrano evidente CPO, alte frequenze delle misorientazioni a basso angolo, e distribuzione non-random degli assi di misorientazione, indicando che i pirosseni si deformano per *dislocation creep*. Il *dislocation creep* è contemporaneo a processi di ricristallizzazione dinamica e alla transizione spinello-granato. Ciò induce una riduzione della grana e una transizione permanente da *disclocation creep* nei porfiroclasti a *grain-size sensitive creep* nei grani ricristallizzati che risulta in un forte indebolimento delle pirosseniti e delle peridotiti quando queste vengono tettonicamente accoppiate alle rocce crostali.

L’area del Monte Duria è uno dei pochi casi di studio dove è possibile osservare l’interazione in alta pressione tra peridotiti e fusi dervati dalle eclogiti, promuovendo la formazione di websteriti a granato. Le websteriti, e le pirosseniti in generale, rappresentano eterogeneità composizionali e reologiche dove la deformazione può essere localizzata. La localizzazione della deformazione può anche avvenire quando queste anisotropie sono già presenti all’interno del mantello, come nel caso delle pirosseniti della zona d’Ultimo, le quali accomodano la maggior parte deformazione durante il processo di *corner flow*. In entrambi i casi l’indebolimento del mantello riduce il contrasto reologico tra la crosta subdotta e il mantello soprastante creando condizioni favorevoli per l’incorporazione delle peridotiti all’interno dello *slab*.

Table of contents

Chapter 1

Introduction

Orogenic garnet peridotites occur within high-pressure (HP) and ultra-high pressure (UHP) metamorphic terranes only in few collisional orogens in the world, e.g. Alps (N-Italy), Caledonides (Norway) and Dabie-Sulu belt (China). These mantle rocks frequently experience metasomatism by fluids, melts or supercritical fluids derived at HP or UHP from the subducted crust, thus representing proxies of the crust-to-mantle element exchange in subduction zones (Beyer et al., 2006; Malaspina et al., 2006, 2009; Rampone & Morten, 2001; Scambelluri et al., 2006, 2008; Tumiati et al., 2007; Zhang et al., 2000). The occurrence of orogenic garnet peridotites in HP or UHP metamorphic terranes is interpreted to be related to the sinking of mantle blobs into the subducting slab due to density contrast between the overlying mantle and underlying crust at HP or UHP conditions (Brueckner, 1998). However, experimental studies and numerical models on mantle rheology highlight that mantle is harder than the crust suggesting that other mechanisms, e.g. mantle deformation and weakening, other than density contrast and gravitational instabilities likely govern the material exchange between crust and mantle at HP and UHP.

In this study we have considered two HP terranes where metasomatised garnet peridotites are associated with high-grade variably migmatised crustal rocks, i.e. the Ulten Zone (Tonale nappe, Eastern Alps, Italy) and the Monte Duria area (Adula-Cima Lunga nappe, Central Alps, Italy). Garnet peridotites of Ulten Zone record interactions with fluids derived by the felsic continental crust at HP and HT (2.7 GPa, 850 °C) conditions (Rampone and Morten, 2001; Tumiati et al., 2003, 2007). Alternatively, in this thesis we report that garnet peridotites of Monte Duria area experienced metasomatism at HP and relatively HT (2.8 GPa and 750 °C) by interaction with melts derived by the mafic crust.

In both study areas, garnet peridotites host pyroxenite veins and dikes which record the same metamorphic history of host peridotites. Pyroxenites occurring in the Ulten Zone are an example of crystal segregation from a basaltic melt rising

from the deeper portions of the mantle wedge (Nimis and Morten, 2000) whereas, as will be demonstrated in the next chapters, garnet websterites (now retrogressed in the tremolite stability field) of Monte Duria area represent the products of the interaction between garnet peridotites and eclogite-derived melts.

Numerous studies indicated that the rheology of the upper mantle is primarily controlled by the strength of olivine (Brace and Kohlstedt, 1980; Goetze & Evans, 1979; Ranalli & Murphy, 1987). Following this idea a series of laboratory experiments have been focussed on the rheology of olivine at different pressure, temperature, stress and water content conditions in order to model the rheological behaviour of the upper mantle (Hirth and Kohlstedt, 2003; Karato and Jung, 2003; Karato et al., 2008; Katayama and Karato, 2008; Michibayashi and Ohara, 2013; Ohuchi and Irifune, 2013). However, other mineral phases such as pyroxenes can play a key role in mantle deformation (e.g. Skemer et al., 2008).

Syn-kinematic phase transformation reactions can accompany dynamic recrystallisation inducing grain-size reduction and crystallisation of new minerals, i.e. the so-called second phases (Brodie, 1980; Furusho and Kanagawa, 1999; Hidas et al., 2013; Jin et al., 1998; Kaczmarek and Tommasi, 2011; Newman et al., 1999). This process has been documented in a range of natural and experimental studies and is supposed to be the principal responsible for mantle weakening as it triggers the transition from dislocation creep to grain-size sensitive (GSS) creep (Karato 2008; Platt and Behr, 2011; Raimbourg et al 2008; Rutter and Brodie, 1988; Rutter et al., 2001; Tullis and Yund, 1985; Tullis et al., 1982). Grain-size reduction by dynamic recrystallisation is believed to be not sufficient to promote a permanent transition to GSS creep, unless grain growth is inhibited by second phases produced by phase transformation reactions (De Bresser et al., 1998).

Second phases can also promote the formation of shear instabilities which has been demonstrated to be intimately related to the presence of compositional heterogeneities in the mantle (e.g. pyroxenites), as documented by Toy et al., (2010) in the folded pyroxenite dikes of the Twin Sisters Range, and by Hidas et al., (2013) in the sheared pyroxenite bands of the Ronda Peridotite massif.

In this thesis we will demonstrate that pyroxenites play a key role in mantle weakening and deformation. We suggest that the interaction between peridotites and slab derived melts has important effects on the mechanism controlling the sampling of peridotites into the subducting crust. Melt-rock reactions promote the formation of compositional and rheological anisotropies, i.e. pyroxenites, which can favour strain localisation and weakening in the mantle thus creating favourable conditions for the emplacement of peridotites into the subducting slab.

Chapter 2

Garnet peridotites from Central and Eastern Alps

2.1 Geological and petrological background

Supra-subduction mantle peridotites occur within high-pressure (HP) and ultra-high pressure (UHP) metamorphic terranes only in few collisional orogens in the world such as Alps (N-Italy), Bohemian massifs (Central Europe), Caledonides (Norway) and Dabie-Sulu belt (China). Concerning the Alpine belt (Fig. 1), examples of supra-subduction peridotites are represented by occurrences in Central and Eastern Alps at Monte Duria (Adula-Cima Lunga nappe) and Ulten zone (Tonale nappe).

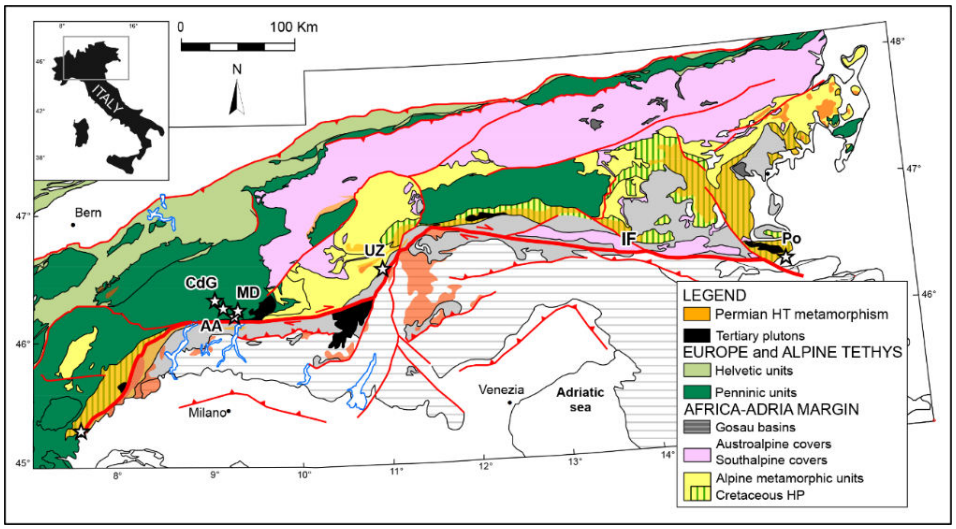

Fig.1 Tectonic scheme of the Alps (Modified after Bergomi et al., 2015). Garnet peridotites are shown. Abbreviations as follows: *CdG* Cima di Gagnone, *AA* Alpe Arami, *MD* Monte Duria, *Po* Pohorje, *IF* Insubric Fault.

2.1.1 Central Alps: Adula-Cima Lunga nappe

The Adula-Cima Lunga nappe (ACL) is located on the eastern flank of the Lepontine Dome (Fig. 2a) and it represents the highest of the Lower Penninic units of the Central Alps (Milnes, 1974; Schmid et al., 1996). It corresponds to the distal European margin located to the north of the North Penninic Ocean, opened in the late Jurassic and later closed during the Tertiary convergence between Europe and Adria plates (Nagel et al., 2008). The ACL nappe consists of a lithospheric mélange (Trommsdorff 1990; Engi et al. 2001) made of ortho- and paragneisses of pre-Mesozoic age, partially retrogressed eclogites, amphibolites, marbles, metasedimentary rocks of supposed Mesozoic origin (Galster et al., 2012) and minor serpentinite and peridotite bodies (Evans and Trommsdorff, 1978; Fumasoli, 1974; Heinrich, 1986; Mockel, 1969).

In the Central Alps nappe stack, the ACL is comprised between the underlying Lower Penninic units of Simano and Leventina nappes and the Middle Penninic units of Tambò, Suretta and Schams nappes above (Fig. 1a; Schmid et al., 1990). The ACL and the overlying Middle Penninic units are separated by the Misox Zone, a narrow N-S trending heterogeneous unit of dominantly North-Penninic provenance made by carbonatic and siliciclastic metasediments (Bündnerschiefer Auct.), MORB-derived amphibolites and slivers of continental basement (Steinmann and Stille, 1999; Stucki et al., 2003). The lower contact of the ACL is somewhat less defined since the lower ACL and the upper Simano nappes are lithologically homogeneous (Jenny et al. 1923; Partzsch 1998; Nagel et al., 2008). To the east the Forcola normal fault (Ciancaleoni & Marquer 2006) separates the ACL nappe (sensu strictu) from the Gruf complex which is generally considered to be part of the ACL (e.g. Davidson et al., 1996). The Gruf complex mainly consists of biotite + garnet + sillimanite + cordierite-bearing metapelitic rocks and migmatitic ortho- and paragneisses. This complex experienced ultrahigh temperature (UHT) metamorphism of still debated age, either considered to be Permian (Galli et al., 2011, 2013) or Oligocene (Droop and Bucher, 1984; Liati and Gebauer, 2003; Nicollet et al., 2018).

The southern limit of the ACL is represented by the Paina fault (or Paina Marble Zone), marked in the field by a thin slice of silicate-bearing marbles interpreted as the upper contact of the ACL (Fig. 1b; Fumasoli, 1974; Heitzmann, 1987; Schmid et al., 1996). The Paina Fault separates the ACL nappe complex by the Bellinzona-Dascio Zone (hereafter BDZ), an E-W striking unit made by metapelitic rocks, orthogneisses, marbles and scattered lenses of amphibolites and metaperidotites (Fig. 1b; Stucki et al., 2003), and is considered to represent the southern continuation of the Misox Zone (Nagel et al., 2008).

In the eastern Lepontine Dome the ACL nappe is the only continental unit that was subducted to mantle depths during both the Variscan (e.g. Biino et al., 1997) and the Alpine orogenic cycles (Becker 1993; Gebauer et al. 1996; Dale and Holland, 2003; Meyre and Frey, 1998; Nagel et al., 2002a). Despite the intensive Alpine metamorphism and deformation, relicts of pre-Alpine (Variscan) HP metamorphism are still preserved in the central and northern sectors of the ACL (Herwartz et al., 2011; Liati et al., 2009). P-T estimates of HP assemblages in eclogites from Confin (Co in Fig. 2a), Val Large (VL in Fig. 2a) and Trescolmen (Tr in Fig.2a) localities, suggest equilibrium conditions of P = 1.4-2.2 GPa and T = 500-700 °C (Dale and Holland, 2003; Heinrich, 1983; Nagel, 2008). The HP metamorphism related to the Alpine subduction is well preserved through the entire ACL nappe. Peak-pressure conditions derived from eclogites increase southward from 1.2 GPa and 500-600 °C in the north to 2.5-3.0 GPa and 750-850 °C in the south (Brouwer et al., 2005; Dale and Holland, 2003; Heinrich, 1986). The highest pressures were recognised in the ultramafic rocks cropping out in the southern part of the nappe (Tab. 1).

In the ACL nappe peridotites were found at Cima di Gagnone (CdG in Fig. 2a; Evans and Trommsdorff, 1978), Alpe Arami (AA in Fig. 2a; Mockel, 1969) and Monte Duria (MD in Fig. 2a; Fumasoli, 1974). At CdG chlorite harzburgites and subordinate garnet lherzolites are embedded within metapelite-derived migmatites and quartzo-feldspatic gneisses. Peridotites contain eclogite and metarodingite boudins interpreted as primary basaltic/gabbroic intrusions with MORB type geochemical affinity (Evans et al., 1979). The occurrence of eclogites indicates that ultramafic and mafic rocks from CdG underwent subduction zone metamorphism. Thermobarometry of the peak garnet-facies assemblages of CdG metaperidotites provided estimates of 750-800 °C and 2.5-3 GPa (Tab. 1; Evans & Trommsdorff, 1978; Nimis & Trommsdorff, 2001). Metarodingites provide evidence for an early serpentinite stage (Evans and Trommsdorff, 1978) indicating that CdG peridotites represent a serpentinised mantle that recorded full antigorite-breakdown during subduction (Evans and Trommsdorff, 1978; Trommsdorff et al., 2000; Scambelluri et al., 2014). Sm-Nd and Lu-Hf garnet-clinopyroxene-whole rock dating of garnet metaperidotites yielded ages of ca. 40 Ma (Becker et al., 1993; Brouwer et al., 2005). Isotope ages of 43-45 Ma were also obtained using U-Pb zircon dating by Gebauer, (1996). At AA garnet lherzolites form the core of a km-sized chlorite peridotite body. The peridotite body is surrounded by migmatitic gneisses and it is locally bordered by slices of kyanite eclogites and clinopyroxenites. The origin of the AA peridotite is still debated since it is believed to represent either a sub-continental lithospheric mantle exhumed during the formation of the Alpine

Tethys and later involved in the Alpine subduction (Trommsdorff et al., 2000) or a supra-subduction mantle sampled by the downgoing European lithosphere during the Alpine orogeny (Brenker and Brey, 1997). P-T estimates for the HP metamorphism experienced by garnet peridotites of AA are controversial and vary from 3.0 GPa and 850 °C (Tab. 1; Nimis and Trommsdorff, 2001), to 5.0 GPa and 1120 °C (Brenker & Brey 1997), to 5.9 GPa and 1180 °C (Paquin & Altherr 2001). Pressure exceeding 10 GPa have been also inferred from exsolved ilmentite rods in olivine (Dobrzhinetskaya et al. 1996) and clinoenstatite in diopside (Green et al., 2010; Bozhilov et al. 1999). Sm-Nd and Lu-Hf garnet-clinopyroxene-whole rock dating of garnet peridotites yielded ages of ca. 40 Ma, consistently with the age of the HP metamorphism recorded by CdG metaperidotites (Becker et al., 1993). At MD garnet and chlorite peridotites occur within migmatitic biotite gneisses (Fumasoli et al., 1974) or associated with variably migmatised HP mafic rocks (Tumiati et al., 2018). Ultramafic rocks from MD experienced HP metamorphism at ca. 3.0 GPa and 750-850 °C (Nimis & Trommsdorff, 2001; Tumiati et al., 2018), and are considered to derive from the supra-subduction mantle above the Late Cenozoic subduction of the European continental margin (Hermann et al., 2006). The age of the HP metamorphism in the Monte Duria area is still unknown. However, the initial stages of decompression (close to the HP peak) are dated at 34 - 33 Ma by U-Pb SHRIMP dating of zircons recording equilibrium conditions with spinel in garnet peridotites (Hermann et al., 2006). Recently Tumiati et al., (2018) provided evidence for a previously unknown LP-(U)HT metamorphic event which post-dates the HP assemblages and pre-dates the Barrovian metamorphism of the Lepontine Dome in peridotites and eclogites of Monte Duria area. Pressure-temperature estimates of LP- (U)HT assemblages found in both mafic and ultramafic rocks yielded T = 850 °C and P = 0.8-1.2 GPa (Tab. 1). It is worthy of note that similar conditions are also reported for the (U)HT stage recorded in the sapphirine-bearing granulites and charnockites of the near Gruf Complex (Galli et al., 2011).

The peridotites and associated crustal rocks of the Monte Duria area, together with the whole ACL complex, eventually experienced the post-collisional metamorphism that affected the entire central Alpine nappe stack (Nagel, 2008). The Barrovian-type metamorphism increases southward from upper green-schists facies in the north to high amphibolite facies in the south (Nagel, 2008; Todd and Engi, 1997), where it promoted crustal anatexis in a narrow belt (Southern Migmatite belt; Berger and Bousquet, 2008; Burri et al., 2005; Rubatto et al., 2009) close to the Insubric Fault. Partial melting was promoted by fluid infiltration and occurred between 32 and 22 Ma suggesting a

protracted high thermal history during Barrovian-type metamorphism (Rubatto et al., 2009).

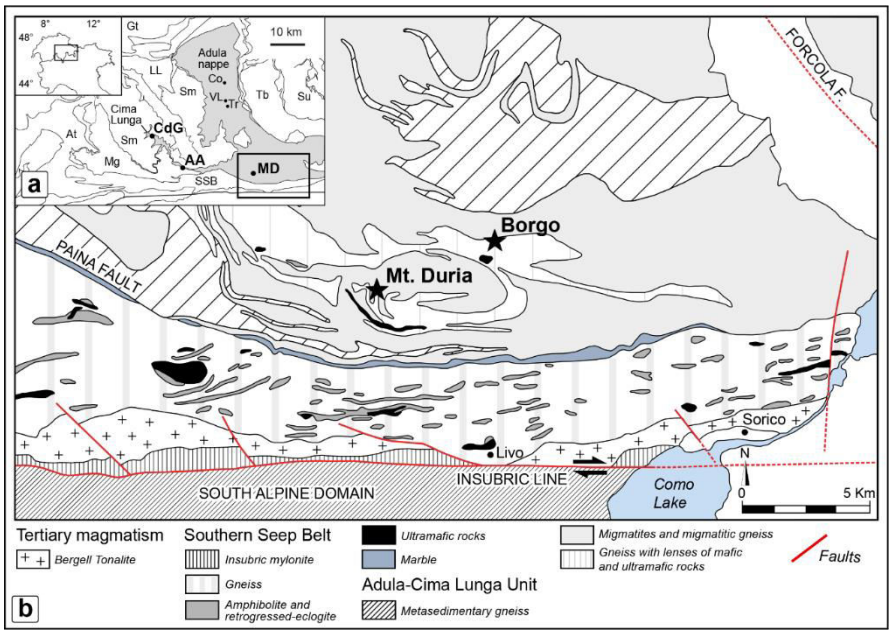

Fig. 2 (a) Tectonic scheme of the Adula-Cima Lunga nappe modified after Burri et al. (2005). The heavy rectangle is the framework for Fig. 2b. (b) Detailed geological scheme of the Monte Duria area with the locations of Mt. Duria and Borgo outcrops modified from Tumiati et al. (2018). Abbreviation as follows: *At* Antigorio; *Mg* Maggia; *Sm* Simano; *LL* Leventina Lucomagno; *Tb* Tambò; *Su* Suretta; *SSB* Southern Steep Belt; *Co* Confin; *VL* Val Large; *Tr* Trescolmen.

Table 1

Locality	Lithology	Pressure (Gpa)	Temperature (°C)	References
Alpe Arami	garnet lherzolite	2.47	ca. 800	Evans and Trommsdorff, (1978)
Alpe Arami	garnet lherzolite	4	950	Ernst, (1981)
Alpe Arami	garnet lherzolite	5.0±0.2	1120±50	Brenker and Brey, (1997)
Alpe Arami	garnet lherzolite	ca. 15	ca. 1600	Dobrzhinetskaya, (1996)
Alpe Arami	garnet lherzolite	>10	ca. 1600	Bozhilov et al., (1999)
Alpe Arami	garnet lherzolite	3.2	840	Nimis and Trommsdorff, (2001)
Alpe Arami	garnet lherzolite	5.9±0.3	1180±40	Paquin and Altherr, (2001)
Cima di Gagnone	garnet lherzolite	2.87	806	Evans and Trommsdorff, (1978)
Cima di Gagnone	garnet lherzolite	2.5	800	Pfiffner at al., (1999)
Cima di Gagnone	garnet lherzolite	3.0	740	Nimis and Trommsdorff, (2001)
Cima di Gagnone	garnet lherzolite	2-3	>800	Scambelluri et al., (2014)
Cima di Gagnone	chlorite harzburgite	ca. 3	720-800	Scambelluri et al., (2014)
Monte Duria	garnet lherzolite	2.48	835	Evans and Trommsdorff, (1978)
Monte Duria	garnet lherzolite	3.0	830	Nimis and Trommsdorff, (2001)
Monte Duria	garnet lherzolite	2.8±0.2	730±20	Tumiati et al., (2018)

Peak pressure-temperature estimates of ultramafic rocks in the ACL nappe complex

2.1.2 Eastern Alps: Tonale nappe

The Tonale nappe is located north of the Insubric Fault in the Italian Eastern Alps (Fig. 3a) and it represents the tectonically highest unit of the middle Austroalpine domain (e.g. Tollmann, 1987). It corresponds to a fragment of the lower continental crust of the European Varisican belt, generated by the collision of Gondwana and Larussia plates during the Carboniferous, and later dismembered along transtensive and normal faults during Late Paleozoic-Mesozoic times becoming part of the Adria microcontinent (Ziegler, 1984; Eberli, 1988; Neugebauer, 1990; Dal Piaz, 1993). The Tonale nappe constitutes a lithospheric mélange consisting of variably migmatised metapelites, orthogneisses, marbles, calc-silicate rocks, quartzites, serpentinite and peridotite bodies, and rare retrogressed eclogite lenses (Obata and Morten, 1987; Godard et al., 1996; Del Moro et al., 1999; Ranalli et al., 2005; Bargossi et al., 2010). The entire Tonale nappe shows HP-HT Variscan metamorphism and only a weak Alpine overprint, mostly restricted near the principal tectonic lineaments (i.e. Pejo, Rumo, Val Clapa, Giudicarie and Tonale lines, Fig. 3a).

In the eastern alpine edifice, the Tonale nappe is comprised between the Pejo, Giudicarie and Tonale lines (Fig. 3a). The Pejo line separates the Tonale nappe from the underlying Ortler-Campo nappe (Andreatta, 1948), a unit consisting of sedimentary covers (Ortler series) and basement rocks including slivers of ultramafic material (Campo basement). The Giudicarie and Tonale lines (segments of the Insubric fault) divide the Tonale nappe from the Permo-Jurassic sedimentary units of the Southern Alps.

The Tonale nappe include the Tonale and Ulten units which are tectonically divided by the Val Clapa and Rumo lines (Fig. 3b) (Morten et al., 1976). The Tonale unit largely consists of sillimanite ± garnet paragneisses, orthogneisses, marbles, calc-silicate rocks, quartzites, amphibolites and serpentinised ultramafic rocks displaying a high-grade pre-Alpine (Variscan) metamorphic overprint (Martin and Prosser, 1993; Godard et al.,1996; Bargossi et al., 2010). This basement unit was later extensively retrogressed during late- or post- Variscan exhumation and was locally deformed at greenschist-facies conditions during the Alpine orogeny (Thöni, 1981).

The Ulten unit, known in literature also as Ultental-Nonsberg area or Ulten zone (hereafter Ulten zone, UZ) mainly consists of variably migmatised high grade garnet + kyanite gneisses (Ranalli et al., 2005) with subordinate retrogressed eclogite bodies (Del Moro et al., 1999) and peridotite lenses (Obata and Morten, 1987; Godard et al., 1996) displaying well-preserved pre-Alpine (Variscan) HP-HT metamorphic signatures only weakly overprinted by the

Alpine metamorphism. Isotopic Sm-Nd garnet-whole-rock and garnet-clinopyroxene dating on peridotites, eclogites and the country migmatitic yielded ages for all rock types at ca. 330 Ma (Tumiati et al., 2003).

The high-grade crustal rocks of the UZ are divided in: i) a lower unit consisting of weakly migmatised blastomylonitic banded garnet + kyanite gneisses (stromatic gneisses or metatexites sensu Sawyer, 2008) and ii) an upper unit made by strongly migmatised garnet + kyanite gneisses (nebulitic migmatites or diatexites sensu Sawyer, 2008). These units include variably retrogressed eclogite bodies with locally preserved peak eclogitic assemblages (Godard et al. 1996). Both gneisses and mafic rocks share a common evolution from eclogite- to granulite- to amphibolite-facies conditions. Maximum pressures and temperatures recorded by stromatic gneisses and migmatites are estimated at 1.5-2.5 GPa and 700-850 °C (Benciolini and Poli 1993; Hoinkes and Thöni 1993; Godard et al. 1996; Tumiati et al. 2003). Migmatisation occurred under fluid-absent condition by phengite dehydration-melting at temperatures of 850 °C and minimum pressures of 1.5-2.5 GPa (Benciolini and Poli, 1993; Hoinkes & Thöni, 1993; Godard et al., 1996; Hauzenberger et al., 1996; Tumiati et al., 2003). Partial melting in the crustal units at HP conditions likely occurred during prograde subduction or during the early stages of exhumation after the pressure peak (see discussion of Tumiati et al., 2003).

Peridotites form metre to hectometre-scale lenses mostly occurring in a narrow horizon at the transition between the stromatic gneisses and the overlying nebulitic migmatites. Peridotites show a transition from coarse protogranular spinel-lherzolites (coarse-type of Obata and Morten, 1987) to fine-grained mylonitic garnet-amphibole peridotites (fine-type of Obata and Morten, 1987). The passage from the coarse to the fine types, is accompanied by the crystallisation of garnet at the expenses of spinel. Garnet initially formed as coronas around spinel and as exsolution lamellae in pyroxenes, and later as neoblasts that are in textural equilibrium with a recrystallized peridotite matrix consisting of olivine, enstatite, amphibole, and minor Cr-rich spinel. P-T estimates on spinel-facies assemblages yielded equilibrium condition of P = 1.3-1.6 GPa and T =1200 °C (Nimis and Morten, 2000). During this stage, peridotites were infiltrated by hydrous melts rising from deep regions of the lithospheric mantle, precipitating coarse-grained pyroxenites in the host peridotites (Nimis and Morten, 2000). Pyroxenites grade to fine-grained garnet-amphibole websterites showing the same textural evolution of the host peridotites. Thermobarometry of the peak garnet-facies assemblages of both peridotites and websterites provided estimates of 2.7 GPa and 850 °C (Nimis and Morten, 2000; Tumiati et al., 2003). This evolution has been interpreted as the result of mantle

corner flow from hot regions of the subcontinental lithospheric mantle to deeper and cooler mantle domains located at the top of the slab (Nimis and Morten, 2000). The transition from spinel- to garnet-amphibole peridotites was accompanied by intense shearing and fluid infiltration to form amphibole-garnet-bearing assemblages (Obata and Morten, 1987; Rampone and Morten, 2001). Hydration promoted the crystallisation of large garnet porphyroclasts (up to 9 cm) with partially resorbed inclusions of pargasite, suggesting crystallisation in environments characterised by high fluid circulation (Tumiati et al., 2003). The formation of amphibole-garnet-bearing paragenesis was accompanied also by the crystallization of phlogopite, dolomite, allanite and dissakisite-(La) (Obata and Morten, 1987; Tumiati et al., 2005), and by significant LILE and LREE enrichments in minerals recording equilibrium conditions with garnet, testifying the input of slab-derived fluids (Rampone and Morten 2001; Scambelluri et al, 2006).

Finally, the retrograde decompressional evolution of UZ peridotites is documented by the development of spinel + orthopyroxene + clinopyroxene + amphibole and orthopyroxene + amphibole + clinopyroxene kelyphites around garnet and, the complete replacement of garnet by chlorite pseudomorphs or by coarse-grained amphibole + spinel aggregates (Martin et al., 1998; Godard et al., 2000).

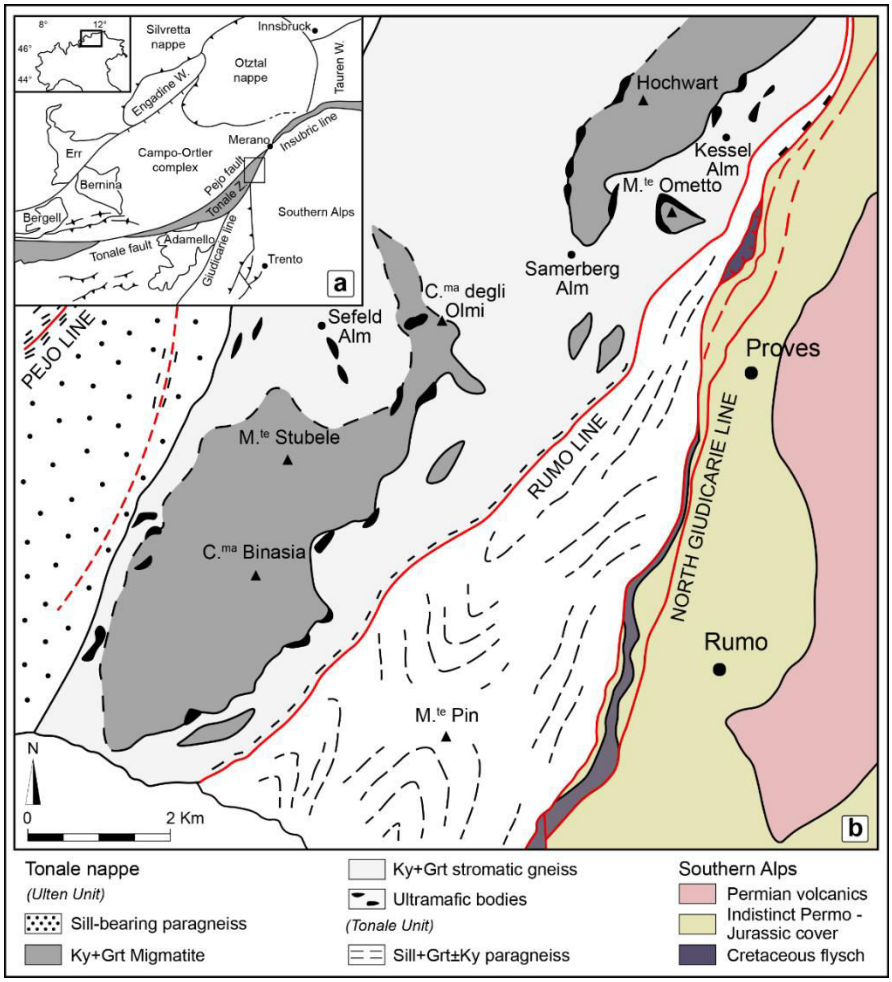

Fig. 3 (a) Geological sketch map of Eastern Alps (modified after Del Moro et al., 1999). The heavy rectangle is the framework for Fig. 2b. (b) Geological map of the Ulten zone (Redrawn after Del Moro at al., 1999).

Chapter 3

Field occurrence

3.1 Monte Duria area

The Monte Duria area is located on the north-western side of the Como Lake (Northern Italy) in the southern ACL nappe complex. In this area peridotites are exposed within variably migmatised crustal rocks at two sites: the SE ridge of Monte Duria and at Borgo, along the Darengo Valley.

At Monte Duria numerous metre- to decametre-scale peridotite lenses are exposed in a narrow horizon of migmatitic biotite gneisses (Fig. 4; Fumasoli, 1974). Peridotites are often garnet-bearing and are characterised by coarse garnet (up to 1-2 cm), clinopyroxene and amphibole porphyroclasts embedded in a fine-grained matrix consisting of olivine, clinopyroxene and orthopyroxene. Garnet is always mantled by spinel + orthopyroxene + clinopyroxene ± amphibole kelyphitic coronas and is progressively replaced by rounded chlorite pseudomorphs close to the outermost part of the peridotite bodies (Fig. 5a and b). Peridotites locally contain garnet + Cr-diopside aggregates (up to 5 cm; Fig. 5c) and clinopyroxenite veinlets characterised by cm-sized emerald-green Cr-diopside (Fig. 5d). Peridotites display a compositional layering marked by garnet-rich and garnet-poor levels with a uniform E-NE-dipping orientation. This layering is transposed close to the outermost part of the peridotite lenses by a chlorite foliation that dips to N-NW parallel to the main foliation of hosting biotite gneisses (Fig. 5e and f).

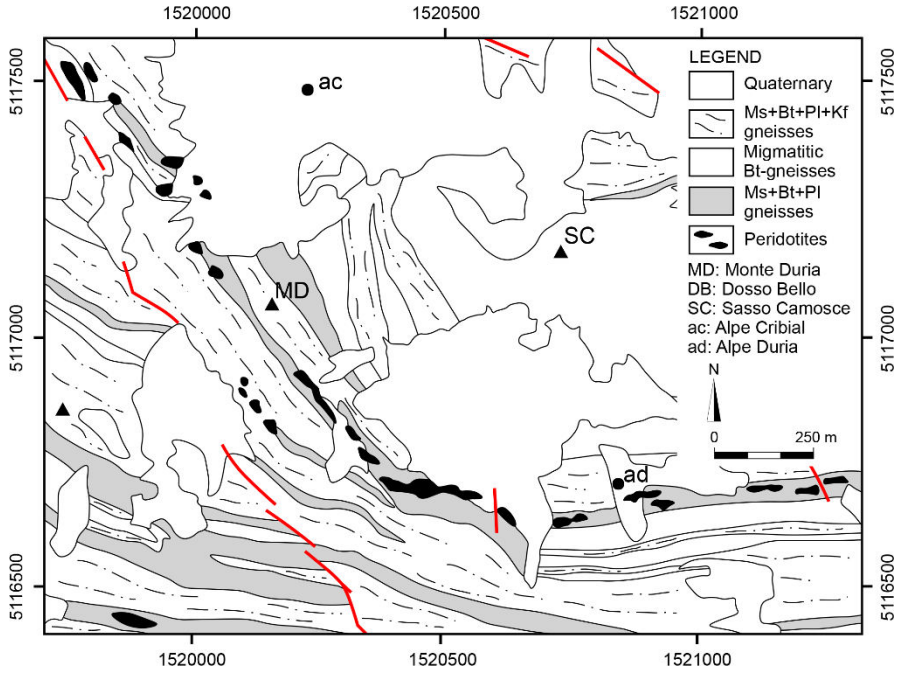

Fig. 4 Occurrence of peridotite lenses in the Monte Duria area (redrawn after Fumasoli, 1974).

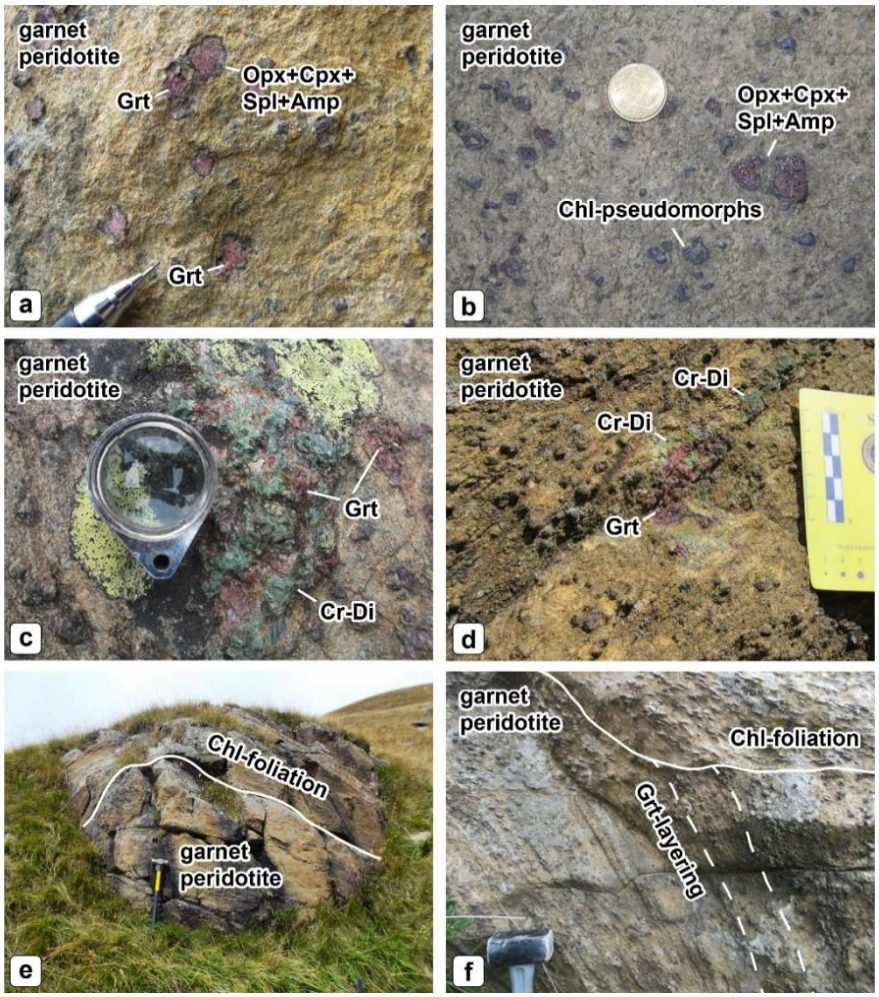

Fig. 5 Structures of ultramafic rocks of Monte Duria. Mineral abbreviations from Whitney and Evans, (2010). (a) Porphyroclastic texture of peridotites. Garnets (up to 1 cm) are mantled by symplectitic Opx + Cpx + Spl ± Amp coronas; (b) Garnets replaced by round-shaped chlorite pseudomorphs; (c) Centimetre-scale (up to 5 cm) garnet + Cr-diopside aggregate in garnet peridotite; (d) Garnet websterite vein transposed along the garnet foliation in the garnet peridotite; (e) Chlorite foliation developed close to the outermost part of the garnet peridotite lens; (f) Detail of the garnet layering transposed by the secondary chlorite foliation garnet in peridotites.

At Borgo, a 100 metre-scale chlorite peridotite body is in direct contact with amphibole-bearing migmatites hosting preserved boudins of mafic eclogites, high-Al_2O_3 eclogites and kyanite eclogites (Fig. 6; Tumiati et al., 2018). The chlorite peridotite body and the associated mafic rocks are enclosed within migmatitic biotite gneisses like those hosting garnet peridotites of Monte Duria. The chlorite peridotite (lilac in Fig. 6) is characterised by fine-grained olivine, minor orthopyroxene and rare clinopyroxene. In the peridotite body garnet was not observed since it is always replaced by chlorite pseudomorphs (Fig. 7a), likely indicating that the chlorite peridotite of Borgo represents the retrogressed variety of the garnet peridotite of Monte Duria. Large garnet porphyroclasts (up to 3 cm) commonly replaced by rounded chlorite pseudomorphs have been observed only in a loose block downstream of the Borgo outcrop (Fig. 7b). Chlorite peridotites preserve a compositional layering made by alternate levels rich or poor in chlorite pseudomorphs after garnet (Fig. 7c). This layering dips to the east and it is locally transposed by a NE-dipping chlorite foliation that becomes more penetrative close to the contact with the country amphibole-bearing migmatites (Fig. 7d).

The contact between chlorite peridotites and mafic rocks at Borgo is marked by the occurrence of a metre-scale tremolitite layer (violet in Fig. 6; Fig. 8a) consisting of tremolite (80-90 vol.%) with subordinate phlogopite + chlorite + talc + tremolite pseudomorphs after garnet and minor Mg-hornblende. This layer shows sharp contacts with the host peridotite and it is folded around isoclinal folds with axial planes (N-NE-dipping) oriented parallel to the chlorite foliation in the peridotite (Fig. 8b-1). Tremolitites are associated with decimetre-sized boudins composed by tremolite and minor phlogopite (Fig. 8b-2). Tremolite + phlogopite rich rocks also form a centimetre-thick rim close to the outermost part of the peridotite body (Fig. 8b-3). Tremolitites also occur as stretched layers within the chlorite peridotite body (Fig. 9a). These layers display sharp limits (Fig. 9b-1) and are interlayered with tremolite + phlogopite levels that show irregular shapes and diffuse contacts with the host peridotite (Fig. 9b-2). Both tremolitites and tremolite + phlogopite levels are transposed along the chlorite foliation in the peridotite and are cut by late NNW-SSE-striking tremolite and serpentinite veins (Fig. 9b). In the innermost part of the peridotite body (about 20 metres from the contact with the surrounding amphibole-bearing migmatites) decametre-scale tremolitites are strongly stretched and boudinaged as pinch-and-swell structures (Fig. 10a). They show sharp limits and strike NW-SE parallel to the now retrogressed garnet foliation in the peridotite (Fig. 10b-1 and b-2). The retrogressed garnet foliation wraps around the boudins and flows into the boudins

necks (Fig. 10b-3) indicating that the deformation of tremolitites occurred during the development of the garnet foliation in the host peridotite.

The amphibole-bearing migmatites of Borgo (pink salmon in Fig. 6) display a stromatic texture with millimetre to decimetre-spaced bands characterised by quartz + plagioclase + K-feldspar + biotite leucosomes and amphibole-rich melanosomes (restites) transposed along a NE-dipping S2 foliation (S1 structures are preserved in the eclogite boudins; Fig. 6). Both leucosomes and restites are folded around tight to isoclinal folds D3 with decimetre- to metre-scale wavelength (Fig. 6 and 11a). Fold axis trend from 88° to 152° and an embryonic biotite-bearing axial plane foliation S3 has been observed in fold hinges. Peculiar deformation structures like lobes and cusps (e.g. McLellan, 1989) locally occur parallel to the S2 foliation (Fig. 11b) indicating that partial melting likely was synkinematic with respect to the D2 deformation phase.

The amphibole-bearing migmatites contain boudins of mafic, high-Al_2O_3 and kyanite eclogites (Pellegrino, 2016; Tumiati et al., 2018). Fine grained, dark green mafic eclogites (dark green in Fig. 5) occur as decimetre to metre-sized boudins (Fig. 11c). These rocks show a S-SW-dipping compositional layering (S1) marked by garnet-rich and garnet-poor horizons cut by the S2 foliation of the surrounding amphibole-bearing migmatites (Fig. 6 and 11c). Larger boudins (up to 10 metres) of light green, kyanite-bearing eclogites also occur (light green in Fig. 6; Fig. 11d). As already described for the mafic eclogites, a NE-dipping compositional layering (S1) consisting of garnet-rich and garnet-poor layers represents the main fabric at the mesoscale. The high-Al_2O_3 eclogite (red rim in Fig. 6) occurs as a cm-thick reddish corundum-rich rim at the contact between kyanite-bearing eclogite and amphibole-bearing migmatites (Fig. 11e). These rocks are garnet-free and only porphyroblastic kyanite and emerald-green zoisite were observed (Tumiati et al., 2018). Several decimetre-sized boudins composed by amphibole and minor phlogopite (blue spots in Fig.6) were also recognised embedded in the amphibole-bearing migmatites (Fig. 11f).

The peridotite body and the associated mafic rocks are both separated from the surrounding migmatitic biotite gneisses (yellow in Fig. 6; Fig. 12a) by a few metre-thick mylonitic shear zone with a NE-dipping orientation (Fig. 6 and 12b). The migmatitic gneisses have a stromatic structure defined by alternating quartz + plagioclase + K-feldspar leucocratic bands and biotite-rich melanocratic domains transposed along a NE-dipping S3 foliation (Fig. 6 and 12c) folded by steeply plunging D4 asymmetric folds (Fig. 6 and 12d). It is worthy of note that from field observations is difficult to link the deformation history of peridotites with that of country crustal rocks.

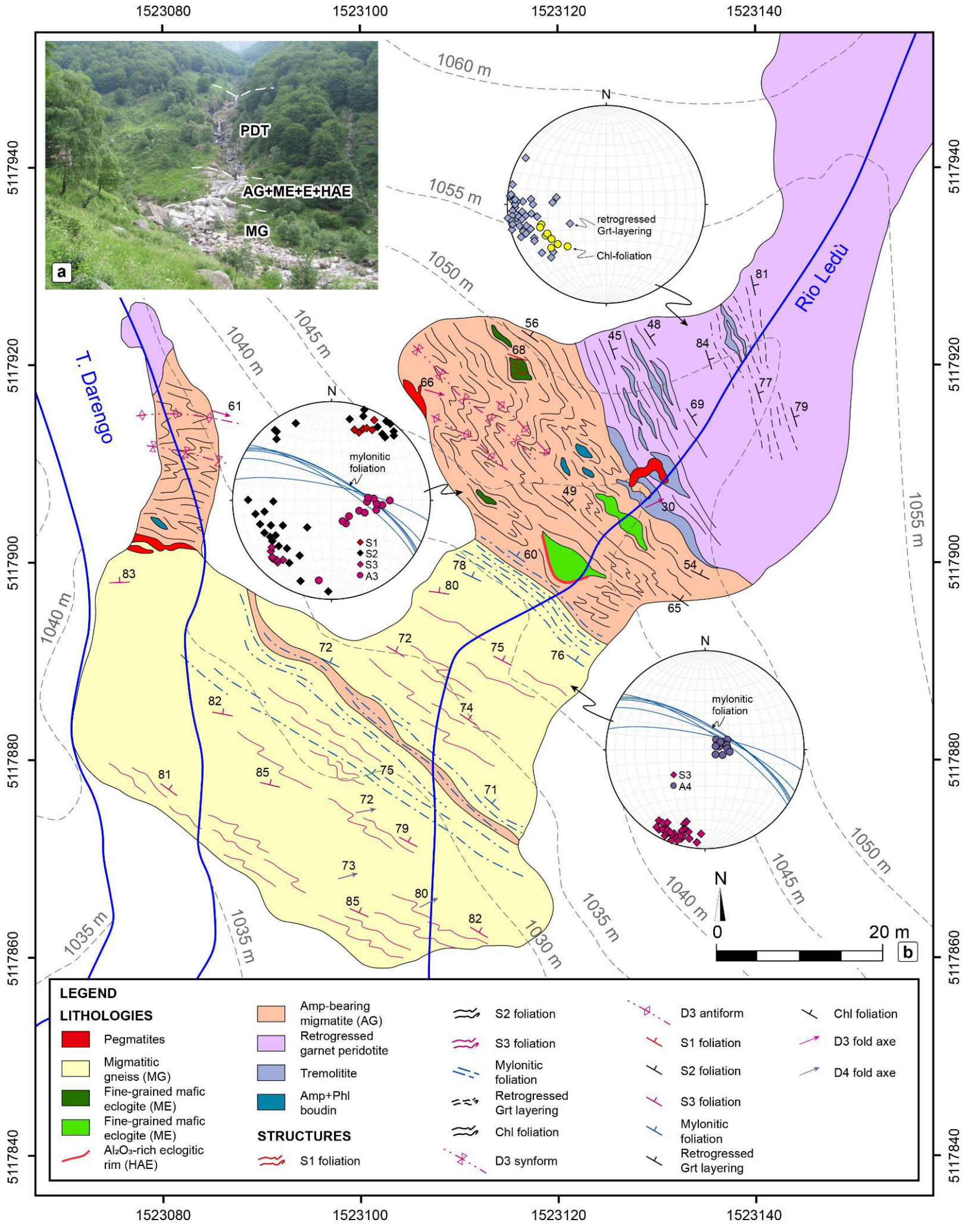

Fig. 6 (a) Borgo outcrop. PDT: retrogressed garnet peridotite; AG: amphibole-bearing migmatites; ME: mafic eclogites; E: kyanite eclogites; HAE: high-Al_2O_3 rim between kyanite eclogites and host amphibole-bearing migmatites. (b) Detailed geological map of the Borgo outcrop.

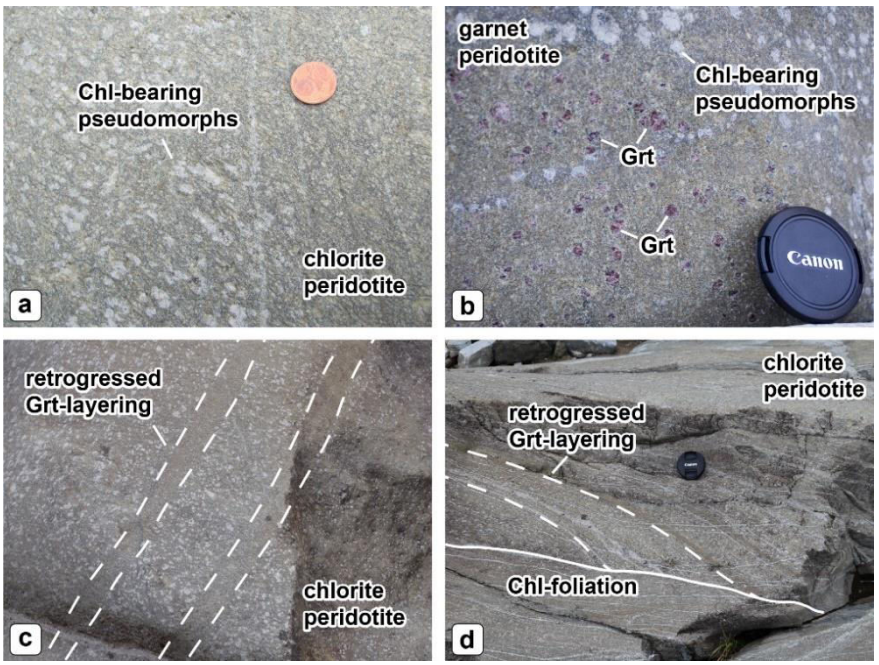

Fig. 7 Structures of ultramafic rocks of Borgo outcrop. (a) Chlorite-bearing pseudomorphs replacing garnets in chlorite peridotite. (b) Preserved garnets in a loose block of peridotite along the Ledù stream. (c) Retrogressed garnet layering marked by alternating levels rich or poor in chlorite pseudomorphs after garnet. (d) Retrogressed garnet layering cut by a chlorite foliation.

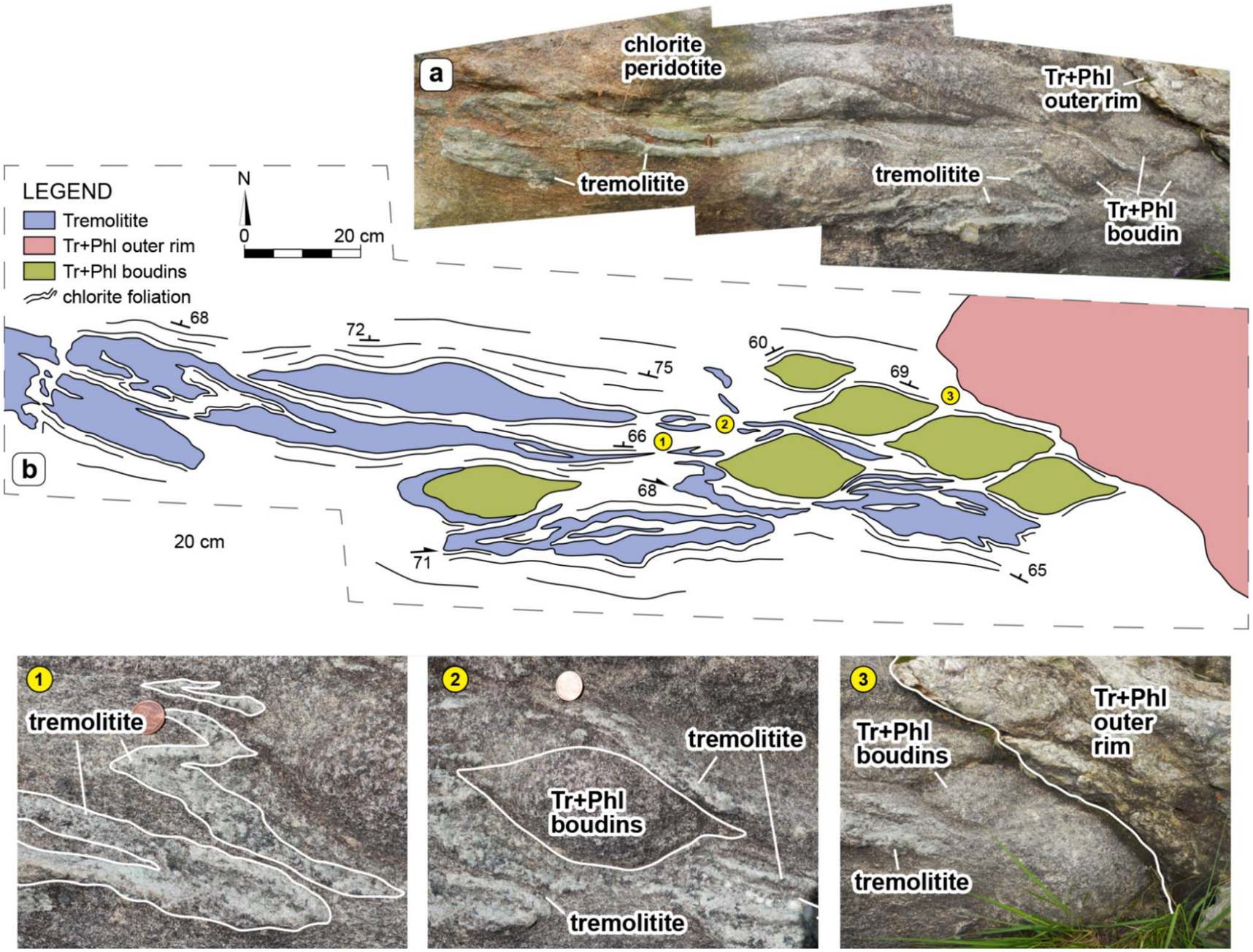

Fig. 8 (a) tremolitite layer at the contact between chlorite peridotites and associated amphibole-bearing migmatites at Borgo outcrop. (b) Detailed geological sketch map of the tremolitite layer. (b-1) Tight to isoclinally folded tremolitite. (b-2) Tr + Phl boudin in the chlorite peridotite. (b-3) Tr + Phl rich rocks at the rim of the chlorite peridotite body.

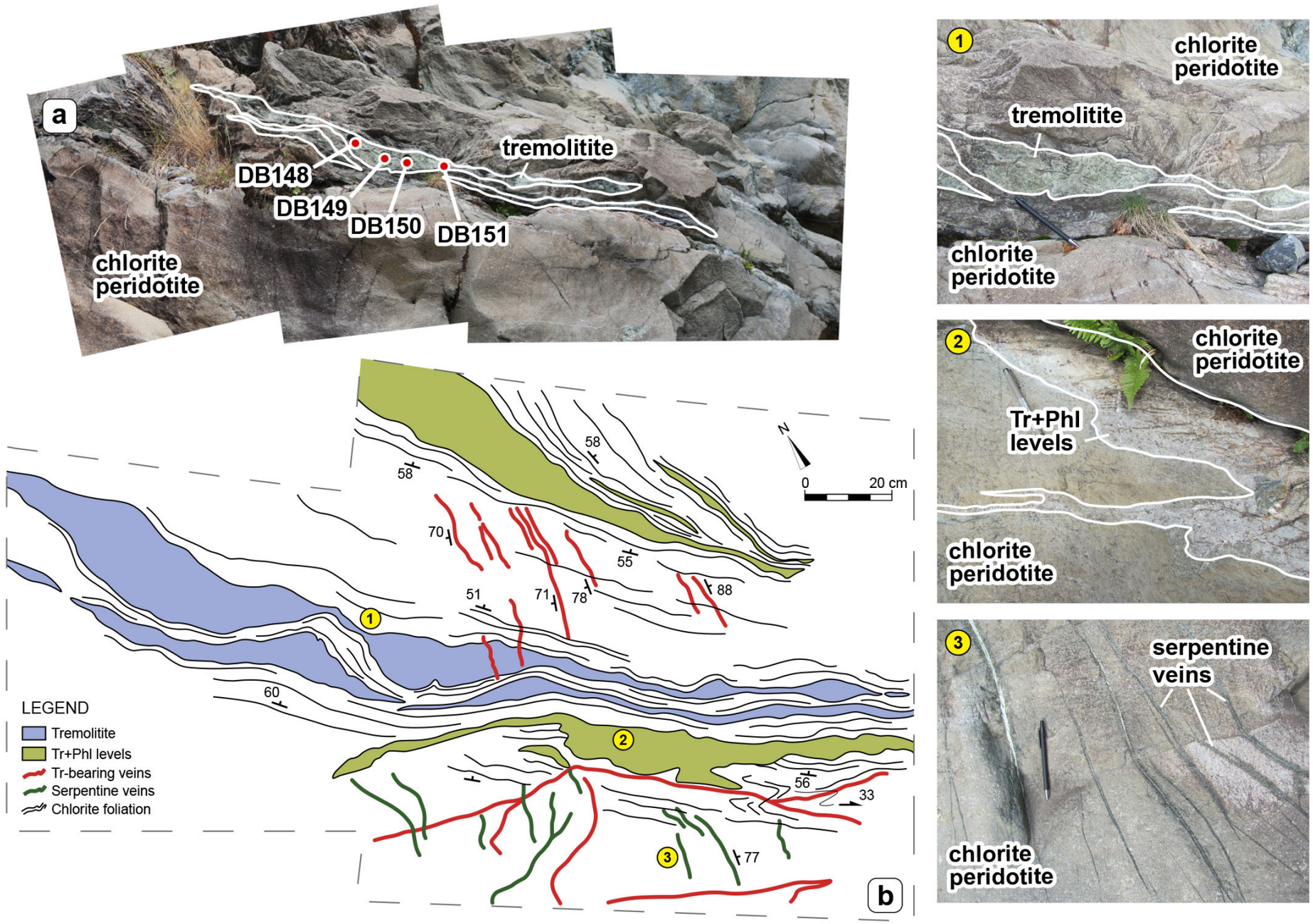

Fig. 9 (a) variably stretched tremolitite layer within the chlorite peridotite of Borgo outcrop. (b) Detailed geological sketch map of the tremolitite layer. (b-1) Tremolitite showing sharp contact with the host chlorite peridotite. (b-2) Tr + Phl level displaying diffuse contact with the host chlorite peridotite. (b-3) Detail of serpentinite vein

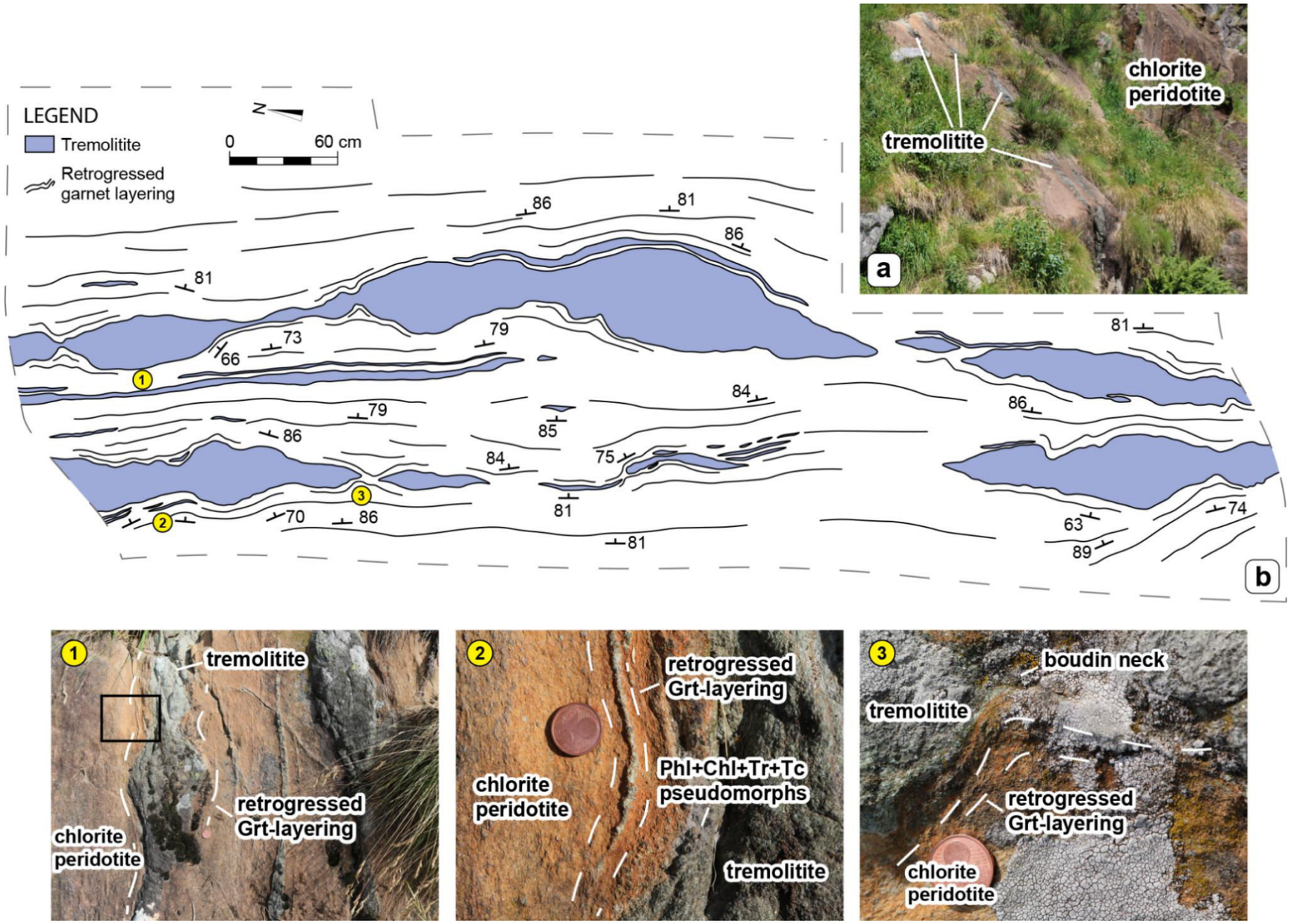

Fig. 10 (a) Tremolitite deformed as pinch and swell structure in the inner portions of the chlorite peridotite of Borgo outcrop. (b) Detailed geological sketch map of the tremolitite layer. (b-1) Retrogressed garnet layering of peridotite wrapping the tremolitite boudins. The heavy rectangle is the framework for Fig. 10b-2. (b-2) Detail of Fig. 9b-1. Tremolitite shows Tr + Phl + Chl + Tc pseudomorph after garnet. (b-3) Retrogressed garnet layering of peridotite flowing in the boudin neck.

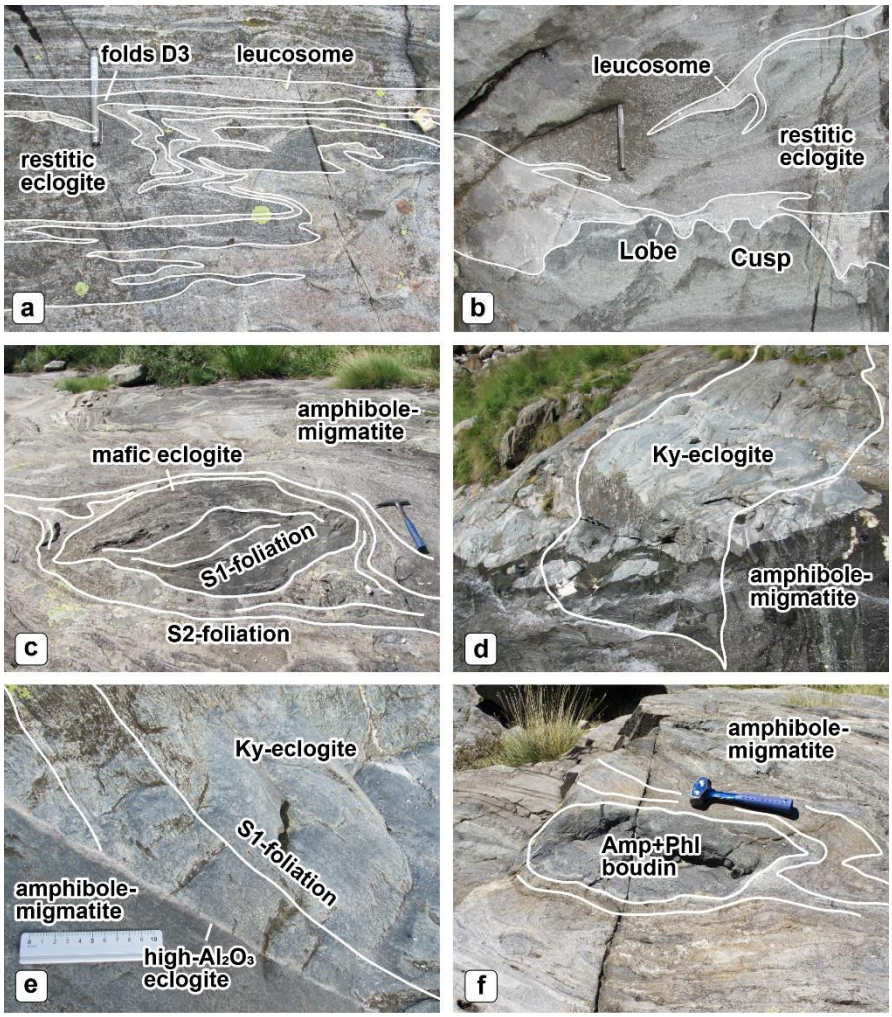

Fig. 11 Structures of crustal rocks of Borgo outcrop. (a) Leucosomes and melanosomes in amphibole-bearing migmatites folded around tight to isoclinal folds D3. (b) Lobes and cusps structures in amphibole-bearing migmatites. (c) Mafic eclogite boudin in amphibole-bearing migmatites. The S1 foliation of the mafic eclogite is cut by the S2 foliation of the amphibole-bearing migmatites. (d) Kyanite eclogite boudin in amphibole-bearing migmatites. (e) High-Al_2O_3 rim at the contact between kyanite eclogites and amphibole-bearing migmatites. (f) Amp + Phl boudin in amphibole-bearing migmatites.

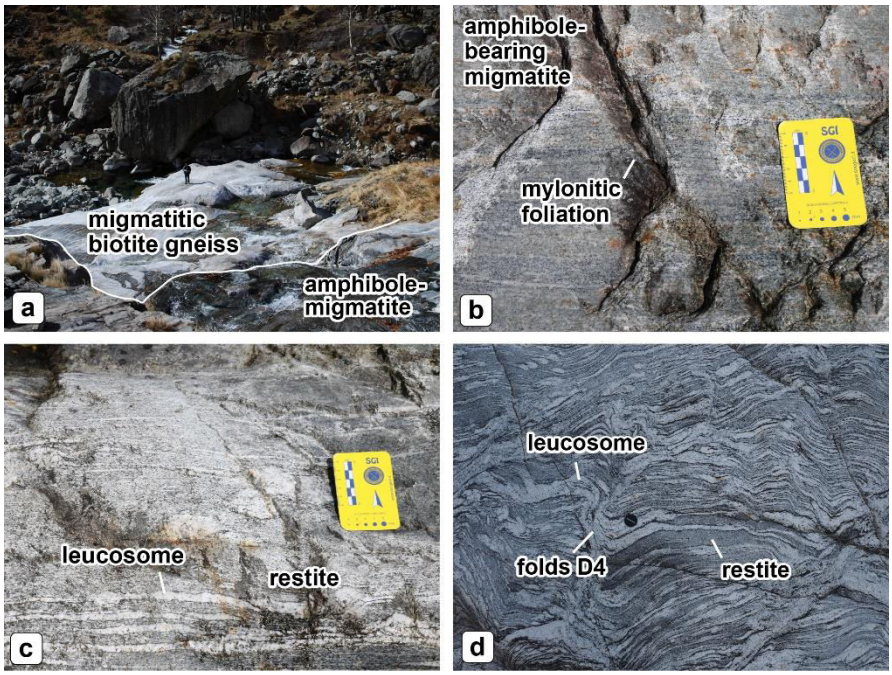

Fig. 12 Structures of crustal rocks of Borgo outcrop. (a) Contact between amphibole-bearing migmatites and migmatitic biotite gneisses at Borgo outcrop. (b) Mylonitic shear zone in amphibole-bearing migmatites close to the contact with the migmatitic biotite gneisses. (c) Stromatic texture in migmatitic biotite gneisses marked by alternating leucosomes and restites. (d) Leucosomes and restites in migmatitic biotite gneisses folded by asymmetric folds D4.

3.2 Monte Hochwart area

The Monte Hochwart area is located in the northern part of the UZ about 3 kilometres south of Santa Valburga village in NW Trentino (N Italy). In this area different types of peridotites, i.e. protogranular spinel-lherzolites, protogranular-to-porphyroclastic spinel-garnet lherzolites, porphyroclastic garnet lherzolites and fine-grained garnet-amphibole peridotites (Scambelluri et al., 2010 for a general review) occur within stromatic garnet + kyanite gneisses. Peridotites and country gneisses are well-exposed along a steep gully on the western ridge of the Monte Hochwart (Fig. 12a and b). The peridotite body is continuous from the base of the gully (2233 m) up to the Hochwart Pass (2475 m). Peridotites (lilac in Fig. 13) are mainly referable to the fine-grained garnet-amphibole type (fine-type of Obata and Morten, 1987) and are characterised by coarse (up to 1-2 cm) amphibole (Fig. 14a) and garnet (Fig. 14b) porphyroclasts embedded in a fine-grained matrix consisting of olivine, clinopyroxene and orthopyroxene. Giant (up

to 9 cm) porphyroclasts of garnet also occur in the inner portions of the peridotite body and often include partly resorbed inclusions of pargasite (Tumiati et al., 2003). Garnets are invariably mantled by spinel + orthopyroxene + clinopyroxene ± amphibole kelyphitic coronas (Fig. 14b) and are progressively replaced by rounded chlorite pseudomorphs (Fig. 14c). Peridotites display a W-dipping compositional layering consisting of garnet-rich and garnet-poor horizons locally transposed by a chlorite foliation that becomes more penetrative close to the contact with the surrounding stromatic gneisses (Fig. 13c and 14d). Peridotites include centimetre-thick garnet websterite veins (fuchsia in Fig. 13c) which occur parallel to the garnet foliation in the peridotite. They are characterised by clinopyroxene and orthopyroxene porphyroclasts (up to 5 mm) enclosed in a fine-grained matrix composed by emerald-green Cr-diopside, orthopyroxene, amphibole and garnet. These rocks display a foliation marked by garnet-rich and garnet-poor horizons that dip to west parallel to garnet layering in the host peridotite. Peridotites also contain metre-scale tremolitite layers (violet in Fig. 13c) consisting of tremolite (80-90 vol.%) with subordinate chlorite pseudomorphs after garnet and minor Mg-hornblende. These layers are strongly stretched and boudinaged as pinch-and-swell structures and occur parallel to the chlorite foliation in the peridotite.

The contact between peridotites and country stromatic gneisses is often marked by metasomatic reaction zones with a composite structure ranging from phlogopite-rich to tremolite-anthophyllite-rich cm-thick bands from the host gneiss towards the peridotite (Fig. 14e; cf. Phillips and Hess, 1936; Rost and Brenneis, 1978; Godard et al., 1996; Tumiati and Martin, 2003; Tumiati et al., 2007; Marocchi et al., 2009; Marocchi et al., 2010). These bands occur discontinuously and show variable thickness along the boundary of the peridotite body. The contact between peridotites and country gneisses sometimes are diffuse (Fig. 14f) and are characterised by the presence of serpentine, talc and tremolite.

The country gneisses (yellow in Fig. 13) have a stromatic texture characterised by cm-spaced bands composed by quartz + plagioclase + K-feldspar ± garnet ± kyanite leucosomes and garnet + kyanite + biotite melanosomes (restites) transposed along the regional S1 foliation (Fig.13; Martin et al., 1998).

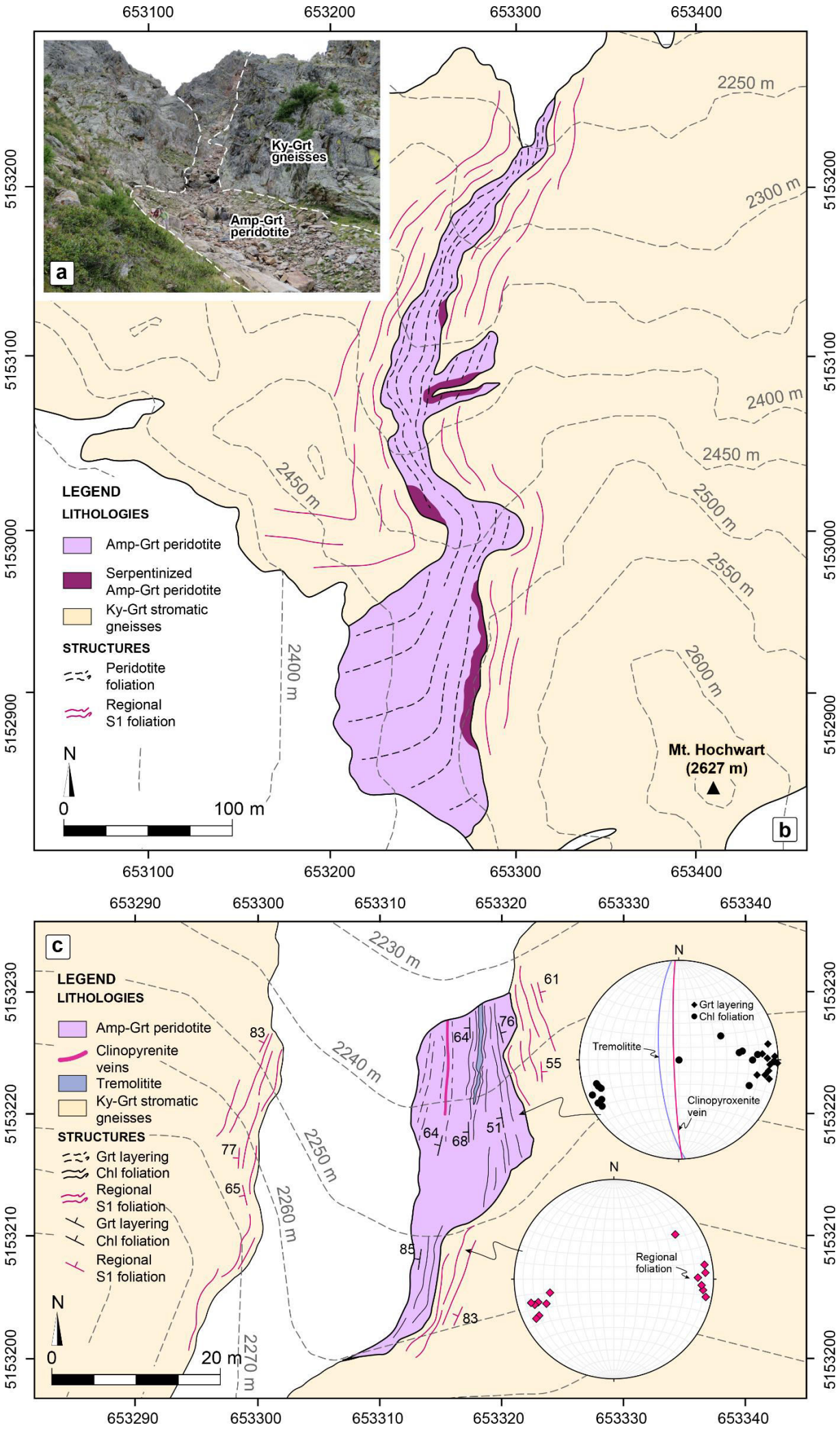

Fig. 13 (a) Monte Hochwart outcrop. (b) Geological sketch map of the amphibole-garnet peridotites exposed along the gully on the western ridge of the Monte Hochwart (redrawn from Marocchi et al., 2009). (c) Detailed geological sketch map of the amphibole-garnet peridotites at the base of the gully.

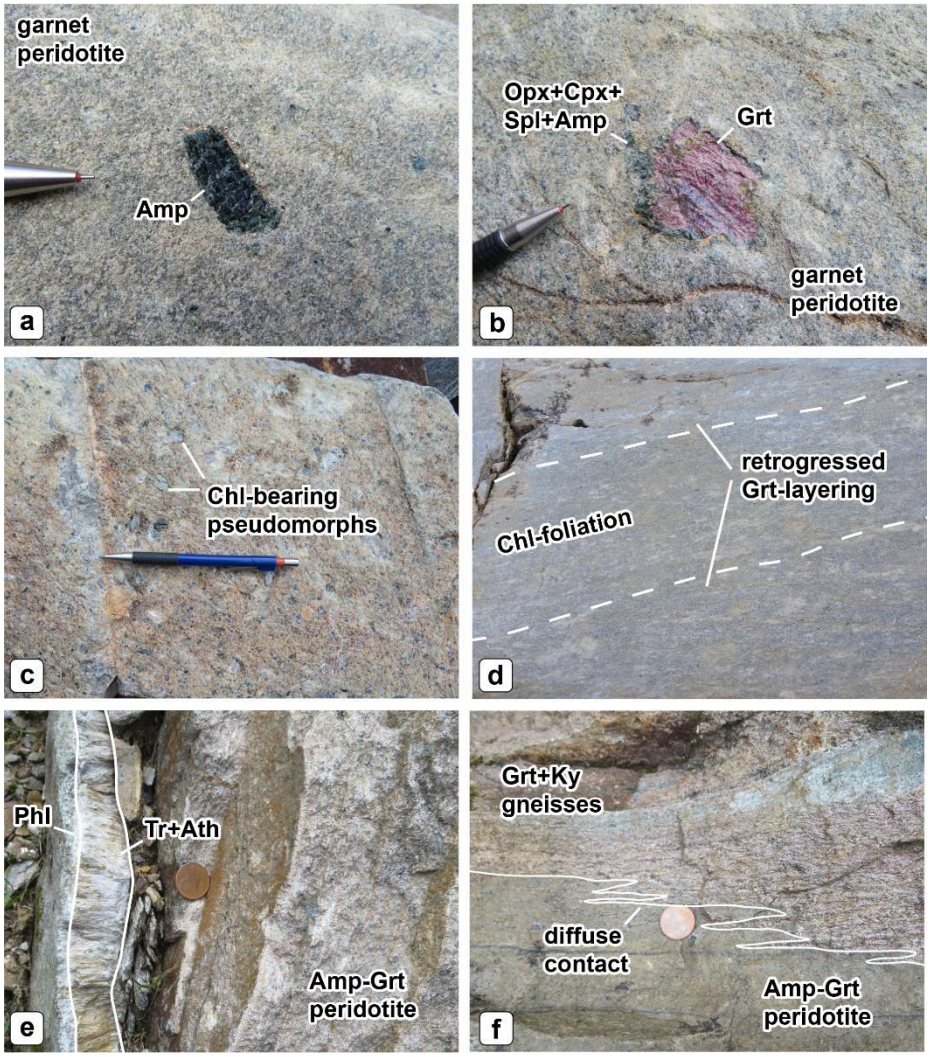

Fig. 14 Structures of amphibole-garnet peridotites of Monte Hochwart outcrop. (a) Porphyroclastic amphibole in peridotites. (b) Large (up to 2 cm) garnet mantled by Opx + Cpx + Spl + Amp symplectites. (c) Rounded chlorite-bearing pseudomorphs after garnet. (d) Retrogressed garnet layering transposed by the chlorite foliation in the peridotite. (e) Metasomatic reaction zones with a composite structure ranging from phlogopite-rich to tremolite-anthophyllite-rich bands from host gneisses towards peridotites (f) Diffuse contact between peridotites and country gneisses characterised by Srp + Tr + Tc assemblage

Chapter 4

Samples petrography

4.1 Monte Duria area

Representative samples among garnet peridotites, garnet clinopyroxenites, chlorite peridotites, tremolitites, mafic eclogites, kyanite eclogites, high-Al_2O_3 eclogites, amphibole + phlogopite boudins and amphibole-bearing migmatites occurring in the Monte Duria area have been selected for this study. All the recognised mineral assemblages and the relative metamorphic conditions are summarised in Table 2. Sample location and coordinates are given in Figure A1 - A2 of appendix. Mineral abbreviations from Whitney and Evans, (2010).

4.1.1 Garnet peridotites

Garnet peridotites show porphyroclastic texture with coarse garnet (up to 2 cm), olivine (Ol_1), clinopyroxene (Cpx_1), orthopyroxene (Opx_1) and amphibole (Amp_1) surrounded by fine-grained recrystallised matrix consisting of olivine (Ol_2), orthopyroxene (Opx_2), clinopyroxene (Cpx_2), minor amphibole (Amp_2) and Cr-spinel (Spl_2) (Fig. 15a and b). The coarse-grained Ol_1 (up to 3 mm) is strongly serpentinised and commonly shows intracrystalline deformation microstructures like undulatory extinction and deformation bands (Fig. 15c). Neoblastic Ol_2 is almost strain-free and occasionally contains 10-50 μm-sized inclusions of Cr-rich Spl_2. Also orthopyroxene occurs both as coarse grains (Opx_1) and as fine-grained crystals (Opx_2) in textural equilibrium with the recrystallised matrix of the rock. Opx_1 displays evident cleavage traces and deformation-induced kink bands while Opx_2 is strain-free and contains inclusions of Ol_2 and minor Cr-rich Spl_2. Cpx_1 commonly occurs close to garnet porphyroclasts or included in garnet cores. It contains numerous exsolution lamellae of edenitic to pargasitic amphibole and rare inclusions of Cr-rich Spl_2 and dolomite. Similarly to porphyroclastic Ol_1 and Opx_1, also Cpx_1 shows

evident deformation bands. Clinopyroxene neoblasts are inclusions-free and contain no exsolution lamellae. Garnet occurs as porphyroclasts of variable size (from 2 mm to 2 cm) that commonly contain inclusions of olivine, orthopyroxene and clinopyroxene. Spinel inclusions have been also observed in garnet cores. Garnet is invariably mantled by orthopyroxene (Opx_{Sym}) + clinopyroxene (Cpx_{Sym}) + spinel (Sp_{Sym}) ± amphibole (Amp_{Sym}) symplectites. Also, composite kelyphitic coronas consisting of orthopyroxene (Opx_{Sym}) after olivine and orthopyroxene (Opx_{Sym}) + clinopyroxene (Cpx_{Sym}) + spinel (Sp_{Sym}) ± amphibole (Amp_{Sym}) after garnet have been observed in correspondence of the previous garnet-olivine grain boundaries. In kelyphites replacing olivine tiny crystals of baddeleyite and srilankite occur (Fig. 15d), while sapphirine crystallises within symplectitic assemblages around garnet (Fig. 15e; Tumiati et al., 2018). Garnet is occasionally statically replaced by chlorite-bearing pseudomorphs surrounded by sapphirine-bearing kelyphitic coronas (Fig. 15f), indicating that garnet peridotites record a hydration stage (HP hydration in Tab. 1) predating the LP-(U)HT metamorphism. Garnet peridotites are locally deformed, especially close to the outermost part of the peridotite bodies, (Fig. 4e and f of paragraph 3.1) and display a strong foliation defined by syn-tectonic chlorite (Chl_3) and minor amphibole (Amp_3) post-dating the porphyroclastic and neoblastic assemblages (Tab. 1).

4.1.2 Garnet clinopyroxenites

Peridotites locally contain garnet clinopyroxenite pods (Fig. 4c of paragraph 3.1) consisting of clinopyroxene, garnet and minor amounts of orthopyroxene and olivine. They display a granoblastic texture characterised by coarse euhedral clinopyroxene, orthopyroxene and garnet showing 120° triple junctions (Fig. 16a).

4.1.3 Chlorite peridotites

Chlorite peridotites of Borgo display a porphyroclastic microstructure with mm-sized chloritised garnet in textural equilibrium with coarse olivine (Ol_1) and orthopyroxene (Opx_1). This porphyroclastic assemblage is surrounded by a finer-grained matrix made of olivine (Ol_2), clinopyroxene (Cpx_2), orthopyroxene (Opx_2), minor amphibole (Amp_2) and Cr-spinel (Spl_2), resembling the recrystallised matrix of garnet peridotite from Mt. Duria (Fig. 16b). Chlorite peridotites are locally deformed, especially close to the contact with eclogites, and display a strong foliation defined by syn-tectonic chlorite (Chl_3) and

amphibole (Amp_3) post-dating the porphyroclastic and neoblastic assemblages (Fig. 16b). Sample DB113 has been collected close to the contact with the innermost tremolitite boudins and shows relict olivine and orthopyroxene extensively statically overgrown by a new generation of porphyroblastic orthopyroxene (Opx_{Porph}), Mg-hornblende ($Amph_{Porph}$) and phlogopite (Phl_{Porph}) (Fig. 16c). These microstructures clearly indicate a metasomatic event pre-dating the chlorite foliation. Several dolomite crystals (Fig. 16d) and round-shaped brucite + calcite pseudomorphs after dolomite also occur within the olivine matrix.

4.1.4 Tremolitites

Tremolitites display an assemblage dominated by tremolite (more than 80 vol.%), Mg-hornblende and minor chlorite. In all the investigated samples, tremolite forms a mosaic-like texture with 120° triple junctions and straight grain boundaries. The tremolite matrix hosts older mm-sized Mg-hornblende porphyroblasts (Fig. 16e). Mg-hornblende is zoned, showing dusty cores with opaque minerals occurring along the cleavages, and clear inclusion-free rims. Isolated phlogopite (Phl_3) + chlorite (Chl_3) + talc + tremolite hexagonal pseudomorphs after garnet have been recognised in textural equilibrium with tremolite (Fig. 16f).

4.1.5 Eclogites, amphibole-bearing migmatites and amphibole + phlogopite boudins

Mafic eclogites display a porphyroblastic microstructure with mm-sized garnet (up to 3 mm), K-feldspar, zoisite and quartz embedded in a fine-grained matrix composed by Mg-hornblende (Amp_2), diopside-rich clinopyroxene (Cpx_2) and albitic plagioclase (Pl_2) (Fig. 17a). Garnet commonly shows inclusions of quartz, omphacite, minor rutile and amphibole. A 30-µm inclusion of dolomite has been also observed in a garnet core. Garnet is always surrounded and often completely replaced by symplectites consisting of Amp_2 + Pl_2. K-feldspar occurs as 500-700 µm-sized porphyroblasts that locally display 50-100-µm thick clinopyroxene (Cpx_2) coronas (Fig. 17a). Few quartz porphyroblasts have irregular shape with lobate-cuspate grain boundaries surrounded by 50 µm thick coronas composed by K-feldspar (Kfs_M) and minor clinopyroxene (Cpx_M) (Fig. 17a). Zoisite occurs as 100-150-µm porphyroblasts locally surrounded by tiny, ameboid allanite crystals (Fig. 17d).

Kyanite-bearing eclogites display a porphyroblastic microstructure with abundant garnet, kyanite and quartz (Fig. 17b). Few tiny inclusions of omphacite and rutile occur within garnet and kyanite porphyroblasts (Fig. 17c). The rock matrix is composed by Amp_2 + diopside-richCpx_2 + albite-rich Pl_2. Garnet is usually replaced by symplectitic intergrowths consisting of Mg-hornblende (Amp_{Sym}) and albitic plagioclase (Pl_{Sym}), whereas symplectites around kyanite are composed by anorthitic plagioclase (Pl_{Sym}), spinel (Sp_{Sym}), and minor sapphirine (Fig. 17b and c). Symplectites made of almost pure anorthite, likely after former zoisite, have been also observed. Similarly to mafic eclogites, quartz locally displays irregular grain boundaries surrounded by Kfs_M + Cpx_M coronitic assemblages (Fig. 17d).

Table 2

Peridotite	HP peak	HP hydration Retrogressed Grt-foliation	HP melt-rock reaction Formation of Grt-websterite	Decompression	LP-(U)HT Spr-Bdy- Sri*	LP-LT hydration Chl-foliation and Tremolitite
Olivine	Ol_1 - Ol in pyroxenite			Ol_2		
Orthopyroxene	Opx_1 Opx in pyroxenite		Opx_{Porph} in Chl-peridotite	Opx_2	Opx_{Sym}	
Clinopyroxene	Cpx_1 Cpx in pyroxenite			Cpx_2	Cpx_{Sym}	
Garnet			Grt in websterite			
Amphibole	Amp_1		Amp_{Porph} in Chl-peridotite	Amp_2 in Grt-peridotite Hbl in websterite	Amp_{Sym}	Amp_3 in Chl-peridotite Tr in websterite
Chlorite		Chl_1				Chl_3
Dolomite						
Phlogopite			Phl_{Porph} in Chl-peridotite			Phl_3
Spinel				Spl_2	Spl_{Sym}	
Talc						
Serpentine						
Calcite						
Brucite						

Eclogite	HP peak Dol*	HP hydration Partial melting	Decompression	LP-(U)HT Sapp-Cor*	LP-LT hydration
Clinopyroxene	Omp	Cpx_M	Cpx_2	Cpx_{Sym}	
Quartz		Qz_M			
Garnet					
K-feldspar		Kfs_M			
Kyanite					
Zoisite					
Rutile					
Amphibole			Amp_2		Amp_3; Hbl in amphibole-bearing migmatites Tr in Amp+Phl boudins
Plagioclase		Pl_M	Pl_2	Pl_{Sym}	
Biotite					Bt
Phlogopite					Phl
Chlorite					Chl
Orthopyroxene				Opx_{Sym}	
Spinel				Sp_{Sym}	

Mineral paragenesis in peridotites, tremolitites, eclogites, amphibole-bearing migmatites and amphibole + phlogopite boudins from Monte Duria area. *Tumiati et al. 2018

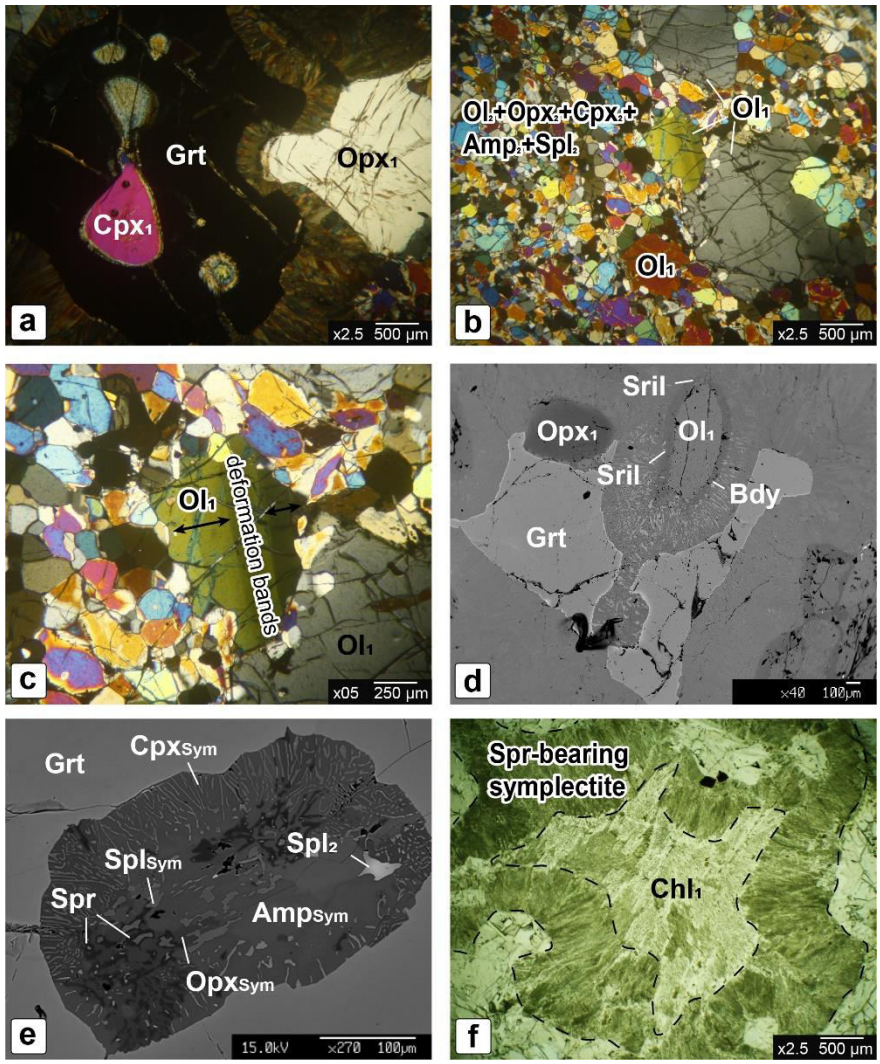

Fig. 15 Photomicrographs and back-scattered electron (BSE) images of Mt. Duria garnet peridotites. Cross polarised light image (XPL) of: (a) Mt. Duria garnet peridotite B3A showing coarse orthopyroxene (Opx_1) and garnet porphyroclasts with inclusions of clinopyroxene (Cpx_1); (b) neoblastic olivine (Ol_2), orthopyroxene (Opx_2), clinopyroxene (Cpx_2), amphibole (Amp_2) and spinel (Sp_2) hosting large olivines (Ol_1) in sample DB173. (c) coarse Ol_1 showing intracrystalline deformation bands; (d) BSE image of double kelyphitic coronas consisting of orthopyroxene (Opx_{Sym}) after Ol_1 and Opx_{Sym} + clinopyroxene (Cpx_{Sym}) + spinel (Sp_{Sym}) ± amphibole (Amp_{Sym}) after garnet in sample A2C2. In kelyphite replacing olivine tiny crystals of baddeleyite and srilankite occur; (e) BSE image of orthopyroxene (Opx_{Sym}) + clinopyroxene (Cpx_{Sym}) + spinel (Sp_{Sym}) ± amphibole (Amp_{Sym}) + sapphirine (Spr) symplectite after garnet in sample MD20; (f)

Plane polarised light (PPL) image of chlorite-bearing pseudomorph after garnet surrounded by sapphirine (Spr)-bearing symplectite in sample DB165.

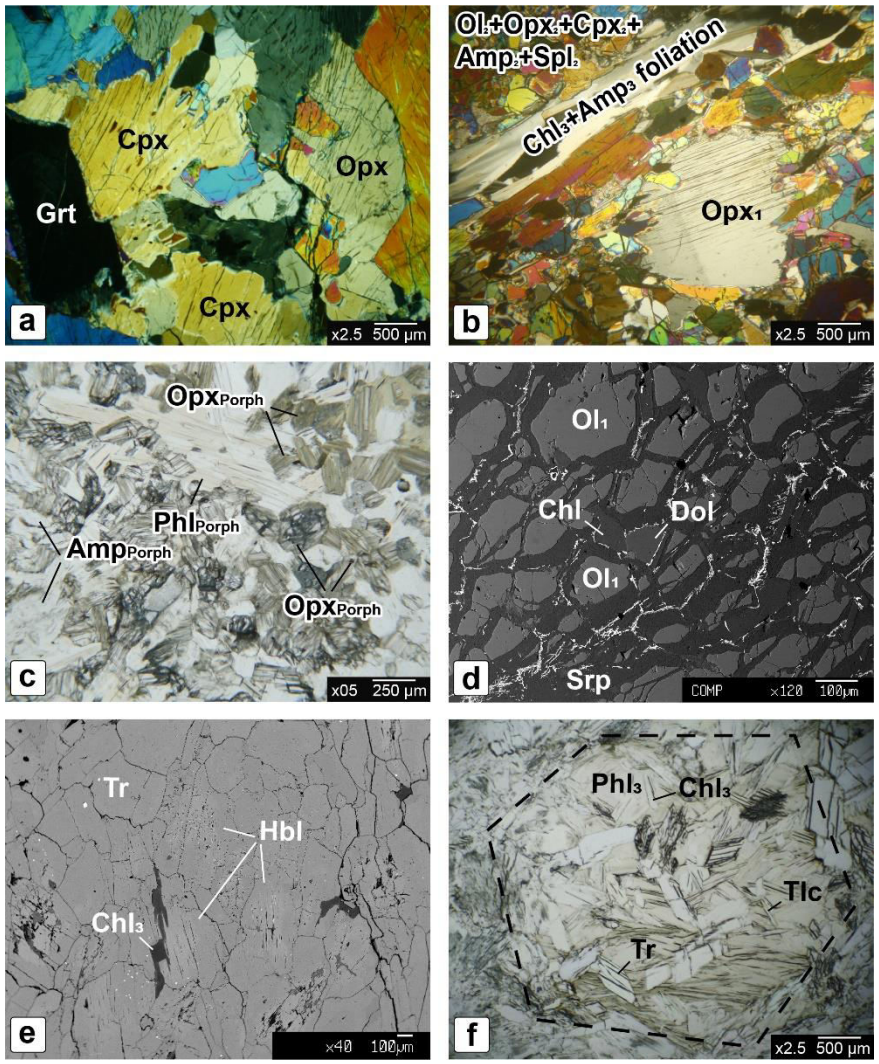

Fig. 16 Photomicrographs and BSE images of garnet pyroxenites of Mt. Duria and chlorite peridotites and tremolitites of Borgo. XPL image of: (a) Mt. Duria garnet pyroxenite MD34 showing granoblastic texture characterised by coarse euhedral clinopyroxene (Cpx), orthopyroxene (Opx) and garnet (Grt) displaying 120° triple junctions; (b) chlorite peridotite C2A. The chlorite (Chl_3) + amphibole (Amp_3) foliation post-dates the recrystallized olivine (Ol_2) + orthopyroxene (Opx_2) + clinopyroxene (Cpx_2) + amphibole (Amp_2) + spinel (Spl_2) peridotite matrix; (c) PPL image of porphyroblastic orthopyroxene (Opx_{Porph}), phlogopite (Phl_{Porph}) and amphibole (Amp_{Porph}) statically growing at the expenses of relict olivine and orthopyroxene in

chlorite peridotite DB113; (d) BSE image of dolomite textural equilibrium with olivine (Ol_1) in sample DB113; (e) BSE image of relict Mg-hornblende overgrown by tremolite (Tr) and minor chlorite (Chl_3) in tremolitite DB148. (f) PPL image of phlogopite (Phl_3), chlorite (Chl_3), talc (Tlc) and tremolite (Tr) pseudomorph after garnet in tremolitite DB179.

The high-Al_2O_3 eclogites display a strong foliation defined by syn-tectonic porphyroblastic kyanite in textural equilibrium with quartz and zoisite porphyroblasts. These minerals are embedded in a fine-grained matrix composed by diopside-rich Cpx_2 + albite-rich Pl_2 + Mg-hornblende Amp_2 pseudomorphs after omphacite. Kyanite is partially replaced by symplectitic coronas consisting of anorthite-rich Pl_{Sym}, Sp_{Sym}, corundum (Crn) and minor sapphirine (Tumiati et al., 2018). Zoisite contains inclusions of pargasite and is commonly replaced by symplectites consisting of almost pure anorthite. Similarly to the other eclogite types, quartz in these samples locally displays corroded edges surrounded by fine-grained intergrowths consisting of anhedral Kfs_M + Cpx_M, representing former crystallised melt films (Fig. 17 e). The Cpx_M + Kfs_M intergrowths are preferentially oriented parallel to the main foliation suggesting that they formed in a deformation regime when the kyanite + omphacite + zoisite + quartz HP assemblage was still stable. Interstitial pocket aggregates made of Kfs_M + Cpx_M + plagioclase (Pl_M)+ quartz (QzM) have been also observed at quartz grain boundaries (Fig. 17f). In all the three types of eclogites, the symplectitic domains are surrounded by coronas defined by porphyroblastic pargasitic hornblende (Amp_3) and biotite (Fig. 18a and b).

The amphibole-bearing migmatites hosting the eclogite boudins display a layered microstructure, consisting of leucocratic domains composed by quartz + plagioclase ± Mg-hornblende and melanocratic domains enriched in hornblende (Fig. 18c). Leucocratic domains display a mosaic-like equilibrium microtexture with grain boundaries triple junctions at 120°. The melanocratic domains are strongly foliated and are dominated by porphyroblastic Mg-hornblende enclosed in a fine-grained matrix consisting of clinopyroxene (Cpx_2), amphibole ($Amph_2$) and albitic plagioclase (Pl_2) replacing previous garnet and omphacite (Fig. 18d). These microtextures indicate that the hornblende-rich domains derive from a previous eclogite precursor.

The amphibole + phlogopite boudins display an assemblage dominated by tremolite (more than 80 vol.%), phlogopite and minor chlorite. In all the investigated samples, tremolite and phlogopite form a mosaic-like texture with 120° triple junctions and straight grain boundaries (Fig. 18e). The tremolite + phlogopite matrix hosts older mm-sized K-feldspar porphyroblasts (Fig. 18f).

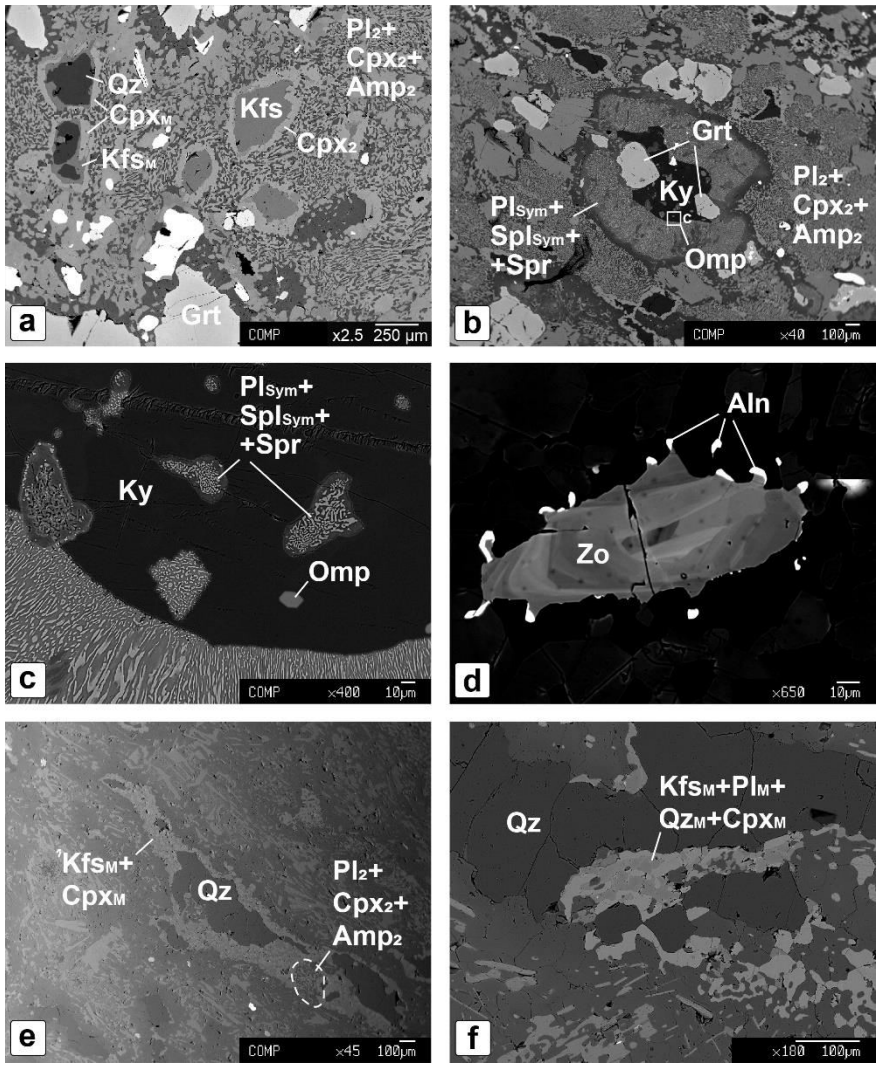

Fig. 17 BSE images of eclogites from Borgo. (a) Garnet (Grt), K-feldspar (Kfs) and quartz (Qz) porphyroblasts embedded in a fine-grained Mg-hornblende (Amp_2), diopside-rich clinopyroxene (Cpx_2) and albitic plagioclase (Pl_2) in mafic eclogite D6. Quartz (Qz) porphyroblasts are surrounded by clinopyroxene (Cpx_M) + K-feldspar (Kfs_M) coronas. K-feldspar (Kfs) porphyroblasts are surrounded by symplectitic clinopyroxene (Cpx_2); (b) Porphyroblastic garnet (Grt) and kyanite (Ky) in kyanite eclogite B5A; (c) Enlarged view of the white rectangle of Fig. 17b showing tiny omphacite (Omp) inclusion in porphyroblastic kyanite; (d) Zoisite porphyroblast surrounded by tiny, bright allanite crystals in mafic eclogite D6; (e) Quartz (Qz) surrounded by clinopyroxene (Cpx_M) + K-feldspar (Kfs_M) coronas in high-Al_2O_3 eclogite D9; (f) Melt pocket of K-feldspar (Kfs_M) + albitic plagioclase (Pl_M) + quartz (Qz_M) + clinopyroxene (Cpx_M) around quartz (Qz) in high-Al_2O_3 eclogite D9.

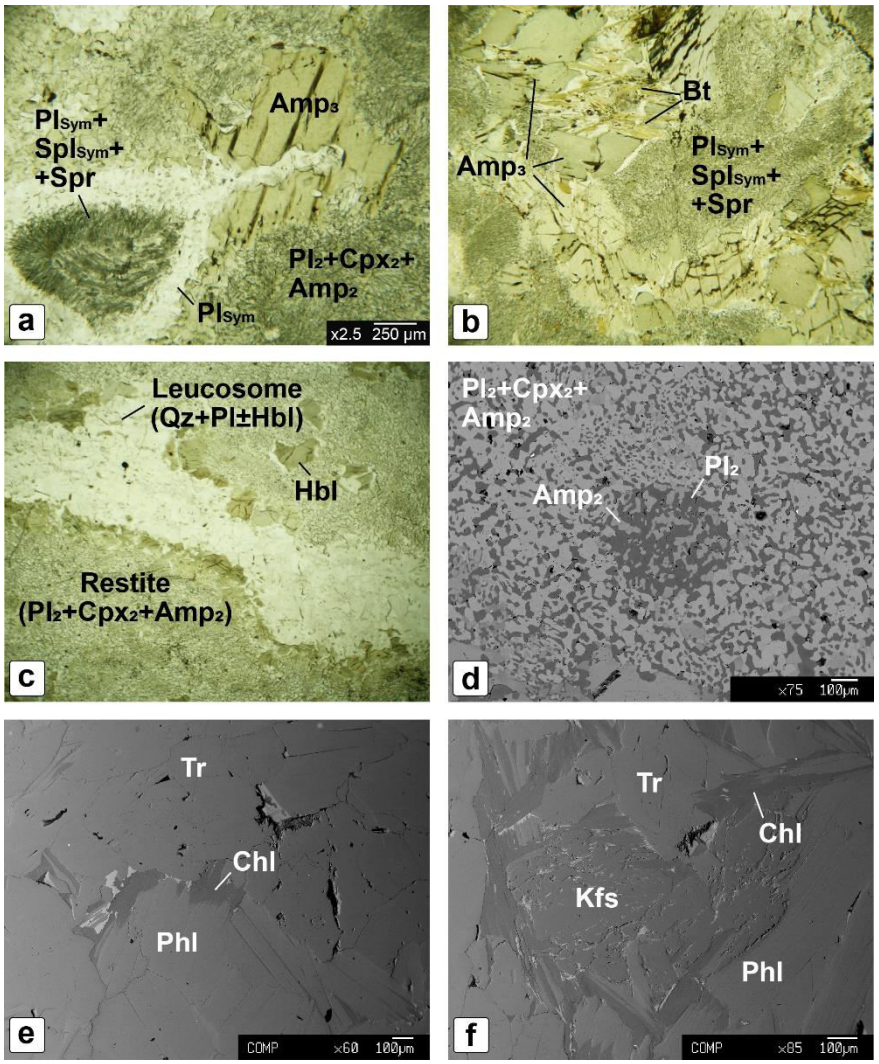

Fig. 18 Photomicrographs and BSE images of eclogites and amphibole-bearing migmatites of Borgo. PPL image of: (a) anorthite-rich plagioclase (Pl_{Sym}) + spinel (Spl_{Sym}) + sapphirine (Spr) symplectite after kyanite surrounded by porphyroblastic amphibole (Amp_3) in high-Al_2O_3 eclogite D9; (b) anorthite-rich plagioclase (Pl_{Sym}) + spinel (Spl_{Sym}) + sapphirine (Spr) symplectite after kyanite surrounded by coronas made of porphyroblastic amphibole (Amp_3) and biotite (Bt) in high-Al_2O_3 eclogite D9; (c) PPL image of amphibole-bearing migmatite D5. Leucosome is composed by quartz (Qz) + plagioclase (Pl) ± hornblende (Hbl). The restitic portion is dominated by Mg-hornblende enclosed in a fine-grained matrix consisting of clinopyroxene (Cpx_2) + amphibole ($Amph_2$) + albitic plagioclase (Pl_2) replacing previous garnet and omphacite. (d) PPL image of amphibole (Amp_2) + albitic plagioclase (Pl_2) symplectite after garnet in amphibole-bearing migmatite D5; (e) BSE image of tremolite (Tr) and phlogopite (Phl) forming a mosaic-

like texture in amphibole + phlogopite boudin DB101; (f) BSE image of tremolite (Tr) + phlogopite (Phl) matrix hosting older K-feldspar (Kfs) porphyroblasts in amphibole + phlogopite boudin DB101.

4.2 Monte Hochwart area

Representative samples among garnet lherzolites, mylonitic garnet-amphibole peridotites, garnet clinopyroxenites and tremolitites occurring in the Monte Hochwart area have been selected for this study. All the recognised mineral assemblages and the relative metamorphic conditions are summarised in Table 3. Sample location and coordinates are given in Figure A3 of appendix.

4.2.1 Garnet peridotites

Different types of peridotites have been recognised in the Monte Hochwart area, i.e. protogranular spinel-lherzolites, protogranular-to-porphyroclastic spinel-garnet lherzolites, porphyroclastic garnet lherzolites and fine-grained mylonitic garnet-amphibole peridotites (Obata and Morten, 1987; Nimis and Morten 2000; Tumiati et al., 2003; Tumiati and Martin, 2003; Scambelluri et al., 2006; Tumiati et al., 2007; Marocchi et al., 2009; Sapienza et al. 2009). The samples considered in this study correspond to porphyroclastic garnet lherzolites and the fine-grained garnet-amphibole peridotites.

Porphyroclastic garnet lherzolites display large partially retrogressed garnet porphyroclasts (Grt_1) in textural equilibrium with olivine (Ol_1), orthopyroxene (Opx_1), clinopyroxene (Cpx_1) and minor amphibole (Amp_1). This porphyroclastic assemblage is surrounded by a finer-grained recrystallised matrix made of olivine (Ol_2), orthopyroxene (Opx_2), clinopyroxene (Cpx_2), subordinate amphibole (Amp_2) and spinel (Spl_2) (Fig. 19a). Olivine is present as strongly serpentinised porphyroclasts that commonly show intracrystalline deformation microstructure like deformation lamellae and kink bands (Fig. 19b). The new olivine grains are less serpentinised and are invariably strain-free. Also clinopyroxene occurs both as porphyroclasts and as fine-grained crystals in textural equilibrium with the recrystallised peridotite matrix. Large clinopyroxenes are often pseudomorphosed by fine-grained tremolite aggregates that occasionally contain preserved exsolution lamellae of garnet and garnet grains (Fig. 19c). Garnet is almost completely replaced by symplectites consisting of orthopyroxene (Opx_{Sym}) + clinopyroxene (Cpx_{Sym}) + amphibole (Amp_{Sym}) + spinel (Spl_{Sym}) or chlorite-bearing pseudomorphs that locally contain relic, pre-garnet spinel grains (Spl_1).

Porphyroclastic garnet peridotites gradually recrystallise in fine-grained mylonitic garnet-amphibole peridotites. These rocks show preserved Grt_1, orthopyroxene Opx_1 and Amp_1 porphyroclasts set in a mylonitic, fine-grained matrix consisting of recrystallised olivine (Ol_3), orthopyroxene (Opx_3), amphibole (Amp_3) and spinel (Spl_3) in textural equilibrium with a second generation of garnet (Grt_2) (Fig. 19d). Porphyroclastic orthopyroxene displays peculiar intracrystalline deformation microstructures like kink bands and undulatory extinction. It also contains numerous exsolution lamellae of garnet and clinopyroxene (Fig. 19e). Neoblastic orthopyroxene is always strain-free and contains neither exsolved garnet nor exsolution lamellae of clinopyroxene. The garnet-amphibole peridotites are characterised by the absence of clinopyroxene, which is likely completely overgrown by amphibole. Porphyroclastic amphibole is colourless or pale green and typically includes relict spinel. Similarly to coarse orthopyroxene, also porphyroclastic amphibole displays traces of deformation such as undulatory extinction and kink bands. The neoblastic amphibole is always undeformed and inclusions-free. Garnet occurs both as large porphyroclasts (up to 2-3 mm) and as small crystals (< 500 μm) in textural equilibrium with the neoblastic assemblage of the rock. Large garnets typically include olivine, orthopyroxene and relic Spl_1 (Fig. 19f). Spinel inclusions are less common in small garnets, but olivine, orthopyroxene and amphibole have been frequently observed. Both garnet generations are invariably mantled or fully replaced by Opx_{Sym} + Cpx_{Sym} + Amp_{Sym} + Spl_{Sym} symplectitic assemblages.

Table 3

	Spinel stage	HP	HP (static recrystallisation)	HP (syn-tectonic recrystallisation)	Decompression	LP-LT hydration (tremolitite formation)
Olivine		Ol_1	Ol_2	Ol_3		
Orthopyroxene		Opx_1	Opx_2	Opx_3 in peridotite Opx_2 in pyroxenite	Opx_{Sym}	
Clinopyroxene		Cpx_1	Cpx_2	Cpx_2 in pyroxenite	Cpx_{Sym}	
Amphibole		Amp_1	Amp_2	Amp_3 in peridotite Amp_2 in pyroxenite	Amp_{Sym}	Tr
Garnet		Grt_1		Grt_2 in peridotite Grt in pyroxenite		
Spinel	Spl_1		Spl_2	Spl_3	Spl_{Sym}	
Serpentine						
Chlorite						Chl

Mineral parageneses in garnet lherzolites, mylonitic garnet-amphibole peridotites, garnet clinopyroxenites and tremolitites from Mt. Hochwart

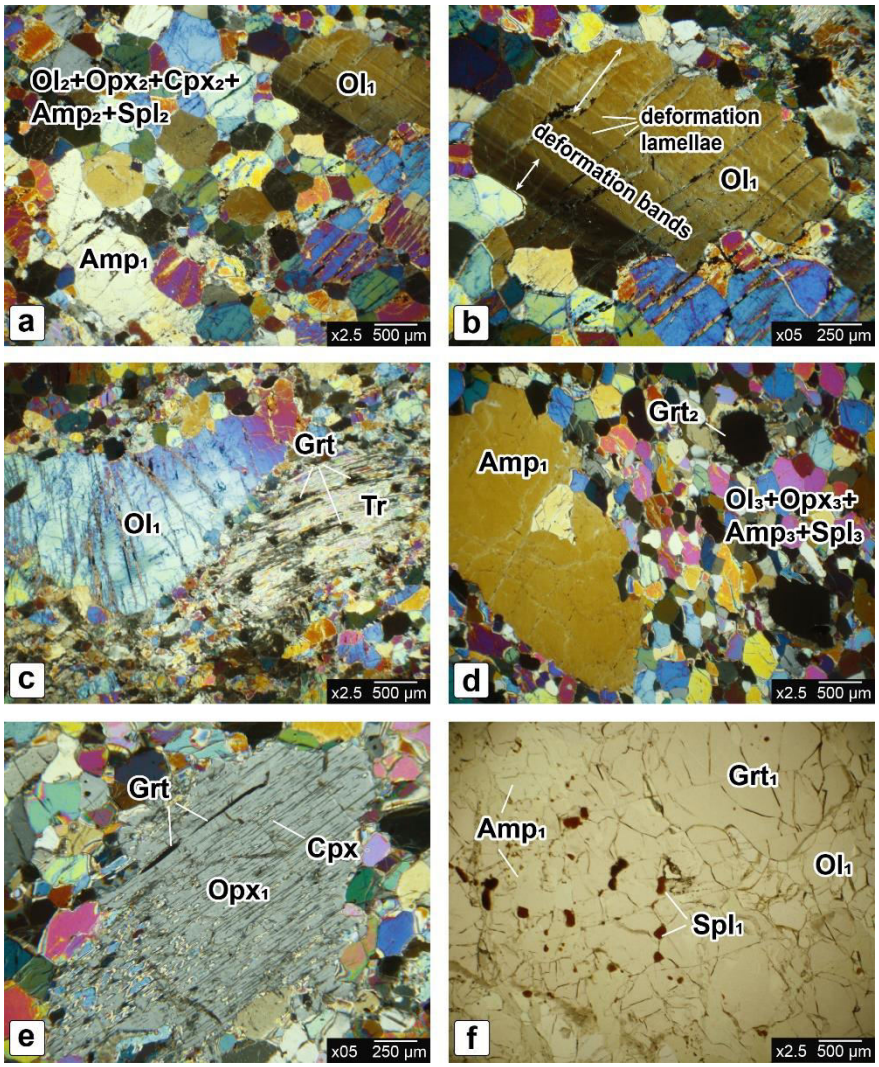

Fig. 19 Photomicrographs of garnet lherzolites and fine-grained mylonitic garnet-amphibole peridotites of Mt. Hochwart. XPL image of (a) large olivine (Ol_1) and amphibole (Amp_1) porphyroclasts surrounded by finer-grained recrystallised olivine (Ol_2), orthopyroxene (Opx_2), clinopyroxene, subordinate amphibole (Amp_2) and spinel (Spl_2) in garnet lherzolite UT22; (b) deformation bands and deformation lamellae in olivine (Ol_1) of garnet lherzolite UT22; (c) porphyroclastic clinopyroxene (Cpx_1) pseudomorphosed by fine-grained tremolite aggregate containing preserved exsolution lamellae of garnet and garnet grains in garnet lherzolite UT22; (d) porphyroclastic amphibole (Amp_1) surrounded by dynamically recrystallised olivine (Ol_3), orthopyroxene (Opx_3), amphibole (Amp_3) and spinel (Spl_3) in textural equilibrium with garnet (Grt_2) in mylonitic garnet-amphibole peridotite UT24; (e) Orthopyroxene (Opx_1) porphyroclasts showing garnet (Grt) and clinopyroxene (Cpx) exsolutions in mylonitic garnet-amphibole peridotite UT24b; (f) PPL image of pale green amphibole (Amp_1) and olivine (Ol_1) in textural equilibrium with mm-sized pink garnet (Grt_1)

containing inclusions of brownish relic, pre-garnet spinel (Spl_1) in mylonitic garnet-amphibole peridotite UT25.

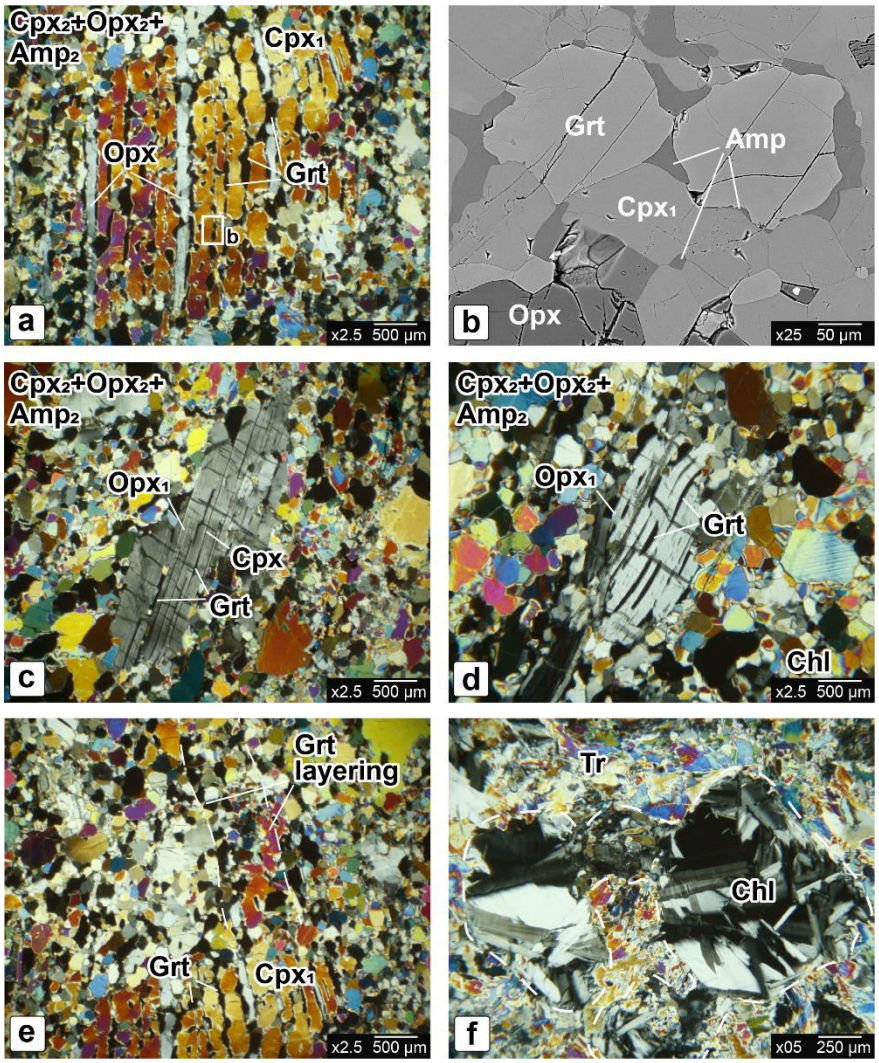

Fig. 20 Photomicrographs and BSE images of garnet clinopyroxenites and tremolitites of Mt. Hochwart. XPL image of: (a) porphyroclastic clinopyroxene (Cpx_1) embedded in a finer-grained matrix of clinopyroxene (Cpx_2) + orthopyroxene (Opx_2) + amphibole (Amp_2) + garnet (Grt) in garnet clinopyroxenite UT23. Cpx_1 shows exsolution lamellae of garnet and orthopyroxene; (b) close view of the white rectangle of Fig. 20a: BSE image showing pargasitic amphibole occurring at garnet (Grt)-orthopyroxene-clinopyroxene triple junctions in garnet clinopyroxenite UT23; (c) porphyroclastic orthopyroxene (Opx_1) embedded in a finer-grained matrix of clinopyroxene (Cpx_2) + orthopyroxene (Opx_2) + amphibole (Amp_2) in garnet clinopyroxenite UT23.

Orthopyroxene (Opx_1) shows exsolution lamellae of garnet (Grt) and clinopyroxene (Cpx); (d) intensely deformed porphyroclastic orthopyroxene (Opx_1) showing garnet (Grt) exsolutions along curved crystal planes in garnet clinopyroxenite UT23; (e) garnet layering in garnet clinopyroxenite UT23. The garnet layering is oriented parallel to the direction of the garnet exsolutions in clinopyroxene (Cpx_1); (f) chlorite (Chl)-bearing pseudomorphs after garnet surrounded by fine-grained tremolite (Tr) in tremolitite UT17.

4.2.2 Garnet clinopyroxenites

Garnet clinopyroxenites display a porphyroclastic microstructure with coarse (up to 2.5 mm) clinopyroxene (Cpx_1), orthopyroxene (Opx_1) and amphibole (Amp_1) embedded in a finer-grained recrystallised matrix consisting of clinopyroxene (Cpx_2), orthopyroxene (Opx_2) and amphibole (Amp_2) in textural equilibrium with small garnet grains. The coarse clinopyroxene shows evident exsolution lamellae of garnet, orthopyroxene and amphibole (Fig. 20a). The lamellae of orthopyroxene are 50-100 μm thick and up to 3 mm long, while garnet exsolutions are typically small with aspect ratios varying from 1:1 to 5:1. The exsolved amphibole occurs as an interstitial phase at garnet-orthopyroxene-clinopyroxene grain boundaries or triple junctions (Fig. 20b). Orthopyroxene porphyroclasts are intensely deformed and show garnet exsolutions along curved crystal planes (Fig. 20c and d). Both neoblastic clinopyroxene and orthopyroxene are undeformed and contain no exsolution lamellae. Garnet occurs as small crystals (up to 600 μm) in paragenesis with the neoblastic Cpx_2 + Opx_2 + Amp_2 assemblage and defines the compositional layering of the rock. Notably, the garnet layering is parallel to the orientation of the garnet exsolution lamellae within orthopyroxene and clinopyroxene (Fig. 20e).

4.2.3 Tremolitites

Tremolitites display an assemblage dominated by tremolite, chlorite and minor Mg-hornblende. Tremolite is the most abundant phase and hosts older mm-sized Mg-hornblende porphyroblasts and numerous Chl-bearing pseudomorphs after garnet (Fig. 20f; cf. tremolitite of Borgo outcrop of paragraph 4.1.4).

Chapter 5

Analytical techniques and methods

5.1 Inductively-coupled plasma mass spectrometry (ICP-MS) and LECO combustion

Major and trace elements whole-rock analyses were performed by inductively-coupled plasma mass spectrometry (ICP-MS) and LECO combustion (total C, S) at Bureau Veritas ACME Mineral Laboratories, Canada.

5.2 Electron microprobe analyses (EMPA)

Major elements composition of minerals was determined using a JEOL 8200 wavelength dispersive electron microprobe at the Department of Earth Sciences of the University of Milano. Quantitative analyses were performed using 15 kV accelerating potential, 5 nA sample current and 1 μm beam diameter. Standards used were omphacite (Na), grossular (Ca, Al and Si), fayalite (Fe), olivine (Mg), orthoclase (K), rhodonite (Mn), ilmenite (Ti), niccolite (Ni), pure Cr (Cr) and zircon (Zr, Hf). A counting time of 30 s was applied for all elements.

Intensity X-ray maps were standardized to concentration maps of oxide weight percentage using spot analyses as internal standard. X-ray maps were processed using XMapTools 2.2.1 (Lanari et al., 2014).

5.3 Laser ablation inductively coupled plasma mass spectrometry

Trace elements composition of minerals was determined using laser ablation inductively coupled plasma mass spectrometry (LA-ICP-MS) at the CNR–IGG–UOS of Pavia. The instrument couples a 213 nm Nd:YAG laser microprobe (NewWave Research) to a quadrupole ICP-MS system (DRCe from PerkinElmer). Trace elements analyses on minerals were performed using 55 μm-sized spot with a fluence of 7.0÷8.0 J/cm^2. The smallest crystals were analysed

using 15 μm-sized spot and a fluence of 4 J/cm^2. NIST610 was used as external standard whereas Ca, Si and Al were used as internal standard depending on the analysed minerals. During each analytical session the USGS reference sample BCR2 was analysed for a quality control.

5.4 Electron backscatter diffraction (EBSD)

EBSD analyses were carried out on a JEOL 6610 VP-SEM equipped with an Oxford Instruments Nordlys Nano EBSD detector and a JEOL 7001 FEG SEM equipped with a NordLys Max EBSD detector (AZTec acquisition software, Oxford Instruments) at the Electron Microscope Centre of Plymouth University. Thin sections were SYTON-polished for ca. 2 hours and carbon coated with a coating thickness of 5-10 nm. EBSD patterns were acquired on rectangular grids with step sizes of 0.6, 1.3, 2.0, 2.8, 3.5 and 4.5 μm. Working conditions were 20 kV accelerating voltage, 10 nA beam current of, high vacuum, 70° sample tilt, and working distance between 17 and 23 mm. EBSD patterns were processed with Channel 5 analysis suite from HKL Technology, Oxford Instruments and MTEX open source software toolbox (Hielscher & Schaeben, 2008; Bachmann et al., 2010). Noise reduction on the raw EBSD data was performed following the procedure tested by Prior et al. (2002) and Bestmann and Prior (2003). Indexed phases and relative symmetry group are forsterite - orthorhombic (mmm), enstatite - orthorhombic (mmm), diopside - monoclinic (2/m), pyrope - cubic (m3m), and pargasite - monoclinic (2/m). Critical misorientation for the distinction between low- and high-angle boundaries is 10°. The pole figures (one-point-per grain unless differently specified) are plotted as equal area, upper hemisphere projections referenced with the pole to the foliation (Z direction) pointing upwards and the lineation (X direction) horizontal. In countered plots, the texture strength is expressed through the multiples of uniform distribution (m.u.d.) value, calculated using a Gaussian Half Width of 10°. Misorientation axis distributions in sample coordinates are plotted as equal area, upper hemisphere projections. The inverse pole figures plots for misorientation axis distribution in crystal coordinates are upper hemisphere projections. The misorientation angle distribution is calculated for neighbouring pixels (correlated misorientations) and unrelated pixels (uncorrelated misorientations). Both correlated and uncorrelated distributions are plotted against the theoretical curve for random-pairs orientations that is specific of the crystal symmetry (Wheeler et al., 2001).

5.5 Sm-Nd isotopic analyses

Rock samples were crushed and split into different grain-size fractions using 80-125-250-500-100 µm sieves. The 80-125 µm fraction was used for mineral separation. Garnet and clinopyroxene concentrates were obtained using a Frantz ® magnetic separator. 280 mg of Optically clean, inclusion-free separates were prepared by careful handpicking under a binocular microscope. The isotope analytical work was performed at the Laboratory of Geochronology, Institute of Geology, University of Vienna. Before decomposition, the concentrates were washed using diluted HCl (0.24 N for clinopyroxene and 2.5 N for garnet) for ca. 30 min on a hot plate (70°C). Sample digestion was performed in Savillex ® beakers using an ultrapure 5:1 mixture of HF and $HClO_4$ for ten days at 110 °C on a hot plate. For whole-rock powders, a minimum dissolution time of three weeks was applied to ensure complete leaching of the rare earth elements (REEs) from refractory material. After evaporating the acids, repeated treatment of the residue using 5.8 N HCl resulted in clear solutions for all samples. Upon cooling, between5 and 10 % of the sample solution was split off and spiked for Sm and Nd concentration determination by isotope dilution (ID) using a mixed REE tracer (147Sm-150Nd spike). The REE fraction was extracted using AGR® 50W-X8 (200–400 mesh, Bio-Rad) resin and 4.0 N HCl. Nd and Sm were separated from the REE fraction using teflon-coated HdEHP, and 0.18N and 0.4 N HCl, respectively, as elution media. Maximum total procedural blanks for both Sm and Nd were <50 pg. Sm and Nd were run as metals from a Re double filament, using a Finnigan® MAT262 (for ID fractions) and a ThermoFinnigan® Triton TI TIMS (for isotope compositions (IC)). A $^{143}Nd/^{144}Nd$ratio of 0.511846 ± 0.000004 (mean value n = 5) was determined for the La Jolla (Nd) international standard during the period of investigation and no correction was applied. Uncertainties on the Nd isotope ratios are quoted as 2σ. For the $^{147}Sm/^{144}Nd$ratio, a mean error of ±1 % is estimated, including blank contribution, uncertainties on spike composition and machine drift. Regression calculation is based on these uncertainties and the isochron calculations follow Ludwig (2003). Age calculations are based on a decay constant of 6.54×10^{-12} a^{-1} for ^{147}Sm (Lugmair & Marti, 1978); age errors are given at the 2σ level. For Nd, a continuous depletion of the upper mantle is assumed throughout geological time using the following depleted mantle model para-meters: $^{147}Sm/^{144}Nd$=0.222, $^{143}Nd/^{144}Nd$ = 0.513114 (Michardet al. 1985).

5.6 Thermodynamic modelling

The thermodynamic modelling was performed with the software package Perple_X (http://www.perplex.ethz.ch; Connolly, 2005), using the thermodynamic database of Holland & Powell (1998) revised in 2002 (hp02ver.dat), and the following solution models described by Holland & Powell (1998) (HP), Holland & Powell (2003) (I1, HP and C1) and Dale et al. (2000) (D): Gt(HP) for garnet, Opx(HP) for orthopyroxene, O(HP) for olivine, Omph(HP) for Ca-Na clinopyroxene, Chl(HP) for chlorite, Sp(HP) for spinel, Pheng(HP) for white mica, Bio(HP) for phlogopite, Pl(I1, HP) + OrFsp(C1) for ternary feldspars, Ca-Amph(D) for calcic amphibole. The water equation of state was taken from Holland & Powell (1998).

Chapter 6

Eclogite-derived melt-peridotite interaction at HP in the Monte Duria area

6.1 Introduction

The partial melting of metasedimentary and metagranitic rocks interacting with garnet peridotites - proxy of the interaction between the subducted crust and the overlying mantle - can be found in high-ultrahigh pressure (HP-UHP) terranes such as Ulten Zone in the Central Italian Alps (Rampone and Morten, 2001; Tumiati et al., 2003; Scambelluri et al., 2006) and the chinese Dabie-Sulu belt (Malaspina et al., 2006; 2009). Alternatively, evidence of partial melting of HP rocks representative of the mafic portions of the subducted slab is very rare and its evidence is seen in the production of peraluminous trondhjemite–tonalite melts (so-called adakites) forming volcanic suites of andesitic to rhyodacitic composition (Drummond et al., 1996). The observation of HP partial melting of eclogites has been reported only by Wang et al. (2014) in the Central Sulu orogen, while to date the direct interaction between eclogite-derived melts and peridotites at HP has never been observed *in situ* in orogenic peridotites.

Melting of mafic rocks in a subducting lithosphere at HP requires at least T = 750 °C at P = 3 GPa, under H_2O saturated conditions (Schmidt and Poli, 2014), typical of low angle subduction systems (Peacock and Wang, 1999) also called “warm subduction” (Syracuse et al., 2010). The Monte Duria area (Adula-Cima Lunga nappe, Central Alps, Italy) is a unique case study where we can observe eclogite-derived melt interacting with garnet peridotite at P-T conditions proxy of “warm” subduction paths. In this area garnet peridotites occur in direct contact with migmatised orthogneiss and eclogites, sharing a common metamorphic history reaching HP peak at 2.8 GPa and 750 °C and post-peak static equilibration at 0.8-1.0 GPa and 850 °C (Tumiati et al., 2018). In this study we will show that garnet peridotites from the Monte Duria area record a multistage

metasomatic event by eclogite-derived adakite-like melts at HP inducing a selective enrichment in LREE, and by retrograde fluids at lower pressures yielding to LILE enrichments in amphiboles. The interaction between garnet peridotites and eclogite leucosomes also produces a modal metasomatism evidenced by the occurrence of garnet websterite layers at the contact between eclogite and peridotite, now retrogressed in the tremolite stability field.

The fate of crust-derived melts in the associated peridotites and their capability to transport crustal components to the mantle is still matter of debate. Many occurrences show that crustal melts may migrate into the mantle by porous flow, producing almost monomineralic metasomatic orthopyroxene and phlogopite layers at the slab-mantle interface (e.g. Malaspina et al., 2006; 2009; Endo et al., 2015). Such a mechanism, however, may limit the crust-to-mantle mass transfer unless they are partitioned into residual aqueous fluids (Malaspina et al., 2009). Alternatively, metasomatic melts may migrate into the mantle by focussed flow, forming a network of pyroxenite veins as shown by metasomatised mantle xenoliths from arc lavas (e.g. Arai et al., 2003; Kepezhinskas et al., 1995). We will show that the melt-peridotite interaction preserved in Borgo outcrop of Monte Duria area occurred under a deformation regime (shearing) at HP, promoting the combination of porous and focussed flow of eclogite-derived melts into the garnet peridotite. The melt-enhanced deformation and flow in garnet peridotites documented in the Monte Duria area may represent an exhumed example of crustal flow channels forming at the slab-mantle interface, that facilitate the migration of crustal melts in the supra-subduction mantle.

6.2 Whole rock chemistry

In this paragraph will be presented the chemical compositions of peridotites, tremolitites, eclogites, amphibole-bearing migmatites and amphibole + phlogopite boudins occurring in the Monte Duria area. The whole rock composition of peridotites, pyroxenites and tremolitites of Ulten Zone will be reported for comparison.

6.2.1 Major elements

The major elements composition of the investigated rocks is reported in Table 4, 5 and portrayed in Figure 21 and 22.

6.2.1.1 Monte Duria area

The composition of garnet peridotites resembles that of the reference Depleted Mantle (DM; Salters and Stracke, 2004), displaying Mg# = 0.90, Ni = 1960-1975 ppm, low Al_2O_3 (2.67-3.05 wt.%) and low CaO (2.16-2.52 wt.%) concentrations (Fig. 21). Chlorite peridotites have a composition comparable to that of garnet peridotites from Monte Duria, showing Mg# of 0.88-0.89, Ni of 2097-2117 ppm, Al_2O_3 and CaO concentrations of 2.96-3.5 wt.% and 2.13-2.60 wt.% respectively (Fig. 21). In Figure 21 the compositions of peridotites from other localities of the Central and Eastern Alps have been also portrayed for comparison. Our samples plot close to the Alpe Arami (AA), Bellinzona-Dascio (BDZ) and Ulten (UZ) peridotites, whereas the ultramafic rocks from Cima di Gagnone (CdG) show lower Ni (1386-1614 ppm), and slightly higher Al_2O_3 (2.87-4.44 wt.%) and CaO (2.48-3.65 wt.%) concentrations.

Tremolitites (purple square in Fig. 21) show Mg# = 0.91 and Al_2O_3 concentrations comparable to mantle values. In the Mg#-Ni variation diagram (Fig. 21a), tremolitites plot into the field of the ultramafic compositions probably indicating that they derive from an ultramafic precursor. Despite this mantle signature, they show high SiO_2 (up to ca. 55 wt.%), high CaO (12.38 wt.%) and low Ni (554 ppm) concentrations (Tab. 4; Fig. 21).

The bulk-rock composition of mafic, kyanite-bearing and high-Al_2O_3 eclogites indicates that they all have a mafic composition (MgO = 8.23-11.26 wt.% and SiO_2 = 47.39-51.17 wt.%; Tab. 4). In figure 21 the composition of investigated eclogites is compared to that of N-MORB (Hofmann, 1988), layered mid ocean-ridge gabbros (Gillis et al., 2014) and ophiolitic gabbros from the Central Alps (i.e. Bellinzona-Dascio Zone; Stucki et al., 2003). The composition of the mafic eclogite overlaps that of the reference N-MORB showing Mg# = 0.61-0.65, Ni = 139-152 ppm, CaO = 9.57-11.29 wt.% and Al_2O_3 = 14.61-15.50 wt.%. The other two types of eclogites display a composition resembling that of reference gabbros with Mg# ranging from 0.73 to 0.83 and the highest CaO (11.52-13.12 wt.%) and Al_2O_3 (16.11-20.83 wt.%) concentrations.

The amphibole-bearing migmatites have a composition comparable to that of the high-Al_2O_3 eclogites showing Mg# of 0.82-0.84, Ni of 226-459 and high CaO and Al_2O_3 concentrations of 11.64-13.24 wt.% and 17.30-17.90 wt.% respectively (Fig. 21).

In Figure 21 the amphibole + phlogopite boudins plot between peridotites and eclogites showing Mg# = 0.78-0.85, Ni = 700-986 ppm, and moderate CaO (8.43-11.20 wt.%) and Al_2O_3 (4.12-8.97 wt.%) concentrations.

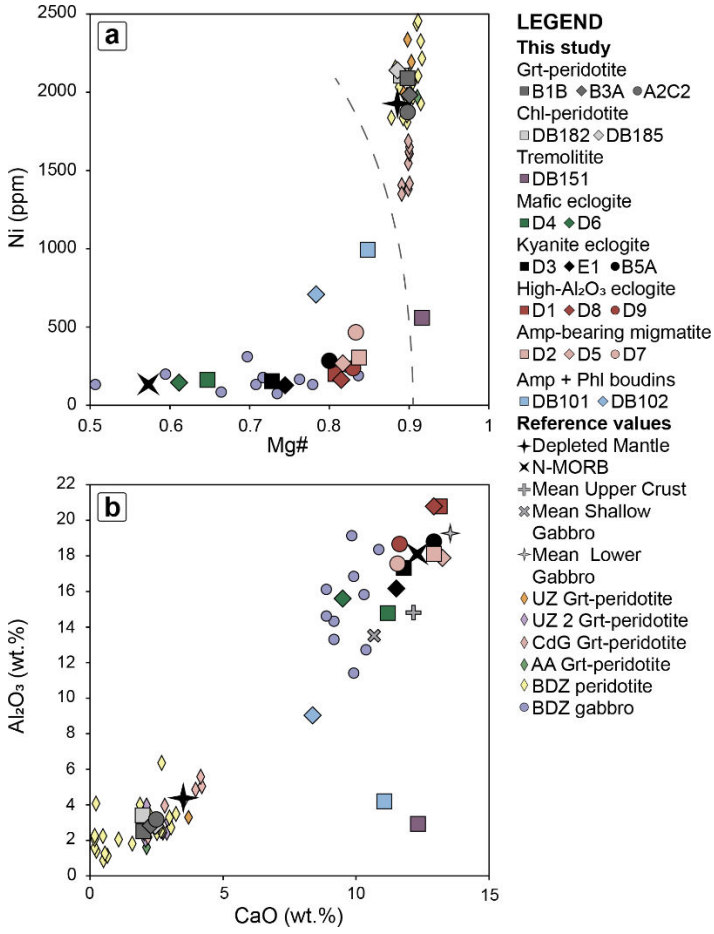

Fig. 21 Mg# versus Ni (ppm) plot (a) and CaO versus Al_2O_3 wt.% concentrations (b) of peridotites, garnet pyroxenites, tremolitites, eclogites, amphibole-bearing migmatites and amphibole + phlogopite boudins of Monte Duria area (data from Table 4) compared with the Depleted Mantle (Salters and Stracke, 2004), average N-MORB (Hofmann, 1988), average composition of Mean Upper Crust, Mean Shallow Gabbro and Mean Lower Gabbro (Gillis et al., 2014), peridotites from Ulten Zone (UZ: Tumiati et al., 2003; UZ2: Rampone and Morten, 2001), Cima di Gagnone (CdG: Scambelluri et al., 2014), Alpe Arami (AA: Ernst et al., 1981) and peridotites and Mg-gabbros from Bellinzona-Dascio Zone (BDZ: Stucki et al., 2003). The dashed grey line separates mafic compositions on the left form the ultramafic compositions on the right (modified after Malaspina et al., 2006).

6.2.1.2 Ulten Zone

The composition of porphyroclastic garnet lherzolites and mylonitic garnet-amphibole peridotites displays Mg# = 0.88-0.90, Ni = 1412-2010 ppm, low Al_2O_3 (2.59-3.35 wt.%) and low CaO (2.33-3.32 wt.%) concentrations (Fig. 22), resembling the composition of Ulten Zone peridotites reported by Rampone and Morten, (2001) and Tumiati et al., (2007).

Garnet clinopyroxenites show Mg# = 0.88 and Ni (1471 ppm) concentrations, falling into the field of ultramafic compositions in the Mg#-Ni variation diagram of Figure 22a. However, compared to the reference DM, garnet clinopyroxenites show lower Ni and higher SiO_2 (50.62 wt.%), Al_2O_3 (5.93 wt.%) and CaO (9.94 wt.%) concentrations (Tab. 4; Fig. 22).

Sample UT17 and UT21 are representative of the tremolitites boudins. Tremolite UT17 show a composition comparable (except for the low Ni = 652 ppm) to that of the garnet clinopyroxenites, showing Mg# of 0.89, and Al_2O_3 and CaO concentrations of 7.05 wt.% and 8.84 wt.% respectively (Fig. 22). Sample UT21 has Mg# = 0.88, Ni = 1937 ppm, low Al_2O_3 (2.92 wt. %) and CaO (2.70 wt.%) concentrations, matching the whole rock composition of the investigated peridotites (Fig. 22).

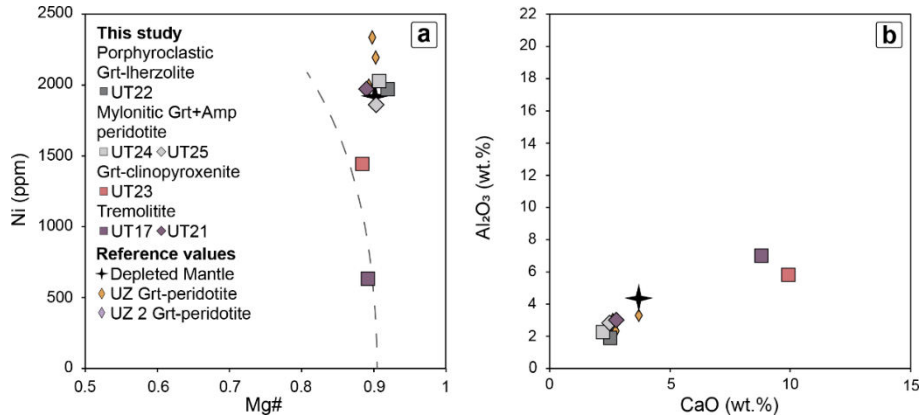

Fig. 22 Mg# versus Ni (ppm) plot (a) and CaO versus Al_2O_3 wt.% concentrations (b) of peridotites, garnet pyroxenites and tremolitites of Ulten Zone (data from Table 5) compared with the Depleted Mantle (Salters and Stracke, 2004) and peridotites from Ulten Zone (UZ: Tumiati et al., 2003; UZ2: Rampone and Morten, 2001). The dashed grey line separates mafic compositions on the left form the ultramafic compositions on the right (modified after Malaspina et al., 2006).

6.2.2. Trace elements

The bulk rock trace elements composition of the analysed samples is reported in Table 4, 5 and portrayed in Figures from 23 to 26, normalised to the Primitive Mantle (McDonough and Sun, 1995).

6.2.2.1 Monte Duria area

Garnet peridotites of Monte Duria show absolute rare earth elements (REE) concentrations slightly lower than the PM, with fractionated patterns enriched in light-REE (LREE) (La/Nd_N = 2.41; La/Er_N = 2.41) relative to the medium-REE (MREE) and heavy-REE (HREE) (Fig. 23a). Chlorite peridotites from Borgo outcrop show REE concentrations broadly comparable to the PM with a slight fractionation between LREE and MREE (Fig. 23c), resembling the REE fractionated patterns of garnet peridotites from monte Duria (c.f. Fig. 23a) The trace elements composition of the studied peridotites is compared to that of the DM (bold blue line in Fig. 23), and peridotites from Cima di Gagnone and Ulten Zone. (Fig. 23a, b, c, d) The studied peridotites overlap the fractionated REE patterns of Ulten peridotites (pink area), whereas Cima di Gagnone ultramafic rocks (light grey area) display LREE depletion with respect to MREE and HREE following the same pattern of the DM. In terms of other trace elements the composition of the investigated garnet and chlorite peridotites broadly resembles that of Ulten Zone and Cima di Gagnone ultramafic rocks, showing relatively high large ion lithophile elements (LILE) concentrations (Cs = 85×PM, Fig. 23b, d).

Tremolitites have REE concentrations up to 2.6×PM with enrichments in MREE and LREE (La/Er_N = 2.15 and Nd/Er_N = 2.97) relative to HREE (Fig. 23e). These rocks do not show any appreciable LILE enrichment except for relatively high Pb concentrations (up to 10×PM; Fig. 23f).

The trace elements composition of mafic, kyanite-bearing and high-Al_2O_3 eclogites is compared with the composition of N-MORB (bold dark grey line in Fig. 24; Hoffman, 1988) and ophiolitic gabbros from BDZ (light grey field in Fig. 24c, e; Stucki et al., 2003). The REE pattern of mafic eclogite broadly resembles that of reference N-MORB with REE absolute concentrations up to10×PM and a slight Eu negative anomaly (Fig. 24a). Kyanite eclogites display REE concentrations almost one order

of magnitude lower than those of mafic eclogites (c.f. Fig. 24c and Fig. 24a), showing a slight fractionation in LREE with respect to MREE and HREE (La/Nd_N = 1.48), falling in the patterns range of BDZ gabbros, except for the lack of a strong positive Eu anomaly. The high-Al_2O_3 eclogites have a composition broadly comparable to that of the reference gabbros showing a slight fractionation in LREE with respect to MREE and HREE (La/Nd_N = 1.93) and a positive anomaly in Eu, likely indicating that some cumulus plagioclase was present in the protolith of these rocks (Fig. 24e). The whole-rock composition of the studied eclogites also shows high LILE concentrations (Cs up to 90×PM), negative anomalies in Ba, very low Nb contents, positive anomalies in Sr (except for the mafic eclogite) and high U/Th ratio (Fig. 24b, d, f). The Cpx_M + Kfs_M pocket aggregates around relict quartz and Pl_2+Cpx_2+Amp_2 symplectite after omphacite in high-Al2O3 eclogite D9 (Fig. 17e, f) have strongly fractionated REE patterns with enrichment in HREE relative to LREE (La_N/Er_N = 0.11), and a marked Eu negative anomaly (Fig. 25a). It also shows high LILE concentrations (Rb = 2645×PM), negative anomalies in Nb and Ti, and low U/Th = 1.5 (Fig. 25b). The inset of Figure 25a also portrays the REE pattern of allanite surrounding zoisite, which shows strong enrichment in LREE and HREE.

The amphibole-bearing migmatites display a composition broadly comparable to that of the high-Al_2O_3 eclogites (c.f. Fig. 25c, d and Fig. 24e, f). They display fractionated REE patterns slightly enriched in LREE (La/Nd_N = 1.7) relative to MREE and a marked Eu positive anomaly. Similarly to high-Al_2O_3 eclogites, amphibole-bearing migmatites also show high LILE concentrations (Cs up to 48×PM), negative anomalies in Ba, very low Nb contents, positive anomalies in Sr and high U/Th ratio.

The REE patterns of amphibole + phlogopite boudins show REE absolute concentration almost one order of magnitude greater than the PM with depletion in LREE with respect to HREE (La/Er_N = 0.19; Fig. 25e). Sample DB101 also show a slight Eu negative anomaly. In terms of other trace elements (Fig. 25f), both DB101 and DB102 are characterised by high LILE concentrations (Cs = 395×PM) and negative anomalies in Ba and Sr but they display different fractionations in HFSE. In addition, sample DB102 shows a strong Ti negative anomaly.

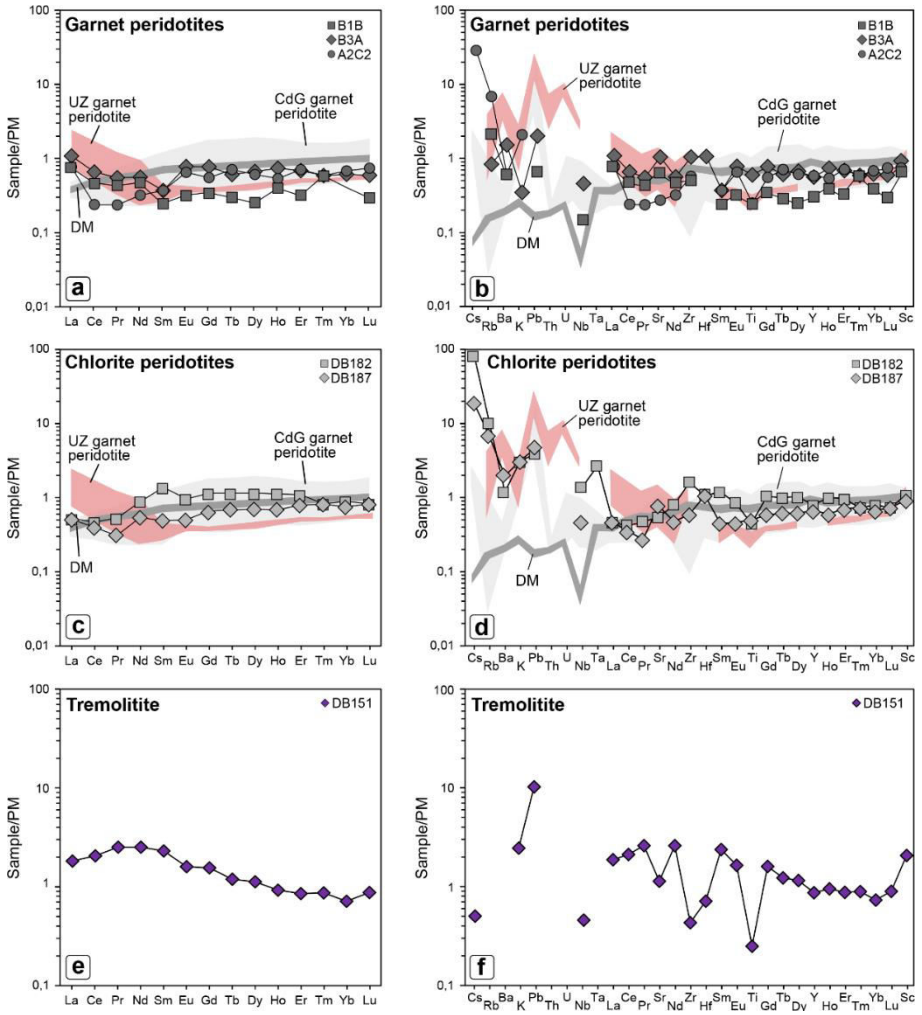

Fig. 23 Primitive Mantle normalised REE and other trace element patterns of the investigated peridotites and tremolitites (data from Table 4). Elements are presented in order of increasing compatibility (left to right) during melting in the upper mantle (Hofmann, 1988; Sun and McDonough, 1989). Normalising values are from McDonough and Sun (1995). (a) and (b) trace elements patterns of B1B, B3A and A2C2 garnet peridotites from Monte Duria; (c) and (d) trace elements patterns of DB182 and DB187 chlorite peridotites from Borgo; (e) and (f) trace elements pattern of tremolitite DB151. Data are compared with the reference Depleted Mantle (DM: bold grey solid line; Salters and Stracke, 2004), garnet peridotites from Cima di Gagnone (CdG: grey area; Scambelluri et al., 2014), and garnet peridotites from Ulten Zone (UZ: pink area; Tumiati et al., 2007).

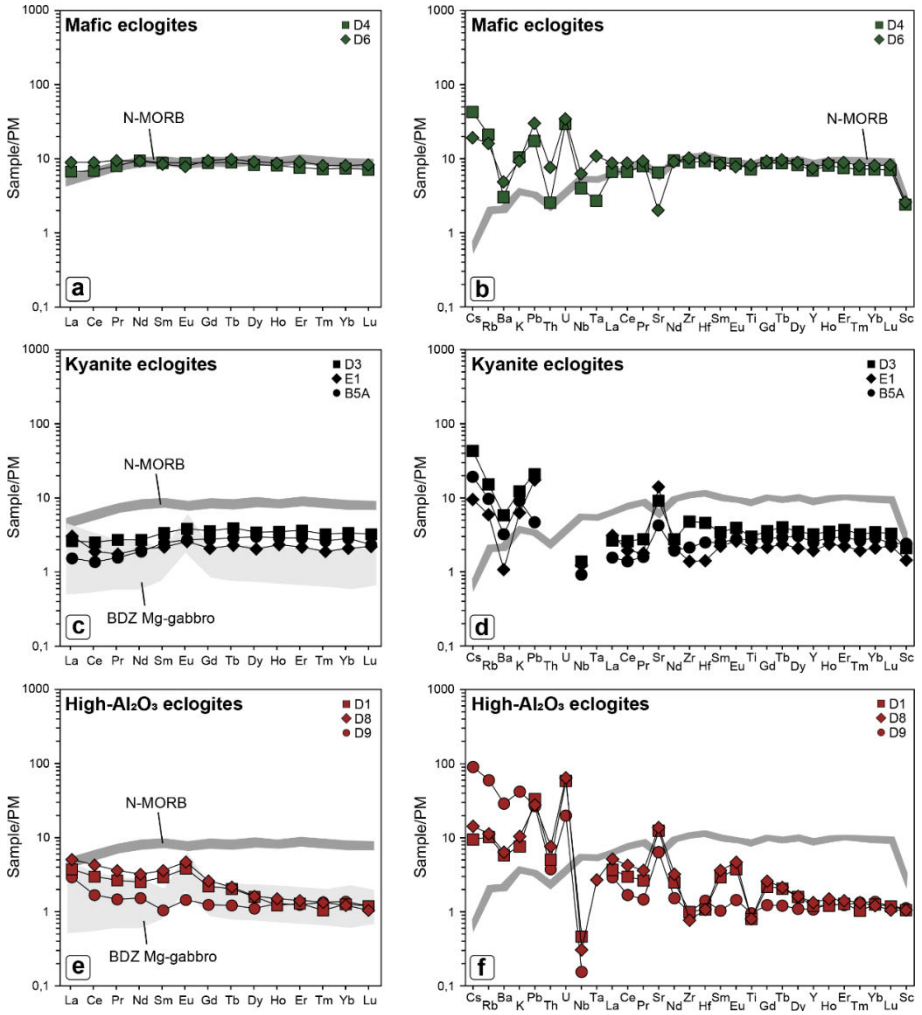

Fig. 24 Primitive Mantle normalised REE and other trace element patterns of eclogites from Borgo outcrop (data from Table 4). (a) and (b) trace elements patterns of D4 and D6 mafic eclogites; (c) and (d) trace elements patterns of D3, E1 and B5A kyanite eclogites; (e) and (f) trace elements patterns of D1, D8 and D9 high-Al_2O_3 eclogites. Data are compared with average N-MORB (bold dark grey solid line; Hofmann, 1988) and Mg-gabbro from Bellinzona-Dascio Zone (light grey area BDZ; Stucki et al., 2003).

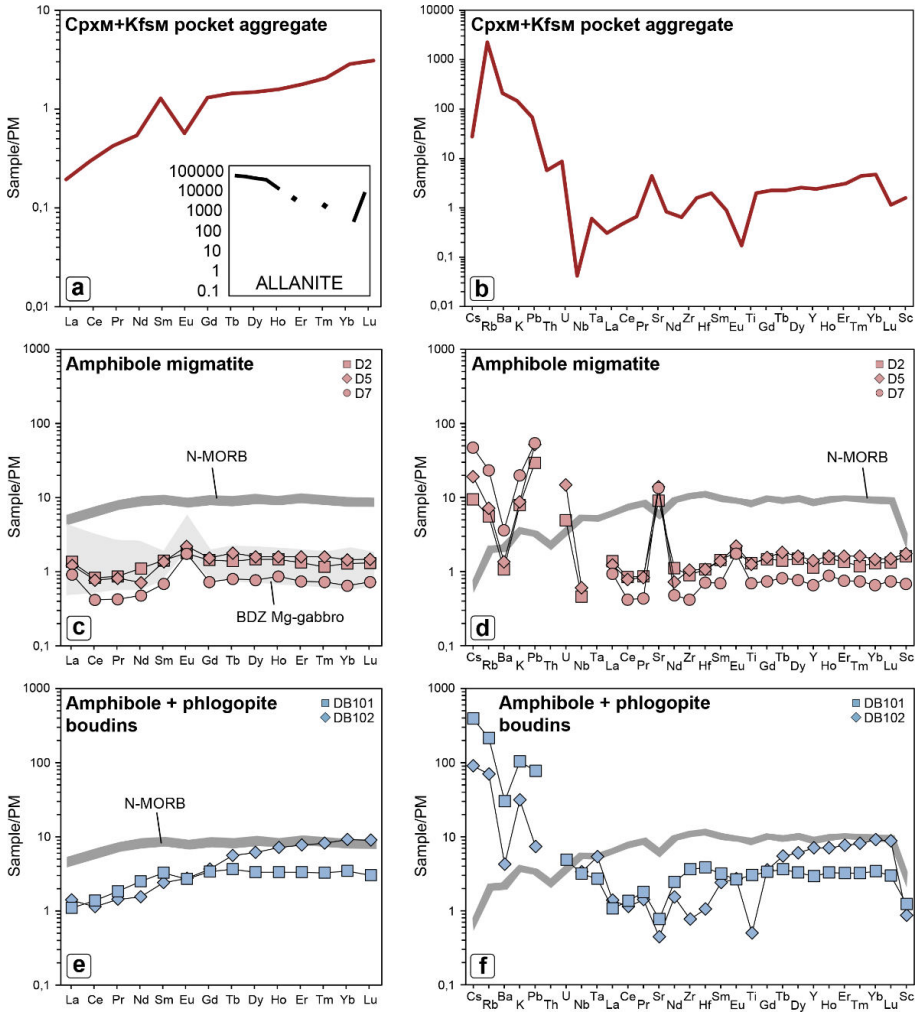

Fig. 25 Primitive Mantle normalised REE and other trace element patterns of amphibole-bearing migmatites and amphibole + phlogopite boudins from Borgo outcrop (data from Table 4). (a) and (b) trace elements pattern of interstitial Cpx_M + Kfs_M pocket aggregate in high-Al_2O_3 eclogite D9 compared with the trace element pattern of allanite from eclogite D6. (c) and (d) trace elements patterns of D2, D5 and D7 amphibole-bearing migmatites. Sample DB104 is representative of the leucosomes; (e) and (f) trace elements patterns of DB101 and DB102 amphibole + phlogopite boudins. Data are compared with average N-MORB (bold dark grey solid line; Hofmann, 1988) and Mg-gabbro from Bellinzona-Dascio Zone (light grey area BDZ; Stucki et al., 2003).

6.2.2.2 Ulten Zone

The trace element composition of Ulten Zone peridotites previously published by Tumiati et al., (2007) compare well with the trace element dataset presented here (Fig. 26a, b). Porphyroclastic garnet lherzolites and mylonitic garnet-amphibole peridotites of Ulten Zone show absolute REE concentrations comparable to that of the PM, with fractionated patterns enriched in LREE (La/Nd_N = 1.76; La/Er_N = 3.38) relative to MREE and HREE (Fig. 26a). They also display high LILE concentrations (Ba = 8.78×PM) and negative anomalies in K, Zr and Ti (fig. 26b).

Garnet clinopyroxenites show REE absolute concentrations slightly higher than the PM with enrichments in LREE (La/Nd_N = 1.93 and La/Er_N = 1.78) relative to MREE and HREE (Fig. 26c). In terms of other trace elements these rocks are characterised by high LILE concentrations (Ba = 6.52×PM) and negative anomalies in K and Zr (Fig. 26d).

Tremolitite UT17 have a REE fractionated pattern (Fig. 26e) with enrichment in LREE and MREE (La/Er_N = 1.29 and Nd/Er_N = 1.39) with respect to HREE, resembling the REE fractionated pattern of tremolitite from Borgo outcrop (c.f. with Fig. 23e). Sample UT21 display lower REE absolute concentrations than sample UT17 but similar fractionations in LREE and MREE (La/Er_N = 1.50 and Nd/Er_N = 1.16) relative to HREE (Fig. 26e). In terms of other trace elements, both samples UT17 and UT21 are characterised by relatively high LILE concentrations (up to 5.34×PM) and negative anomalies in K and Ti but they display different fractionations in HFSE (Fig. 26f). In addition, sample UT17 shows a strong Sr negative anomaly.

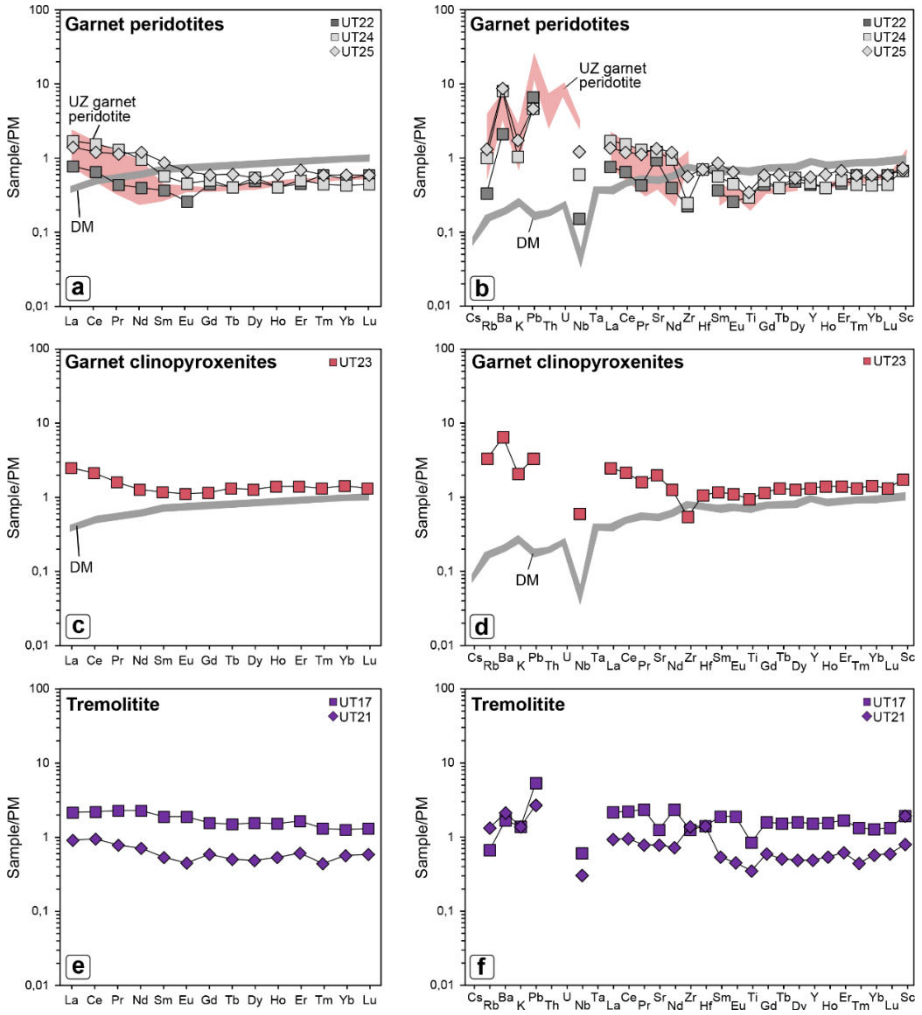

Fig. 26 Primitive Mantle normalised REE and other trace element patterns of garnet peridotites, garnet clinopyroxenites and tremolitites of Ulten Zone (data from Table 5). (a) and (b) trace elements patterns of UT22, UT24 and UT 25 garnet peridotites; (c) and (d) trace elements patterns of UT23 garnet clinopyroxenite; (e) and (f) trace elements patterns of UT17 and UT21 tremolitite. Data are compared with the reference Depleted Mantle (DM: bold grey solid line; Salters and Stracke, 2004) and garnet peridotites from Ulten Zone (UZ: pink area; Tumiati et al., 2007).

Table 4

Lithology	Garnet peridotite			Chlorite peridotite		Tremolitite	Mafic eclogite		Kyanite eclogite		
Sample	B3A	A2C2	B1B	DB182	DB187	DB151	D4	D6	E1	D3	B5
SiO_2	45.66	43.45	48.03	43.58	45.31	55.70	48.02	48.96	47.39	49.74	51.17
Al_2O_3	2.67	3.05	2.28	3.50	2.96	2.75	14.61	15.50	18.68	17.21	16.11
FeO†	7.21	8.73	8.33	7.52	8.48	3.48	10.59	10.66	5.59	7.02	5.98
MgO	36.68	38.58	37.62	34.50	35.75	21.60	9.88	9.40	11.26	9.55	9.85
CaO	2.16	2.52	2.08	2.13	2.60	12.38	11.29	9.57	12.99	11.78	11.52
Na_2O	0.14	0.21	0.10	0.12	0.27	0.36	2.09	2.01	1.86	2.56	3.03
K_2O	0.06	0.01	b.d.l.	0.09	0.09	0.07	0.30	0.27	0.18	0.35	0.26
TiO_2	0.05	0.12	0.05	0.09	0.10	0.05	1.44	1.65	0.42	0.60	0.54
P_2O_5	b.d.l.	b.d.l.	0.01	b.d.l.	0.02	0.02	0.20	0.10	0.01	0.04	b.d.l.
MnO	0.12	0.13	0.12	0.11	0.12	0.07	0.18	0.19	0.09	0.12	0.13
Cr_2O_3	0.37	0.41	0.38	0.37	0.37	0.62	0.05	0.05	0.12	0.08	0.07
LOI	3.20	2.40	0.10	7.60	3.60	2.00	1.10	0.20	1.10	0.70	0.40
CO_2	0.15	b.d.l.	b.d.l.	0.05	0.04	0.10	b.d.l.	0.11	b.d.l.	0.03	0.07
SO_2	0.06	b.d.l.	b.d.l.	0.05	b.d.l.	b.d.l.	0.08	0.10	0.02	0.04	0.34
Total	98.53	99.61	99.37	99.93	99.93	99.21	99.74	98.77	99.76	99.78	99.48
Mg#	0.90	0.90	0.90	0.89	0.88	0.91	0.65	0.61	0.80	0.73	0.75
Be	1.00	b.d.l.	b.d.l.	b.d.l.	b.d.l.	b.d.l.	b.d.l.	b.d.l.	b.d.l.	b.d.l.	b.d.l.
Sc	12.0	15.0	11.0	18.0	15.0	33.0	39.0	42.0	23.0	34.0	39.0
V	50.0	65.0	46.0	66.0	61.0	131	245	254	131	159	161
Co	91.1	113	95	107	109	37.9	44.8	42.1	31.7	37.3	42.2
Ni	1975	1862	2085	2097	2117	554	152	139	274	140	121
Cu	15.8	15.8	18.7	10.3	10.0	0.80	73.30	59.2	38.0	44.5	359
Zn	24.0	16.0	13.0	32.0	27.0	5.00	27.00	15.0	5.0	8.0	3.00
Ga	0.90	b.d.l.	1.40	2.20	1.40	2.70	15.70	12.7	9.9	13.0	10.9
As	b.d.l.	3.00	1.20	6.20	1.90	b.d.l.	0.60	1.80	1.10	3.10	1.00
Rb	4.10	0.50	1.30	6.10	4.00	0.30	12.70	9.60	3.50	9.00	5.80
Sr	5.40	20.7	12.9	11.0	15.5	22.3	129.4	39.5	279.2	179.2	83.8
Y	2.50	2.40	1.30	3.40	2.90	3.70	29.40	32.3	8.2	13.7	10.7
Zr	6.00	10.9	5.3	17.0	6.3	4.50	93.90	107	15	50	22.4
Nb	b.d.l.	0.30	0.10	0.90	0.30	0.30	2.60	4.10	0.80	0.90	0.60
Mo	0.10	b.d.l.	b.d.l.	b.d.l.	b.d.l.	b.d.l.	b.d.l.	b.d.l.	b.d.l.	b.d.l.	b.d.l.
Cs	0.60	b.d.l.	b.d.l.	1.80	0.40	b.d.l.	0.90	0.40	0.20	0.90	0.40
Ba	4.00	10.0	4.0	8.0	13.0	b.d.l.	20.00	32.0	7.0	38.0	21.0
La	0.50	0.70	0.50	0.30	0.30	1.20	4.30	5.70	2.00	1.70	1.00
Ce	0.40	1.10	0.80	0.70	0.60	3.50	11.20	14.7	3.2	4.3	2.30
Pr	0.06	0.14	0.11	0.12	0.07	0.65	2.01	2.37	0.45	0.70	0.40
Nd	0.40	0.70	0.60	1.00	0.60	3.20	11.70	11.4	2.6	3.4	2.40
Sm	0.15	0.15	0.10	0.49	0.18	0.95	3.53	3.36	0.89	1.38	1.01
Eu	0.10	0.12	0.05	0.13	0.07	0.25	1.32	1.19	0.40	0.60	0.42
Gd	0.30	0.42	0.19	0.56	0.32	0.86	4.70	5.07	1.15	1.94	1.52
Tb	0.07	0.06	0.03	0.10	0.06	0.12	0.87	0.96	0.23	0.39	0.29
Dy	0.41	0.45	0.17	0.69	0.42	0.77	5.49	6.01	1.40	2.35	2.04
Ho	0.08	0.11	0.06	0.15	0.09	0.14	1.19	1.29	0.35	0.52	0.43
Er	0.31	0.30	0.14	0.43	0.31	0.38	3.25	3.91	0.96	1.60	1.28
Tm	0.04	0.04	0.04	0.05	0.05	0.06	0.49	0.55	0.13	0.22	0.18
Yb	0.30	0.27	0.18	0.35	0.30	0.32	3.19	3.55	0.92	1.50	1.26
Lu	0.05	0.04	0.02	0.05	0.05	0.06	0.47	0.55	0.15	0.22	0.16
Hf	b.d.l.	0.30	b.d.l.	0.30	0.30	0.20	2.60	2.90	0.40	1.30	0.70
Ta	b.d.l.	b.d.l.	b.d.l.	0.10	b.d.l.	b.d.l.	0.10	0.40	b.d.l.	b.d.l.	b.d.l.
W	b.d.l.	0.80	b.d.l.	1.80	0.70	b.d.l.	1.10	1.60	b.d.l.	0.60	0.70
Tl	b.d.l.	b.d.l.	b.d.l.	b.d.l.	b.d.l.	b.d.l.	b.d.l.	b.d.l.	b.d.l.	b.d.l.	b.d.l.
Pb	b.d.l.	0.30	0.10	0.60	0.70	1.50	2.60	4.50	2.60	3.10	0.70
Bi	0.10	b.d.l.	b.d.l.	0.40	b.d.l.	1.30	b.d.l.	b.d.l.	b.d.l.	b.d.l.	0.10
Th	b.d.l.	b.d.l.	b.d.l.	b.d.l.	b.d.l.	b.d.l.	0.20	0.60	b.d.l.	b.d.l.	b.d.l.
U	b.d.l.	b.d.l.	b.d.l.	b.d.l.	b.d.l.	b.d.l.	0.60	0.70	b.d.l.	b.d.l.	b.d.l.

(continued)

Table 4

Lithology	High-Al_2O_3 eclogite			Melt pocket	Amp-bearing migmatite			Amp+Phl boudins	
Sample	D1	D8	D9	D9	D2	D5	D7	DB101	DB102
SiO_2	49.47	49.55	51.04	62.47	48.64	49.24	47.56	49.18	55.26
Al_2O_3	20.76	20.83	18.63	8.84	17.90	17.86	17.30	8.97	4.12
FeO†	3.87	3.77	3.23	2.13	4.35	4.22	5.13	9.39	6.56
MgO	8.41	8.23	8.91	7.94	11.47	10.56	13.03	17.13	18.74
CaO	13.12	13.01	11.67	12.28	13.08	13.24	11.64	8.43	11.20
Na_2O	2.90	2.84	3.20	1.90	1.92	2.06	1.49	0.36	0.28
K_2O	0.22	0.30	1.21	4.16	0.23	0.25	0.57	3.04	0.91
TiO_2	0.16	0.16	0.19	0.02	0.26	0.25	0.14	0.61	0.10
P_2O_5	b.d.l.	b.d.l.	b.d.l.	-	b.d.l.	b.d.l.	b.d.l.	0.02	b.d.l.
MnO	0.07	0.07	0.06	0.10	0.08	0.09	0.08	0.16	0.19
Cr_2O_3	0.08	0.08	0.12	0.01	0.20	0.16	0.09	0.11	0.21
LOI	0.70	1.00	1.10	-	1.60	1.30	2.60	2.20	2.00
CO_2	0.04	0.04	0.26	-	b.d.l.	0.11	0.03	0.09	0.08
SO_2	0.04	0.03	0.08	-	0.05	b.d.l.	b.d.l.	b.d.l.	b.d.l.
Total	99.82	99.81	99.69	99.86	99.77	99.34	99.73	99.65	99.67
Mg#	0.81	0.81	0.83	0.87	0.84	0.82	0.83	0.78	0.85
Be	b.d.l.	b.d.l.	b.d.l.	0.10	b.d.l.	b.d.l.	b.d.l.	b.d.l.	b.d.l.
Sc	17.0	17.0	18.0	21.3	26.0	28.0	11.0	20.0	14.00
V	77	76	84.0	125.4	94.0	104	55	144.0	56.00
Co	23.2	23.0	24.2	13.5	36.9	32.3	45.4	58.4	45.40
Ni	202	181	213	57	279	226	459	700.0	986.00
Cu	44	45	60.1	1.4	66.2	34.6	24.7	5.2	1.00
Zn	3.00	2.00	9.00	24.64	3.00	6.00	21.00	56.0	19.00
Ga	10.9	10.6	10.9	n.a.	8.8	9.50	9.10	11.6	6.60
As	0.80	b.d.l.	0.60	n.a.	2.20	1.70	b.d.l.	b.d.l.	b.d.l.
Rb	6.10	6.80	35.8	113.2	3.3	4.30	13.90	131	42.20
Sr	247.8	271.1	126	140	180	276	267	16	8.90
Y	5.2	5.7	4.60	6.50	4.90	6.10	2.80	12.7	30.40
Zr	10.3	8.0	10.4	6.3	9.4	11.0	4.4	38	8.10
Nb	0.30	0.20	0.10	0.01	0.30	0.40	b.d.l.	2.10	2.20
Mo	b.d.l.	b.d.l.	b.d.l.	b.d.l.	b.d.l.	b.d.l.	b.d.l.	0.30	0.20
Cs	0.20	0.30	1.90	0.88	0.20	0.40	1.00	8.30	1.90
Ba	38.0	42.0	189	3111	7	9.00	24.00	200	28.00
La	2.40	3.30	1.90	0.16	0.90	0.80	0.60	0.7	0.90
Ce	5.00	7.10	2.80	0.63	1.40	1.30	0.70	2.3	1.90
Pr	0.67	0.92	0.37	0.14	0.22	0.21	0.11	0.46	0.36
Nd	3.10	4.00	1.90	0.90	1.40	0.90	0.60	3.1	1.90
Sm	1.18	1.46	0.42	0.58	0.58	0.56	0.28	1.30	0.97
Eu	0.58	0.72	0.22	0.17	0.28	0.34	0.27	0.41	0.42
Gd	1.18	1.41	0.67	0.63	0.80	0.84	0.40	1.83	1.96
Tb	0.20	0.21	0.12	0.13	0.14	0.18	0.08	0.36	0.54
Dy	1.07	1.09	0.74	0.92	1.00	1.09	0.52	2.21	4.05
Ho	0.18	0.22	0.19	0.20	0.22	0.24	0.13	0.49	1.05
Er	0.56	0.61	0.54	0.81	0.59	0.70	0.33	1.43	3.34
Tm	0.07	0.09	0.09	0.14	0.08	0.11	0.05	0.22	0.55
Yb	0.55	0.53	0.60	1.27	0.57	0.65	0.29	1.50	4.02
Lu	0.08	0.07	0.08	0.19	0.09	0.10	0.05	0.20	0.60
Hf	0.30	0.30	0.40	0.39	0.30	0.30	0.20	1.10	0.30
Ta	b.d.l.	0.10	b.d.l.	0.00	b.d.l.	b.d.l.	b.d.l.	0.10	0.20
W	1.80	b.d.l.	b.d.l.	0.04	0.50	b.d.l.	b.d.l.	0.80	b.d.l.
Tl	b.d.l.	b.d.l.	0.20	n.a.	b.d.l.	b.d.l.	b.d.l.	0.70	0.20
Pb	5.00	4.20	4.00	16.19	4.40	7.80	8.20	11.60	1.10
Bi	b.d.l.	b.d.l.	b.d.l.	n.a.	b.d.l.	b.d.l.	b.d.l.	0.10	0.10
Th	0.40	0.60	0.30	0.38	b.d.l.	b.d.l.	b.d.l.	b.d.l.	b.d.l.
U	1.20	1.30	0.40	0.10	0.10	0.30	b.d.l.	0.10	b.d.l.

† total iron; LOI = loss on ignition; Mg#=Mg/(Mg+Fe2+)

Table 5

Lithology	Grt-lherzolite	Mylonitic Grt+Amp peridotite		Grt-clinopyroxenite	Tremolitite	
Sample	UT22	UT24	UT25	UT23	UT17	UT21
SiO_2	46.11	48.31	46.76	50.62	49.39	43.74
Al_2O_3	2.63	2.59	3.05	5.93	7.05	2.92
FeO†	8.52	8.59	8.13	5.95	4.86	8.44
MgO	35.05	36.35	37.42	23.91	23.20	35.51
CaO	2.49	2.33	2.71	9.94	8.84	2.70
Na_2O	0.10	0.22	0.25	0.60	0.27	0.13
K_2O	b.d.l.	0.03	0.05	0.06	0.04	0.04
TiO_2	0.06	0.06	0.07	0.19	0.17	0.07
P_2O_5	b.d.l.	0.02	0.02	0.01	b.d.l.	0.02
MnO	0.13	0.12	0.12	0.12	0.09	0.12
Cr_2O_3	0.33	0.29	0.34	0.68	0.38	0.34
LOI	3.70	0.20	0.20	1.30	5.20	5.10
CO_2	0.03	0.05	0.28	0.03	0.03	0.10
SO_2	0.02	0.02	b.d.l.	0.10	b.d.l.	0.02
Total	99.17	99.18	99.40	99.44	99.52	99.25
Mg#	0.88	0.88	0.89	0.88	0.89	0.88
Be	b.d.l.	b.d.l.	b.d.l.	b.d.l.	b.d.l.	b.d.l.
Sc	11.0	11.0	12.0	28.0	31.0	13.0
V	51.0	53.0	60.0	160	199	69
Co	102.5	107	101	64.5	49.4	99.5
Ni	1989	2010	1840	1471	652	1937
Cu	37.5	36.1	24.8	183.70	1.10	5.9
Zn	37.0	12.0	10.0	13.00	12.00	39.0
Ga	1.50	1.70	2.20	4.40	4.70	2.0
As	2.70	b.d.l.	0.50	b.d.l.	b.d.l.	11.50
Rb	0.20	0.60	0.80	2.00	0.40	0.80
Sr	19.00	24.5	26.9	39.6	25.0	15.6
Y	1.90	2.00	2.40	5.70	6.50	2.1
Zr	2.40	2.6	6.0	5.80	13.20	15
Nb	0.10	0.40	0.80	0.40	0.40	0.20
Mo	b.d.l.	b.d.l.	b.d.l.	b.d.l.	b.d.l.	b.d.l.
Cs	b.d.l.	b.d.l.	b.d.l.	b.d.l.	b.d.l.	b.d.l.
Ba	14.00	53.0	58.0	43.00	11.00	14.0
La	0.50	1.10	0.90	1.60	1.40	0.60
Ce	1.10	2.60	2.00	3.60	3.70	1.6
Pr	0.11	0.33	0.29	0.41	0.59	0.20
Nd	0.50	1.20	1.50	1.60	2.90	0.9
Sm	0.15	0.23	0.35	0.48	0.77	0.22
Eu	0.04	0.07	0.10	0.17	0.29	0.07
Gd	0.24	0.27	0.32	0.63	0.86	0.32
Tb	0.04	0.04	0.06	0.13	0.15	0.05
Dy	0.33	0.37	0.36	0.86	1.06	0.33
Ho	0.06	0.06	0.09	0.21	0.23	0.08
Er	0.20	0.22	0.30	0.61	0.73	0.27
Tm	0.04	0.03	0.04	0.09	0.09	0.03
Yb	0.23	0.19	0.26	0.63	0.56	0.25
Lu	0.04	0.03	0.04	0.09	0.09	0.04
Hf	b.d.l.	0.20	0.20	0.30	0.40	0.40
Ta	b.d.l.	b.d.l.	b.d.l.	b.d.l.	b.d.l.	b.d.l.
W	b.d.l.	b.d.l.	b.d.l.	b.d.l.	b.d.l.	0.50
Tl	b.d.l.	b.d.l.	b.d.l.	b.d.l.	b.d.l.	b.d.l.
Pb	1.00	0.70	0.70	0.50	0.80	0.40
Bi	b.d.l.	b.d.l.	b.d.l.	b.d.l.	b.d.l.	0.10
Th	b.d.l.	b.d.l.	b.d.l.	b.d.l.	b.d.l.	b.d.l.
U	b.d.l.	b.d.l.	b.d.l.	b.d.l.	b.d.l.	b.d.l.

† total iron; LOI = loss on ignition; $Mg_{\#}=Mg/(Mg+Fe^{2+})$

6.3 Mineral chemistry

The description of the chemical compositions of rock-forming minerals in peridotites and pyroxenites of the Ulten Zone has been provided by numerous petrological and geochemical studies (Marocchi et al., 2009, 2010; Nimis and Morten, 2000; Obata and Morten, 1987; Rampone and Morten, 2001; Scambelluri et al., 2006; Tumiati et al., 2007). For this reason, in this chapter will be presented only the chemical compositions of minerals constituting peridotites, tremolitites, eclogites, amphibole-bearing migmatites and amphibole + phlogopite boudins of the Monte Duria area.

6.3.1 Major elements

The major elements composition of the analysed rock-forming minerals is reported in Table 6 and portrayed in Figures from 27 to 36.

6.3.1.1 Peridotites

In garnet peridotites, olivine has forsteritic composition with X_{Mg} comparable to that of the bulk rock (0.90). Garnet is pyrope-rich ($Py_{67}Alm_{18}Gr_{15}$) with a core-to-rim increase of Al and Fe^{2+} ($Py_{64}Alm_{21}Gr_{15}$) and a complementary decrease of Mg, likely related to a retrograde equilibration (Tab. 6; Fig. 27). Clinopyroxenes have a diopside-rich composition (Tab. 6). In the Na-$Al^{(VI)}$ diagram (Fig. 28a) clinopyroxene of samples B1B and B3A displays a progressive decrease of Na and $Al^{(VI)}$ from Cpx_1, to neoblastic Cpx_2, to symplectitic Cpx_{Sym}. Cpx_1 of sample A2C2 displays a sharp zonation with a core-to-rim decrease of Na and $Al^{(VI)}$ (Fig. 28b). The composition of the analysed rims approach that of clinopyroxene in equilibrium with post-peak minerals (Cpx_2), in agreement with a retrograde equilibration of clinopyroxenes towards lower pressure. Cpx_2 also shows Al-rich composition with Al up to 0.07 a.p.f.u. (Tab. 6). Orthopyroxenes are enstatites with X_{Mg} = 0.91. In the Si-Al diagram they display an increase of Al from orthopyroxene in equilibrium with garnet to orthopyroxene observed in kelyphites (Opx_{Sym}), and a complementary decrease in Si (Fig. 28c, d), following the same retrogression equilibration recorded by garnet and clinopyroxene. Amp_1 and Amp_2 are pargasitic to edenitic in composition, while symplectitic amphiboles (Amp_{Sym}) vary from tschermakite to Mg-hornblende in samples MD20 and A2C2, to pargasite in peridotites B1B and B3A (Tab. 6). In both Na-$Al^{(IV)}$ and $Al^{(VI)}$-$Al^{(IV)}$ diagrams amphiboles follow the

pargasitic substitution, with Amp_{Sym} that shows the highest $Al^{(IV)}$ and $Al^{(VI)}$ (Fig. 29).

In chlorite peridotites olivine, Opx_1, Opx_2 and Opx_{Porph} all show X_{Mg} ranging between 0.89 and 0.91, and clinopyroxene is diopside-rich ($Di_{90}Jd_4Hd_6$, Tab. 6). In the Si-Al diagram all orthopyroxene generations display similar compositions (Fig. 30b) which are comparable to those of orthopyroxenes of garnet peridotites B3A and MD20 (c.f. with Fig. 28c, d). Porphyroblastic amphibole in equilibrium with Opx_{Porph} and Phl_{Porph} is a hornblende (Amp_{Porph}, Tab. 6), whereas Amp_2 in the recrystallised matrix and Amp_3 along the chlorite foliation vary in composition from edenite to tremolitic-hornblende. In the Na-$Al^{(IV)}$ and $Al^{(VI)}$-$Al^{(IV)}$ diagrams (Fig. 30c, d) also amphiboles of chlorite peridotite plot along the pargasite exchange vector.

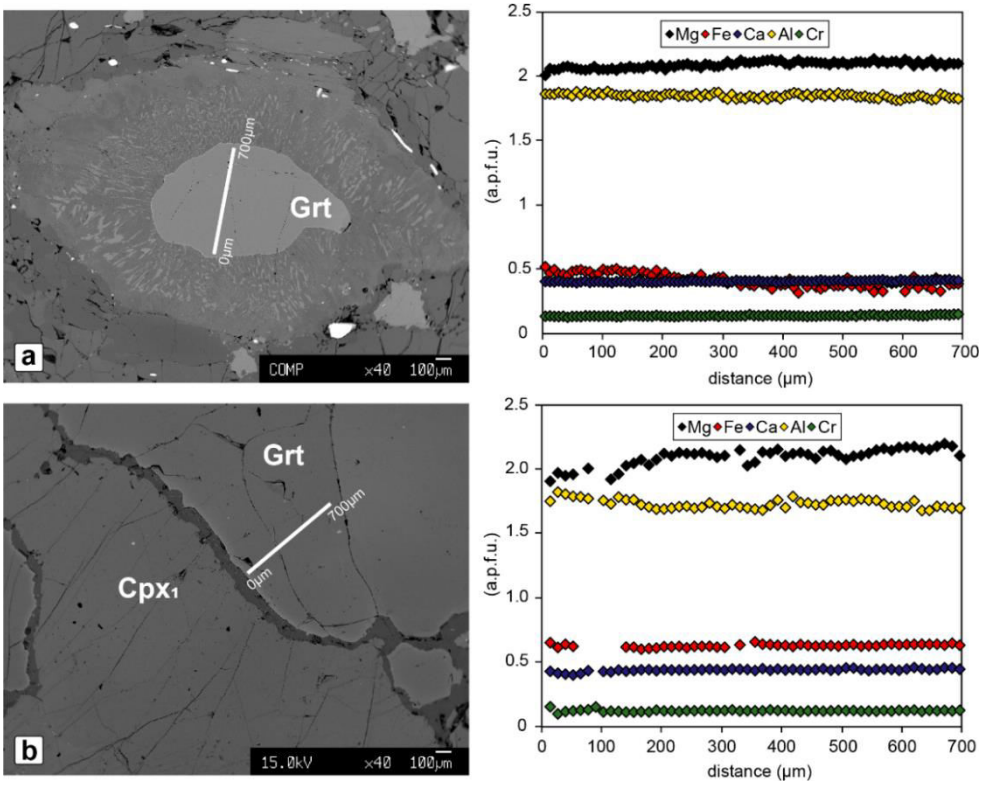

Fig. 27 BSE images and microprobe traverses of garnet of garnet peridotite B1B (a) and MD20 (b)

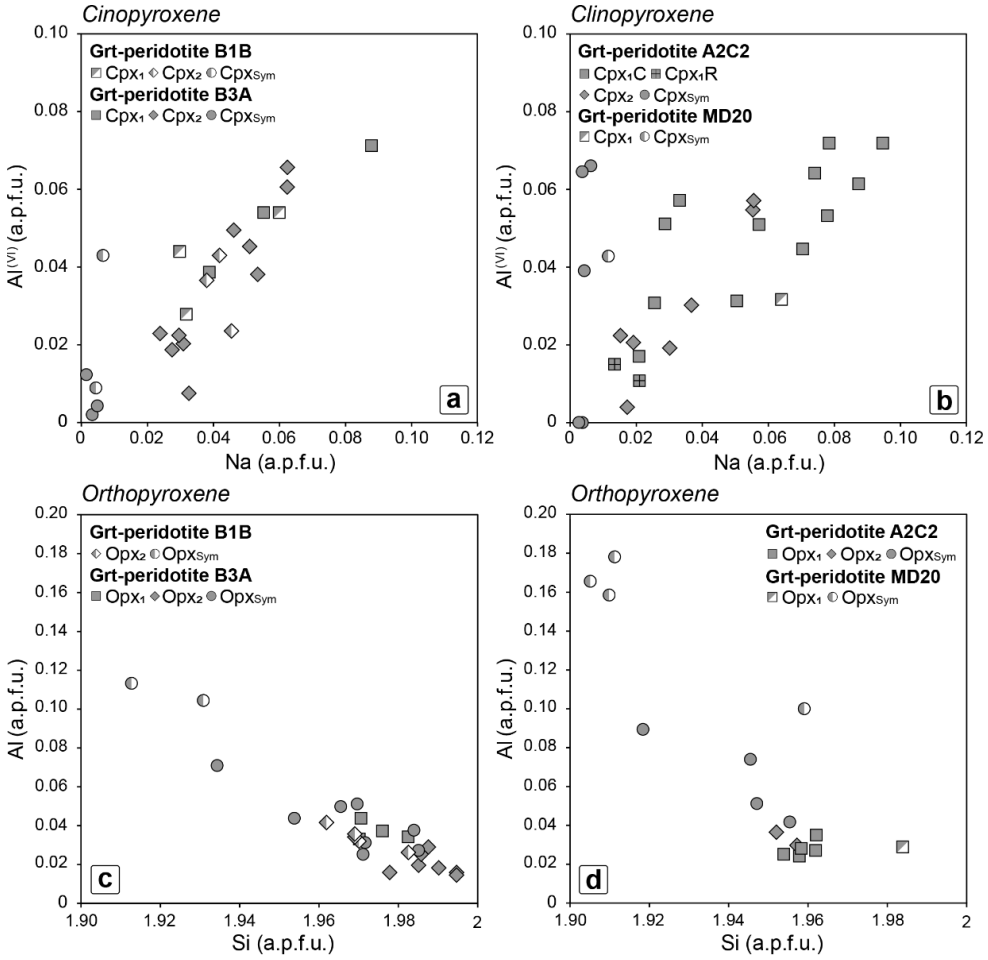

Fig. 28 (a, b) Compositional variation of clinopyroxenes (octahedral Al versus Na) in garnet peridotites from Mt. Duria; (c, d) Al versus Si content of porphyroclastic, neoblastic and symplectitic orthopyroxenes of garnet peridotites from Mt. Duria.

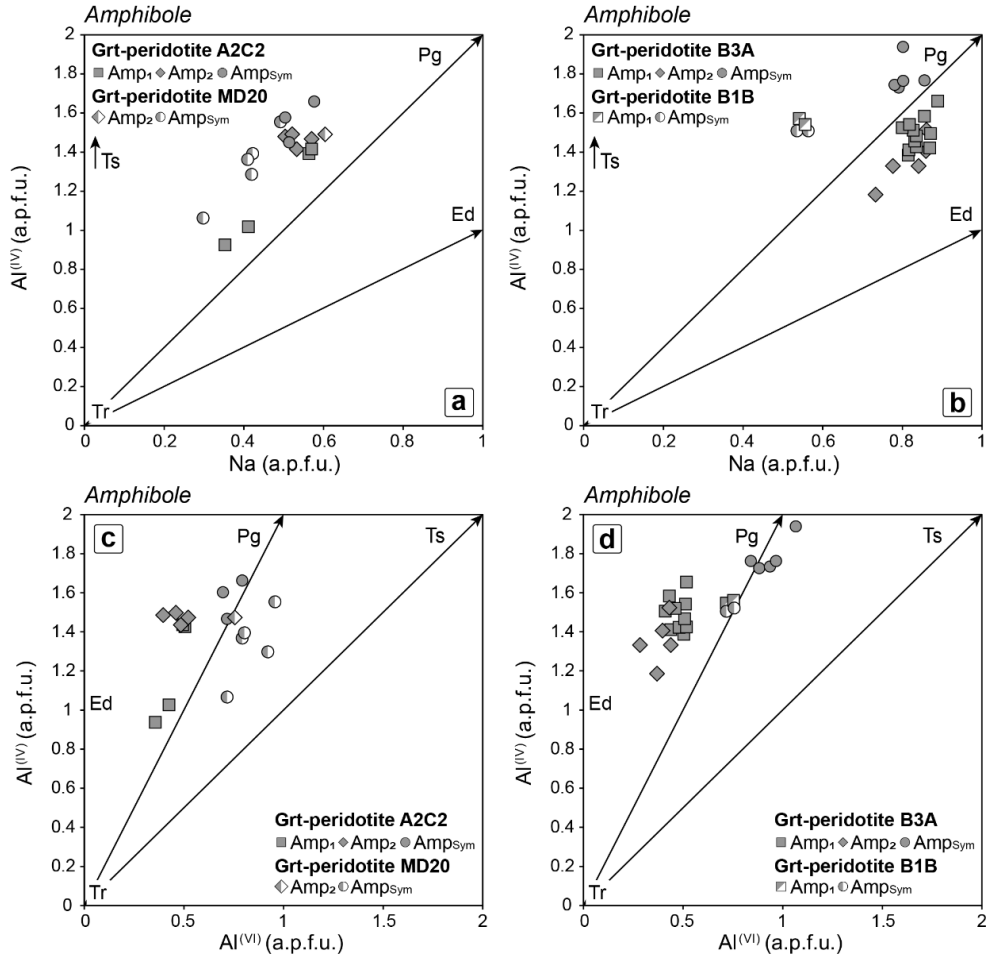

Fig. 29 Compositional variations of amphiboles from garnet peridotites of Mt. Duria. Tetrahedral aluminium (Al^{IV}) is plotted with respect to total Na. (a, b) octahedral aluminium (Al^{VI}) (c, d). Ts = tschermakite, Ed = edenite, Pg = pargasite, Tr = tremolite.

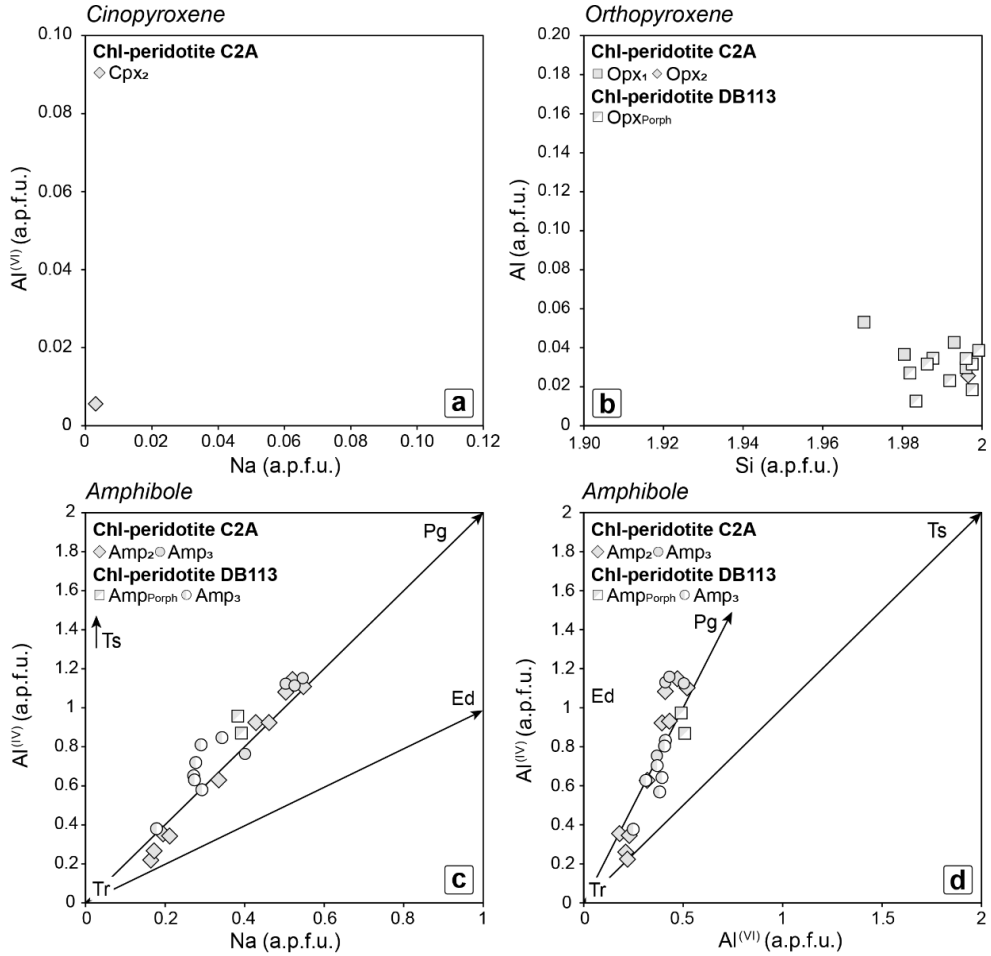

Fig. 30 (a) Compositional variation of clinopyroxenes (octahedral Al versus Na) in chlorite peridotites; (b) Al versus Si content of orthopyroxenes of chlorite peridotites; (c, d) compositional variations of amphiboles from chlorite peridotites. Tetrahedral aluminium (Al^{IV}) is plotted with respect to total Na and octahedral aluminium (Al^{VI}); Ts = tschermakite, Ed = edenite, Pg = pargasite, Tr = tremolite.

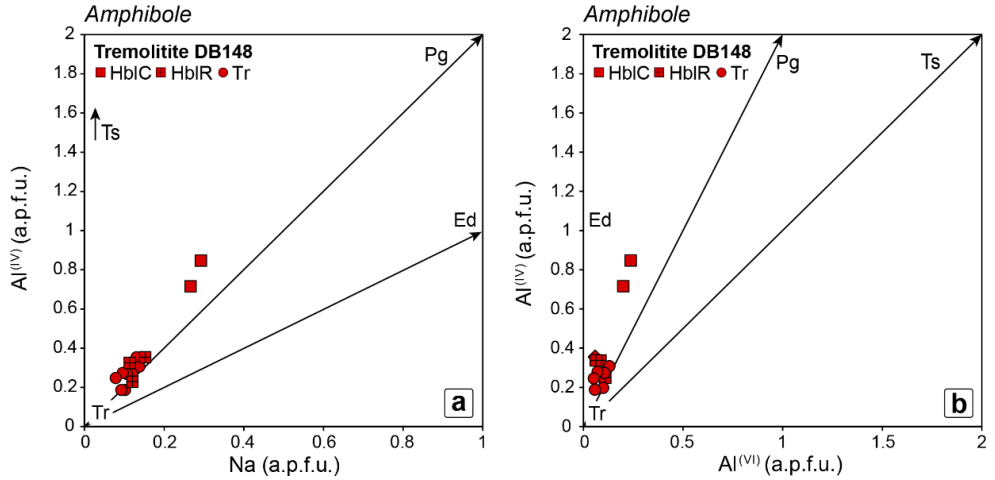

Fig. 31 Compositional variations of amphiboles from tremolitites. Tetrahedral aluminium (Al^{IV}) is plotted with respect to total Na (a) and octahedral aluminium (Al^{VI}) (b); Ts = tschermakite, Ed = edenite, Pg = pargasite, Tr = tremolite.

6.3.1.2 Tremolitite

Relict amphibole porphyroblasts in tremolitites are hornblende and their compositional variation is closely related to the optical zoning (Tab. 6). The analysed dusty cores correspond to Mg-hornblende while the inclusion-free rims are tremolites (Fig. 31a, b) with compositions resembling those of retrogression tremolites, characterised by lower Al, Na and Fe content with respect to porphyroblastic hornblende (Tab. 6, Fig. 31a, b).

6.3.1.3 Eclogites, amphibole-bearing migmatites and amphibole + phlogopite boudins

In both mafic and kyanite-bearing eclogites, garnets are zoned and their core-to-rim composition varies from $Py_{35}Alm_{40}Gr_{25}$ to $Py_{28}Alm_{52}Gr_{20}$ at rim (Tab. 6; Fig. 32). The composition of omphacite included in garnet corresponds to $Di_{60}Jd_{30}Hd_{10}$, whereas Cpx_2 in symplectites is diopside-rich ($Di_{80}Jd_6Hd_{14}$; Tab. 6). Diopside-rich compositions ($Di_{82}Jd_6Hd_{12}$) are also displayed by clinopyroxenes in interstitial pocket aggregates (Cpx_M) in kyanite and high-Al_2O_3 eclogites (Tab. 6). In the Na versus $Al^{(VI)}$ variation diagram (Fig. 33a) clinopyroxenes show a decrease of Na and $Al^{(VI)}$ from omphacites to Cpx_M to symplectitic Cpx_2. Orthopyroxene occurs only in symplectites replacing kyanite in kyanite eclogite B5A. Symplectitic orthopyroxenes (Opx_{Sym}) are enstatites

with X_{Mg} of 0.71-0.77, Si of 1.96-1.99 a.p.f.u. and Al of 0.01-0.05 a.p.f.u. (Tab 6; Fig. 33b). All amphiboles in eclogites are calcic. Amphiboles after garnet and omphacite (Amp_2) vary from Mg-hornblende to actinolite, whereas coronitic Amp_3 varies in composition from pargasite to Mg-hornblende to tremolite (Tab. 6). In the Na-$Al^{(IV)}$ and $Al^{(VI)}$-$Al^{(IV)}$ variation diagrams of Figure 34, both Amp_2 and Amp_3 plot along the pargasite exchange vector. Amp_3 shows a variable Na-$Al^{(IV)}$ trend depending on its microstructural site. Coronitic amphiboles around symplectites post-omphacite in fact show the highest Na concentration, comparable to some grains included in garnet representing retrogressed omphacites. In mafic eclogite, porphyroblastic K-feldspar corresponds to almost pure orthoclase X_{Or} = 0.98. Slightly lower X_{Or} = 0.90 characterises Kfs_M occurring within interstitial pockets aggregates together with Cpx_M + Qz_M + Pl_M in high-Al_2O_3 eclogites (Tab. 6). Plagioclase in interstitial pocket aggregates (Pl_M) and in symplectites replacing garnet and omphacite (Pl_2) are albite-rich (Tab. 6) whereas Pl_2 in symplectites replacing zoisite show variation from albite-rich (Ab_{75}) to anorthite-rich compositions (An_{82}). Anorthite-rich compositions (An_{88}) are also displayed by plagioclase in symplectites replacing kyanite (Pl_{Sym}) in kyanite and high-Al_2O_3 eclogites (Tab. 6).

In amphibole-bearing migmatites, Cpx_2 is diopside-rich ($Di_{86}Jd_3Hd_{11}$) and shows X_{Mg} ranging between 0.88 and 0.92 (Tab. 6), resembling the composition of symplectitic diopsides in eclogites. Amphibole porphyroblasts (Hbl), and amphiboles in symplectites replacing garnet and omphacite (Amp_2) are Mg-hornblende (Tab. 6). In the Na-$Al^{(IV)}$ and $Al^{(VI)}$-$Al^{(IV)}$ variation diagrams of Figure 35, both amphibole generations plot along the pargasite exchange vector. The composition of symplectitic plagioclase (Pl_2) is albite-rich resembling the composition of Pl_2 and Pl_M in eclogites (Ab_{66}; Tab. 6).

In amphibole + phlogopite boudins, tremolite shows X_{Mg} of 0.79-0.81, low Al (0.62-0.87 a.p.f.u.) and very low Na (0.10-0.16 a.p.f.u.) contents (Fig. 36; Tab. 6). Phlogopite displays X_{Mg} = 0.71-0.72, high Fe (0.72-0.74 a.p.f.u.) and high Al (1.41-1.45 a.p.f.u.) contents (Tab. 6). K-feldspar corresponds to almost pure orthoclase X_{Or} = 0.98-0.99 (Tab. 6)

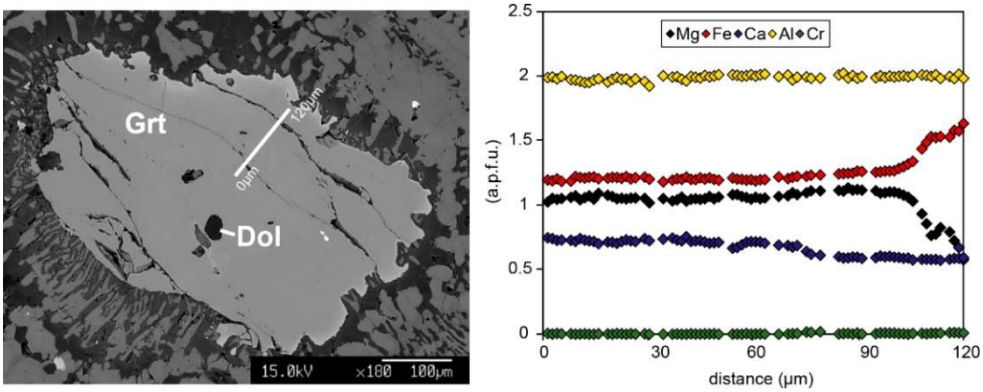

Fig. 32 BSE image and microprobe traverse of garnet of mafic eclogite D6.

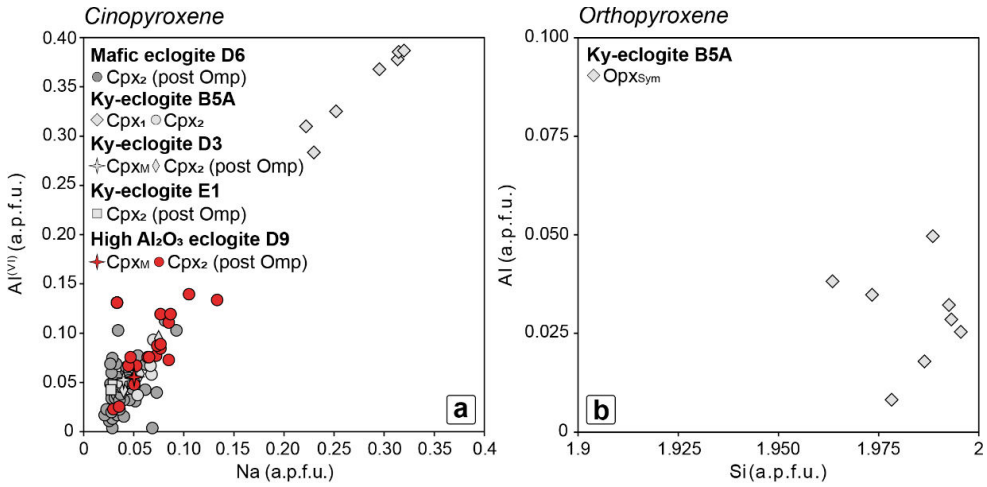

Fig. 33 (a) Compositional variation of clinopyroxene (octahedral Al versus Na) in eclogites; (b) Al versus Si content of orthopyroxene in kyanite eclogite B5A.

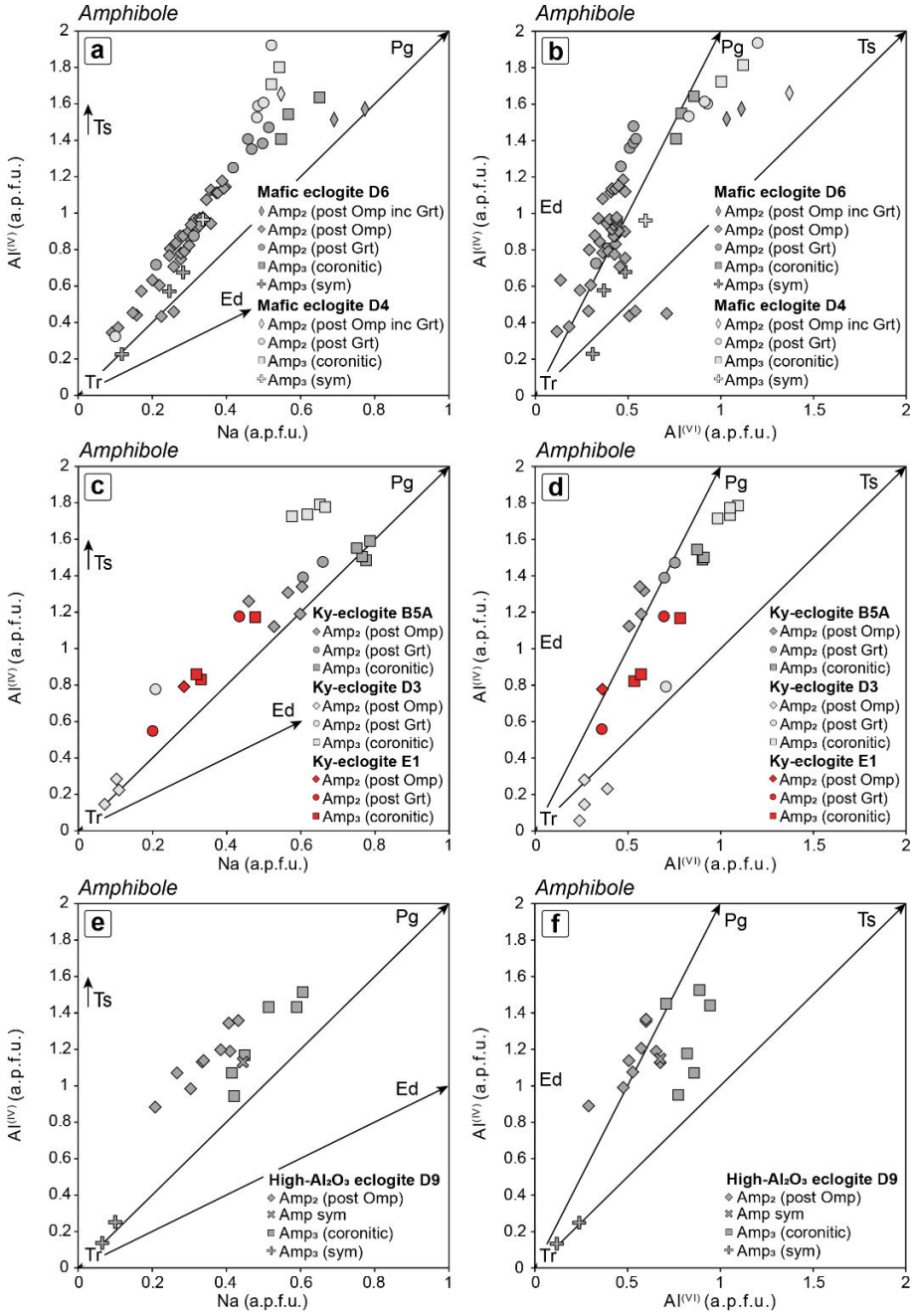

Fig. 34 Compositional variations of amphiboles from eclogites. Tetrahedral aluminium (Al^{IV}) is plotted with respect to total Na (a, c, e) and octahedral aluminium (Al^{VI}) (b, d, f); Ts = tschermakite, Ed = edenite, Pg = pargasite, Tr = tremolite.

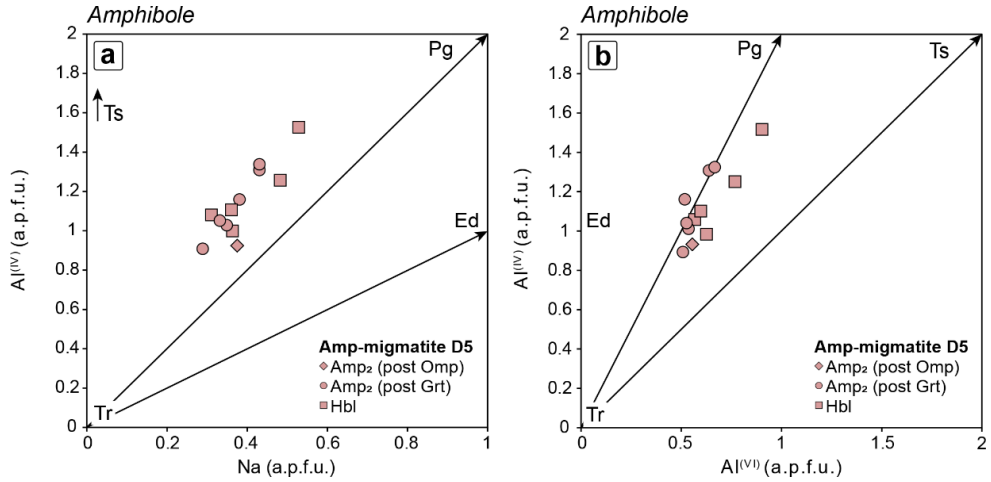

Fig. 35 Compositional variations of amphiboles from amphibole-bearing migmatites. Tetrahedral aluminium (Al^{IV}) is plotted with respect to total Na (a) and octahedral aluminium (Al^{VI}) (b); Ts = tschermakite, Ed = edenite, Pg = pargasite, Tr = tremolite.

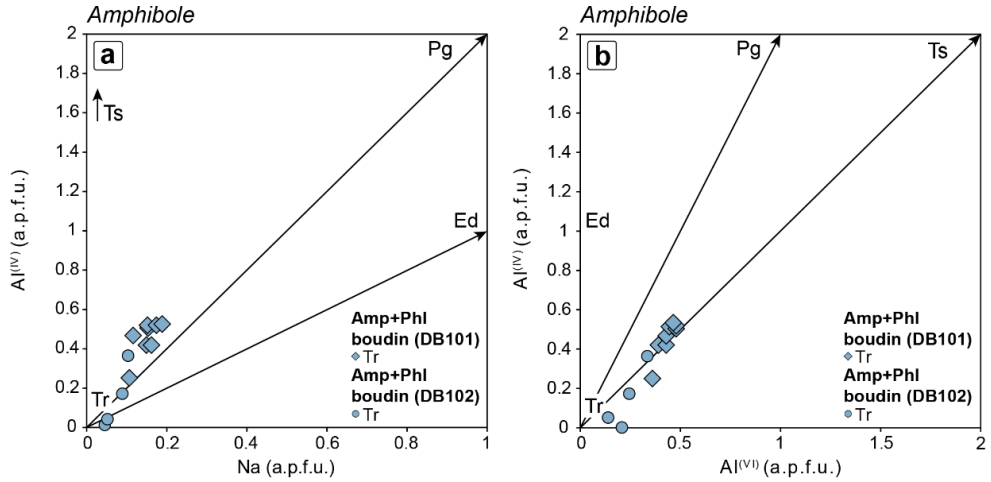

Fig. 36 Compositional variations of amphiboles from amphibole + phlogopite boudins. Tetrahedral aluminium (Al^{IV}) is plotted with respect to total Na (a) and octahedral aluminium (Al^{VI}) (b); Ts = tschermakite, Ed = edenite, Pg = pargasite, Tr = tremolite.

Table 6

Lithology	Grt-peridotite																
Sample	A2C2													B3A			
Mineral	Grt	Grt	Cpx_1	Cpx_1	Cpx_2	Cpx_{Sym}	Opx_1	Opx_2	Opx_{Sym}	Ol	Amp_1	Amp_2	Amp_{Sym}	Grt	Grt	Cpx_1	Cpx_2
Comment	core	rim	core	rim										core	rim		
SiO_2	42.31	41.84	54.07	54.46	54.96	55.19	56.92	56.28	56.32	39.74	46.49	45.55	46.70	42.47	42.29	54.91	55.09
TiO_2	0.08	0.15	0.13	0.13	0.04	0.24	0.10	0.05	0.06	0.01	0.70	0.52	0.35	0.08	0.09	0.04	0.07
Al_2O_3	21.69	22.50	1.98	0.94	1.53	1.40	0.80	1.04	1.91	0.00	11.52	11.19	13.22	21.39	21.40	1.68	1.18
Cr_2O_3	2.75	1.81	1.34	0.31	0.95	0.03	0.21	0.12	0.01	0.00	1.42	1.82	0.93	2.62	2.82	1.05	0.65
FeO†	9.87	10.28	2.46	1.75	1.95	1.84	6.52	6.54	8.43	9.72	3.03	2.70	3.43	10.26	11.28	2.28	1.87
MgO	19.02	18.48	16.04	17.57	16.64	17.91	34.95	34.77	33.22	49.88	18.93	19.01	18.51	18.90	18.08	16.18	16.79
MnO	0.58	0.57	0.11	0.08	0.08	0.10	0.09	0.13	0.32	0.14	0.05	0.01	0.10	0.58	0.62	0.06	0.02
NiO	0.05	0.00	0.00	0.02	0.01	0.00	0.04	0.13	0.05	0.43	0.15	0.15	0.05	0.00	0.02	0.00	0.00
CaO	5.69	5.02	23.15	24.53	23.14	24.29	0.22	0.14	0.19	0.01	12.51	12.62	12.50	5.76	5.69	21.84	23.15
Na_2O	0.00	0.01	0.81	0.20	0.78	0.06	0.01	0.01	0.03	0.00	2.08	1.77	1.88	0.00	0.00	1.25	0.66
K_2O	0.00	0.01	0.00	0.00	0.00	0.01	0.00	0.00	0.01	0.01	0.23	0.77	0.03	0.00	0.00	0.00	0.01
Sum	102.04	100.67	100.09	99.99	100.08	101.07	99.86	99.21	100.55	99.94	97.11	97.80	97.70	102.06	102.29	99.29	99.49
Si	2.99	2.99	1.97	1.97	1.99	1.98	1.96	1.95	1.95	0.97	6.58	6.52	6.53	3.00	3.00	2.00	2.01
Ti	0.00	0.01	0.00	0.00	0.00	0.01	0.00	0.00	0.00	0.00	0.07	0.06	0.04	0.00	0.00	0.00	0.00
Al	1.80	1.90	0.08	0.04	0.07	0.06	0.03	0.04	0.08	0.00	1.92	1.89	2.18	1.78	1.79	0.07	0.05
Cr	0.15	0.10	0.04	0.01	0.03	0.00	0.01	0.00	0.00	0.00	0.16	0.21	0.10	0.15	0.16	0.03	0.02
Fe^{3+}	0.06	0.01	0.00	0.01	0.00	0.00	0.03	0.05	0.03	0.00	0.01	0.13	0.07	0.06	0.05	0.00	0.00
Fe^{2+}	0.52	0.61	0.07	0.04	0.06	0.06	0.16	0.14	0.21	0.20	0.35	0.20	0.33	0.54	0.62	0.07	0.06
Mg	2.00	1.97	0.87	0.95	0.90	0.96	1.80	1.80	1.71	1.82	3.99	4.06	3.86	1.99	1.91	0.88	0.91
Mn	0.03	0.03	0.00	0.00	0.00	0.00	0.00	0.00	0.01	0.00	0.01	0.00	0.01	0.03	0.04	0.00	0.00
Ni	0.00	0.00	0.00	0.00	0.00	0.00	0.00	0.00	0.00	0.01	0.02	0.02	0.01	0.00	0.00	0.00	0.00
Ca	0.43	0.38	0.90	0.95	0.90	0.93	0.01	0.01	0.01	0.00	1.90	1.94	1.87	0.44	0.43	0.85	0.90
Na	0.00	0.00	0.06	0.01	0.06	0.00	0.00	0.00	0.00	0.00	0.57	0.49	0.51	0.00	0.00	0.09	0.05
K	0.00	0.00	0.00	0.00	0.00	0.00	0.00	0.00	0.00	0.00	0.04	0.14	0.00	0.00	0.00	0.00	0.00
Cation Sum	8.00	8.00	4.00	4.00	4.00	4.00	4.00	3.99	4.00	3.00	15.61	15.63	15.51	8.00	8.00	4.00	4.00
X_{Mg}	0.77	0.76	0.92	0.95	0.94	0.95	0.91	0.93	0.88	0.90	0.92	0.93	0.91	0.77	0.74	0.93	0.94
$Al^{(IV)}$	-	-	0.03	0.03	0.01	0.02	-	-	-	-	1.42	1.48	1.47	-	-	0.00	0.00
$Al^{(VI)}$	-	-	0.05	0.02	0.06	0.04	-	-	-	-	0.50	0.41	0.71	-	-	0.07	0.05

(continued)

Table 6

Lithology	Grt-peridotite																
Sample	B1B										MD20						
Mineral	Grt	Grt	Opx_2	Opx_{Sym}	Ol	Cpx_1	Cpx_2	Cpx_{Sym}	Amp_1	Amp_{Sym}	Grt	Grt	Cpx_1	Cpx_{Sym}	Opx_1	Opx_{Sym}	Ol
Comment	core	rim									core	rim					
SiO_2	41.18	40.66	57.24	54.88	40.12	54.12	53.81	52.90	45.49	45.86	42.37	42.37	53.16	54.70	58.39	55.36	41.07
TiO_2	0.07	0.07	0.02	0.06	0.00	0.03	0.09	0.02	0.31	0.27	0.04	0.04	0.17	0.16	0.01	0.02	0.00
Al_2O_3	22.76	22.37	0.87	2.77	0.00	0.90	1.07	1.33	13.56	13.52	21.61	22.44	1.55	1.79	0.63	4.45	0.02
Cr_2O_3	2.43	2.45	0.11	0.19	0.02	0.27	0.61	0.18	1.43	0.70	2.76	2.11	0.75	0.26	0.04	0.31	0.01
FeO†	8.85	12.64	6.39	7.28	9.19	1.64	1.62	1.95	3.26	3.44	10.07	9.92	2.04	1.67	6.19	6.79	9.95
MgO	19.53	16.89	34.55	33.39	48.82	17.19	17.01	17.23	17.72	18.14	18.57	19.11	16.41	16.95	0.19	0.14	49.62
MnO	0.39	0.96	0.12	0.25	0.12	0.07	0.05	0.08	0.07	0.05	0.52	0.47	0.10	0.01	0.07	0.01	0.23
NiO	0.00	0.00	0.00	0.00	0.00	0.00	0.00	0.00	0.00	0.00	0.05	0.00	0.00	0.10	35.41	32.90	0.42
CaO	5.29	5.18	0.15	0.18	0.01	23.76	23.69	24.55	12.59	12.61	5.68	5.43	22.94	25.22	0.16	0.17	0.03
Na_2O	0.00	0.04	0.00	0.00	0.00	0.45	0.54	0.06	2.01	2.05	0.01	0.01	0.88	0.16	0.00	0.00	0.02
K_2O	0.02	0.00	0.00	0.00	0.00	0.00	0.00	0.00	0.12	0.06	0.00	0.01	0.00	0.00	0.00	0.00	0.01
Sum	100.70	101.46	99.45	99.00	98.27	98.45	98.56	98.43	96.56	96.70	101.72	101.99	98.12	101.03	101.10	100.15	101.38
Si	2.93	2.93	1.98	1.92	1.00	1.99	1.98	1.95	6.47	6.49	3.01	2.99	1.96	1.97	1.99	1.91	0.99
Ti	0.00	0.00	0.00	0.00	0.00	0.00	0.00	0.00	0.03	0.03	0.00	0.00	0.00	0.00	0.00	0.00	0.00
Al	1.91	1.90	0.04	0.11	0.00	0.04	0.05	0.06	2.27	2.25	1.81	1.86	0.07	0.08	0.03	0.18	0.00
Cr	0.14	0.14	0.00	0.01	0.00	0.01	0.02	0.01	0.16	0.08	0.15	0.12	0.02	0.01	0.00	0.01	0.00
Fe^{3+}	0.09	0.11	0.00	0.05	-	0.00	0.01	0.04	0.00	0.06	0.02	0.05	0.04	0.00	0.00	0.00	-
Fe^{2+}	0.43	0.65	0.19	0.17	0.19	0.05	0.04	0.02	0.39	0.35	0.58	0.54	0.03	0.05	0.18	0.20	0.20
Mg	2.07	1.81	1.78	1.74	1.81	0.94	0.93	0.95	3.75	3.83	1.96	2.01	0.90	0.91	0.01	0.00	1.79
Mn	0.02	0.06	0.00	0.01	0.00	0.00	0.00	0.00	0.01	0.01	0.03	0.03	0.00	0.00	0.00	0.00	0.00
Ni	0.00	0.00	0.00	0.00	0.00	0.00	0.00	0.00	0.00	0.00	0.00	0.00	0.00	0.00	1.80	1.69	0.01
Ca	0.40	0.40	0.01	0.01	0.00	0.94	0.93	0.97	1.92	1.91	0.43	0.41	0.91	0.97	0.01	0.01	0.00
Na	0.00	0.01	0.00	0.00	0.00	0.03	0.04	0.00	0.55	0.56	0.00	0.00	0.06	0.01	0.00	0.00	0.00
K	0.00	0.00	0.00	0.00	0.00	0.00	0.00	0.00	0.02	0.01	0.00	0.00	0.00	0.00	0.00	0.00	0.00
Cation Sum	8.00	8.00	4.00	4.00	3.00	4.00	4.00	4.00	15.57	15.57	8.00	8.00	4.00	4.00	4.00	4.00	3.00
X_{Mg}	0.83	0.74	0.91	0.91	0.90	0.95	0.96	0.98	0.91	0.92	0.77	0.79	0.97	0.95	0.91	0.90	0.89
$Al^{(IV)}$	0.07	0.07	0.02	0.08	-	0.01	0.02	0.05	1.53	1.51	0.00	0.01	0.04	0.03	0.01	0.09	-
$Al^{(VI)}$	1.84	1.82	0.02	0.03	-	0.03	0.02	0.01	0.74	0.74	1.81	1.85	0.03	0.04	0.01	0.09	-

(continued)

Table 6

Lithology	Grt-peridotite		Chl-peridotite										Tremolitite			Mafic eclogite	
Sample	MD20		C2A						DB113				DB148			D6	
Mineral	Amp_2	Amp_{Sym}	Cpx_2	Opx_1	Opx_2	Ol	Amp_2	Amp_3	Opx_{Porph}	Amp_{Porph}	Amp_3	Ol	Hbl	Hbl	Tr	Grt	Grt
Comment													core	rim		core	rim
SiO_2	46.33	49.61	53.87	57.74	58.58	41.28	52.56	49.06	57.80	50.86	53.19	41.84	52.66	55.88	56.22	40.76	39.64
TiO_2	0.54	0.54	0.08	0.05	0.01	0.00	0.31	0.48	0.06	0.30	0.24	0.00	0.16	0.11	0.02	0.15	0.07
Al_2O_3	13.46	10.85	0.16	0.89	0.26	0.00	6.35	9.63	0.86	8.64	5.74	0.01	5.59	2.56	2.11	22.62	22.27
Cr_2O_3	1.00	1.37	0.00	0.18	0.00	0.00	0.77	1.08	0.00	0.59	0.80	0.00	0.52	0.33	0.23	0.02	0.14
FeO†	2.82	2.29	8.90	6.70	6.63	10.30	2.95	3.35	7.19	2.93	2.62	10.87	3.58	3.21	2.87	19.74	24.25
MgO	18.25	18.64	11.86	34.71	34.59	48.50	20.87	19.86	34.30	20.39	21.16	48.06	21.42	22.48	22.69	9.50	7.33
MnO	0.06	0.05	1.62	0.13	0.17	0.12	0.09	0.08	0.17	0.03	0.09	0.13	0.04	0.07	0.11	0.47	1.12
NiO	0.04	0.08	0.00	0.00	0.00	0.00	0.00	0.00	0.00	0.00	0.00	0.00	0.11	0.13	0.05	0.00	0.00
CaO	12.73	12.78	25.27	0.15	0.18	0.02	12.56	12.39	0.16	12.63	12.66	0.00	12.65	12.78	12.89	9.39	7.07
Na_2O	2.25	1.12	0.06	0.00	0.01	0.00	1.32	2.00	0.00	1.43	1.02	0.01	0.98	0.44	0.45	0.01	0.05
K_2O	0.18	0.02	0.01	0.00	0.00	0.00	0.24	0.40	0.01	0.21	0.13	0.00	0.27	0.07	0.07	0.00	0.01
Sum	99.79	99.50	101.83	100.55	100.44	100.22	98.02	98.33	100.55	98.01	97.65	100.93	97.98	98.06	97.71	102.66	101.95
Si	6.51	6.93	2.00	1.98	2.01	1.01	7.30	6.85	1.99	7.06	7.38	1.02	7.29	7.67	7.73	3.00	3.00
Ti	0.06	0.06	0.00	0.00	0.00	0.00	0.03	0.05	0.00	0.03	0.03	0.00	0.02	0.01	0.00	0.01	0.00
Al	2.23	1.79	0.01	0.04	0.01	0.00	1.04	1.59	0.03	1.41	0.94	0.00	0.91	0.41	0.34	1.96	1.98
Cr	0.11	0.15	0.00	0.00	0.00	0.00	0.08	0.12	0.00	0.06	0.09	0.00	0.06	0.04	0.03	0.00	0.01
Fe^{3+}	0.00	0.00	0.00	0.00	0.00	-	0.00	0.00	0.00	0.00	0.00	-	0.11	0.06	0.03	0.02	0.02
Fe^{2+}	0.33	0.27	0.28	0.19	0.19	0.21	0.34	0.39	0.21	0.34	0.30	0.22	0.30	0.31	0.30	1.19	1.51
Mg	3.83	3.88	0.66	1.78	1.77	1.77	4.32	4.14	1.76	4.22	4.37	1.75	4.42	4.60	4.65	1.04	0.83
Mn	0.01	0.01	0.05	0.00	0.00	0.00	0.01	0.01	0.01	0.00	0.01	0.00	0.01	0.01	0.01	0.03	0.07
Ni	0.01	0.01	0.00	0.00	0.00	0.00	0.00	0.00	0.00	0.00	0.00	0.00	0.01	0.01	0.01	0.00	0.00
Ca	1.92	1.91	1.00	0.01	0.01	0.00	1.87	1.85	0.01	1.88	1.88	0.00	1.88	1.88	1.90	0.74	0.57
Na	0.61	0.30	0.00	0.00	0.00	0.00	0.36	0.54	0.00	0.38	0.27	0.00	0.26	0.12	0.12	0.00	0.01
K	0.03	0.00	0.00	0.00	0.00	0.00	0.04	0.07	0.00	0.04	0.02	0.00	0.05	0.01	0.01	0.00	0.00
Cation Sum	15.65	15.31	4.00	4.00	4.00	3.00	15.40	15.61	4.00	15.42	15.30	3.00	15.31	15.13	15.13	8.00	8.00
X_{Mg}	0.92	0.94	0.70	0.90	0.90	0.89	0.93	0.91	0.90	0.93	0.94	0.89	0.91	0.93	0.93	0.47	0.35
$Al^{(IV)}$	1.49	1.07	0.00	0.02	0.00	-	0.70	1.15	0.01	0.94	0.62	-	0.71	0.33	0.27	-	-
$Al^{(VI)}$	0.75	0.72	0.01	0.02	0.01	-	0.34	0.44	0.02	0.47	0.32	-	0.20	0.08	0.07	-	-

(continued)

Table 6

Lithology	Mafic eclogite														
Sample	D6											D4			
Mineral	Cpx_2	Amp_2	Amp_2	Amp_2	Amp_3	Amp_3	Pl_2	Pl_2	Kfs	Zo	Aln	Grt	Grt	Amp_2	Amp_2
Comment		inc Grt	post Omp	post Grt	coronitic	symp	post Omp	post Grt				core	rim	inc Grt	post Grt
SiO_2	54.41	45.11	49.13	50.73	45.51	51.15	65.21	62.49	65.72	39.04	35.39	40.82	39.78	44.13	43.72
TiO_2	0.06	0.63	0.99	0.55	1.05	0.42	0.01	0.02	0.00	0.14	0.11	0.09	0.12	1.97	0.68
Al_2O_3	1.92	15.19	8.16	7.14	12.70	6.93	21.82	24.40	18.85	29.65	22.12	22.90	22.13	17.99	14.61
Cr_2O_3	0.02	0.00	0.08	0.00	0.05	0.01	0.00	0.00	0.00	b.d.l.	b.d.l.	0.09	0.01	0.00	0.02
FeO†	5.07	7.62	10.30	10.10	11.44	10.62	0.28	0.40	0.02	4.19	7.83	20.33	24.84	7.59	13.9
MgO	15.26	15.06	15.54	16.32	13.47	15.82	0.40	0.02	0.00	0.44	1.63	9.66	5.54	13.40	11.14
MnO	0.08	0.05	0.09	0.02	0.18	0.09	0.00	0.04	0.00	0.02	0.07	0.45	1.63	0.10	0.24
NiO	0.00	0.00	0.05	0.02	0.00	0.00	0.00	0.02	0.00	n.a.	n.a.	0.00	0.00	0.00	0.00
CaO	22.26	11.39	12.10	12.39	11.60	11.78	3.31	4.52	0.00	22.36	14.19	8.47	8.03	10.58	11.62
Na_2O	0.82	2.49	1.13	0.96	1.96	1.01	8.73	8.54	0.16	n.a.	n.a.	0.03	0.08	1.97	1.72
K_2O	0.00	0.46	0.29	0.22	0.12	0.22	0.24	0.12	16.57	n.a.	n.a.	0.00	0.02	0.56	0.48
Sum	99.90	98.00	97.86	98.45	98.08	98.05	100.00	100.57	101.32	98.59*	100.74*	102.84	102.18	98.29	98.13
Si	1.99	6.47	7.06	7.20	6.59	7.32	2.90	2.76	3.00	4.53	4.59	3.00	3.03	6.33	6.41
Ti	0.00	0.07	0.11	0.06	0.11	0.05	0.00	0.00	0.00	0.01	0.01	0.01	0.01	0.21	0.08
Al	0.08	2.57	1.38	1.19	2.17	1.17	1.14	1.27	1.02	4.06	3.38	1.98	1.98	3.04	2.52
Cr	0.00	0.00	0.01	0.00	0.01	0.00	0.00	0.00	0.00	-	-	0.01	0.00	0.00	0.00
Fe^{3+}	0.00	0.00	0.00	0.00	0.00	0.00	0.00	0.00	0.00	0.41	0.00	0.01	0.00	0.00	0.00
Fe^{2+}	0.16	0.91	1.24	1.20	1.39	1.27	0.01	0.01	0.00	0.00	0.85	1.24	1.58	0.91	1.7
Mg	0.83	3.22	3.33	3.45	2.91	3.37	0.03	0.00	0.00	0.08	0.32	1.06	0.63	0.01	0.03
Mn	0.00	0.01	0.01	0.00	0.02	0.01	0.00	0.00	0.00	0.00	0.01	0.03	0.11	0.00	0.00
Ni	0.00	0.00	0.01	0.00	0.00	0.00	0.00	0.00	0.00	-	-	0.00	0.00	2.87	2.43
Ca	0.87	1.75	1.86	1.88	1.80	1.81	0.16	0.21	0.00	2.78	1.97	0.67	0.65	1.63	1.82
Na	0.06	0.69	0.32	0.26	0.55	0.28	0.75	0.73	0.01	-	-	0.00	0.01	0.55	0.49
K	0.00	0.08	0.05	0.04	0.02	0.04	0.01	0.01	0.97	-	-	0.00	0.00	0.10	0.09
Cation Sum	4.00	15.78	15.37	15.30	15.57	15.32	5.00	5.00	5.00	12.00*	12.00*	8.00	8.00	15.65	15.58
X_{Mg}	0.84	0.78	0.73	0.74	0.68	0.73	-	-	-	0.16	0.27	0.46	0.28	0.76	0.59
$Al^{(IV)}$	0.01	1.53	0.94	0.80	1.41	0.68	-	-	-	-	-	-	-	1.67	1.59
$Al^{(VI)}$	0.08	1.04	0.44	0.40	0.76	0.49	-	-	-	-	-	-	-	1.37	0.93

(continued)

Table 6

Lithology	Mafic eclogite				Kyanite eclogite										
Sample	D4				B5A										
Mineral	Amp_3	Amp_3	Pl_2	Kfs	Grt	Grt	Omp	Cpx_2	Opx_{Sym}	Amp_2	Amp_2	Amp_3	Pl_2	Pl_2	Pl_{Sym}
Comment	coronitic	symp	post Grt		core	rim		post Omp	post Ky	post Omp	post Grt	coronitic	post Omp	post Grt	post Ky
SiO_2	42.85	48.55	54.78	66.49	40.41	39.83	54.30	53.93	53.20	46.89	45.02	45.29	58.13	58.27	53.68
TiO_2	0.15	0.72	0.00	0.00	0.07	0.07	0.16	0.05	0.00	1.77	0.40	0.56	0.01	0.00	0.00
Al_2O_3	15.78	9.08	30.50	18.73	22.68	22.50	10.14	1.77	0.88	10.27	12.98	14.17	28.22	26.72	29.87
Cr_2O_3	0.05	0.05	0.00	0.00	0.00	0.19	0.04	0.01	0.04	0.19	0.11	0.05	0.00	0.02	0.02
FeO†	15.70	15.18	0.23	0.00	19.66	24.25	2.77	4.79	17.86	7.24	8.27	8.33	0.07	0.31	0.07
MgO	9.99	12.97	0.00	0.01	9.69	7.06	10.96	15.01	25.83	16.19	15.52	16.24	0.02	0.00	0.00
MnO	0.20	0.35	0.03	0.00	0.43	1.19	0.04	0.11	0.36	0.11	0.12	0.19	0.02	0.00	0.00
NiO	0.00	0.00	0.00	0.00	0.00	0.00	0.04	0.00	0.00	0.00	0.00	0.00	0.00	0.00	0.00
CaO	11.64	10.51	11.49	0.09	8.99	7.18	17.30	22.79	0.34	11.62	11.57	9.97	7.03	7.73	11.32
Na_2O	1.81	1.19	5.20	0.11	0.04	0.04	4.26	0.75	0.02	2.12	2.34	2.68	6.20	6.52	4.95
K_2O	0.57	0.23	0.04	16.59	0.00	0.00	0.01	0.01	0.00	0.44	0.47	0.50	0.10	0.13	0.09
Sum	98.74	98.83	102.27	102.02	101.97	102.31	100.02	99.22	98.65	96.84	96.80	97.99	99.79	99.70	100.01
Si	6.29	7.04	2.42	3.02	2.99	3.00	1.94	1.99	1.96	6.82	6.54	6.45	2.61	2.62	2.42
Ti	0.02	0.08	0.00	0.00	0.00	0.00	0.00	0.00	0.00	0.19	0.04	0.06	0.00	0.00	0.00
Al	2.73	1.55	1.59	1.00	1.98	2.00	0.43	0.08	0.04	1.76	2.22	2.38	1.50	1.42	1.59
Cr	0.01	0.01	0.00	0.00	0.00	0.01	0.00	0.00	0.00	0.02	0.01	0.01	0.00	0.00	0.00
Fe^{3+}	0.04	0.00	0.01	0.00	0.04	0.00	0.00	0.00	0.04	0.00	0.00	0.49	0.00	0.00	0.00
Fe^{2+}	1.88	1.84	0.00	0.00	1.17	1.53	0.08	0.15	0.52	0.88	1.00	0.51	0.00	0.01	0.00
Mg	0.03	0.04	0.00	0.00	1.07	0.79	0.58	0.83	1.42	3.51	3.36	3.45	0.00	0.00	0.00
Mn	0.00	0.00	0.00	0.00	0.03	0.08	0.00	0.00	0.01	0.01	0.01	0.02	0.00	0.00	0.00
Ni	2.18	2.80	0.00	0.00	0.00	0.00	0.00	0.00	0.00	0.00	0.00	0.00	0.00	0.00	0.00
Ca	1.83	1.63	0.54	0.00	0.71	0.58	0.66	0.90	0.01	1.81	1.80	1.52	0.34	0.37	0.55
Na	0.51	0.33	0.44	0.01	0.01	0.01	0.30	0.05	0.00	0.60	0.66	0.74	0.54	0.57	0.43
K	0.11	0.04	0.00	0.96	0.00	0.00	0.00	0.00	0.00	0.08	0.09	0.09	0.01	0.01	0.01
Cation Sum	15.62	15.38	5.00	5.00	8.00	8.00	4.00	4.00	4.00	15.68	15.75	15.71	5.00	5.00	5.00
X_{Mg}	0.54	0.60	-	-	0.48	0.34	0.88	0.85	0.73	0.77	0.87	-	-	-	-
$Al^{(IV)}$	1.72	0.96	-	-	-	-	0.06	0.01	0.04	1.46	1.55	-	-	-	-
$Al^{(VI)}$	1.01	0.59	-	-	-	-	0.37	0.07	0.00	0.76	0.83	-	-	-	-

(continued)

Table 6

Lithology	Kyanite eclogite														
Sample	D3													E1	
Mineral	Ky	Grt	Grt	Cpx_M	Cpx_2	Amp_2	Amp_2	Amp_3	Pl_2	Pl_2	Pl_2	Pl_{Sym}	Kfs_M	Grt	Grt
Comment		core	rim		post Omp	post Omp	post Grt	coronitic	post Omp	post Grt	post Zo	post Ky		core	rim
SiO_2	37.00	41.15	40.46	54.60	54.54	54.92	50.79	43.27	63.07	50.52	58.76	45.56	67.67	41.05	40.20
TiO_2	0.00	0.00	0.01	0.08	0.05	0.21	0.15	0.61	0.00	0.00	0.00	0.03	0.00	0.02	0.04
Al_2O_3	65.06	23.04	22.74	1.18	1.02	3.71	8.86	15.83	24.31	33.20	27.05	35.75	18.71	23.15	22.77
Cr_2O_3	0.09	0.11	0.06	0.04	0.01	0.15	0.26	0.09	0.00	0.03	0.04	0.04	0.00	0.05	0.05
FeO†	0.32	18.87	21.92	6.21	5.79	8.50	9.13	11.00	0.08	0.39	0.02	0.21	0.02	15.75	20.89
MgO	0.02	10.79	8.89	14.46	14.55	17.05	15.05	12.99	0.02	0.00	0.00	0.00	0.01	12.04	8.80
MnO	0.00	0.43	0.88	0.22	0.13	0.10	0.11	0.13	0.00	0.00	0.01	0.00	0.00	0.43	1.45
NiO	0.00	0.00	0.00	0.00	0.00	0.00	0.00	0.00	0.00	0.00	0.00	0.00	0.00	0.00	0.00
CaO	0.00	7.74	7.23	22.64	23.27	12.87	12.76	11.28	5.17	14.97	8.09	18.33	0.00	8.98	6.99
Na_2O	0.00	0.00	0.00	0.59	0.58	0.38	0.76	2.03	8.47	3.10	6.93	0.94	0.24	0.01	0.00
K_2O	0.00	0.00	0.00	0.01	0.00	0.13	0.13	0.65	0.15	0.05	0.10	0.00	16.15	0.01	0.00
Sum	102.54	102.13	102.19	100.02	99.94	98.02	98.00	97.88	101.27	102.31	101.00	100.86	102.81	101.49	101.19
Si	0.97	3.02	3.01	2.01	2.01	7.77	7.23	6.29	2.77	2.25	2.60	2.08	3.05	3.00	3.02
Ti	0.00	0.00	0.00	0.00	0.00	0.02	0.02	0.07	0.00	0.00	0.00	0.00	0.00	0.00	0.00
Al	2.02	1.99	2.00	0.05	0.04	0.62	1.49	2.71	1.26	1.75	1.41	1.93	0.99	1.99	2.02
Cr	0.00	0.01	0.00	0.00	0.00	0.02	0.03	0.01	0.00	0.00	0.00	0.00	0.00	0.00	0.00
Fe^{3+}	0.01	0.00	0.00	0.00	0.00	0.00	0.00	0.00	0.00	0.01	0.00	0.00	0.00	0.01	0.00
Fe^{2+}	0.00	1.16	1.37	0.19	0.18	1.01	1.09	1.34	0.00	0.00	0.00	0.01	0.00	0.95	1.31
Mg	0.00	1.18	0.99	0.80	0.80	3.60	3.19	2.81	0.00	0.00	0.00	0.00	0.00	1.31	0.99
Mn	0.00	0.03	0.06	0.01	0.00	0.01	0.01	0.02	0.00	0.00	0.00	0.00	0.00	0.03	0.09
Ni	0.00	0.00	0.00	0.00	0.00	0.00	0.00	0.00	0.00	0.00	0.00	0.00	0.00	0.00	0.00
Ca	0.00	0.61	0.58	0.90	0.92	1.95	1.95	1.76	0.24	0.72	0.38	0.90	0.00	0.70	0.56
Na	0.00	0.00	0.00	0.04	0.04	0.10	0.21	0.57	0.72	0.27	0.59	0.08	0.02	0.00	0.00
K	0.00	0.00	0.00	0.00	0.00	0.02	0.02	0.12	0.01	0.00	0.01	0.00	0.93	0.00	0.00
Cation Sum	3.00	8.00	8.00	4.00	4.00	15.13	15.23	15.69	5.00	5.00	5.00	5.00	5.00	8.00	8.00
X_{Mg}	-	0.51	0.42	0.81	0.82	0.78	0.75	0.68	-	-	-	-	-	0.58	0.43
$Al^{(IV)}$	-	-	-	0.00	0.00	0.23	0.77	1.71	-	-	-	-	-	-	-
$Al^{(VI)}$	-	-	-	0.05	0.04	0.39	0.72	1.00	-	-	-	-	-	-	-

(continued)

Table 6

Lithology	Kyanite eclogite										High-Al_2O_3 eclogite				
Sample	E1										D9				
Mineral	Cpx_2	Amp_2	Amp_2	Amp_3	Pl_M	Pl_2	Pl_2	Pl_2	Pl_{Sym}	Kfs_M	Cpx_M	Cpx_2	Amp_2	Amp_3	Amp_3
Comment	post Omp	post Omp	post Grt	coronitic		post Omp	post Grt	post Zo	post Ky			post Omp	post Omp	coronitic	sym
SiO_2	53.39	50.74	52.97	50.84	67.70	56.90	58.88	44.50	43.27	65.06	54.93	54.27	50.62	45.95	54.86
TiO_2	0.04	0.17	0.31	0.19	0.00	0.00	0.00	0.00	0.00	0.00	0.00	0.04	0.28	0.32	0.17
Al_2O_3	1.78	6.84	5.53	8.61	21.10	27.32	27.25	36.20	37.05	18.69	1.60	2.53	7.12	12.76	3.31
Cr_2O_3	0.00	0.12	0.06	0.11	0.06	0.00	0.00	0.00	0.08	0.01	0.00	0.05	0.14	0.04	0.11
FeO†	4.70	7.49	7.16	7.42	0.10	0.16	0.17	0.06	0.11	0.25	3.70	4.01	5.83	7.85	5.30
MgO	15.65	18.22	17.86	17.65	0.02	0.01	0.03	0.00	0.01	0.44	15.47	14.95	17.72	16.17	19.34
MnO	0.12	0.12	0.14	0.09	0.00	0.01	0.02	0.03	0.02	0.00	0.17	0.10	0.09	0.11	0.08
NiO	0.00	0.00	0.00	0.00	0.00	0.00	0.00	0.00	0.00	0.00	0.00	0.00	0.02	0.08	0.00
CaO	23.08	12.01	13.19	11.99	0.74	8.36	8.33	18.43	19.16	0.63	23.31	22.96	14.86	11.99	12.88
Na_2O	0.45	1.03	0.74	1.16	10.34	6.77	7.08	0.94	0.43	0.15	0.82	1.06	0.77	1.87	0.37
K_2O	0.00	0.10	0.08	0.11	0.04	0.05	0.06	0.00	0.00	15.48	0.03	0.01	0.35	0.82	0.16
Sum	99.26	96.84	98.04	98.17	100.10	99.61	101.84	100.18	100.14	100.72	100.03	99.98	97.80	97.96	96.58
Si	1.97	7.22	7.45	7.15	2.98	2.55	2.58	2.04	1.99	2.99	2.00	1.98	7.12	6.57	7.76
Ti	0.00	0.02	0.03	0.02	0.00	0.00	0.00	0.00	0.00	0.00	0.00	0.00	0.03	0.03	0.02
Al	0.08	1.15	0.92	1.43	1.09	1.45	1.41	1.96	2.01	1.01	0.07	0.11	1.18	2.15	0.55
Cr	0.00	0.01	0.01	0.01	0.00	0.00	0.00	0.00	0.00	0.00	0.00	0.00	0.02	0.00	0.01
Fe^{3+}	0.02	0.06	0.00	0.00	0.00	0.01	0.01	0.00	0.00	0.00	0.00	0.01	0.23	0.00	0.00
Fe^{2+}	0.13	0.83	0.84	0.87	0.00	0.00	0.00	0.00	0.00	0.01	0.11	0.12	0.46	0.94	0.63
Mg	0.86	3.86	3.74	3.70	0.00	0.00	0.00	0.00	0.00	0.00	0.84	0.81	3.72	3.45	4.08
Mn	0.00	0.01	0.02	0.01	0.00	0.00	0.00	0.00	0.00	0.00	0.01	0.00	0.01	0.01	0.01
Ni	0.00	0.00	0.00	0.00	0.00	0.00	0.00	0.00	0.00	0.03	0.00	0.00	0.00	0.01	0.00
Ca	0.91	1.83	1.99	1.81	0.04	0.40	0.39	0.91	0.95	0.03	0.91	0.90	2.24	1.84	1.95
Na	0.03	0.28	0.20	0.32	0.88	0.59	0.60	0.08	0.04	0.01	0.06	0.07	0.21	0.52	0.10
K	0.00	0.02	0.01	0.02	0.00	0.00	0.00	0.00	0.00	0.91	0.00	0.00	0.06	0.15	0.03
Cation Sum	4.00	15.30	15.21	15.34	5.00	5.00	5.00	5.00	5.00	5.00	4.00	4.00	15.27	15.67	15.13
X_{Mg}	0.87	0.82	0.82	0.81	-	-	-	-	-	-	0.88	0.87	0.89	0.79	0.87
$Al^{(IV)}$	0.03	0.78	0.55	0.85	-	-	-	-	-	-	0.00	0.02	0.88	1.43	0.24
$Al^{(VI)}$	0.05	0.37	0.37	0.58	-	-	-	-	-	-	0.07	0.09	0.30	0.72	0.31

(continued)

Table 6

Lithology	High-Al_2O_3 eclogite		Amphibole-bearing migmatite						Amphibole+phlogopite boudin				
Sample	D9		D5						DB101			DB102	
Mineral	Pl_M	Kfs_M	Cpx_2	Amp_2	Amp_2	Hbl	Pl_2	Pl_2	Tr	Phl	Kfs	Tr	Phl
Comment			post Omp	post Omp	post Grt		post Omp	post Grt					
SiO_2	63.17	65.11	54.42	49.79	48.94	45.60	58.16	60.47	55.01	40.04	66.50	56.13	39.71
TiO_2	0.00	0.02	0.03	0.63	0.70	0.49	0.03	0.01	0.15	1.69	0.00	0.04	0.81
Al_2O_3	22.42	19.31	1.56	8.73	9.26	14.41	27.43	26.16	3.75	16.77	19.13	2.53	16.43
Cr_2O_3	0.00	0.00	0.34	1.14	1.43	0.27	0.00	0.02	0.03	0.24	0.01	0.11	0.47
FeO†	0.00	0.04	3.64	7.02	7.27	6.93	0.23	0.18	7.67	12.05	0.09	6.21	10.00
MgO	0.00	0.01	15.62	16.43	16.18	15.57	0.04	0.00	17.91	16.48	0.03	19.83	18.35
MnO	0.00	0.00	0.10	0.12	0.07	0.18	0.00	0.00	0.11	0.15	0.00	0.23	0.10
NiO	0.00	0.00	0.04	0.01	0.03	0.03	0.00	0.03	0.00	0.00	0.00	0.00	0.00
CaO	3.77	0.06	24.21	12.81	12.75	12.34	8.86	7.06	12.97	0.01	0.00	12.51	0.06
Na_2O	9.54	0.99	0.42	1.31	1.17	1.89	6.62	7.70	0.37	0.17	0.14	0.32	0.04
K_2O	0.21	15.08	0.01	0.26	0.30	0.50	0.06	0.05	0.17	9.38	16.48	0.09	9.10
Sum	99.11	100.62	100.39	98.25	98.10	98.21	101.43	101.68	98.14	96.98	102.38	98.00	95.07
Si	2.81	2.98	1.98	7.07	6.96	6.48	2.57	2.65	7.74	2.92	3.01	7.83	2.90
Ti	0.00	0.00	0.00	0.07	0.08	0.05	0.00	0.00	0.02	0.09	0.00	0.00	0.04
Al	1.18	1.04	0.07	1.46	1.55	2.41	1.43	1.35	0.62	1.44	1.02	0.42	1.41
Cr	0.00	0.00	0.01	0.13	0.16	0.03	0.00	0.00	0.00	0.01	0.00	0.01	0.03
Fe^{3+}	0.00	0.00	0.00	0.00	0.00	0.00	0.00	0.00	0.00	0.00	0.00	0.00	0.00
Fe^{2+}	0.00	0.00	0.11	0.83	0.86	0.82	0.01	0.00	0.90	0.73	0.00	0.72	0.61
Mg	0.00	0.00	0.85	3.48	3.43	3.30	0.00	0.00	3.75	1.79	0.00	4.12	2.00
Mn	0.00	0.00	0.00	0.01	0.01	0.02	0.00	0.00	0.01	0.01	0.00	0.03	0.01
Ni	0.00	0.00	0.00	0.00	0.00	0.00	0.00	0.00	0.00	0.00	0.00	0.00	0.00
Ca	0.18	0.00	0.95	1.95	1.94	1.88	0.42	0.33	1.95	0.00	0.00	1.87	0.00
Na	0.82	0.09	0.03	0.36	0.32	0.52	0.57	0.65	0.10	0.02	0.01	0.09	0.01
K	0.01	0.88	0.00	0.05	0.05	0.09	0.00	0.00	0.03	0.87	0.95	0.02	0.85
Cation Sum	5.00	5.00	4.00	15.41	15.38	15.61	5.00	5.00	15.13	7.90	5.00	15.10	7.86
X_{Mg}	-	-	0.88	0.81	0.80	0.80	-	-	0.81	0.71	-	0.85	0.77
$Al^{(IV)}$	-	-	0.02	0.93	1.04	1.52	-	-	0.27	1.08	-	0.17	1.10
$Al^{(VI)}$	-	-	0.05	0.53	0.51	0.89	-	-	0.36	0.36	-	0.24	0.31

Garnet is normalised on the basis of 8 cations and 12 oxygens. Clino- and orthopyroxene are normalised on the basis of 4 cations and 6 oxygens. Olivine is normalised on the basis of 3 cations. Amphibole is normalised on the basis of 23 oxygens. Epidotes are normalised on the basis of 12 cations. * REE wt.% and a.p.f.u. are given in Tab.A-1 of appendix. † total iron as FeO. Fe2+ and Fe3+ are calculated from stoichiometry. M=melt Sym=symplectite XMg = (Mg/Mg+Fe2+)

6.3.2 Trace elements

The trace elements compositions of analysed rock-forming minerals are listed in Table 7 and portrayed in Figures from 37 to 39.

6.3.2.1 Peridotites

Garnet from garnet peridotites shows the classic REE pattern with enrichment in HREE (up to 10×PM) and depletion in LREE (dark grey area in Fig. 37a, b). Clinopyroxenes (light grey area in Fig. 37a, b) and pargasites (Amp_1) of sample B3A (black circles and diamonds in Fig. 37a) display REE patterns characterised by relative depletions in HREE (La/Er_N ca. 3), indicating that they grew in chemical equilibrium with garnet. They also show high LREE and MREE concentrations reflecting the enrichment in LREE of the bulk rock (c.f. Fig. 23a). In sample A2C2 Amp_1 is zoned with REE patterns (grey circles and diamond in Fig. 37a, b) enriched in HREE with respect to Amp_1 of sample B3A. This different HREE fractionation is in contrast with the microstructural observation that this $Amph_1$ is in paragenesis with garnet and likely indicates that an equilibration with post-peak minerals already occurred. As shown in Tab. 7, orthopyroxene is generally depleted in all incompatible elements. In terms of other trace elements, both garnet and clinopyroxene display a general depletion in LILE whereas amphibole of B3A is slightly enriched in LILE with K and Pb ca. 10×PM (Fig. 37b). Also concerning the LILE, amphibole of sample A2C2 displays a different patter with higher LILE concentrations (up to 200×PM) with respect to amphibole of sample B3A.

In chlorite peridotites (DB113), porphyroblastic amphibole (Amp_{Porph}) in equilibrium with Opx_{Porph} and Phl_{Porph} (Fig. 16c) has been analysed and its REE pattern is enriched in LREE with respect to HREE (Fig. 37c; Tab. 7). Its LILE concentrations reaches only up to 10×PM with a strong Ba negative anomaly. Opx_{Porph} growing at the expenses of olivine shows only detectable LREE with La/Ce_N = 1.9 (Tab. 7). Chlorite from the retrogressed chlorite foliation (Chl_3) represents the major host of fluid mobile elements displaying high Cs, Rb and K (Cs up to 300×PM), a negative anomaly in Ba and positive U/Th ratios (Fig. 37d).

In tremolitites, the REE patterns of Mg-hornblende porphyroblasts and tremolite neoblasts resemble that of the bulk-rock (c.f. Fig. 23e) showing higher LREE (maximum La = 5×PM) with respect to the HREE (Fig. 37e). Concerning the LILE, both amphibole generations show concentrations up to 10×PM with a strong Ba negative anomaly and a relatively high U/Th ratio (Fig. 37f).

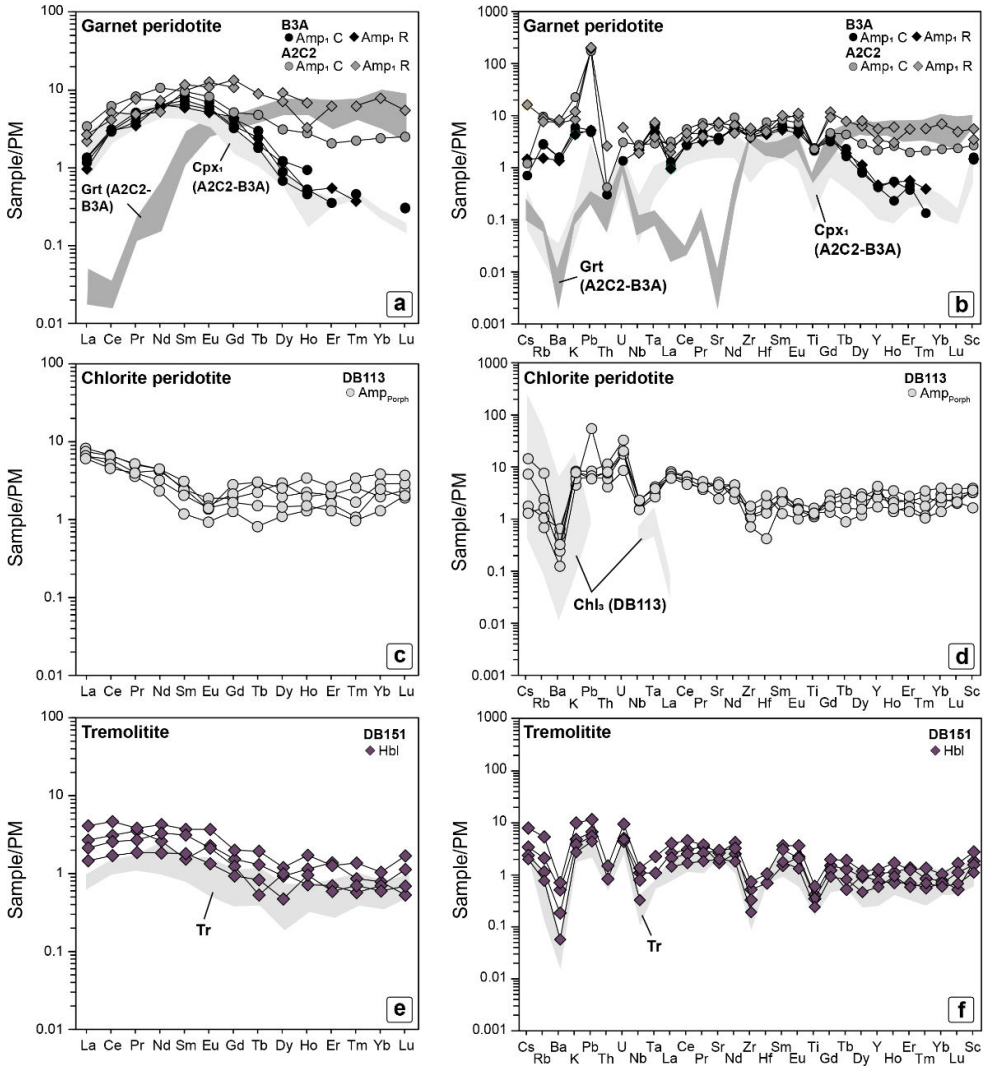

Fig. 37 Primitive mantle normalised REE and other trace elements patterns of (a) and (b) porphyroclastic garnets, clinopyroxenes and amphiboles of garnet peridotites from Mt. Duria; (c) and (d) porphyroblastic metasomatic amphibole of chlorite peridotites from Borgo; (e) and (f) relict hornblendes and tremolites from tremolitite boudins at the contact between chlorite peridotite and amphibole-bearing migmatites at Borgo.

6.3.2.2 Eclogites, amphibole-bearing migmatites and amphibole + phlogopite boudins

Garnets from all eclogite samples have HREE-enriched and LREE-depleted patterns with REE normalised concentrations up to 20×PM. Garnets from mafic eclogites display variable HREE concentrations with Lu varying from 4 to 14×PM but no important differences are observed between analysed cores and rims (Fig. 38a). By contrast, garnets of kyanite-bearing eclogites show a relative enrichment in MREE and a sharp core-to-rim zonation with progressive depletion in HREE (cores: Lu = 8×PM; rims: Lu =2-4×PM; Fig. 38b). In terms of other trace elements garnet is depleted in LILE except for Cs and Pb (Tab. 7). Zoisite from mafic eclogite D6 is almost homogeneous in composition and a slight difference in Yb concentration can be observed between core and rim (Fig. 38c). Zoisite has REE absolute concentrations up to 11000×PM with a slight fractionation between LREE and HREE (e.g. LaN/YbN = 5.3×PM). Allanite growing around zoisite (Fig. 17d) shows the REE concentrations up to 40000×PM, with strong enrichment in LREE (Fig. 38d). Amp_2 of the lower pressure paragenesis was too small to be analysed. Therefore in Figure 38c, d are portrayed only the patterns of coronitic Amp_3 of the investigated eclogites. All amphiboles display a relative enrichment in MREE with respect to HREE, resembling that of garnet from kyanite-eclogite (Fig. 38c). $Amph_3$ represents the major host of fluid mobile elements with spikes in Rb and K and high U/Th ratio, and is likely the responsible for the LILE enrichment of the bulk rock (Fig. 38d).

In amphibole-bearing migmatites, porphyroblastic Mg-hornblende displays fractionated REE patterns characterised by relative depletion in LREE (La/Er_N = 0.18) and a marked Eu positive anomaly (Fig. 39a). It also shows relatively high LILE concentrations (K up to19×PM) and a negative anomaly in Ba (Fig. 39b)

Tremolite of amphibole + phlogopite boudins shows REE patterns with fractionations between LREE and HREE (La/Er_N = 5.68) and slight Eu negative anomalies (Fig. 39c). In terms of other trace elements, tremolitites display relatively high LILE concentrations (Pb up to 20×PM), negative anomalies in Ba and Sr, relative depletions in HFSE and high U/Th ratio (Fig. 39d).

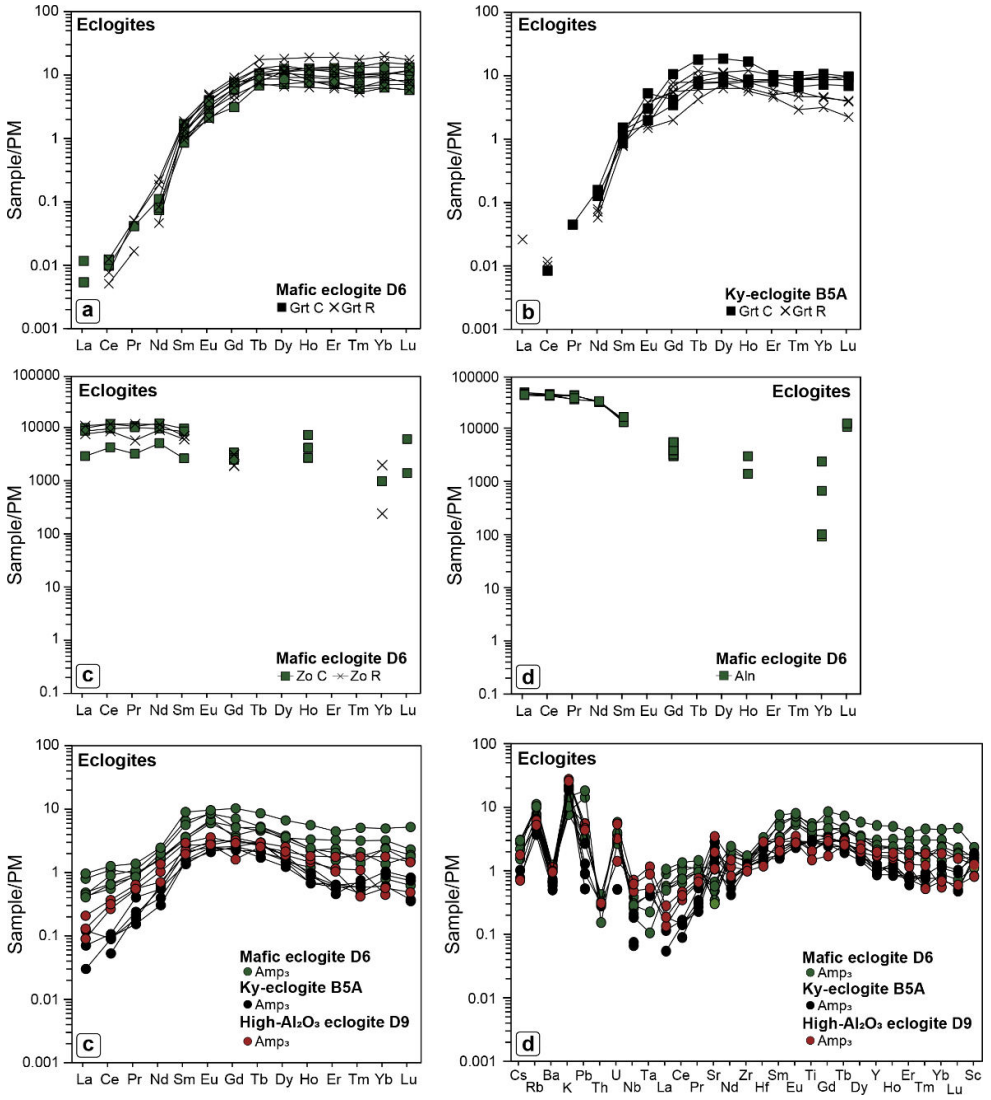

Fig. 38 Primitive mantle normalised REE and other trace elements patterns of garnets (a) and (b), zoisites (c), allanites (d) and amphiboles (e) and (f) from all eclogite types at Borgo.

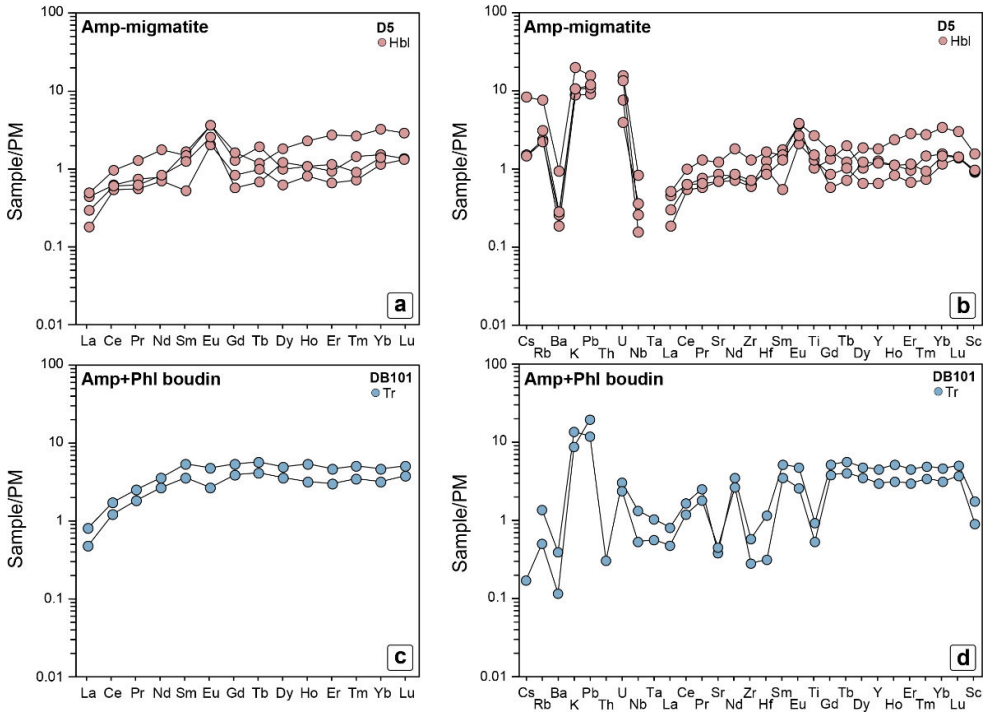

Fig. 39 Primitive mantle normalised REE and other trace elements patterns of amphiboles of amphibole-bearing bearing migmatites (a) and amphibole + phlogopite boudins from Borgo (b)

Table 7

Lithology	Grt-peridotite												
Sample	A2C2							B3A					
Mineral	Grt	Grt	Cpx_1	Cpx_1	Opx_1	Amp_1	Amp_1	Grt	Grt	Cpx_1	Cpx_1	Opx_1	
Comment	core	rim	core	rim		core	rim	core	rim	core	rim		
Cs	b.d.l.	b.d.l.	0.01	b.d.l.	b.d.l.	0.03	b.d.l.	0.00	b.d.l.	b.d.l.	b.d.l.	b.d.l.	
Rb	0.06	b.d.l.	0.07	b.d.l.	b.d.l.	5.75	4.68	b.d.l.	b.d.l.	b.d.l.	b.d.l.	0.06	
Ba	0.08	0.03	0.44	0.05	b.d.l.	51.77	48.33	0.04	0.01	0.21	0.03	b.d.l.	
K	b.d.l.	b.d.l.	20.88	25.66	12.48	5475.04	2865.80	b.d.l.	b.d.l.	39.71	b.d.l.	b.d.l.	
Pb	b.d.l.	0.11	1.99	0.30	0.08	26.27	29.41	b.d.l.	b.d.l.	0.08	0.06	b.d.l.	
Th	0.03	0.01	0.01	0.02	b.d.l.	0.03	0.21	0.01	0.01	0.01	b.d.l.	0.01	
U	b.d.l.	b.d.l.	b.d.l.	b.d.l.	b.d.l.	0.06	b.d.l.	b.d.l.	b.d.l.	b.d.l.	b.d.l.	b.d.l.	
Nb	0.02	0.03	0.04	b.d.l.	0.01	1.80	1.61	0.04	0.04	b.d.l.	b.d.l.	0.03	
Ta	b.d.l.	b.d.l.	b.d.l.	b.d.l.	b.d.l.	0.11	0.15	b.d.l.	b.d.l.	b.d.l.	b.d.l.	0.01	
La	b.d.l.	b.d.l.	1.41	1.99	b.d.l.	2.04	1.61	b.d.l.	0.04	0.48	0.62	b.d.l.	
Ce	0.08	0.07	7.29	8.28	0.03	9.25	6.28	0.03	0.05	3.57	3.57	0.03	
Pr	0.07	0.06	1.27	1.53	b.d.l.	1.83	1.70	0.03	0.04	0.93	0.81	b.d.l.	
Sr	0.11	0.19	132.39	108.85	0.04	121.32	142.60	0.17	0.04	64.02	62.88	0.51	
Nd	0.61	0.70	7.47	8.77	b.d.l.	11.52	8.03	0.61	0.40	4.93	5.26	b.d.l.	
Zr	47.95	50.60	17.12	27.15	0.15	40.53	50.61	62.27	43.68	26.37	24.24	0.37	
Hf	0.45	0.79	1.28	1.24	0.08	2.12	1.52	0.71	0.55	1.21	0.71	b.d.l.	
Sm	0.52	0.81	2.17	2.47	0.06	3.38	4.08	0.80	0.69	2.00	1.79	b.d.l.	
Eu	0.44	0.48	0.57	0.59	b.d.l.	1.11	1.45	0.63	0.46	0.62	0.49	b.d.l.	
Ti	1033.06	1194.72	541.84	676.48	350.63	2745.52	2756.66	810.80	726.14	762.58	673.22	382.30	
Gd	1.93	2.52	1.19	1.45	0.08	2.53	6.27	2.18	1.84	1.24	0.79	b.d.l.	
Tb	0.57	0.55	0.20	0.14	b.d.l.	0.43	0.77	0.57	0.40	0.12	0.14	0.04	
Dy	4.16	4.19	0.48	0.41	b.d.l.	1.94	4.24	4.26	3.27	0.58	0.38	0.09	
Y	22.81	23.70	1.56	1.50	0.04	9.32	14.42	26.18	20.71	1.27	1.01	b.d.l.	
Ho	0.90	1.05	0.03	0.05	b.d.l.	0.39	0.45	0.94	0.78	0.02	0.06	b.d.l.	
Er	2.84	2.29	0.18	b.d.l.	b.d.l.	0.86	2.41	2.78	2.25	0.15	0.14	b.d.l.	
Tm	0.35	0.35	0.04	b.d.l.	b.d.l.	0.14	b.d.l.	0.33	0.40	0.01	0.03	0.03	
Yb	2.73	2.61	b.d.l.	0.11	0.11	0.99	b.d.l.	3.10	2.27	0.12	0.09	0.12	
Lu	0.37	0.36	b.d.l.	b.d.l.	0.02	0.16	b.d.l.	0.36	0.37	b.d.l.	b.d.l.	0.01	
Sc	102.30	91.78	26.09	26.18	2.87	43.14	56.35	134.08	122.52	33.09	34.01	2.58	

(continued)

Table 7

Lithology	Grt-peridotite		Chl-peridotite				Tremolitite			Mafic eclogite			
Sample	B3A		DB113				DB148			D6			
Mineral	Amp_1	Amp_1	Opx_{Porph}	Amp_{Porph}	Amp_{Porph}	Chl_3	Hbl	Hbl	Tr	Grt	Grt	Amp_3	Amp_3
Comment	core	rim		core	rim		core	rim		core	rim	core	rim
Cs	0.02	0.03	0.15	0.17	0.03	6.40	0.17	0.22	b.d.l.	b.d.l.	b.d.l.	0.06	0.05
Rb	1.07	0.91	0.06	1.50	1.03	41.11	3.32	1.84	0.28	0.03	b.d.l.	4.20	5.89
Ba	10.23	9.02	0.19	3.32	1.62	48.96	4.80	4.06	0.37	0.02	b.d.l.	5.36	6.41
K	1052.16	1030.24	8.98	2140.32	2008.18	5068.54	2471.57	1271.24	794.80	b.d.l.	7.91	1812.25	3160.76
Pb	0.93	0.79	b.d.l.	1.35	1.09	0.14	1.79	0.86	0.65	b.d.l.	b.d.l.	0.37	0.46
Th	b.d.l.	b.d.l.	b.d.l.	0.99	0.66	0.07	0.12	0.12	b.d.l.	0.00	0.00	0.03	b.d.l.
U	b.d.l.	b.d.l.	0.01	0.74	0.39	0.02	0.20	0.13	b.d.l.	b.d.l.	b.d.l.	0.07	0.05
Nb	1.81	1.55	0.04	1.57	1.54	0.51	0.91	0.86	0.07	b.d.l.	b.d.l.	0.14	0.13
Ta	0.21	0.25	0.01	0.16	0.16	0.07	0.09	b.d.l.	b.d.l.	b.d.l.	0.00	0.01	b.d.l.
La	0.85	0.61	0.03	5.67	4.58	0.02	2.69	2.00	0.57	b.d.l.	b.d.l.	0.48	0.28
Ce	4.81	4.64	0.02	12.12	9.27	0.02	7.89	5.40	2.30	0.02	b.d.l.	1.67	1.38
Pr	1.17	0.81	b.d.l.	1.38	1.00	b.d.l.	0.98	0.92	0.37	b.d.l.	b.d.l.	0.23	0.25
Sr	71.74	68.75	0.30	96.73	107.80	1.25	53.83	34.30	32.88	0.03	0.06	5.18	17.54
Nd	6.81	7.14	b.d.l.	6.01	3.21	b.d.l.	5.38	4.16	2.79	0.09	0.05	1.81	2.54
Zr	42.80	39.24	0.18	11.61	19.53	b.d.l.	7.96	5.92	1.53	1.26	3.52	12.93	13.55
Hf	1.60	1.21	0.03	0.39	0.84	b.d.l.	0.30	0.44	b.d.l.	0.11	0.10	0.62	0.60
Sm	3.05	2.15	0.06	1.08	0.54	0.15	1.52	1.12	0.41	0.47	0.54	1.16	2.22
Eu	0.94	0.71	b.d.l.	0.32	0.16	0.01	0.58	0.59	0.13	0.55	0.73	0.77	1.08
Ti	2522.41	2736.18	233.17	2039.24	1641.15	850.93	744.38	472.37	268.45	122.47	169.74	3934.54	6349.61
Gd	2.10	2.22	0.03	1.13	0.77	b.d.l.	1.10	0.96	0.26	3.99	4.79	1.79	3.21
Tb	0.27	0.19	b.d.l.	0.24	0.09	b.d.l.	0.19	0.17	0.08	0.82	1.68	0.41	0.44
Dy	0.80	0.76	0.04	2.17	0.83	b.d.l.	0.81	0.85	0.48	5.58	11.88	1.90	2.20
Y	1.98	1.98	0.18	11.61	19.53	b.d.l.	5.63	4.36	2.15	31.81	75.87	9.27	9.66
Ho	0.14	0.08	0.01	0.32	0.22	b.d.l.	0.26	0.18	0.10	1.11	2.75	0.30	0.31
Er	b.d.l.	0.24	0.12	1.04	0.78	0.05	0.56	0.95	0.36	3.35	8.20	0.91	0.79
Tm	0.03	0.03	0.02	0.13	0.08	0.01	0.09	0.05	0.04	0.39	1.16	0.09	0.11
Yb	b.d.l.	b.d.l.	0.15	1.39	1.19	b.d.l.	0.46	0.54	0.36	2.67	8.49	0.94	0.91
Lu	0.02	b.d.l.	0.01	0.21	0.14	0.01	0.12	0.12	0.07	0.37	1.14	0.11	0.09
Sc	27.70	23.72	12.06	55.92	62.12	11.65	46.03	32.89	23.27	68.29	41.23	18.05	22.84

(continued)

Table 7

Lithology	Mafic eclogite		Ky-bearing eclogite				High-Al2O3 eclogite		Amphibole-bearing migmatite		Amp+Phl boudin	
Sample	D6		B5A				D9		D5		DB101	
Mineral	Zo	Aln	Grt	Grt	Amp_3	Amp_3	Amp_3	Amp_3	Hbl	Hbl	Tr	Tr
Comment			core	rim	core	rim	core	rim				
Cs	n.a.	n.a.	b.d.l.	b.d.l.	b.d.l.	0.02	b.d.l.	0.03	0.03	0.17	b.d.l.	0.00
Rb	n.a.	n.a.	b.d.l.	0.12	2.91	3.79	3.56	2.98	1.35	4.41	0.83	0.31
Ba	n.a.	n.a.	0.04	0.15	3.39	3.96	5.38	5.20	1.20	6.01	2.65	0.77
K	n.a.	n.a.	b.d.l.	11.63	4974.62	4695.91	7132.48	6682.31	2055.03	4591.42	3299.20	2160.98
Pb	287	b.d.l.	b.d.l.	0.05	0.16	0.11	0.65	0.62	1.32	2.26	1.83	3.01
Th	67.7	6699	0.02	0.02	0.02	b.d.l.	0.02	0.02	b.d.l.	b.d.l.	0.02	b.d.l.
U	612	301	b.d.l.	b.d.l.	b.d.l.	0.01	0.02	0.11	0.15	0.30	0.06	0.05
Nb	n.a.	n.a.	b.d.l.	b.d.l.	0.10	b.d.l.	0.38	0.32	0.10	0.53	0.89	0.36
Ta	n.a.	n.a.	b.d.l.	b.d.l.	b.d.l.	0.01	0.04	0.03	b.d.l.	b.d.l.	0.04	0.02
La	1759	27882	b.d.l.	b.d.l.	0.02	0.09	0.14	0.09	0.29	0.33	0.53	0.31
Ce	6624	68214	b.d.l.	0.02	0.17	0.17	0.60	0.53	1.04	1.60	2.85	2.01
Pr	775	10253	0.01	b.d.l.	0.07	0.05	0.16	0.14	0.19	0.32	0.64	0.47
Sr	4623	30.4	0.04	0.05	18.17	28.71	63.35	17.87	16.77	23.36	7.66	9.22
Nd	5992	40114	0.18	0.08	0.52	0.81	1.58	0.84	0.99	2.17	4.44	3.36
Zr	n.a.	n.a.	2.09	1.27	9.96	10.94	9.75	8.60	6.40	13.24	6.10	3.01
Hf	n.a.	n.a.	0.12	b.d.l.	0.55	0.33	0.72	0.28	0.35	0.45	0.33	0.09
Sm	1015	5917	0.58	0.47	0.63	1.06	1.07	0.72	0.68	0.60	2.14	1.43
Eu	b.d.l.	b.d.l.	0.45	0.24	0.37	0.41	0.49	0.38	0.55	0.57	0.74	0.41
Ti	839	659	278.50	234.42	3025.05	3123.65	2175.60	1526.07	1198.11	3140.44	1129.09	654.62
Gd	1735	1762	5.66	3.56	1.19	1.67	1.42	0.81	0.70	0.89	2.88	2.09
Tb	b.d.l.	b.d.l.	1.75	1.17	0.21	0.25	0.26	0.23	0.19	0.12	0.56	0.41
Dy	b.d.l.	b.d.l.	12.34	7.21	1.01	1.22	1.54	1.31	0.66	1.22	3.27	2.41
Y	b.d.l.	b.d.l.	57.85	31.60	4.02	4.00	6.46	7.45	5.24	7.41	19.92	13.05
Ho	1014	453	2.46	1.14	0.13	0.14	0.22	0.25	0.16	0.34	0.79	0.48
Er	b.d.l.	b.d.l.	4.38	2.54	0.25	0.28	0.43	0.71	0.41	1.19	2.01	1.32
Tm	b.d.l.	b.d.l.	0.66	0.30	b.d.l.	0.05	0.03	0.11	0.10	0.18	0.34	0.23
Yb	b.d.l.	308	4.61	1.97	0.41	0.46	0.24	0.72	0.67	1.42	2.06	1.40
Lu	380	836	0.64	0.25	0.05	0.06	0.03	0.09	0.09	0.20	0.34	0.26
Sc	n.a.	n.a.	82.36	66.40	26.60	22.21	10.71	16.94	14.37	24.65	29.03	14.65

6.4 Sm-Nd data

Sm-Nd analytical results for 4 whole-rock powders and 6 optically clean mineral concentrates of garnet peridotites (MD20), garnet clinopyroxenites (MD34) and kyanite eclogites (E1 and B5A) from Monte Duria area are presented in Table 8. Sm-Nd isochrons (Fig. 40) were calculated using garnet as the high $^{147}Sm/^{144}Nd$ mineral phase and the whole rock and clinopyroxene (if present) as the low $^{147}Sm/^{144}Nd$ terms. Uncertainties reported for age determinations are two standard deviations (2σ).

6.4.1 Garnet peridotite (sample MD20)

Optically clean garnet and clinopyroxene fractions and a whole rock split from garnet peridotite MD20 were analysed. Garnet shows low Sm and Nd concentrations and $^{147}Sm/^{144}Nd$ and $^{143}Nd/^{144}Nd$ ratios of 0.9443 and 0.513018 respectively (Tab. 8). Clinopyroxene has low Sm and Nd contents and shows a $^{147}Sm/^{144}Nd$ ratio of 0.1548 and a $^{143}Nd/^{144}Nd$ value of 0.512891 (Tab. 8). The whole rock has the lowest Sm and Nd concentrations among all analysed samples and shows a $^{147}Sm/^{144}Nd$ ratio of 0.2201 and a $^{143}Nd/^{144}Nd$ value of 0.512912 (Tab. 8). In the $^{147}Sm/^{144}Nd$ - $^{143}Nd/^{144}Nd$ plot of Figure 40a, the whole rock and the garnet and clinopyroxene fractions do not define a straight line, indicating severe Nd isotope disequilibrium. The individual garnet-clinopyroxene isochron yields an age of 24.6 ± 5.2 Ma with an initial $^{143}Nd/^{144}Nd$ of 0.5128658 ± 0.0000067 and an εNd(t) of 5.35 (Fig. 40a) while the garnet-whole rock isochron gives an age of 22.2 ± 5.7 with an initial $^{143}Nd/^{144}Nd$ = 0.5128804 ± 0.0000098 and an εNd(t) of 5.35 (Fig. 40a). Notably, all these ages are much younger than the ages obtained by the Sm-Nd geochronology of garnet clinopyroxenites and kyanite eclogites reported in the next paragraphs.

6.4.2 Garnet clinopyroxenite (sample MD34)

Inclusions-free garnet and clinopyroxene separates and a whole rock split from garnet clinopyroxenite MD20 were analysed. Garnet displays low Sm and Nd concentrations, a favourable $^{147}Sm/^{144}Nd$ ratio (0.892) and a $^{143}Nd/^{144}Nd$ value of 0.51306 (Tab. 8). Clinopyroxene has high Sm and Nd contents and displays $^{147}Sm/^{144}Nd$ and $^{143}Nd/^{144}Nd$ ratios of 0.1645 and 0.512901 respectively (Tab. 8). The whole rock has the highest Sm and Nd contents among all investigated samples and shows $^{147}Sm/^{144}Nd$ (0.1782) and $^{143}Nd/^{144}Nd$ (0.512904) values comparable to those of clinopyroxene (Tab. 8). Thus the three points regression in Figure 40b almost corresponds to a two-points isochron and

gives an age of 34.4 ± 3.4 (MSWD = 0.086) with an initial $^{143}Nd/^{144}Nd$ of 0.5128640 ± 0.0000054 and an εNd(t) value of 5.18 (Fig. 40b).

6.4.3 Kyanite eclogite (sample B5A)

In kyanite eclogite B5A, omphacite is almost completely replaced by plagioclase + clinopyroxene ± amphibole symplectites, thus only a garnet fraction and the whole rock were analysed. Garnet shows relatively high Sm and Nd concentrations, a favourable $^{147}Sm/^{144}Nd$ ratio (1.374) and a $^{143}Nd/^{144}Nd$ value of 0.51333 (Tab. 8). The whole rock has moderate Sm and Nd contents and shows $^{147}Sm/^{144}Nd$ and $^{143}Nd/^{144}Nd$ ratios of 0.234 and 0.513092 respectively (Tab. 8). The garnet-whole rock regression yields an age of 31.9 ± 2.9 Ma with an initial $^{143}Nd/^{144}Nd$ of 0.513043 and an εNd(t) value of 8.86. (Fig. 40c) The age of 31.9 ± 2.9 is with-in error comparable to the age obtained for the garnet clinopyroxenite MD34 (34.5 ± 3.4 Ma).

6.4.4 Kyanite eclogite (sample E1)

Kyanite eclogite E1 is free of omphacite since it is completely replaced by plagioclase + clinopyroxene ± amphibole symplectitic assemblages, thus only a garnet fraction and the whole rock were analysed. Garnet has Sm and Nd concentrations comparable to those of garnet of sample B5A and displays $^{147}Sm/^{144}Nd$ and $^{143}Nd/^{144}Nd$ ratios of 1.007 and 0.513318 respectively (Tab. 8). The whole rock shows moderate Sm and Nd concentrations, a $^{147}Sm/^{144}Nd$ value of 0.230 and a $^{143}Nd/^{144}Nd$ ratio of 0.513134 (Tab. 8). The two points garnet-whole-rock regression yields an age of 36.2 ± 7.9 Ma with an initial $^{143}Nd/^{144}Nd$ ratio of 0.513079 ± 0.000014 and an εNd(t) value of 9.68 (Fig. 40d). The age of 36.2 ± 7.9 Ma is with-in error comparable to the age obtained for garnet clinopyroxenite MD34 (34.5 ± 3.4 Ma) and kyanite eclogite B5A (31.9 ± 1.9 Ma).

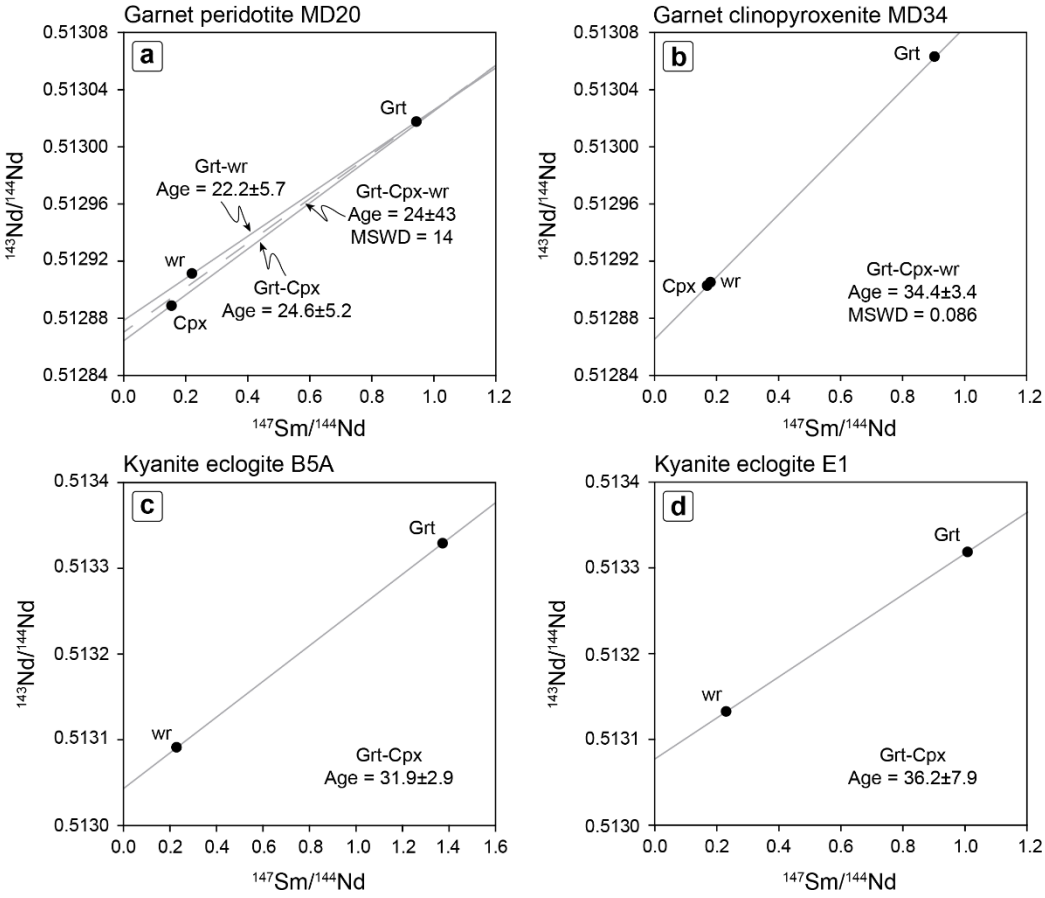

Fig. 40 Sm-Nd isochrons for the studied lithologies. Uncertainties are smaller than the size of the symbols.

Table 8

Lithology	Material	Nd [ppm]	Sm [ppm]	$^{143}Nd/^{144}Nd$	± 2σ
Garnet	wr	0.45	0.17	0.512912	0.000004
peridotite MD20	Cpx	3.32	0.85	0.512891	0.000004
	Grt	0.22	0.35	0.513018	0.000027
	wr-Cpx	-	-	-	-
Garnet	wr	4.06	1.20	0.512904	0.000005
clinopyroxenite MD34	Cpx	7.60	2.07	0.512901	0.000004
	Grt	0.37	0.54	0.513065	0.000016
	wr-Cpx	-	-	-	-
Kyanite	wr	2.21	0.86	0.513092	0.000004
eclogite B5A	Grt	0.11	0.26	0.513330	0.000022
Kyanite	wr	2.09	0.80	0.513134	0.000005
eclogite E1	Grt	0.08	0.13	0.513318	0.000041

(continued)

Table 8

Lithology	Material	$^{147}Sm/^{144}Nd$	1% error	Grt age	± 2σ
Garnet	wr	0.220	0.002	22.2	5.7
peridotite MD20	Cpx	0.155	0.002	24.6	5.2
	Grt	0.944	0.009	-	-
	wr-Cpx	-	-	24	43
Garnet	wr	0.178	0.002	34.5	3.5
clinopyroxenite MD34	Cpx	0.164	0.002	34.3	3.4
	Grt	0.893	0.009	-	-
	wr-Cpx	-	-	34.4	3.4
Kyanite	wr	0.234	0.002	31.9	2.9
eclogite B5A	Grt	1.374	0.014	-	-
Kyanite	wr	0.230	0.002	36.2	7.9
eclogite E1	Grt	1.008	0.010	-	-

(continued)

Table 8

Lithology	Material	Initial $^{143}Nd/^{144}Nd$	± 2σ	εNd(t)
Garnet peridotite MD20	wr	0.512880	0.000010	5.35
	Cpx	0.512866	0.000007	-
	Grt	-	-	-
	wr-Cpx	0.512870	0.000100	-
Garnet clinopyroxenite MD34	wr	0.512863	0.000007	5.18
	Cpx	0.512865	0.000006	-
	Grt	-	-	-
	wr-Cpx	0.512864	0.000005	-
Kyanite eclogite B5A	wr	0.513043	0.000007	8.86
	Grt	-	-	-
Kyanite eclogite E1	wr	0.513079	0.000014	9.68
	Grt	-	-	-

Sm-Nd data of peridotites, pyroxenites and eclogites of Monte Duria area

6.5 Discussion

Numerous field-based, petrological and geochemical studies have described the chemical interaction between mantle peridotites and felsic continental crust via aqueous fluids, melts and supercritical liquids released at HP and UHP conditions, during prograde or retrograde metamorphism along a subduction pathway (e.g. Rampone and Morten, 2001; van Roermund et al., 2002; Scambelluri et al., 2006; Janák et al., 2006; Malaspina et al., 2006, 2017; Tumiati et al., 2007; Scambelluri et al., 2008; Malaspina et al., 2010; Gudelius et al., 2019). Concerning the Alpine belt, the best examples of supra-subduction garnet peridotites metasomatised by crust-derived agents at HP are represented by occurrences in the Eastern and Central Alps at Pohorje (Janák et al., 2006), Ulten Zone (Rampone and Morten, 2001; Scambelluri et al., 2006; Tumiati et al., 2007; Gudelius et al., 2019), Alpe Arami (Nimis and Trommsdorff, 2001; Paquin and Altherr, 2001) and Monte Duria (Fumasoli, 1974; Evans and Trommsdorff, 1978; Hermann et al., 2006). They all show evidence for metasomatism by the presence of metasomatic phases like amphibole, phlogopite, dolomite and REE-minerals (Tumiati et al., 2005; Lavina et al., 2006; Sapienza et al., 2009; Malaspina and Tumiati, 2012) and by the whole rock enrichment of some incompatible elements such as LREE (Rampone and Morten, 2001; Scambelluri et al., 2006; Tumiati et al., 2007; Gudelius et al., 2019). Similarly to Ulten zone amphibole + garnet peridotites, Monte Duria garnet peridotites and the retrogressed chlorite peridotites show abundant porphyroblasts of pargasitic amphibole, dolomite, phlogopite and porphyroblastic orthopyroxene forming at the expenses of a previous olivine, indicating that they experienced metasomatism and interaction with crust-derived agents, enriched in SiO_2, Al_2O_3, K_2O, CO_2 and H_2O. Similar features in metasomatised supra-subduction peridotites have been described by Malaspina et al. (2006) and Endo et al. (2015) who demonstrated that replacive orthopyroxene derives by the reaction of the peridotite with a slab-derived silicate melt at HP/UHP. In addition, experimental results on olivine solubility in COH fluids (Tiraboschi et al., 2018) and mass balance modelling of solid-solution equilibrium between slab-derived aqueous fluids and garnet peridotite (Campione et al., 2017) indicate that also H_2O-rich fluids released from a subducted eclogite are able to crystallise metasomatic orthopyroxene in the mantle. Whether the metasomatic agent responsible for the modal metasomatism of Monte Duria peridotites is a C-bearing silicate melt or an aqueous COH fluid (Hermann et al., 2006) must be searched in the associated crustal rocks and in their reconstructed P-T path.

Further evidence of metasomatism recorded by Monte Duria garnet peridotites is the peculiar fractionation of LREE ($La_N/Nd_N = 2.4$; Fig. 23a) related to the LREE enrichment in Cpx_1 and Amp_1, both crystallised in the garnet stability field, as shown by the relative depletion in HREE (Fig. 37a). The "spoon-shaped" LREE pattern of Monte Duria peridotites strongly resembles that of the Ulten Zone peridotites (pink area in Fig. 23a), which has been interpreted as acquired by the interaction with a hydrous melt (Rampone and Morten, 2001; Scambelluri et al., 2006). Interestingly, Monte Duria peridotites also show a selective enrichment in some LILE (Fig. 23b), which were mainly incorporated by those amphiboles equilibrated in the spinel stability field. Indeed, as shown in Figure 37a and b, the most LILE enriched Amp1 (yellow symbols) shows HREE enriched patterns indicating non-equilibrium with garnet. This observation suggests that the LREE and LILE enrichment occurred at different pressure conditions (garnet and spinel stability fields) and likely by different metasomatic agents, silicate melt and aqueous fluids, respectively.

6.5.1 The HP partial melting of Borgo eclogites

In the Monte Duria area, garnet peridotites occur embedded in low-grade migmatitic gneiss (Mt. Duria) or in direct contact with variably migmatised HP mafic rocks (Borgo). Bulk rock and mineral phase assemblages indicate that these mafic migmatites derive from an eclogite precursor, with a basaltic or gabbroic protolith (Tab. 4 and Fig. 21 and 25a). Peridotites and HP mafic migmatites of Borgo share a common metamorphic evolution, reaching peak conditions at 2.5-3 GPa and 750-800 °C and post-peak static equilibration at 0.8-1.0 GPa and 850 °C (Tumiati et al., 2018). Field occurrence of mafic rocks in Borgo indicates that partial melting started in a deformation regime that is neither related to the shear zone at the contact with migmatitic gneiss (Fig. 6), nor to the static re-equilibration at HT conditions, recorded by sapphirine-baddeleyite-srilankite and sapphirine-corundum assemblages in coronas around garnet (peridotites) and kyanite (eclogites), respectively (Tumiati et al., 2018). Moreover, the strong layered structure of melanosome and leucosome containing zoisite, omphacite and garnet of amphibole-bearing migmatites (Fig. 11a), along with the occurrence of peculiar deformation structures like lobes and cusps, characteristics of syn-melting deformation (Fig. 11b), strongly suggest that Borgo eclogitic rocks underwent partial melting during prograde-to-peak HP metamorphic conditions. Field structures are supported by microstructural evidence in eclogite boudins enclosed in amphibole-bearing migmatites. Both mafic (D6) and high-Al2O3 (D9) eclogites show thin films of clinopyroxene +

K-feldspar around both quartz relicts and symplectite aggregates post-omphacite (Fig. 17a, d, e), together with interstitial pocket aggregates of K-feldspar + plagioclase + quartz + clinopyroxene (Fig. 17f). The reported mineral assemblages closely resemble the one reported in multiphase melt inclusions trapped by peritectic garnets in felsic granulites and migmatites from the indian Kerala Khondalite Belt, namely "nanogranites" (Cesare et al., 2009). Also the microstructural features constraining the direct observation of HP partial melting of eclogites are in agreement with the ones reported in the Central Sulu Orogen by Wang et al. (2014), who recognised melt droplets of leucosome composed of quartz-plagioclase-K-feldspar formed along grain boundaries in the eclogites of the General's Hill. Interestingly, our Cpx_M + Kfs_M rims (Fig. 17e) and Kfs_M + Pl_M + Qz_M + Cpx_M pockets (Fig. 17f) are preferentially oriented parallel to the HP foliation of the high-Al2O3 eclogites, suggesting that the crystallisation of these microstructures was sin-kynematic to the HP deformation regime that led to the formation of the Ky + Omp + Qz + Zo ± Kfs assemblage.

Moreover, evidence of viscous shearing syn-kinematic melt-rock interaction during the infiltration of a felsic melt in mafic rocks has been reported in the Seiland Igneous Province, northern Norway (Degli Alessandrini et al., 2017). In this work a polyphase mixture of clinopyroxene + orthopyroxene + plagioclase + quartz + ilmenite ± K-feldspar wrap porphyroclasts of orthopyroxene, clinopyroxene and plagioclase along the mylonitic foliation and pools of former melt are preserved as K-feldspar surrounding rounded plagioclase and quartz grains.

The partial melting of MORB systems at HP has been experimentally studied by several works (e.g. Lambert and Wyllie, 1972; Schmidt and Poli 1998; Yaxley and Green, 1998; Rapp et al., 1999; Schmidt et al., 2004; Kessel et al., 2005; Klimm et al., (2008); Liu et al., 2009), giving indication on the P-T conditions at which eclogites undergo flush or fluid absent melting in subduction zones. As pointed out by Schmidt and Poli (2014), fluid-saturated melting of K-bearing basaltic rocks can be achieved at 650 °C and 1.5 GPa, reaching 750 °C at 3 GPa and ending at 950 °C and 5.5 GPa by the addition of an aqueous fluid from the external system (Lambert and Wyllie, 1972; Schmidt and Poli, 1998; Schmidt et al., 2004) At higher pressures, fluid absent melting of K-bearing MORB is mainly controlled by the dehydration of phengite, which starts at 850 °C and 2-2.5 GPa and continues up to 900-950 °C at 3 GPa (Hermann and Green, 2001; Liu et al., 2009). In Figure 41 we portrayed the peak conditions recorded by our samples (green is Mt. Duria garnet peridotite, red is Borgo eclogite) compared with the P-T conditions of wet and dry basalt solidi, along with the phengite dehydration melting for a MORB composition. The stable paragenesis

at the peak conditions (750 °C and 3 GPa; Tumiati et al., 2018) is represented by garnet + omphacite + kyanite + zoisite + K-feldspar + quartz/coesite (Tab. 2 and Fig. 17; Fig. 6d of Tumiati et al., 2018). The presence of K-feldspar relict porphyroblasts instead of phengite suggests that the eclogites were almost dry at peak conditions. Indeed, the K-feldspar composition of Borgo eclogites (X_{Or} = 0.98) indicates its stability with a garnet + omphacite + kyanite + quartz at average H_2O content of 0.05 wt.% at P = 3 GPa and T = 750 °C (Tumiati et al., 2018). These observations, therefore, preclude the possibility that our eclogites underwent phengite dehydration melting, because the temperature equilibration conditions recorded by the peak mineral assemblage are too low.

As shown in Figure 41, the P-T peak conditions of Borgo eclogites are slightly beyond the wet basalt solidus, thus suggesting that the partial melting occurred at fluid present conditions. It must be considered that Monte Duria area garnet peridotites record a first hydration stage in a static regime given by chlorite pseudomorphic crystallisation on garnet (Chl_1) predating the development of a penetrative LP-LT chlorite foliation (Chl_3) cutting the garnet layering (Fig. 7d). Moreover, some garnets of Mt. Duria peridotites show Chl_1 pseudomorphs which are surrounded by the sapphirine-baddeleyite-srilankite bearing kelyphitic corona (Fig. 15f, suggesting that a hydration event likely occurred before the LP-(U)HT metamorphic event at 850 °C and 1.2 GPa (Tumiati et al., 2018). Because at the peak conditions of both peridotites and eclogites chlorite is stable in an ultramafic system (Fumagalli and Poli, 2005; grey curve of Fig. 41), the hydration event likely occurred at HP lead to the chloritisation of garnets in the peridotites and flushed the associated eclogites, therefore triggering partial melting.

Melting of mafic crust at high pressures produces the so-called adakites, which are characterised by a peculiar geochemical imprint, with high SiO_2, Al_2O_3, La/Yb and Sr/Y, coupled with low Y and Yb concentrations (Drummond et al. 1996; Schmidt and Poli, 2014). The comparison between the major element compositions of the melt pockets in eclogite of Borgo (D9 in Tab. 4) and the composition of archean adakite and low-Al trondhjemite-tonalite-dacite (TTD) of Drummond et al. (1996) show some similarities between two sample groups. In terms of major element composition, a significant difference is the CaO content, which is higher in our melt pockets, likely due to the occurrence of several clinopyroxene grains, and the Na_2O/K_2O ratio, which is >>1 for archean adakite and ca. 0.5 for our leucosome. This difference due to the fact that omphacite is still stable in the residual eclogite(Tumiati et al., 2018) that retains Na_2O from the melt, with $Na^{cpx/melt}$ partition coefficient close to unity at 3 GPa (Schmidt et al. 2004), supporting that the partial melting of Borgo mafic rocks

occurred at high pressure. In terms of trace elements, instead, Borgo leucosome shows very different La/Yb = 0.1, Sr/Y = 8.16, and Zr/Sm (8.2) vs La/Sm (0.24) ratios with respect to adakites l.s. of Drummond et al. (1996). These differences are mainly due to the strong partitioning of LREE and Sr into the residual allanite and zoisite, respectively, in the restitic portions of eclogites as shown in Figure 8e, f. This partitioning results in a relative enrichment of HREE of our leucosome despite the occurrence of garnet (together with zoisite and allanite) in the residue.

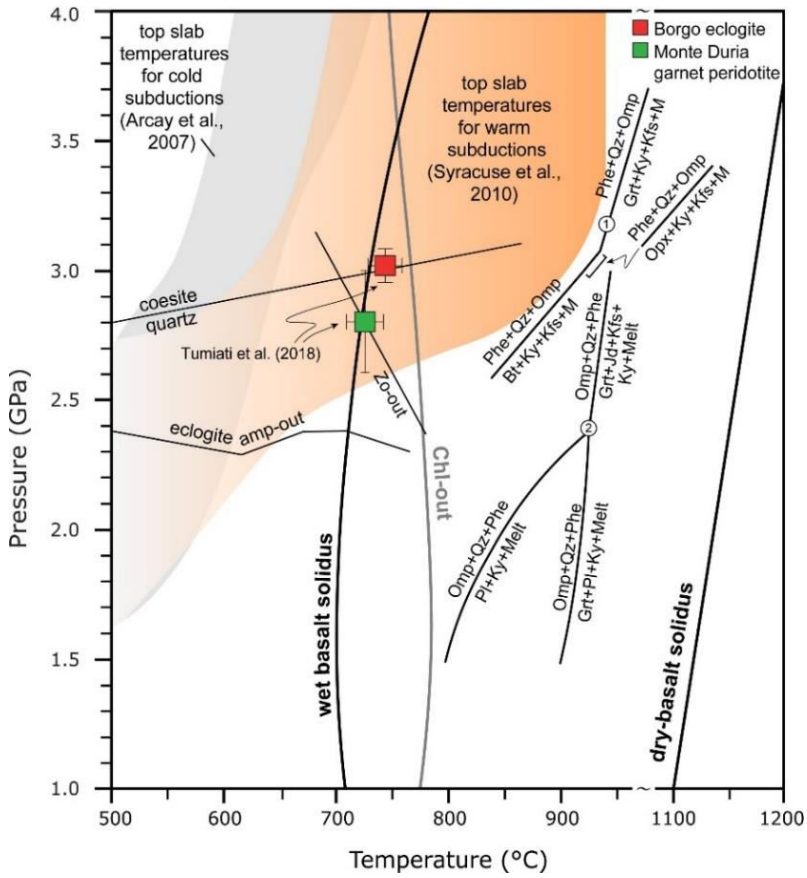

Fig. 41 Peak P-T conditions of mafic (red square) and ultramafic (green square) rocks in the Monte Duria area (from Tumiati et al., 2018). In the P-T space are reported: i) basalt wet solidus (Schmidt and Poli, 1998); ii) zoisite and amphibole-out curves (Schmidt and Poli, 1998); iii) phengite dehydration melting curves in basalt ((1) Hermann and Green, 2001; (2) Liu et al., 2009); iv) basalt dry solidus (Lambert and Wyllie, 1972); v) chlorite-out curve in the peridotite system (Fumagalli and Poli, 2005); vi) top slab geotherms of warm subduction zones (orange field; Syracuse et al., 2010) and of cold subduction zones (grey field, Arcay et al., 2007).

6.5.2 Melt/rock interaction and formation of garnet websterites

The contact between the chlorite peridotite body of Borgo and the HP mafic migmatites is marked by the occurrence of a tremolitite layer (Fig. 6). Such rocks also occur as variably stretched layers within the peridotite body (Fig. 8, 9, 10) showing sharp contacts with the host peridotite and a marked boudinage parallel to the garnet layering of the peridotite. The now retrogressed garnet-bearing foliation of the peridotite, in fact, wraps the boudins and is deflected into the necks (Fig. 10), indicating that the tremolitite boudinage occurred during a deformation event when Borgo peridotites were in the garnet stability field. These layers display relict Mg-hornblende extensively overgrown by tremolite and contain Phl_3 + Chl + Tc + Tr pseudomorphs after garnet (Fig. 16e, f). As shown in Fig. 16e, the crystallisation of tremolite and chlorite occurred in a static regime together with the pseudomorphic replacement of garnets (Fig. 16f). This indicate that the Tr + Chl ± Tc ± Phl_3 mineral assemblage of the tremolitite layers postdates the boudinage deformation event, suggesting that they derive from a precursor that during the formation of the peridotite garnet-foliation was more rigid than the host peridotite. Two hypotheses may explain these structural and microstructural observations. The first one is that the tremolitites of Borgo derive from a Mg-hornblende-bearing precursor as indicated by the presence of relict Mg-hornblende porphyroblasts (Fig. 16e). The alternative hypothesis is that the tremolitites derive from a garnet websterite with a relatively high clinopyroxene modal content. In both cases, these hybrid layers, characterised by high Mg# (>90, Fig. 21a) and high CaO (12.38 wt%, Fig. 21b) formed in the garnet stability field, and subsequently retrogressed in tremolitites during the LP-LT re-equilibration at fluid-present conditions.

The peculiar hybrid composition of the tremolitite layers strongly suggests that they formed after the reaction between the eclogite leucosome and the garnet peridotite at HP (Fig. 21). To test this hypothesis, we modelled the mineral assemblage that would be thermodynamically stable when the pristine garnet peridotite (composition of A2C2, Tab. 4) chemically mixes with a felsic adakite-like melt (HP melt pockets in D9 eclogite, Tab. 4). The result is shown in Figure 42a, where the weight fraction (X) of different degrees of chemical mixing between the garnet peridotite (X = 0) and the eclogite leucosome (X = 1) is plotted versus the activity of water (log $a H_2O$) at fixed P-T conditions corresponding to the peak recorded by both peridotite and eclogite. We also assume that most of infiltrating melt is consumed in the reactions. This assumption is supported by field observations that show no evidence of preserved eclogite-derived melt within the peridotite bodies.

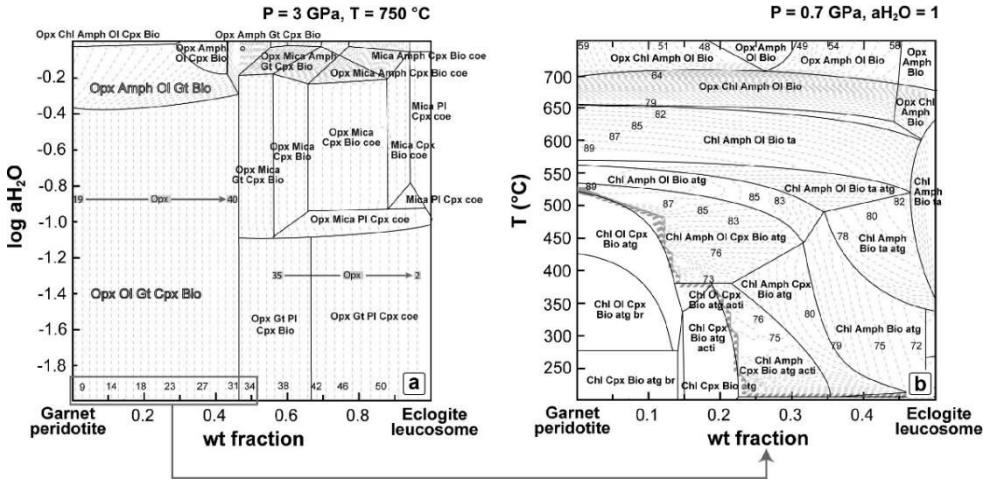

Fig. 42 (a) log aH2O–X diagram calculated at fixed P = 3 GPa and T = 750°C for garnet websterite forming after the melt-peridotite reaction. X = 0 corresponds to garnet peridotite (A2C2, Tab. 4), while X = 1 corresponds to the bulk of adakite-like eclogite leucosome composition (DB104, Tab. 4). Dashed lines are the isomodes of clinopyroxene (vol%) increasing from peridotite to adakite composition, whereas orthopyroxene increases from 18 to 53 vol% in the range 0<X<0.4 and decreases from 53 to 2 vol.% in the range 0.45<X<0.9. (b) P-T isochemical section at H_2O saturated condition of the websterite forming at X=0.39 after the reaction between peridotite and eclogite leucosome (composition in wt%: Na_2O=1.23, MgO =25.95, Al_2O3=8.24, SiO_2=52.85, K_2O=0.98, CaO=3.16, FeO=7.22). Thin grey lines are the isopleths of the tremolite molar content in the amphibole solid solution (mol.%).

At X = 0 (no melt infiltration), and aH_2O = 0.02 the garnet peridotite is represented by the olivine + orthopyroxene + clinopyroxene + garnet + phlogopite mineral assemblage. At higher water activities (aH_2O > 0.4) pargasitic amphibole is stable, while at the maximum water activity (aH_2O > 0.9) chlorite is stable together with pargasite and phlogopite. This scenario is supported by the petrographic and microstructural evidence that Chl_1 forms at HP and at water saturated conditions after the prograde-to-peak Amp_1 formation (Tab. 2). Additional clino- and orthopyroxene are expected to form when the peridotite composition is mixed with increasing weight fraction of leucosome, reaching the maximum modal proportion at X = 0.45 (31 Cpx vol% and 40 Opx vol%). In addition, for X = 0.45 and aH_2O > 0.4 chlorite and olivine are not stable. The presence of high modal amounts of porphyroblastic orthopyroxene, amphibole and phlogopite growing at the expenses of relict olivine and orthopyroxene in Borgo peridotite (Fig. 16c) close to the contact with inner tremolitite layers indicates mixing of more than 35 wt% of leucosome with the garnet peridotite (Fig. 42a). Therefore, from a structural and thermodynamic point of view, the

tremolitite layers likely derive from a previous garnet websterite or garnet amphibole-phlogopite-bearing websterite, depending on the water activity of the melt infiltrating the garnet peridotite. It is worth noting that the trace element composition of relict hornblende of the tremolitite DB148 and the metasomatic porphyroblastic amphibole of DB113 peridotite are identical, both in terms of REE (Fig. 37c, e) and LILE (Fig. 37d, f).

A metasomatic origin for clinopyroxenites/websterites with a similar major element compositions has been also proposed for group D-Ronda pyroxenites of the Betic Cordillera, Southern Spain (Garrido and Bodinier, 1999), for the supra-subduction San Jorge and Santa Isabel pyroxenites of Solomon Islands, West Pacific (Berly et al., 2006) and for peridotite-hosted garnet clinopyroxenites from the Granulitgebirge in the Bohemian Massif, central Europe (Borghini et al., 2018). These pyroxenites are characterised by high Mg#, CaO > 10 wt% and Al_2O_3 ca. 2 wt% similarly to our tremolitite (Tab. 4). It is worth noting that Borgo peridotite shows several dolomite crystals in equilibrium with amphibole and chlorite (Fig. 16d), indicating that the melt interacting with the peridotite carried additional CaO and CO_2. The water-assisted retrogression of the hybrid garnet ±amphibole-bearing websterite has been modelled in Figure 42b, where the T-X section of the peridotite-leucosome mixing in the representative range of $0<X<0$ has been calculated at H_2O saturated condition at P = 0.7 GPa, interpreted as the beginning of retrogression after the HT event. Even considering the uncertainties of some solid solution models (e.g. amphibole, see Tumiati et al., 2013), this pseudosection indicates that tremolitic amphibole (80 to 90 mol.% of tremolite) forms when metasomatic websterites equilibrate at LP-LT conditions.

As summarised in Table 2 and supported by structural, microstructural, chemical and thermodynamic evidences, a HP hydration event formed static chlorite on garnets of the Monte Duria peridotites (Fig. 5b) and flushed the associated eclogites. At 3 GPa and 750 °C water saturated eclogites underwent partial melting (Fig. 11a, b), producing Ca-rich leucosomes (Fig. 17a, d, e, f), which reacted with the associated garnet peridotite forming garnet-amphibole-phlogopite websterites (Fig. 8, 9, 10, 16c) and dolomite in the chlorite peridotite (Fig. 16d). The melt-rock interaction occurred at high deformation regimes, yielding to the formation of garnet layering in the peridotite and the consequent boudinage of the websterite, particularly in the layers within the garnet peridotite (Fig. 6 and 10b-1). The garnet peridotite and associated (partially melted) eclogites subsequently underwent decompression in the spinel stability field (Fig. 15b) forming symplectites after garnet and omphacite (Fig. 18d; Tumiati et al., 2018). Water-absent LP-HT re-equilibration at 1 GPa and 850 °C crystallised sapphirine-baddeleyite-srilankite coronas around garnet in the peridotites and

sapphirine-corundum coronas around kyanite in eclogites (Tumiati et al., 2018). Finally, a LP-LT water-present deformation event formed a chlorite foliation cutting the garnet layering in the peridotites (Fig. 7d), yielded to the hydration of the amphibole-phlogopite bearing websterites with the crystallisation of tremolite and Phl_3 + Chl + Tc + Tr pseudomorphs after garnet (Fig. 16f) and the formation of amphibole (Amp_3) coronas around symplectites after omphacite in the eclogites (Fig. 18a, b).

6.5.3 Timing of the HP metamorphism

Available geochronological data for Monte Duria ultramafic rocks are scarce. To date, U-Pb SHRIMP data on zircons were reported only by Hermann et al. (2006) who obtained ages at 34.2± 0.2 and 32.9±0.3 Ma dating zircons in garnet peridotites from Monte Duria. These authors interpreted the age at 34.2± 0.2 Ma to be related to decompression of garnet peridotites at P < 2.0 GPa whereas the age at 32.9±0.3 Ma should be related to an influx of aqueous fluids at low-pressure conditions.

Sm-Nd dating of garnet pyroxenite pods (Fig. 5c) in garnet peridotites from Monte Duria yielded an age of 34.4±3.4 Ma (Fig. 40b) which is within error comparable to the Sm-Nd garnet-whole rock ages of 31.9±1.9 and 36.2±7.9 Ma obtained for eclogites occurring at Borgo outcrop (Fig. 40c, d). These ages are younger than the Sm-Nd ages of 40 Ma reported by Becker et al., (1993) for the garnet peridotites of Alpe Arami and Cima di Gagnone but compare well with those reported by Hermann et al., (2006) for the initial stages of decompression of garnet peridotites in the Monte Duria area, indicating that the HP metamorphism in the Monte Duria area still needs to be constrained.

Chapter 7

Deformation processes and rheology of peridotites and pyroxenites

In this chapter detailed analyses of microstructures and crystallographic preferred orientations (CPOs) of garnet peridotites and garnet pyroxenites from Monte Duria and Ulten Zone are described. The obtained results are compared with published data on slip systems active in olivine, pyroxenes, and garnet in a range of pressure and temperature conditions broadly similar to the ones experienced by rocks from the Ulten and Duria areas. These comparisons show how EBSD data on Duria and Ulten mantle peridotites and pyroxenites provide invaluable insights on rheological behaviour and deformations processes of the mantle wedge close to the slab-mantle interface.

7.1 EBSD results

Representative samples among garnet peridotites (DB173; Monte Duria), mylonitic garnet + amphibole peridotites (UT25; Ulten Zone) and garnet clinopyroxenites (UT23; Ulten Zone) have been selected for electron backscattered diffraction (EBSD) analyses. EBSD orientation data were processed with Channel 5 analysis suite from HKL Technology, Oxford Instruments and MTEX open source software toolbox (Hielscher & Schaeben, 2008; Bachmann et al., 2010). Noise reduction on the raw EBSD data was performed following the procedure tested by Prior et al. (2002) and Bestmann and Prior (2003). EBSD maps in Figures from 21 to 37 are inverse pole figure maps with respect to the X sample direction. Critical misorientation for the distinction between low- and high-angle boundaries is 10°. Pole figures are plotted as equal area, upper hemisphere projections referenced with the pole to the foliation (Z direction) pointing upwards and the lineation (X direction) horizontal. Crystallographic orientation data in pole figures are presented as one point per grain (OPPG; unless differently specified in figure captions)

orientations. OPPG orientations are calculated as the average orientation of all the pixels in the grain. Misorientation axis distributions in sample coordinates (SCS) are plotted as equal area, upper hemisphere projections. The inverse pole figures plots for misorientation axis distribution in crystal coordinates (CCS) are upper hemisphere projections. The misorientation angle distribution is calculated for neighbouring pixels (correlated misorientations) and unrelated pixels (uncorrelated misorientations). Both correlated and uncorrelated distributions are plotted against the theoretical distribution for random-pairs orientations (Wheeler et al., 2001). For samples DB173 and UT25 we present only the crystallographic orientation data of olivine (paragraphs 7.1.1 and 7.1.2).

7.1.1 Garnet peridotites from Monte Duria area

The analysed peridotite sample show porphyroblastic texture with coarse (up to 3 mm) olivine and orthopyroxene surrounded by fine-grained (< 400 μm) recrystallised olivine, orthopyroxene, minor clinopyroxene, amphibole and Cr-spinel (Fig. 15 b; chapter 4). Olivine porphyroblasts do not display an obvious crystallographic preferred orientation (CPO), even though there is the tendency of the [100] and [010] axes to be aligned subparallel to the lineation and the (100) and (010) planes to be oriented subparallel to the foliation (Fig. 43b). Few olivine grains show 50-μm spaced deformation bands (Fig. 43a and Fig. 15c) typically separated by low-angle boundaries (LAB). Misorientation profiles across deformation bands highlight a rotation as large as 9° of the [100] and [010] axes around the [001] axis (profile AA' in Fig. 43b and d). The low- (2° - 10°) and high-angle (10° - 120°) misorientation axes distribution in both sample coordinates and crystal coordinates do not display any clear maximum (Fig. 43c). The misorientation angle distribution of both correlated and uncorrelated pairs shows an excess in misorientation angles lower than 10° (Fig. 43e).

The recrystallised olivine grains exhibit a random CPO (Fig. 44b). In addition, the grains in proximity of the porphyroblasts lack of an evident CPO (subsets 1 and 2 in Fig. 44b). The olivine grains in the matrix are mostly internally strain-free and do not contain evident substructures. The low- and high-angle misorientation axes in sample coordinates and crystal coordinates are almost uniformly distributed (Fig. 44c). The misorientation angle distribution of correlated and uncorrelated pairs follow the theoretical random curve (Fig. 44d), pointing again to an absence of any significant CPO.

Fig. 43 EBSD map and crystallographic orientation data of porphyroblastic olivine in garnet peridotite of Monte Duria (DB173). EBSD data are rotated to make foliation parallel to the X plane. (a) EBSD-derived inverse pole figure map with respect to X sample direction. Grain boundaries are coloured in black. Subgrain boundaries are coloured in white. (b) Upper row: pole figures of olivine (OPPG). Lower row: pole figures of olivine crystallographic directions along profile AA' . (c) Misorientation axis distributions for olivine in sample (upper row) and crystal (lower row) coordinate system. (d) Cumulative misorientations relative to the first analysed point along the profile AA' in olivine. (e) Misorientation angle distribution for olivine. SCS: sample coordinates. CCS: crystal coordinates, here and in following figures.

Porphyroclastic olivine

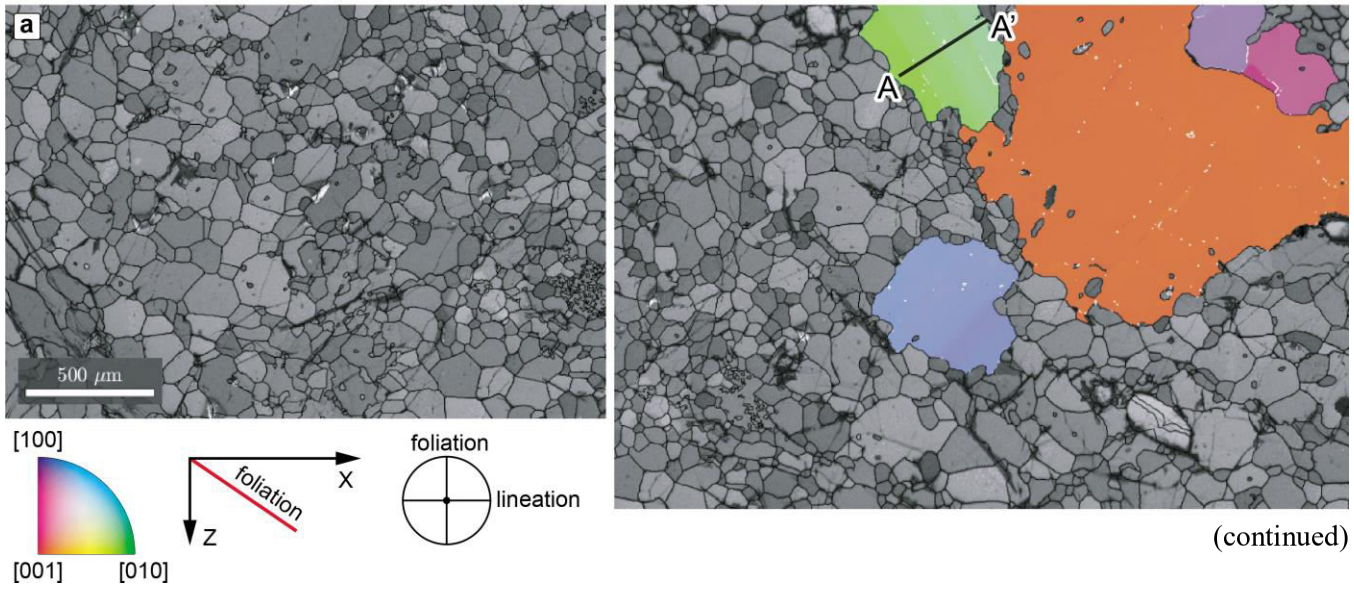

(continued)

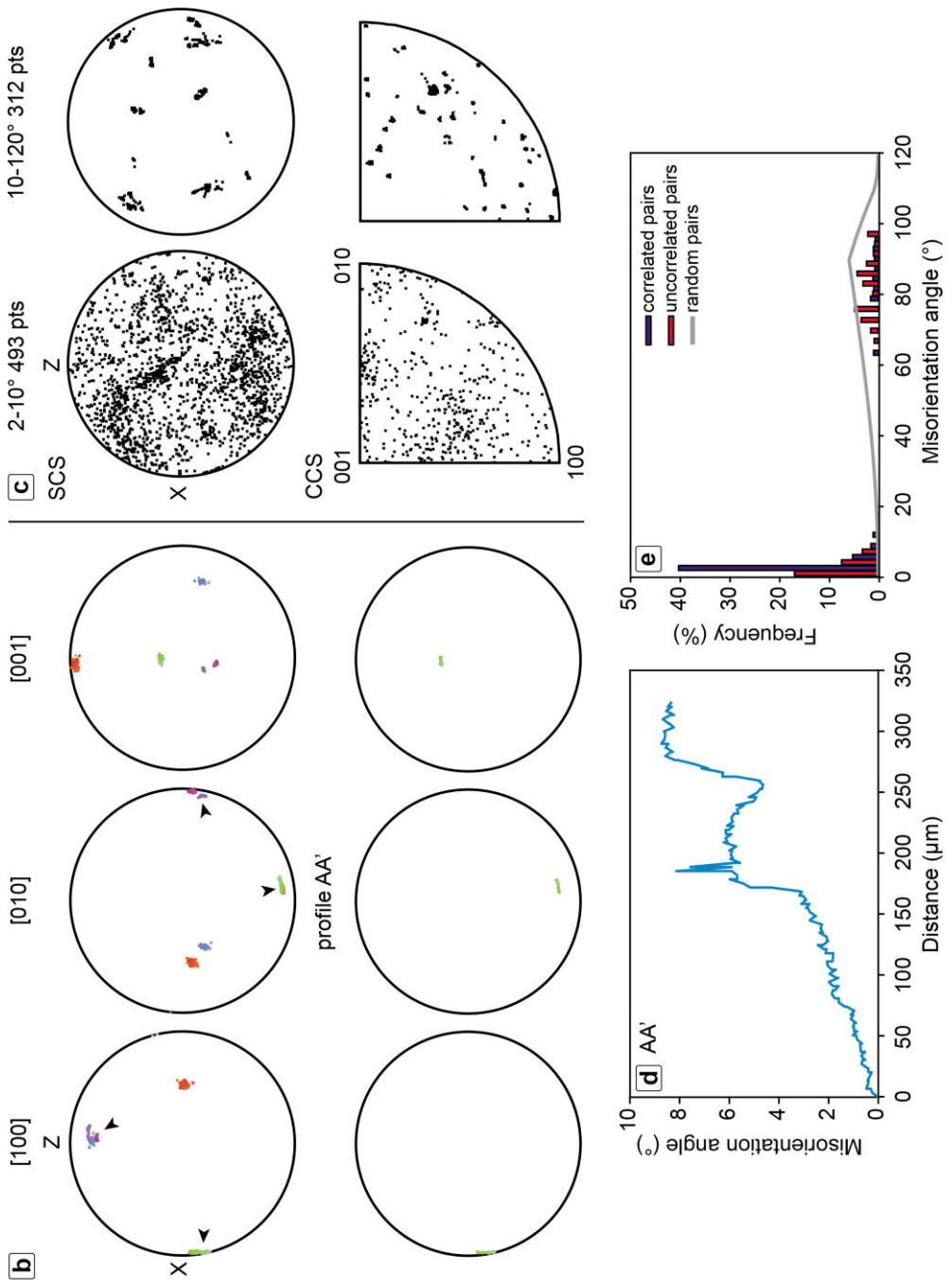
b
[100]
[010]
[001]
Z
X
profile AA'
c
2-10° 493 pts
10-120° 312 pts
SCS
Z
X
CCS
001
010
100
d
AA'
Misorientation angle (°)
Distance (µm)
e
correlated pairs
uncorrelated pairs
random pairs
Frequency (%)
Misorientation angle (°)

Fig. 44 EBSD map and crystallographic orientation data of neoblastic olivine in garnet peridotite of Monte Duria (DB173). EBSD data are rotated to make foliation parallel to the X plane. (a) EBSD-derived inverse pole figure map with respect to X sample direction. Grain boundaries are coloured in black. Subgrain boundaries are coloured in white. (b) Upper row: pole figures of olivine (OPPG). Central row: pole figures of olivine crystallographic directions along profile AA' . Lower row: pole figures of olivine crystallographic directions along profile BB' . (c) Misorientation axis distributions for olivine in SCS (upper row) and CCS (lower row). (d) Cumulative misorientations relative to the first analysed point along the profile AA' in olivine. (e) Misorientation angle distribution for olivine.

Neoblastic olivine

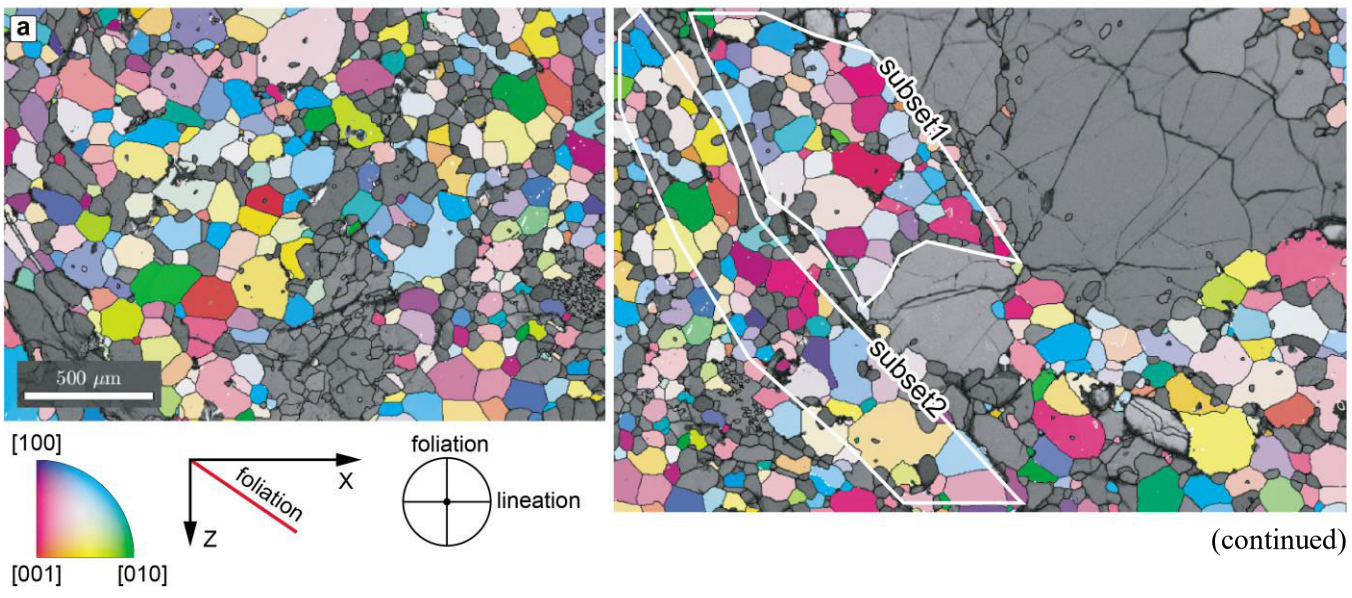

(continued)

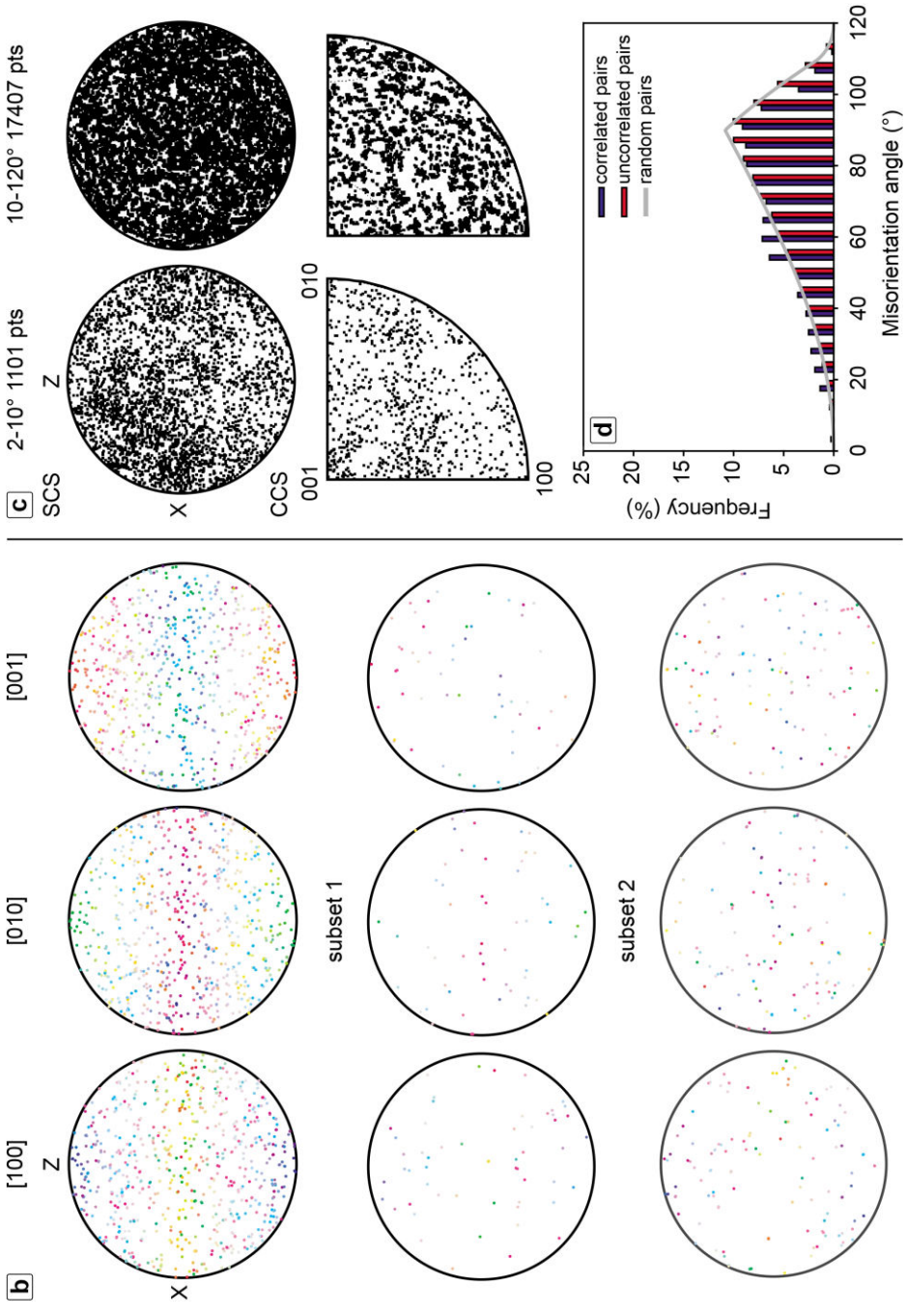
b
[100]
[010]
[001]
Z
X
subset 1
subset 2
c
2-10° 1101 pts
10-120° 17407 pts
SCS
CCS
001
010
100
d
correlated pairs
uncorrelated pairs
random pairs
Frequency (%)
Misorientation angle (°)

7.1.2 Mylonitic garnet + amphibole peridotites from Ulten Zone

Mylonitic garnet + amphibole peridotites display garnet, olivine and amphibole porphyroblasts (up to 6 mm) set in a mylonitic fine-grained (< 500 μm) matrix consisting of recrystallized olivine, orthopyroxene, amphibole, garnet, Cr-rich spinel, and rare clinopyroxene (Fig. 19d; chapter 4). Although olivine shows a strong shape preferred orientation (SPO) (Fig. 45a), it does not display any clear CPO (Fig. 45b). Olivine grains commonly have internal misorientations less than 1° and are strongly misoriented with respect to each other (up to 90°; profile AA' in Fig. 45d). The density of low-angle boundaries is very low, indicating the scarce development of substructures. Misorientation profiles across low-angle boundaries highlight that misorientations are sharp and that subgrains are slightly rotated with respect to each other, dominantly around the [010] and [001] axes (profile BB' and CC' in Fig. 45b). The low- (2° - 10°) and high-angle (10° - 120°) misorientation axes distribution in sample coordinates do not display any clear maximum (Fig. 45c). The low-angle misorientation axes in crystal coordinates show a weak maximum close to the [001] axis, whereas misorientation axes related to high-angle misorientations are almost uniformly distributed (Fig. 45c). The misorientation angle distribution of correlated and uncorrelated pairs follow the theoretical random curve (Fig. 45g).

Fig. 45 EBSD map and crystallographic orientation data of neoblastic olivine in mylonitic garnet + amphibole peridotite of Ulten Zone (UT25). (a) EBSD-derived inverse pole figure map with respect to X sample direction. Grain boundaries are coloured in black. Subgrain boundaries are coloured in white. (b) Upper row: pole figures of olivine (OPPG). Central row: pole figures of olivine crystallographic directions along profile BB' ' . Lower row: pole figures of olivine crystallographic directions along profile CC' . (c) Misorientation axis distributions for olivine in SCS (upper row) and CCS (lower row). (d) Cumulative misorientations relative to the first analysed point along the profile AA' in olivine. (e) Cumulative misorientations relative to the first analysed point along the profile BB' in olivine (f) Cumulative misorientations relative to the first analysed point along the profile CC' in olivine. (g) Misorientation angle distribution for olivine.

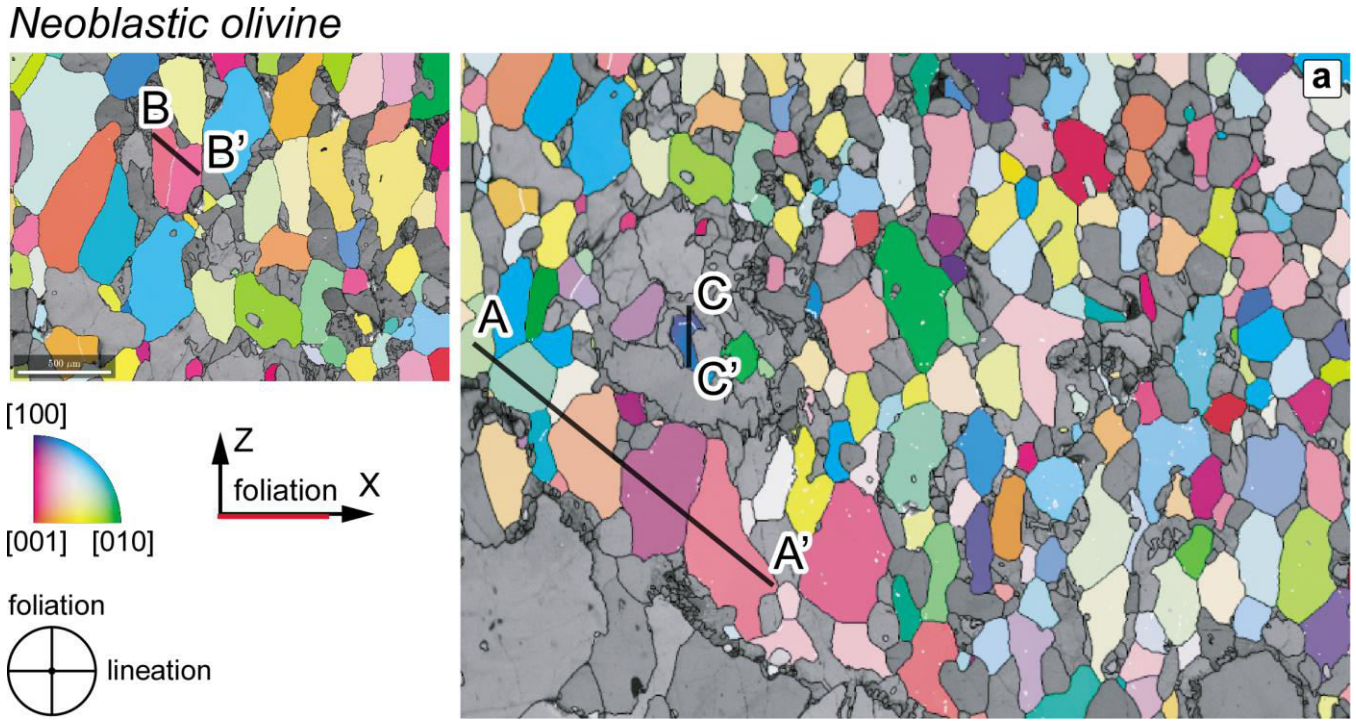

(continued)

b
[100]
[010]
[001]
Z
X
profile BB'
profile CC'
c
2-10° 1615 pts
10-120° 10169 pts
SCS
Z
X
CCS
001
010
100

(continued)

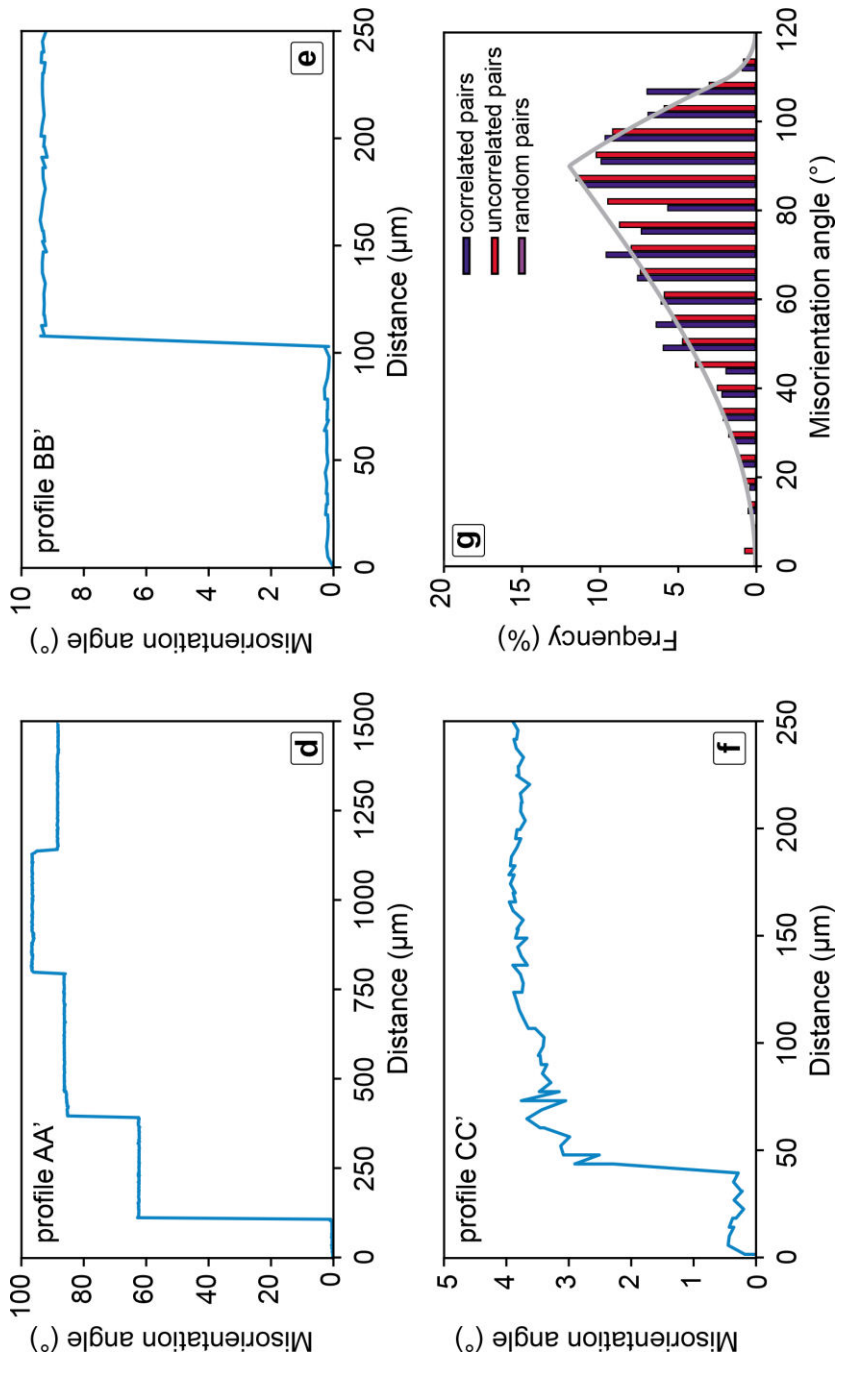
d
profile AA'
Misorientation angle (°)
Distance (µm)
e
profile BB'
Misorientation angle (°)
Distance (µm)
f
profile CC'
Misorientation angle (°)
Distance (µm)
g
correlated pairs
uncorrelated pairs
random pairs
Frequency (%)
Misorientation angle (°)

7.1.3 Garnet clinopyroxenites from Ulten Zone

Garnet clinopyroxenites (UT23) display a porphyroblastic microstructure with coarse (up to 5 mm) clinopyroxene, orthopyroxene (up to 3 mm) and amphibole (up to 3 mm) embedded in a finer-grained recrystallised matrix (< 500 μm) consisting of clinopyroxene, orthopyroxene and amphibole in textural equilibrium with small garnet grains (Fig. 20a, b, c, d, e; chapter 4). Figures from 46 to 61 show the results of EBSD analysis of four different microstructural domains of garnet clinopyroxenites. Domain 1 includes a clinopyroxene porphyroclast with exsolutions of garnet, orthopyroxene and amphibole. Domain 2 contains an orthopyroxene porphyroclast with exsolutions of garnet, clinopyroxene and amphibole. Domain 3 comprises an orthopyroxene porphyroclast with exsolutions of garnet. Domain 4 is representative of the recrystallised clinopyroxene + orthopyroxene + amphibole + garnet assemblage.

7.1.3.1 Domain 1: Porphyroclastic clinopyroxene with exsolutions of garnet, orthopyroxene and amphibole

Porphyroclastic clinopyroxene (5 mm in size) is preferentially oriented with the [010] axes subparallel to the lineation and the (100) planes subparallel to the foliation (Fig. 46b). It displays a little internal distortion with misorientations as large as 12° (profile AA' in Fig. 46b and d). The density of low-angle boundaries in clinopyroxene is very low indicating a limited development of subgrains. The low-angle (2° - 10°) misorientation axes in sample coordinates cluster close (but slightly offset from) to the centre of the pole figures, while the high-angle (10° - 180°) misorientation axes do not show any clear clustering (Fig. 46c). The low-angle misorientation axes in crystal coordinates show a maximum close to the [001] axis, whereas misorientation axes related to high-angle misorientations are almost uniformly distributed (Fig. 46c). The misorientation angle distribution of correlated and uncorrelated pairs shows deviations from the theoretical random distribution at misorientations lower than 10° and at ca. 50° (Fig. 46e).

Garnet exsolutions do not display any evident CPO and show scarce low-angle boundaries (Fig. 47a and b). Misorientation profiles across low-angle boundaries indicate that misorientations are sharp and that subgrains are slightly rotated with respect to each other around the <100> and <110> directions (profile AA' in Fig. 47b, d). The low- (2° - 10°) and high-angle (10° - 62.8°) misorientation axes in both sample and crystal coordinates are almost uniformly distributed (Fig. 47c). The misorientation angle distribution of correlated pairs

displays an evident peak at low-angle misorientations, while the uncorrelated-pair distribution follows the theoretical random curve (Fig. 47e).

Orthopyroxene exsolutions show a CPO that is well-correlated to the CPO of the host clinopyroxene with the [010] axes that cluster at low angle with respect to the lineation and the (100) planes oriented subparallel to the foliation (Fig. 48b). The orthopyroxene lamellae show scarce low-angle boundaries and a little internal distortion characterised by small rotations (up to 7°) of the [100] and [010] axes around the [001] axis (profile AA' in Fig. 26b, d). The low-angle (2° - 10°) misorientation axes in sample coordinates display three distinct maxima in the XY plane while misorientation axes related to high-angle (10° - 120°) misorientations do not show any evident clustering (Fig. 48c). The low-angle misorientation axes in crystal coordinates display a maximum close to the [001] axis, while high-angle misorientation axes do not display any clear maximum (Fig. 48c). The misorientation angle distribution of both correlated and uncorrelated pairs deviates from the random theoretical distribution at low angle misorientations (Fig. 48e).

Amphibole exsolutions show a CPO that is strongly related to the CPO of the host clinopyroxene with the [010] axes oriented subparallel to the lineation and the (100) planes oriented subparallel to the foliation (Fig. 49b). The density of low-angle boundaries is relatively high (Fig. 49a). Misorientation profiles across low-angle boundaries show that misorientations are sharp and that subgrains are slightly misoriented with respect to each other (profile AA' in Fig. 49b). The low-angle (2° - 10°) misorientation axes in sample coordinates cluster close to the centre (but slightly offset from) of the pole figures while the high-angle (10° - 180°) misorientation axes do not show any clear clustering (Fig. 49c). The low-angle misorientation axes in crystal coordinates cluster close to the [001] axis, while misorientation axes related to high-angle misorientations do not display any clear clustering (Fig. 49c). The misorientation angle distribution of correlated pairs display a distinct peak (frequency of 43 %) at low-angle misorientations while the uncorrelated-pair distribution deviates from the random theoretical curve showing peaks at misorientation angles lower than 40° (Fig. 49e).

Porphyroclastic clinopyroxene

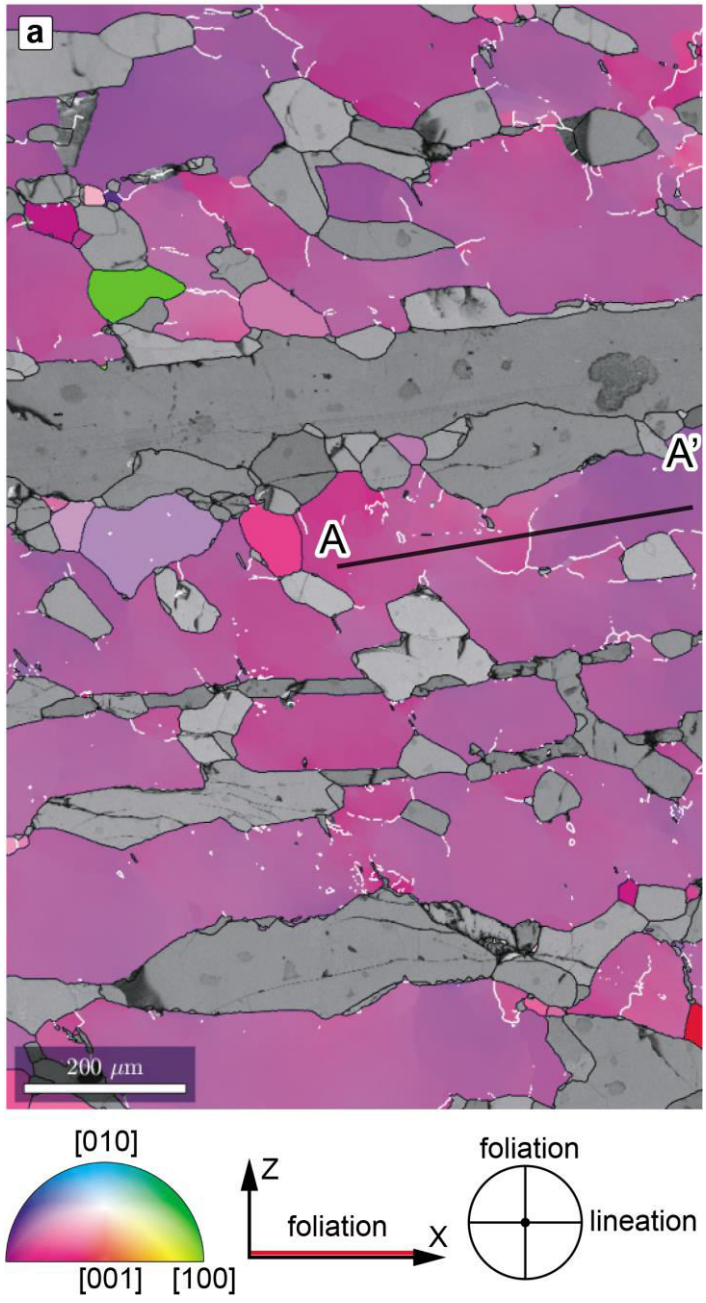

(continued)

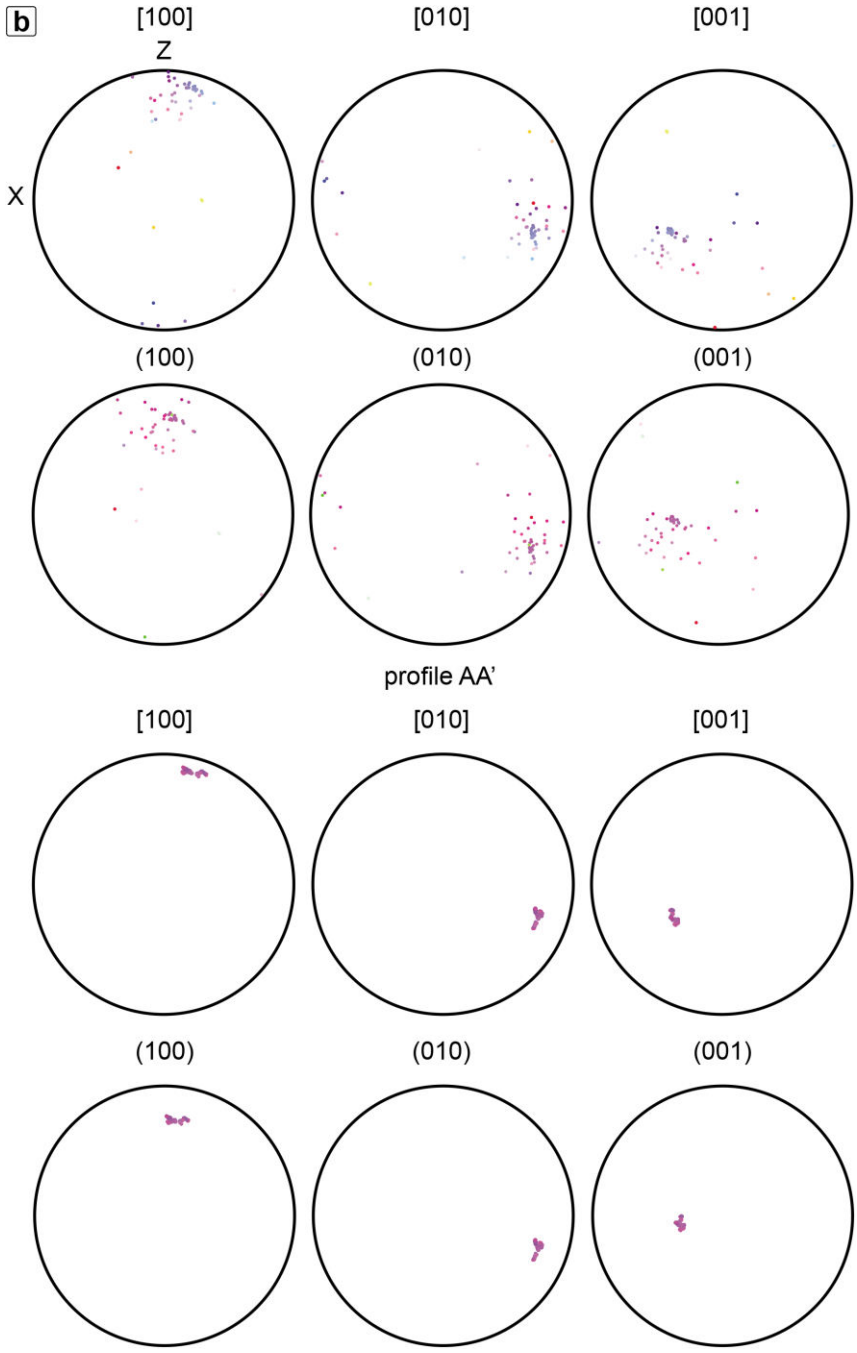

(continued)

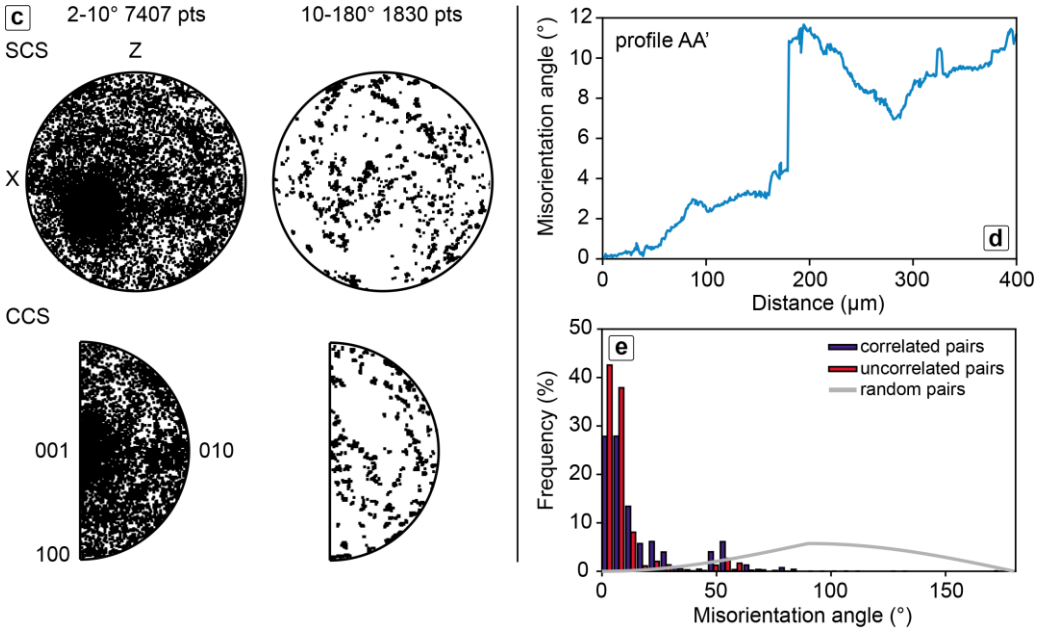

Fig. 46 EBSD map and crystallographic orientation data of porphyroclastic clinopyroxene in garnet clinopyroxenite of Ulten Zone (UT23). (a) EBSD-derived inverse pole figure map with respect to X sample direction. Grain boundaries are coloured in black. Subgrain boundaries are coloured in white. (b) First and second row: pole figures of clinopyroxene (OPPG). Third and fourth row: pole figures of clinopyroxene crystallographic directions along profile AA'. (c) Misorientation axis distributions for clinopyroxene in SCS (upper row) and CCS (lower row). (d) Cumulative misorientations relative to the first analysed point along the profile AA' in clinopyroxene. (e) Misorientation angle distribution for clinopyroxene.

Garnet exsolutions

(continued)

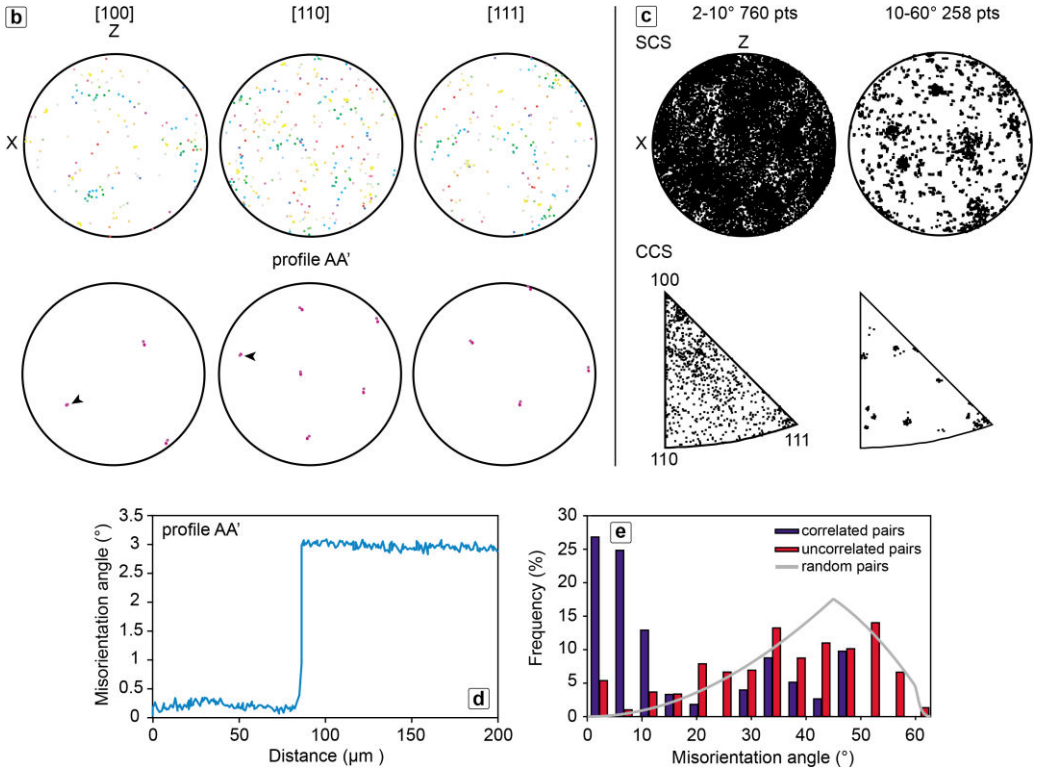

Fig. 47 EBSD map and crystallographic orientation data of garnet exsolutions in clinopyroxene of garnet clinopyroxenite of Ulten Zone (UT23). (a) EBSD-derived inverse pole figure map with respect to X sample direction. Grain boundaries are coloured in black. Subgrain boundaries are coloured in white. (b) Upper row: pole figures of garnet (OPPG). Lower row: pole figures of garnet crystallographic directions along profile AA'. (c) Misorientation axis distributions for garnet in SCS (upper row) and CCS (lower row). (d) Cumulative misorientations relative to the first analysed point along the profile AA' in garnet. (e) Misorientation angle distribution for garnet.

Orthopyroxene exsolutions

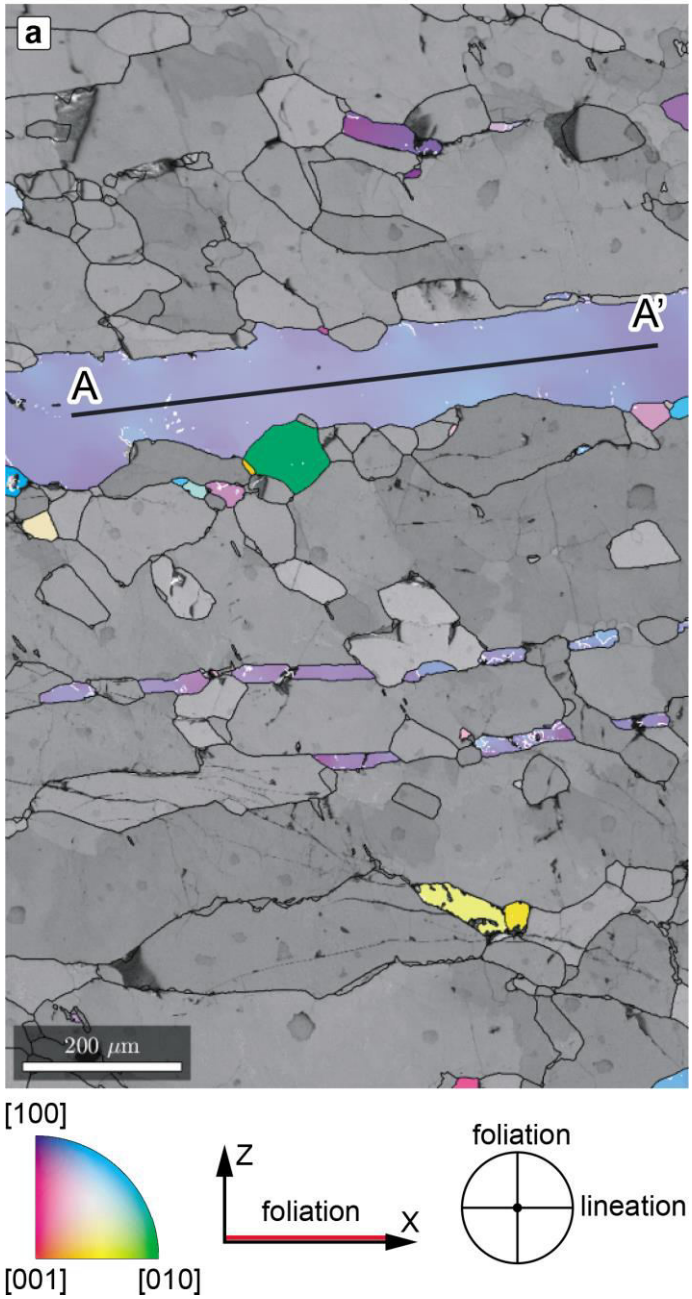

(continued)

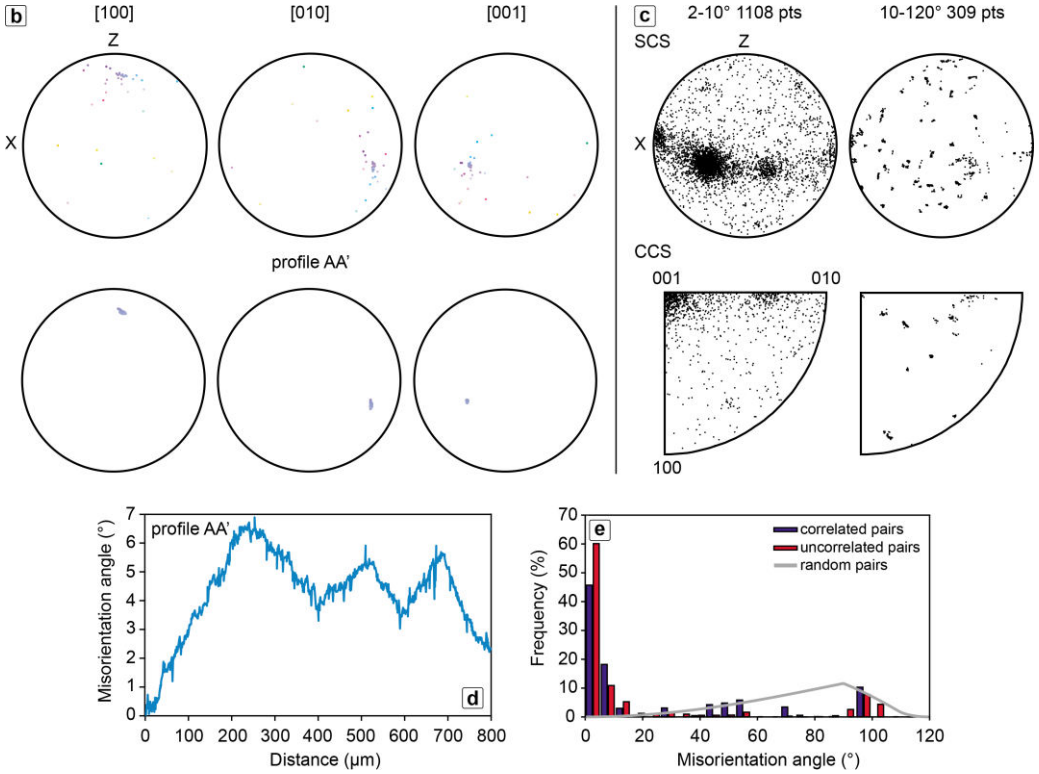

Fig. 48 EBSD map and crystallographic orientation data of orthopyroxene exsolutions in clinopyroxene of garnet clinopyroxenite of Ulten Zone (UT23). (a) EBSD-derived inverse pole figure map with respect to X sample direction. Grain boundaries are coloured in black. Subgrain boundaries are coloured in white. (b) Upper row: pole figures of orthopyroxene (OPPG). Lower row: pole figures of orthopyroxene crystallographic directions along profile AA'. (c) Misorientation axis distributions for orthopyroxene in SCS (upper row) and SCS (lower row). (d) Cumulative misorientations relative to the first analysed point along the profile AA' in orthopyroxene. (e) Misorientation angle distribution for orthopyroxene.

Amphibole exsolutions

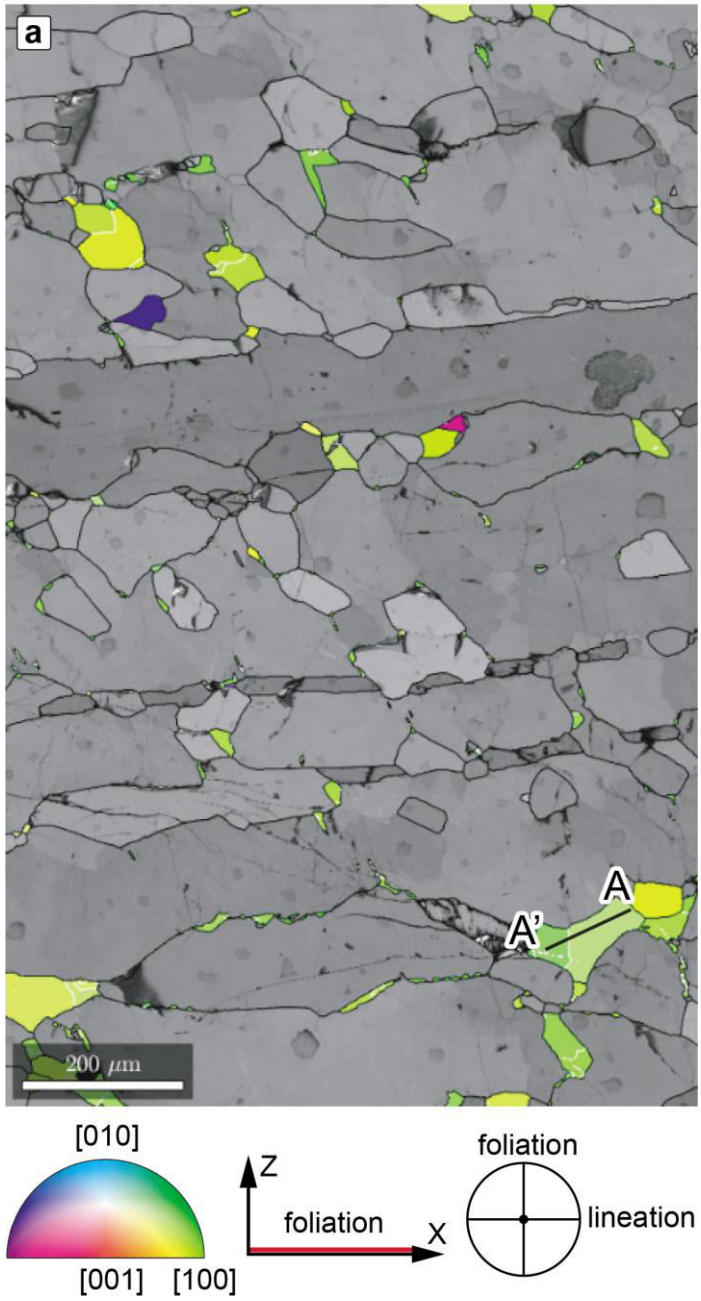

(continued)

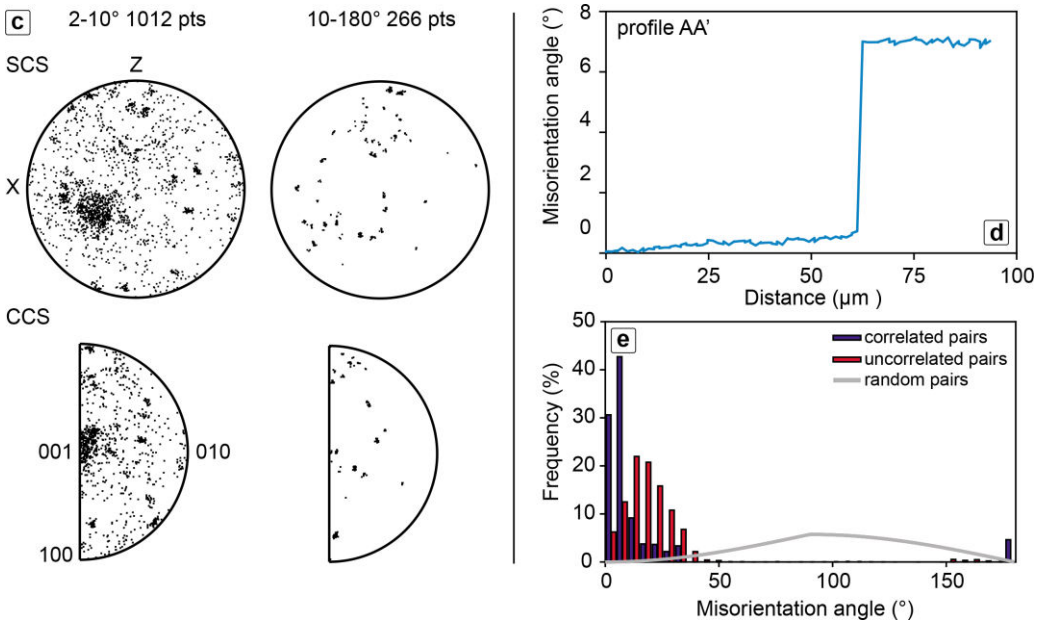

Fig. 49 EBSD map and crystallographic orientation data of amphibole exsolutions in clinopyroxene of garnet clinopyroxenite of Ulten Zone (UT23). (a) EBSD-derived inverse pole figure map with respect to X sample direction. Grain boundaries are coloured in black. Subgrain boundaries are coloured in white. (b) First and second row: pole figures of amphibole (OPPG). Third and fourth row: pole figures of amphibole crystallographic directions along profile AA'. (c) Misorientation axis distributions for amphibole in SCS (upper row) and CCS (lower row). (d) Cumulative misorientations relative to the first analysed point along the profile AA' in amphibole. (e) Misorientation angle distribution for amphibole.

7.1.3.2 Domain 2: Porphyroclastic orthopyroxene with exsolutions of garnet, clinopyroxene and amphibole

Porphyroclastic orthopyroxene (3 mm in size) is preferentially oriented with the [010] axes subparallel to the lineation and the (100) planes subparallel to the foliation (Fig. 50b). It displays a strong internal distortion with rotation of the crystalline lattice up to 32° (Fig. 50d). Misorientation profiles indicate the rotation of the [100] and [010] axes around the [001] axis (Fig. 50b). The low-angle (2° - 10°) misorientation axes in sample coordinates cluster close to the centre of the pole figure, while high-angle (10° - 120°) misorientation axes display two weak maxima close to centre of the pole figure and close to the pole to the foliation (Fig. 50c). The low-angle misorientation axes distribution in crystal coordinates cluster close to the [001] axis, while misorientation axes related to high-angle misorientations show two weak maxima close to the [001] and [010] axes (Fig. 50c). The misorientation angle distribution of both correlated and uncorrelated pairs show higher frequency than the random-pair distribution for misorientations < 40°, and lower frequency for misorientations > 40° (Fig. 50e).

The passage from porphyroblastic to fine-grained, neoblastic orthopyroxenes is marked by abrupt, large misorientation angles between the new grains and the neighbouring porphyroblast (profile B-B' in Fig. 51). The orientation of the neoblastic orthopyroxenes is strongly controlled by the CPO of the porphyroblastic orthopyroxene since they have the [010] axes aligned subparallel to the lineation and the (100) planes oriented subparallel to the foliation (Fig. 51b). The recrystallised orthopyroxenes show internal misorientations less than 1° and are strongly misoriented with respect to each other (Fig. 51c). The misorientation angle distribution of both correlated and uncorrelated pairs show higher frequency than the random-pair distribution for misorientations < 60° and lower frequency for misorientations > 60° (Fig. 51d).

Garnet exsolutions do not display any obvious CPO (Fig. 52b). The density of low-angle boundaries is relatively low indicating the scarce development of subgrains. Misorientation profiles across low-angle boundaries indicate that misorientations are sharp and that subgrains are slightly rotated with respect to each other (profile AA' in Fig. 52b). The low- (2° - 10°) and high-angle (10° - 62.8°) misorientation axes in sample coordinates do not show any clear clustering (Fig. 52c) while the low- and high-angle misorientation axes distribution in crystal coordinates show a weak maximum close to the <111> (Fig. 52c). The misorientation angle distribution of correlated pairs displays an excess in

misorientations angles < 15°, while the uncorrelated-pair distribution follows the random theoretical curve (Fig. 52e).

Clinopyroxene exsolutions have a CPO which is well-correlated with the CPO of host orthopyroxene since they show the [010] axes aligned subparallel to the lineation and the (100) planes oriented subparallel to the foliation (c.f. Fig. 53b and Fig. 50b). The low- (2° - 10°) and high-angle (10° - 180°) misorientation axes distribution in sample and crystal coordinates do not display any clear clustering likely because of the limited number data (Fig. 53c). The misorientation angle distribution of both correlated and uncorrelated pairs show two distinct peaks at misorientation angles < 20° and > 170° (Fig. 53d).

Amphibole exsolutions display a CPO which is strongly influenced by the CPO of the host orthopyroxene since they have the [010] axes aligned to the lineation and the (100) planes oriented subparallel to the foliation (c.f. Fig. 54b and Fig. 50b). The low- (2° - 10°) and high-angle (10° - 180°) misorientation axes in sample coordinates show a clear maximum close to the centre of the pole figures (Fig. 54c) while the distribution of low- and high-angle misorientation axes in crystal coordinates cluster close to the [001] axis (Fig. 54c). The misorientation angle distribution of correlated pairs show evident peaks at misorientation angles < 20° and > 170°, whereas the uncorrelated-pair distribution shows an excess in misorientations angles < 50°, and a deficit in misorientation angles ranging between 60° and 85° (Fig. 54e).

Porphyroclastic orthopyroxene

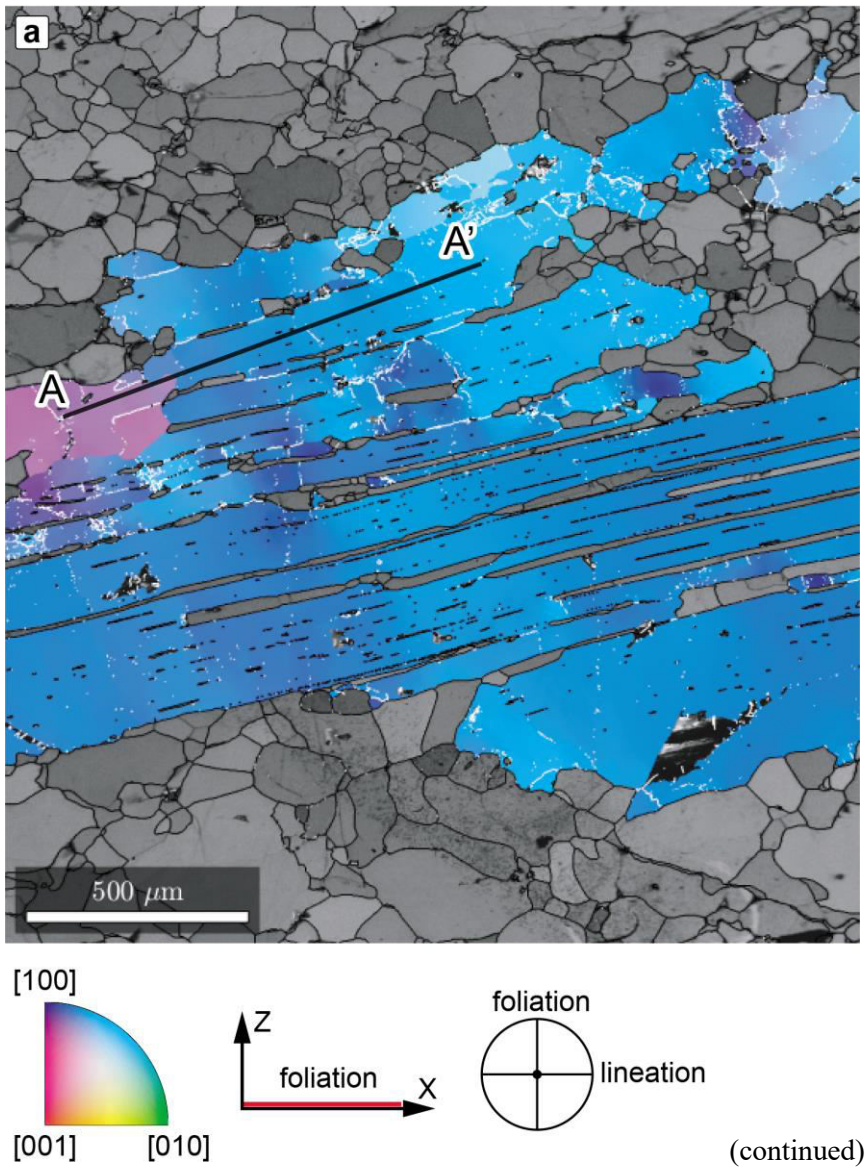

(continued)

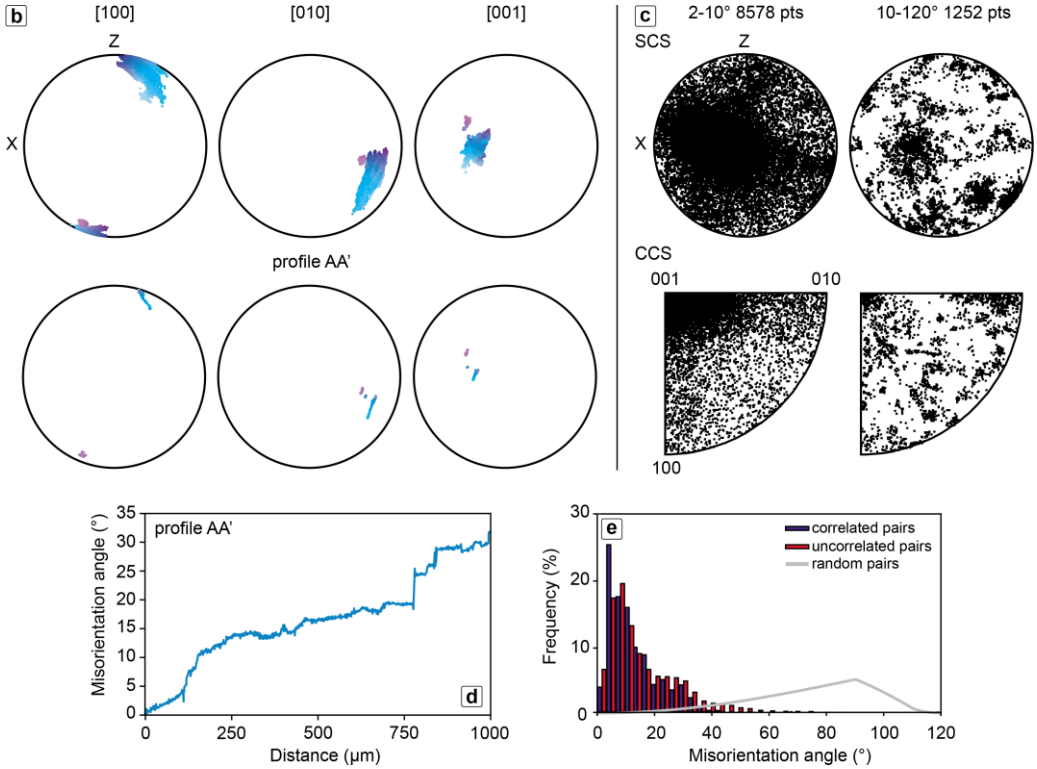

Fig. 50 EBSD map and crystallographic orientation data of porphyroblastic orthopyroxene in garnet clinopyroxenite of Ulten Zone (UT23). (a) EBSD-derived inverse pole figure map with respect to X sample direction. Grain boundaries are coloured in black. Subgrain boundaries are coloured in white. (b) Upper row: pole figures of orthopyroxene (all data points). Lower row: pole figures of orthopyroxene crystallographic directions along profile AA'. (c) Misorientation axis distributions for orthopyroxene in SCS (upper row) and crystal (lower row). (d) Cumulative misorientations relative to the first analysed point along the profile AA' in orthopyroxene. (e) Misorientation angle distribution for orthopyroxene.

Neoblastic orthopyroxene

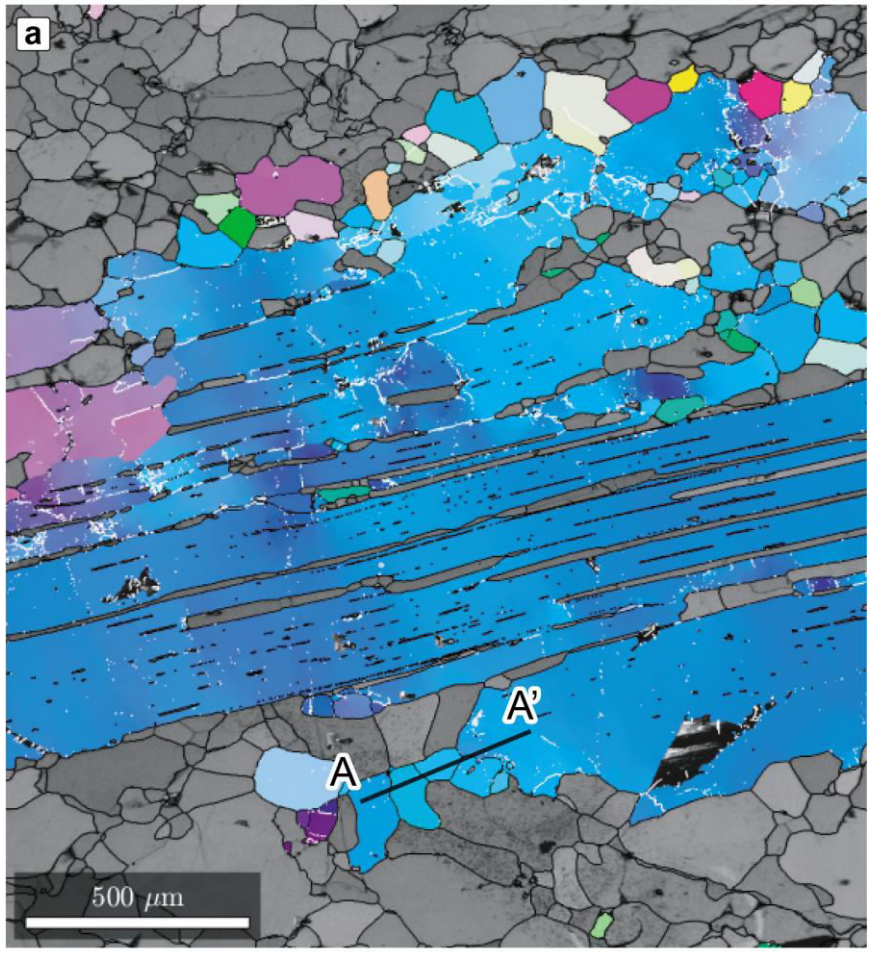

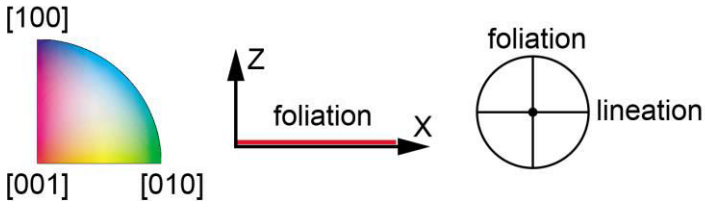

(continued)

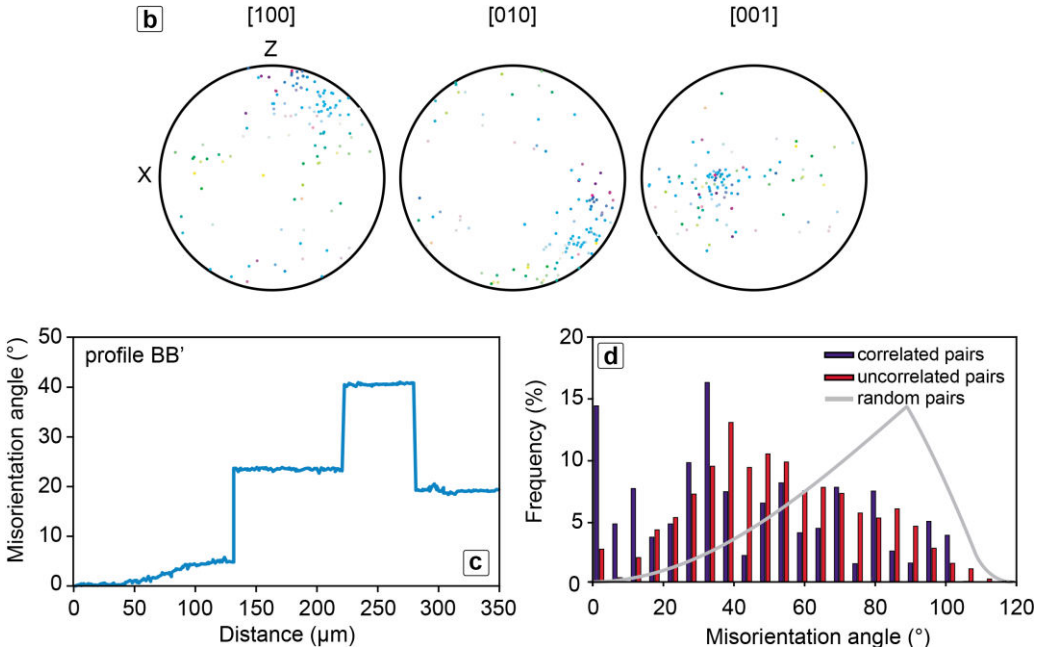

Fig. 51 EBSD map of porphyroblastic and neoblastic orthopyroxene in garnet clinopyroxenite of Ulten Zone (UT23). Crystallographic orientation data only for neoblastic orthopyroxene. (a) EBSD-derived inverse pole figure map with respect to X sample direction. Grain boundaries are coloured in black. Subgrain boundaries are coloured in white. (b) pole figures of orthopyroxene. (c) Cumulative misorientations relative to the first analysed point along the profile AA' in orthopyroxene. (d) Misorientation angle distribution for orthopyroxene.

Garnet exsolutions

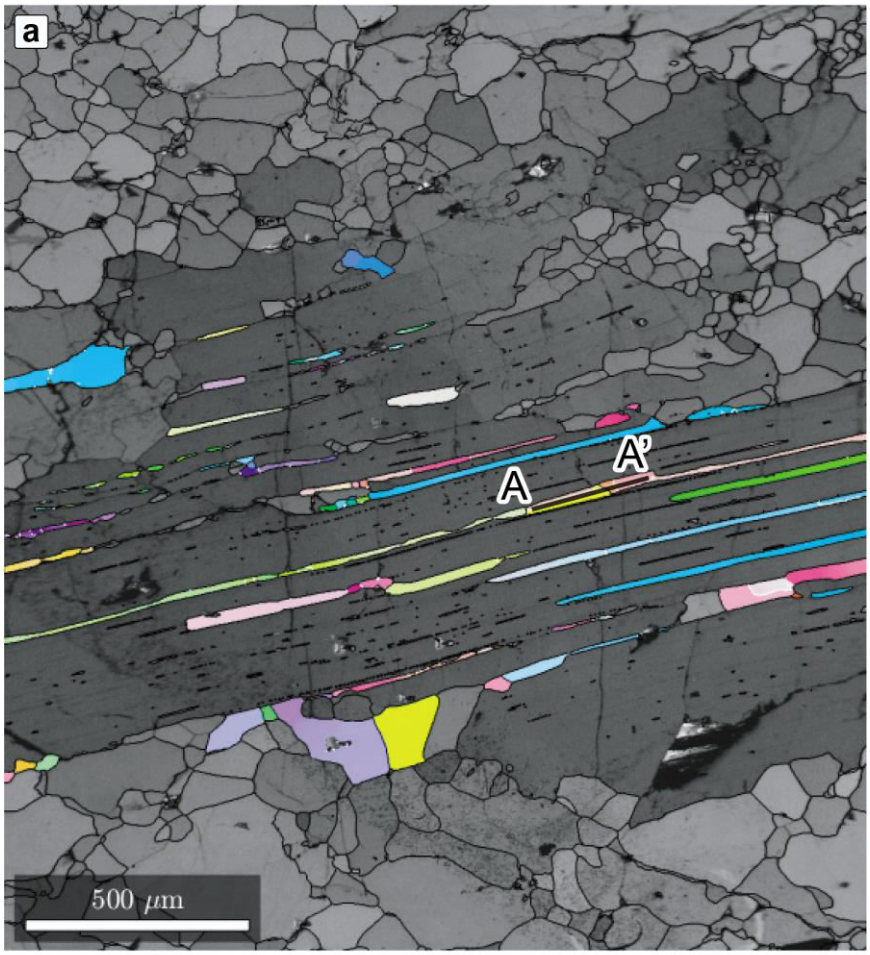

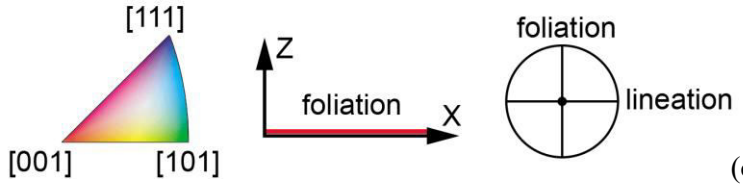

(continued)

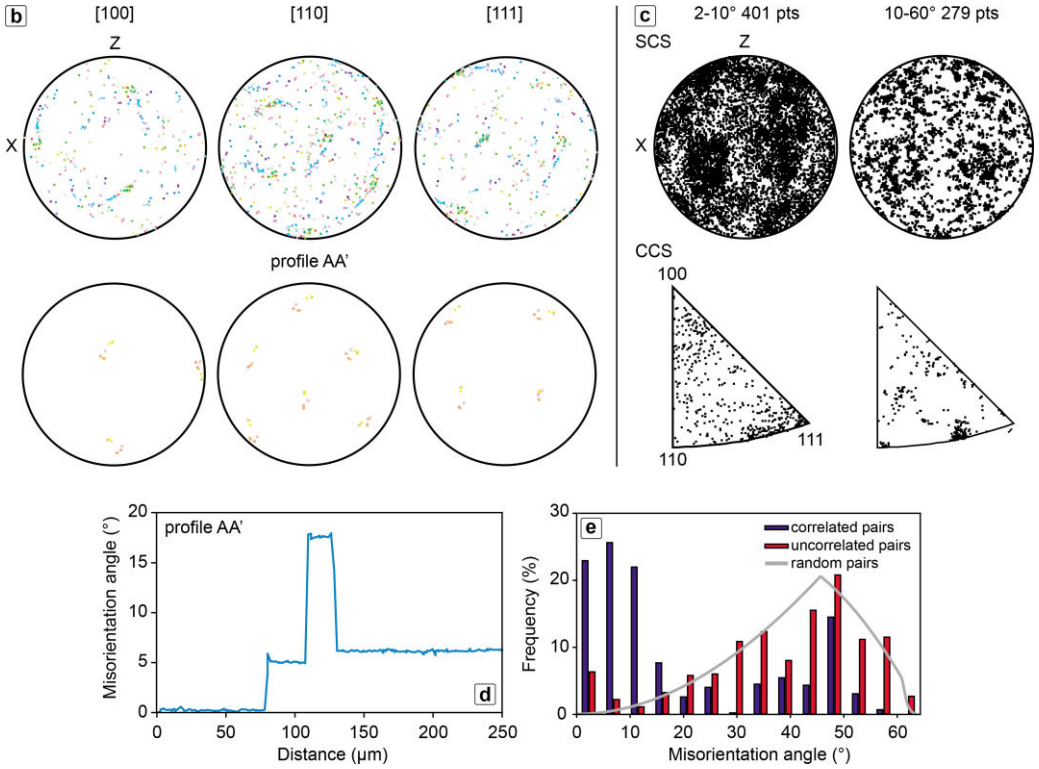

Fig. 52 EBSD map and crystallographic orientation data of garnet exsolutions in orthopyroxene of garnet clinopyroxenite of Ulten Zone (UT23). (a) EBSD-derived inverse pole figure map with respect to X sample direction. Grain boundaries are coloured in black. Subgrain boundaries are coloured in white. (b) Upper row: pole figures of garnet (OPPG). Lower row: pole figures of garnet crystallographic directions along profile AA'. (c) Misorientation axis distributions for garnet in SCS (upper row) and CCS (lower row). (d) Cumulative misorientations relative to the first analysed point along the profile AA' in garnet. (e) Misorientation angle distribution for garnet.

Clinopyroxene exsolutions

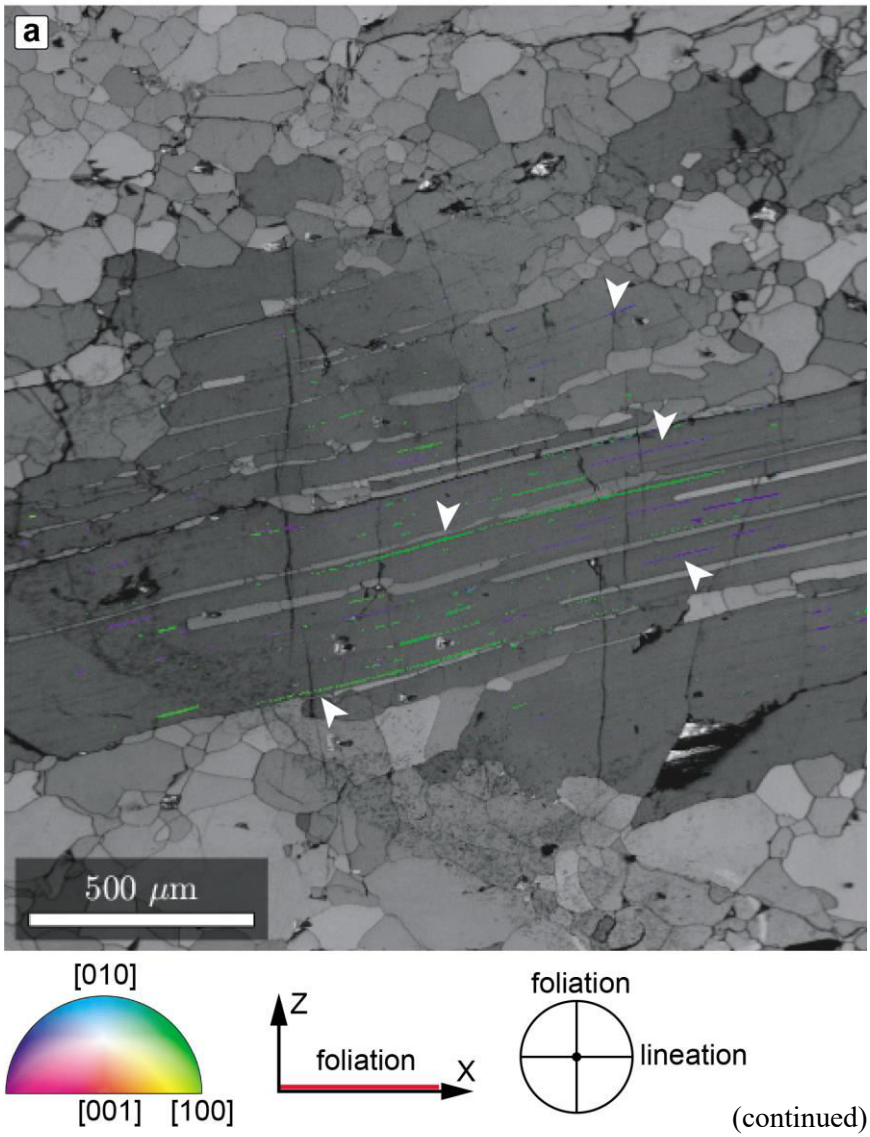

(continued)

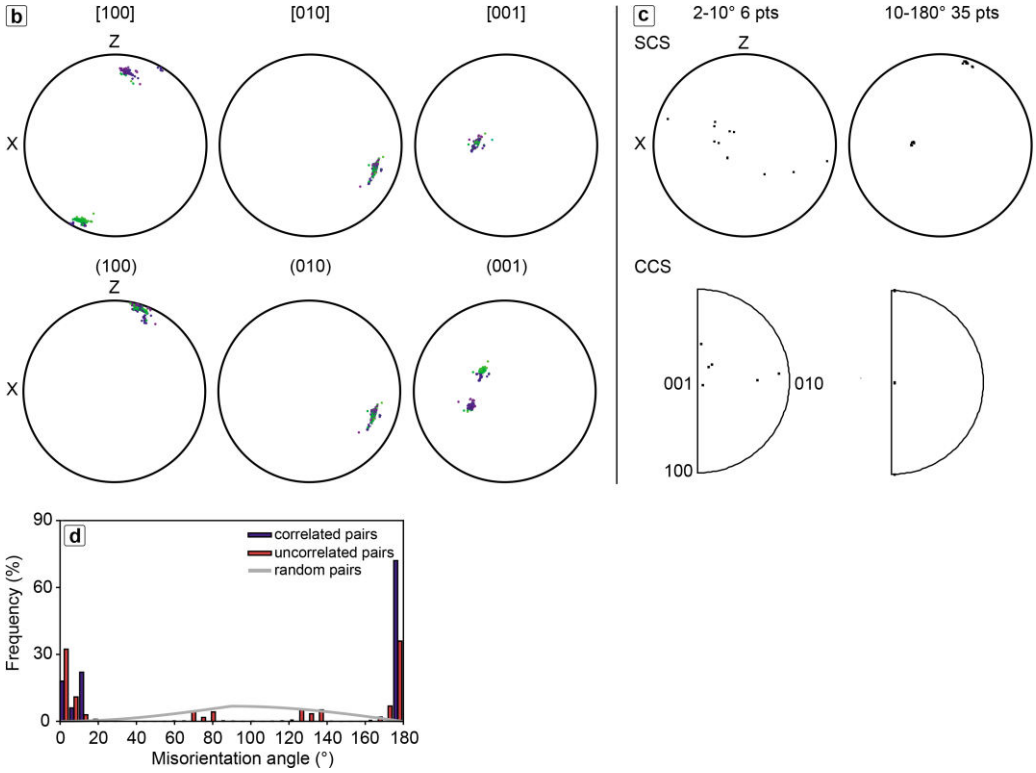

Fig. 53 EBSD map and crystallographic orientation data of clinopyroxene exsolutions in orthopyroxene of garnet clinopyroxenite of Ulten Zone (UT23). (a) EBSD-derived inverse pole figure map with respect to X sample direction. Grain boundaries are and subgrain boundaries are not shown due to the small size of clinopyroxene exsolutions. (b) Pole figures of clinopyroxene (OPPG). (c) Misorientation axis distributions for amphibole in SCS (upper row) and CCS (lower row). (d) Misorientation angle distribution for clinopyroxene.

Amphibole exsolutions

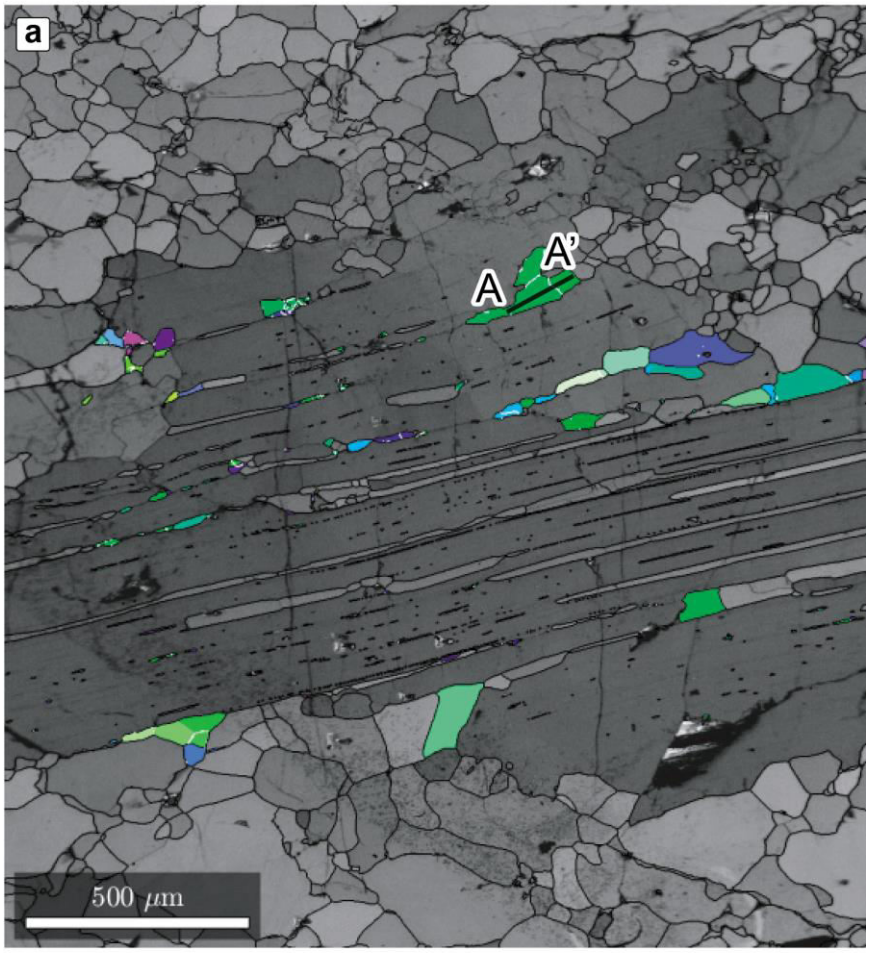

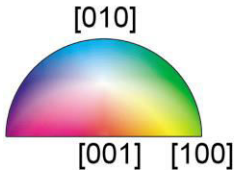

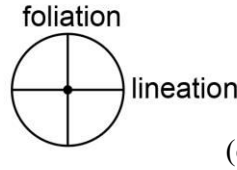

(continued)

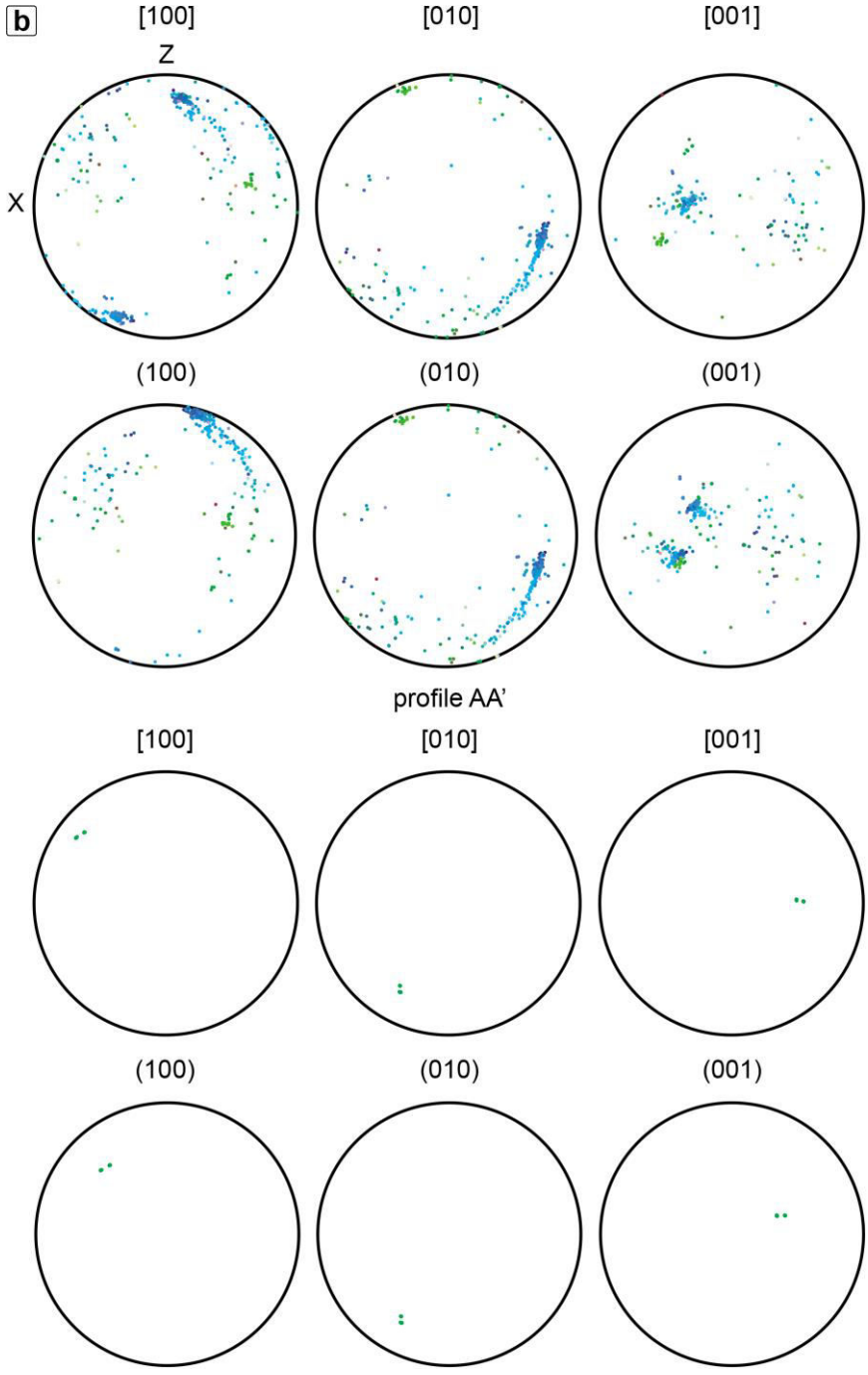

(continued)

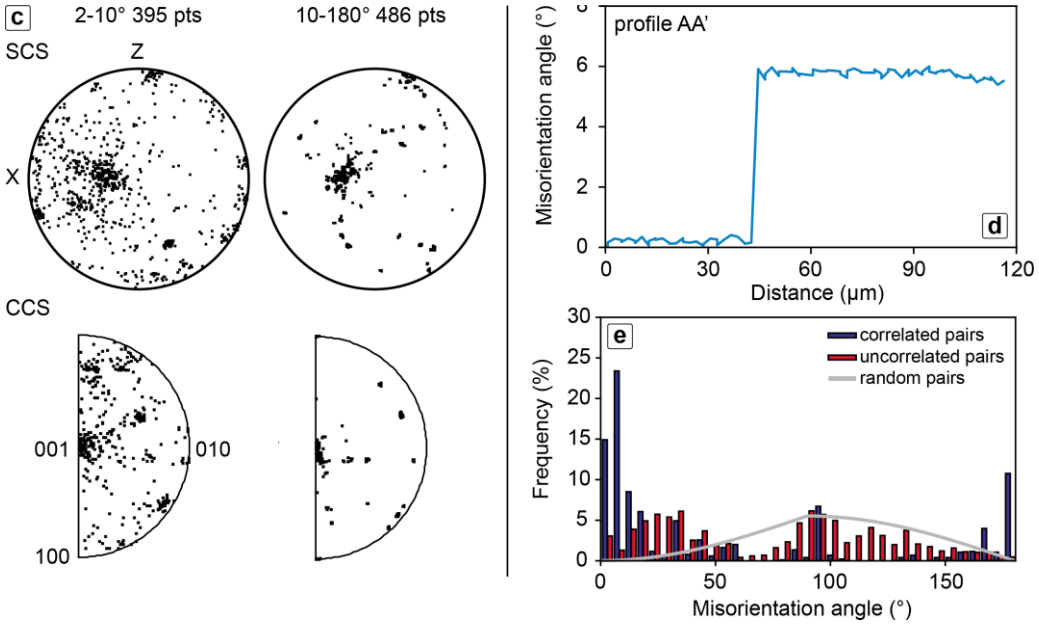

Fig. 54 EBSD map and crystallographic orientation data of amphibole exsolutions in orthopyroxene of garnet clinopyroxenite of Ulten Zone (UT23). (a) EBSD-derived inverse pole figure map with respect to X sample direction. Grain boundaries are coloured in black. Subgrain boundaries are coloured in white. (b) First and second row: pole figures of amphibole (OPPG). Third and fourth row: pole figures of amphibole crystallographic directions along profile AA'. (c) Misorientation axis distributions for amphibole in SCS (upper row) and CCS (lower row). (d) Cumulative misorientations relative to the first analysed point along the profile AA' in amphibole. (e) Misorientation angle distribution for amphibole.

7.1.3.3 Domain 3: Porphyroclastic orthopyroxene with exsolutions of garnet

Porphyroclastic orthopyroxene (1 mm in size) shows a clear CPO with the [010] axes subparallel to the lineation and the (100) planes subparallel to the foliation (Fig. 55b). Misorientation profiles indicate that orthopyroxene displays a distortion of the crystalline lattice up to 16° (Fig. 55d) mostly accommodated by the rotation of the [100] and [010] axes around the [001] direction (profile A-A' in Fig. 55b). However, low-angle boundaries are scarce. The low- (2° - 10°) and high angle (10° - 120°) misorientation axes in sample coordinates show two maxima close to the centre of the pole figure and close to the pole to the foliation (Fig. 55c). The low-angle misorientation axes distribution in crystal coordinates display two maxima close to the [001] and the [100] axes, while the distribution of the high-angle misorientation axes does not display any clear maximum (Fig. 55c). The misorientation angle distribution of both correlated and uncorrelated pairs significantly differs from the random theoretical curve. The correlated-pair distribution shows an excess in misorientation angles < 60° and a deficit in misorientation angles > 60°, while the uncorrelated-pair distribution shows higher frequency than the random-pair distribution for misorientations < 50° and lower frequency for misorientations > 50° (Fig. 55e).

The transition from porphyroblastic to fine-grained, neoblastic orthopyroxenes is marked by abrupt, large misorientation angles between the new grains and the neighbouring porphyroblast (profile AA' in Fig. 56c). The orientation of the neoblastic orthopyroxenes is only slightly controlled by the CPO of the porphyroclastic orthopyroxene (Fig. 56b). The recrystallised grains also show internal misorientations less than 1° and are strongly misoriented with respect to each other (Fig. 56c). The misorientation angle distribution of correlated pairs displays higher frequency than the random-pair distribution for misorientations < 60°, and lower frequency for misorientations > 100°, while the uncorrelated-pair distribution broadly resembles the random theoretical curve (Fig. 56d)

Garnet exsolutions do not display any obvious CPO and show very rare low-angle boundaries (Fig. 57a). Misorientation profiles parallel to the long axis of the garnet exsolutions highlight a distortion of the crystalline lattice up to 18° (Fig. 57d) accommodated by rotation dominantly around <111> and <110> (profile AA' in Fig. 57b). The low- (2° - 10°) and high-angle (10° - 62.8°) misorientation axes in sample and crystal coordinates do not show any clear clustering even though there is the tendency of the low-angle misorientation axes to form a weak maximum close to the centre of the pole figure (Fig. 57c). The misorientation angle distribution of correlated pairs displays distinct peaks at

low-angle misorientations and at ca. 50°, while the uncorrelated-pair distribution follows the random theoretical curve (Fig. 57e).

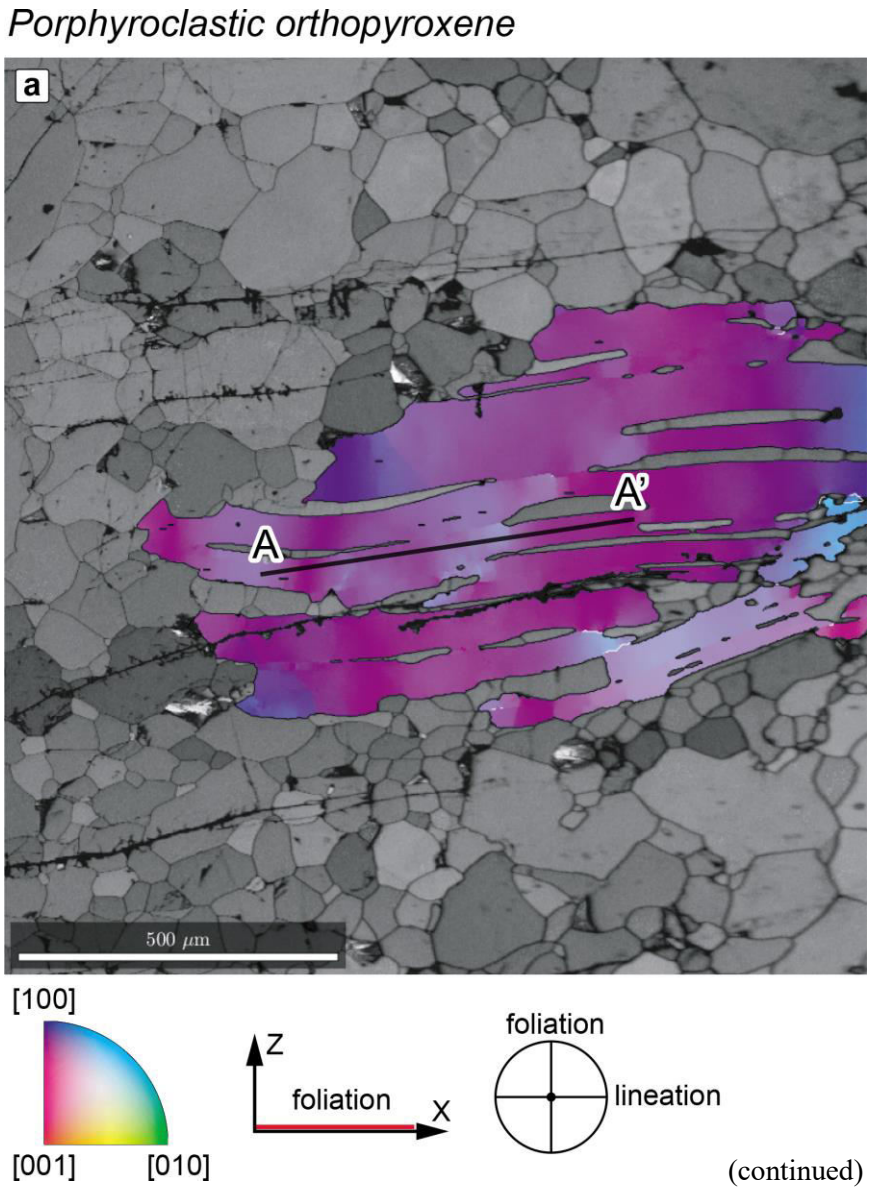

(continued)

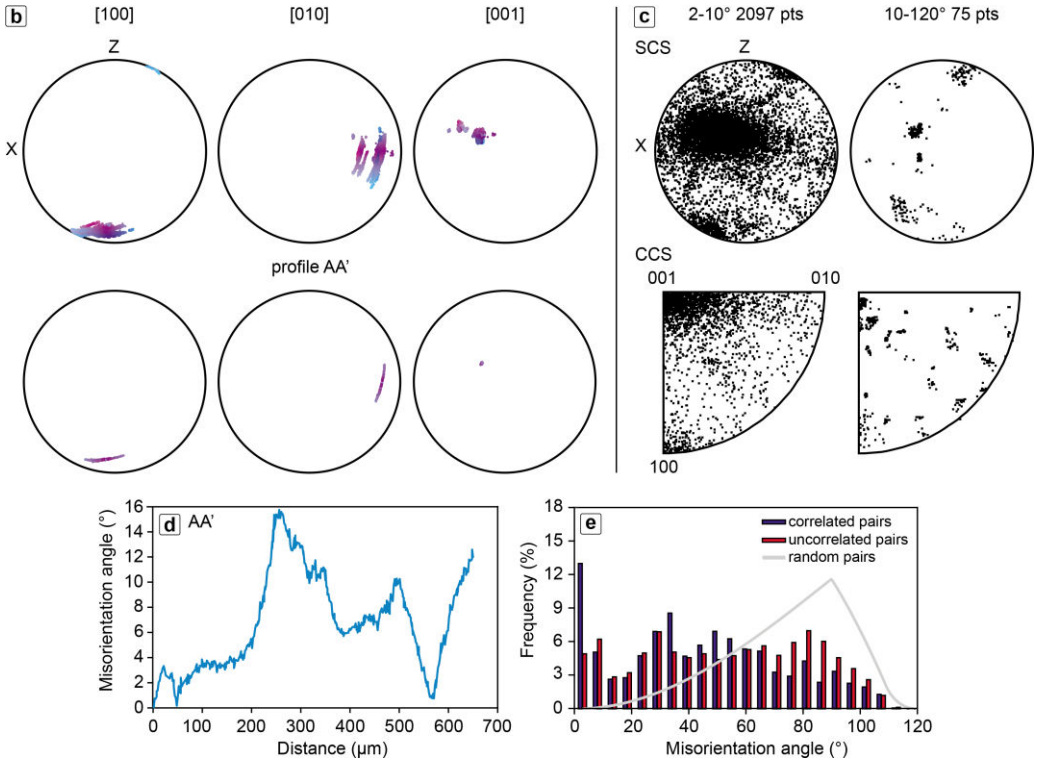

Fig. 55 EBSD map and crystallographic orientation data of porphyroblastic orthopyroxene in garnet clinopyroxenite of Ulten Zone (UT23). (a) EBSD-derived inverse pole figure map with respect to X sample direction. Grain boundaries are coloured in black. Subgrain boundaries are coloured in white. (b) Upper row: pole figures of orthopyroxene (all data points). Lower row: pole figures of orthopyroxene crystallographic directions along profile AA'. (c) Misorientation axis distributions for orthopyroxene in SCS (upper row) and CCS (lower row). (d) Cumulative misorientations relative to the first analysed point along the profile AA' in orthopyroxene. (e) Misorientation angle distribution for orthopyroxene.

Neoblastic orthopyroxene

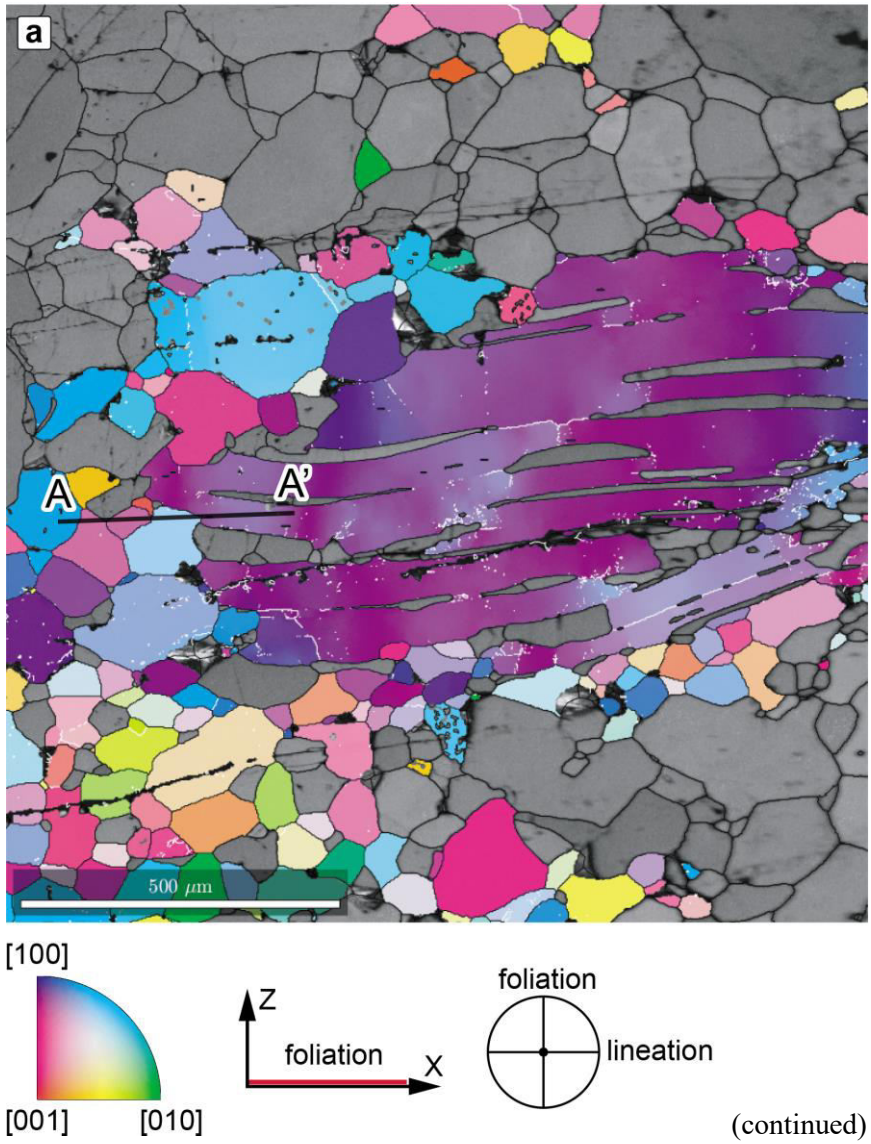

(continued)

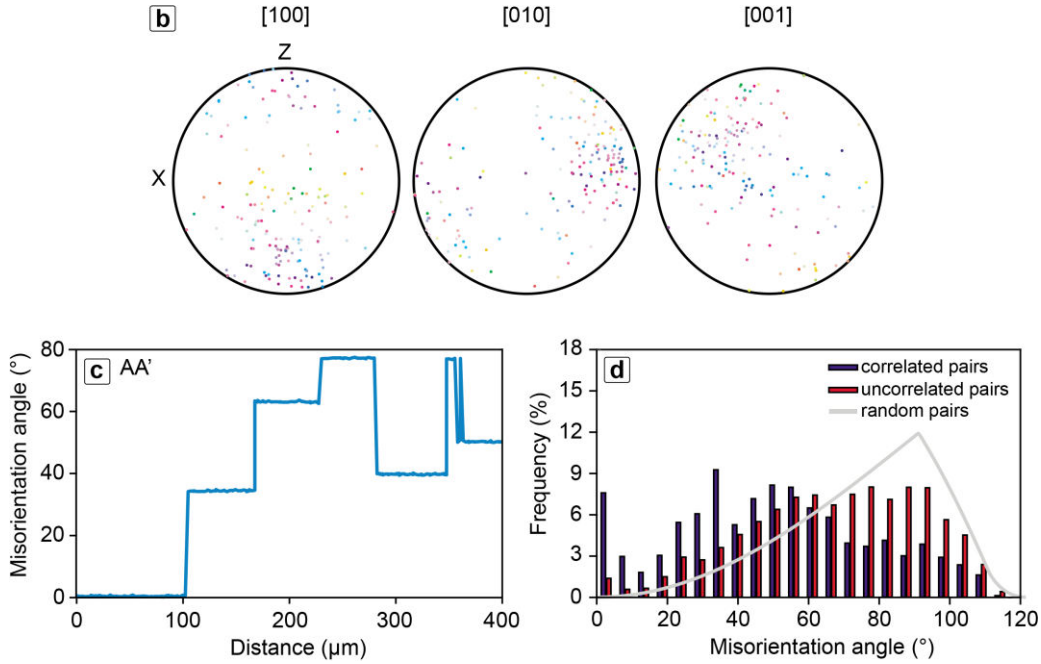

Fig. 56 EBSD map of porphyroblastic and neoblastic orthopyroxene in garnet clinopyroxenite of Ulten Zone (UT23). Crystallographic orientation data only for neoblastic orthopyroxene. (a) EBSD-derived inverse pole figure map with respect to X sample direction. Grain boundaries are coloured in black. Subgrain boundaries are coloured in white. (b) pole figures of orthopyroxene. (c) Cumulative misorientations relative to the first analysed point along the profile AA' in orthopyroxene. (d) Misorientation angle distribution for orthopyroxene.

Garnet exsolutions

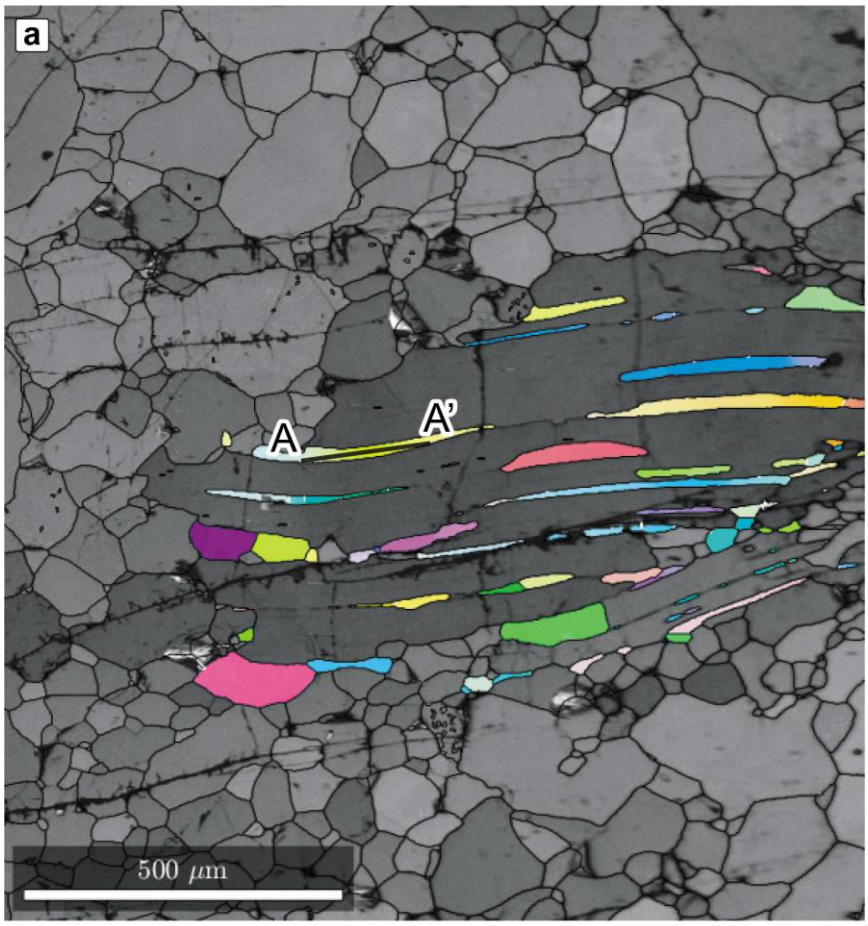

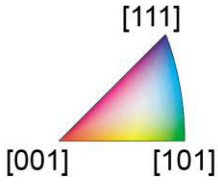

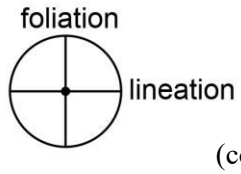

(continued)

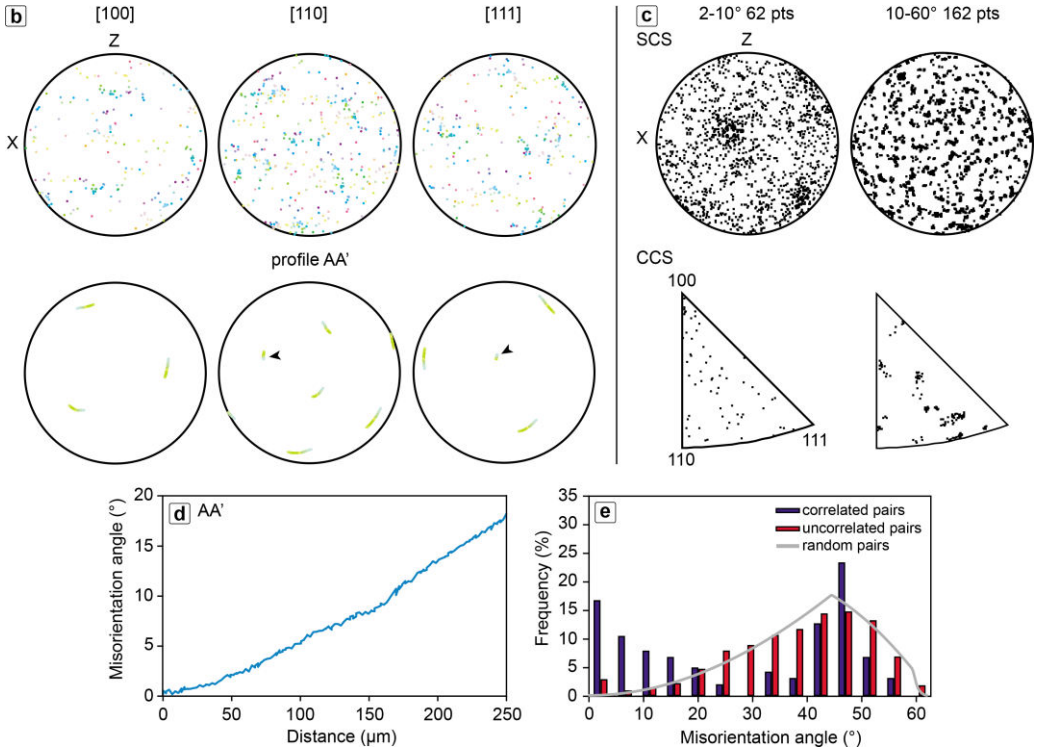

Fig. 57 EBSD map and crystallographic orientation data of garnet exsolutions in orthopyroxene of garnet clinopyroxenite of Ulten Zone (UT23). (a) EBSD-derived inverse pole figure map with respect to X sample direction. Grain boundaries are coloured in black. Subgrain boundaries are coloured in white. (b) Upper row: pole figures of garnet (OPPG). Lower row: pole figures of garnet crystallographic directions along profile AA'. (c) Misorientation axis distributions for garnet in SCS (upper row) and CCS (lower row). (d) Cumulative misorientations relative to the first analysed point along the profile AA' in garnet. (e) Misorientation angle distribution for garnet.

7.1.3.4 Domain 4: Recrystallised clinopyroxene + orthopyroxene + amphibole + garnet assemblage

Neoblastic clinopyroxene display the [010] axes aligned subparallel to the lineation and the (100) planes oriented subparallel to the foliation (Fig. 58b). The recrystallized clinopyroxene grains have internal misorientation less than 1° and are strongly misoriented with respect to each other (Fig. 58d). The low- angle (2° - 10°) misorientations in sample coordinates display a weak maximum close to the lineation (X direction), while high-angle (10° - 180°) misorientations do not show any clear clustering (Fig. 58c). The low- and high angle misorientation axes in crystal coordinates are almost uniformly distributed (Fig. 58c). The misorientation angle distribution of correlated and uncorrelated pairs deviate from the random theoretical curve showing an excess in misorientations angles lower than 75°, and a deficit in misorientation angles greater than 90° (Fig. 58e).

Recrystallised orthopyroxenes do not display a clear CPO, likely because of the scarce number of analysed points (2.47 % of the total dataset). However there is the tendency of the [010] axes to be aligned to the lineation and the (100) planes to be oriented subparallel to the foliation (Fig. 59b). The low-angle boundaries are very rare, indicating a limited development of substructures. The low- (2° - 10°) and high-angle (10° - 120°) misorientation axes in sample and crystal coordinates do not show any clear clustering (Fig. 59c). The misorientation angle distribution of correlated pairs display distinct peaks at misorientations of 5°, 15°, 40° and 80°, while the uncorrelated-pair distribution, although resembles the random theoretical distribution, shows two distinct peaks at misorientations angles < 10° and at 80° (Fig. 59d).

Neoblastic garnets do not display any obvious CPO and show scarce low-angle boundaries (Fig. 60a, b). Misorientation profiles across these low-angle boundaries indicate that misorientations are sharp and that subgrains are slightly rotated with respect to each other around the <100> direction (Fig. 60b). The low-angle (2° - 10°) misorientation axes in sample coordinates show four distinct maxima whereas high-angle (10° - 62.8°) misorientation axes are almost uniformly distributed (Fig. 60c). The low-angle misorientations in crystal coordinates show a weak maximum close to the [100] axis, while misorientation axes related to high-angle misorientations do not show any clear clustering (Fig. 60c). The misorientation angle distribution of correlated pairs display distinct peaks at misorientations lower than 20° and at 40°, while the uncorrelated-pair distribution resembles the random theoretical curve (Fig. 60e).

Neoblastic amphiboles show a clear CPO with the [010] axes subparallel to the lineation and the (100) planes subparallel to the foliation (Fig. 61b). The

density of low-angle boundaries is very low, indicating a limited development of substructures. The low- (2° - 10°) and high-angle (10° - 180°) misorientation axes in sample and crystal coordinates do not show any evident maximum (Fig. 61c). The misorientation angle distribution of both correlated and uncorrelated pairs significantly differs from the random theoretical curve. The correlated-pair distribution shows an excess in misorientation angles < 70° and a deficit in misorientation angles > 70°, while the misorientation angle distribution of uncorrelated pairs shows higher frequency than the random-pair distribution for misorientations < 90° and lower frequency for misorientations > 100° (Fig. 61d).

Neoblastic clinopyroxene

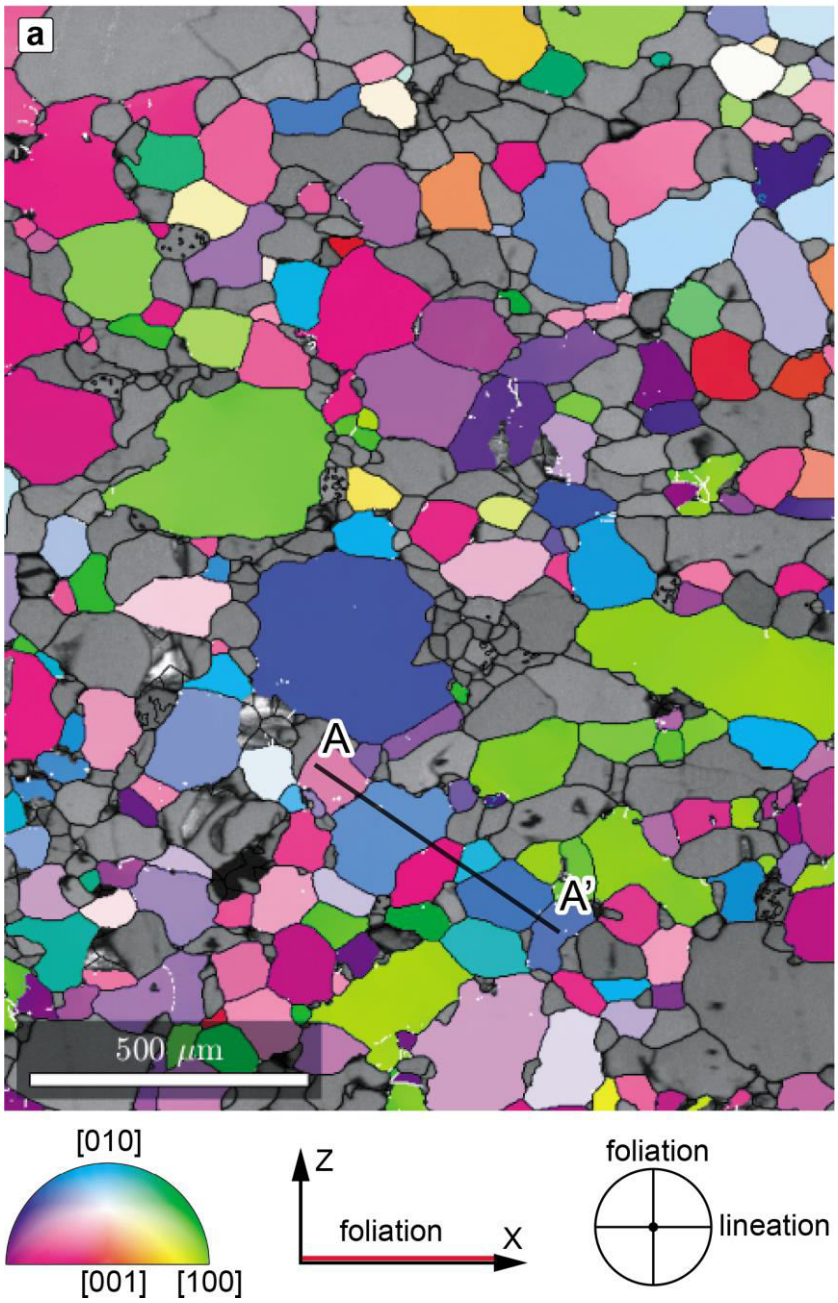

(continued)

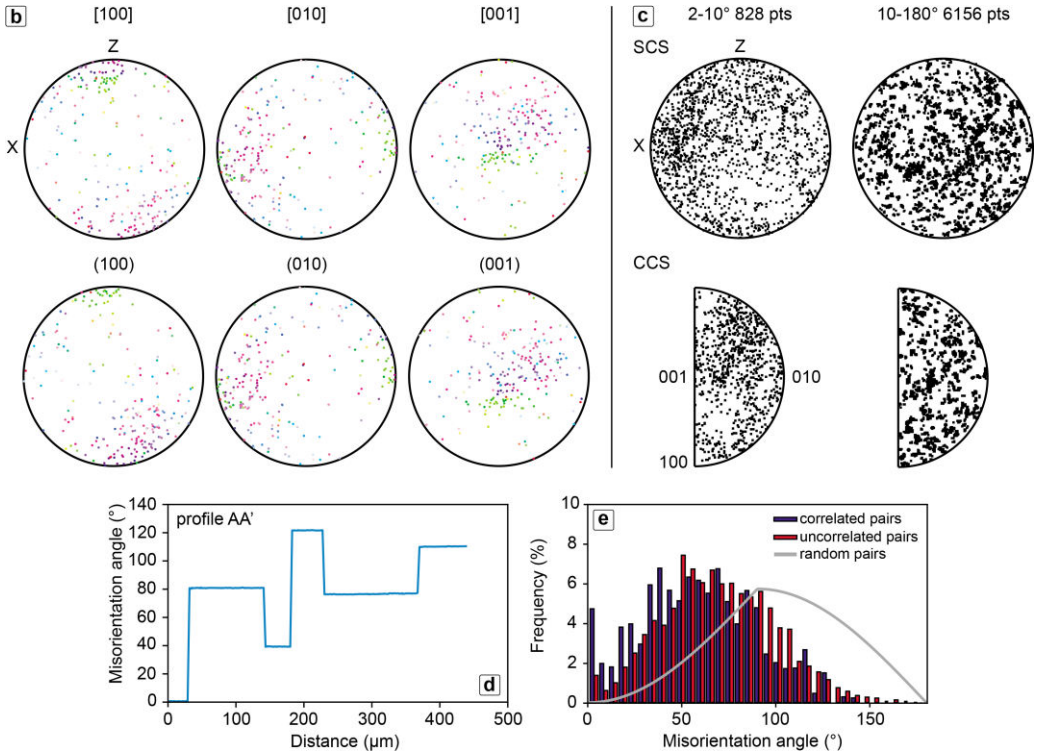

Fig. 58 EBSD map and crystallographic orientation data of neoblastic clinopyroxene in garnet clinopyroxenite of Ulten Zone (UT23). (a) EBSD-derived inverse pole figure map with respect to X sample direction. Grain boundaries are coloured in black. Subgrain boundaries are coloured in white. (b) Pole figures of clinopyroxene (OPPG). (c) Misorientation axis distributions for clinopyroxene in SCS (upper row) and CCS (lower row). (d) Cumulative misorientations relative to the first analysed point along the profile AA' in clinopyroxene. (e) Misorientation angle distribution for clinopyroxene.

Neoblastic orthopyroxene

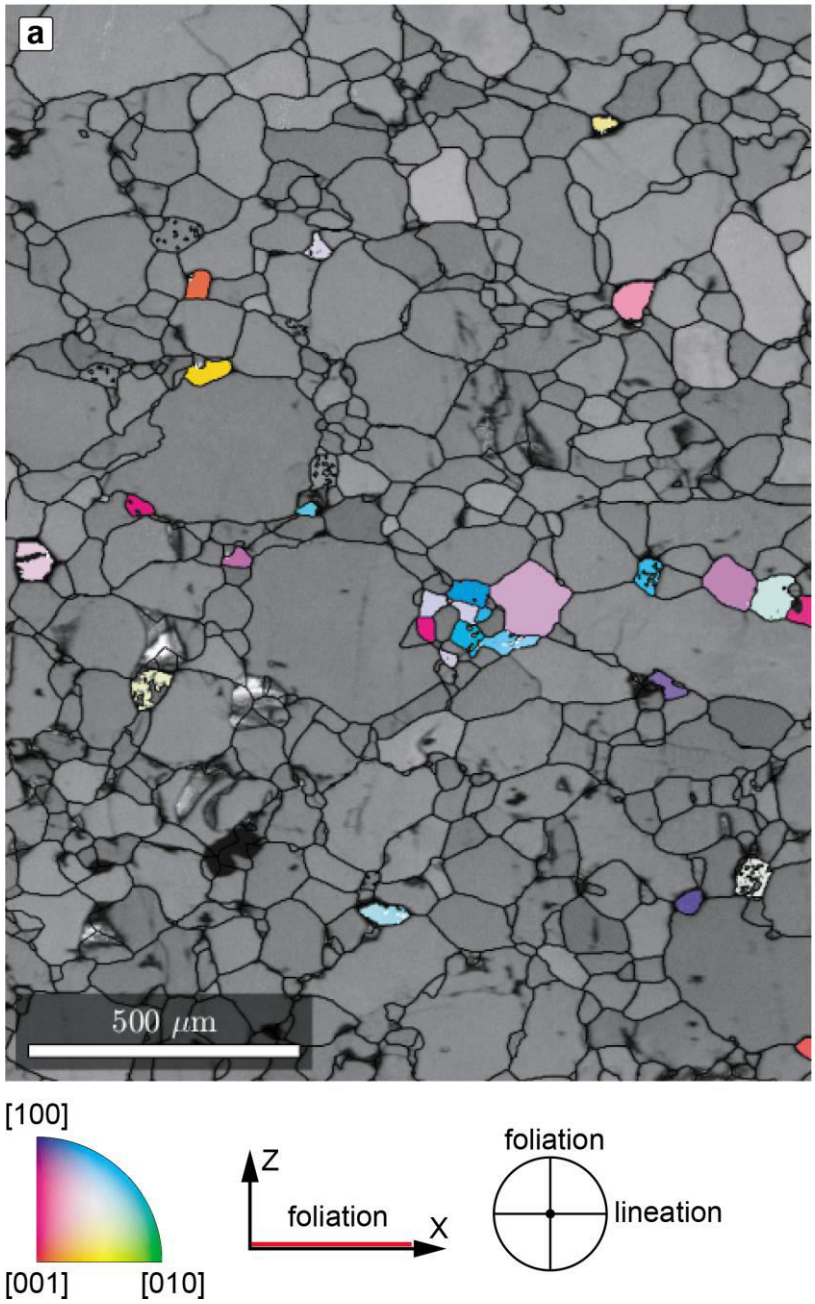

(continued)

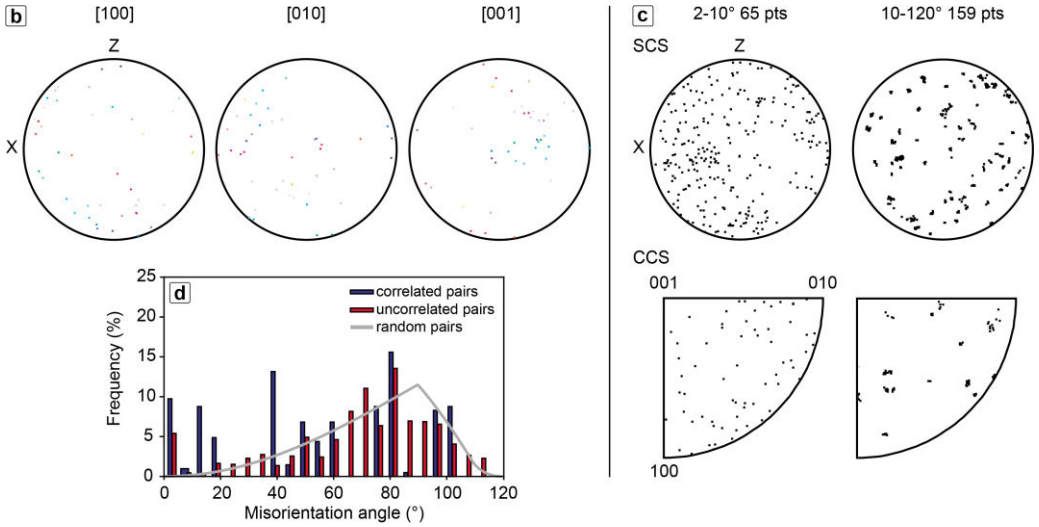

Fig. 59 EBSD map and crystallographic orientation data of neoblastic orthopyroxene in garnet clinopyroxenite of Ulten Zone (UT23). (a) EBSD-derived inverse pole figure map with respect to X sample direction. Grain boundaries are coloured in black. Subgrain boundaries are coloured in white. (b) Pole figures of orthopyroxene (OPPG). (c) Misorientation axis distributions for clinopyroxene in SCS (upper row) and CCS (lower row). (d) Misorientation angle distribution for clinopyroxene.

Neoblastic garnet

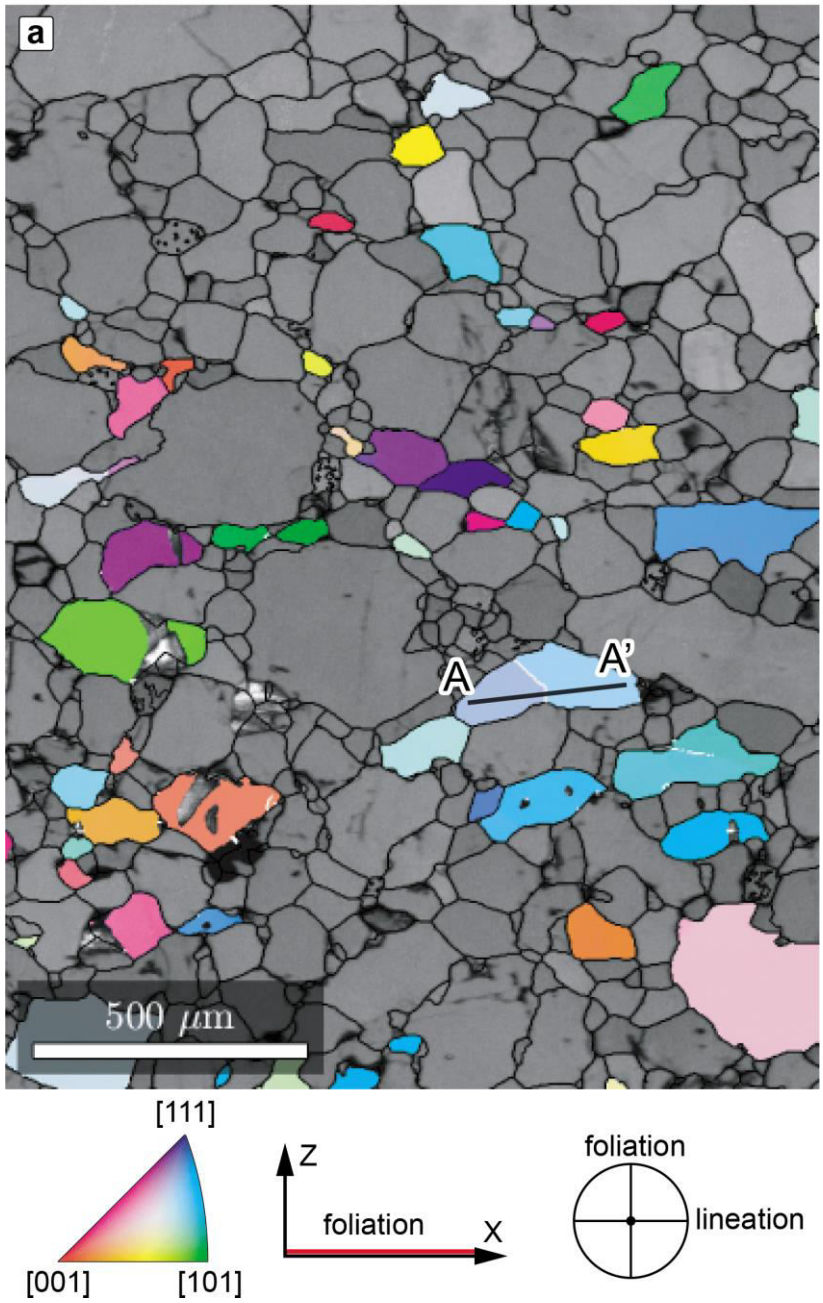

(continued)

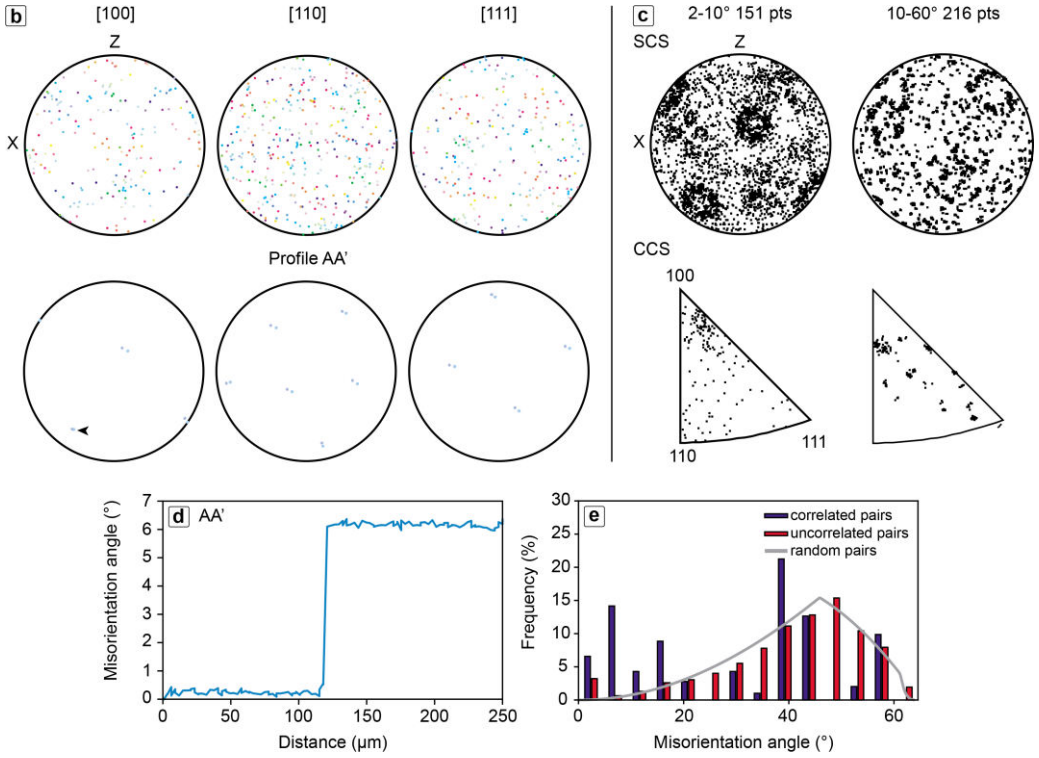

Fig. 60 EBSD map and crystallographic orientation data of neoblastic garnet in garnet clinopyroxenite of Ulten Zone (UT23). (a) EBSD-derived inverse pole figure map with respect to X sample direction. Grain boundaries are coloured in black. Subgrain boundaries are coloured in white. (b) Upper row: pole figures of garnet (OPPG). Lower row: pole figures of garnet crystallographic directions along profile AA' (c) Misorientation axis distributions for garnet in SCS (upper row) and CCS (lower row). (d) Cumulative misorientations relative to the first analysed point along the profile AA' in garnet. (e) Misorientation angle distribution for garnet.

Neoblastic amphibole

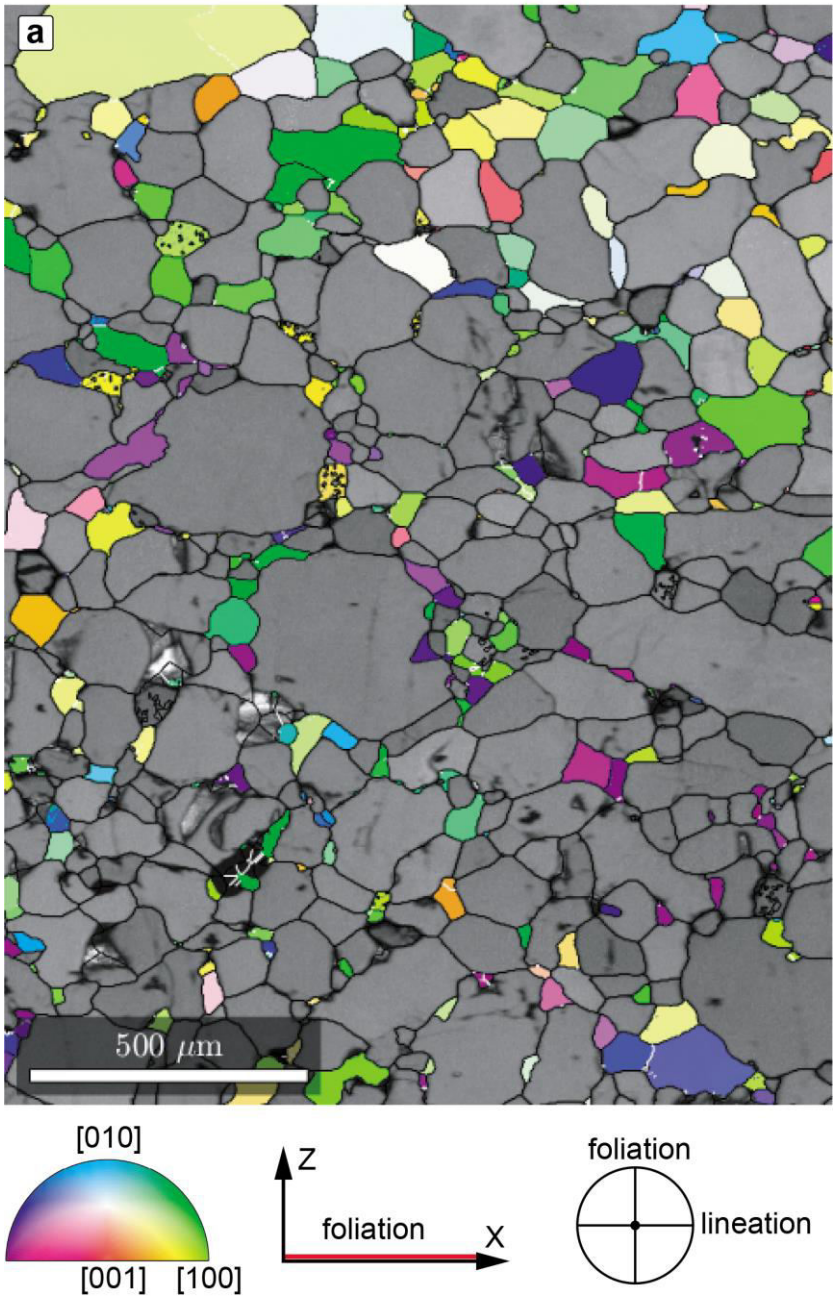

(continued)

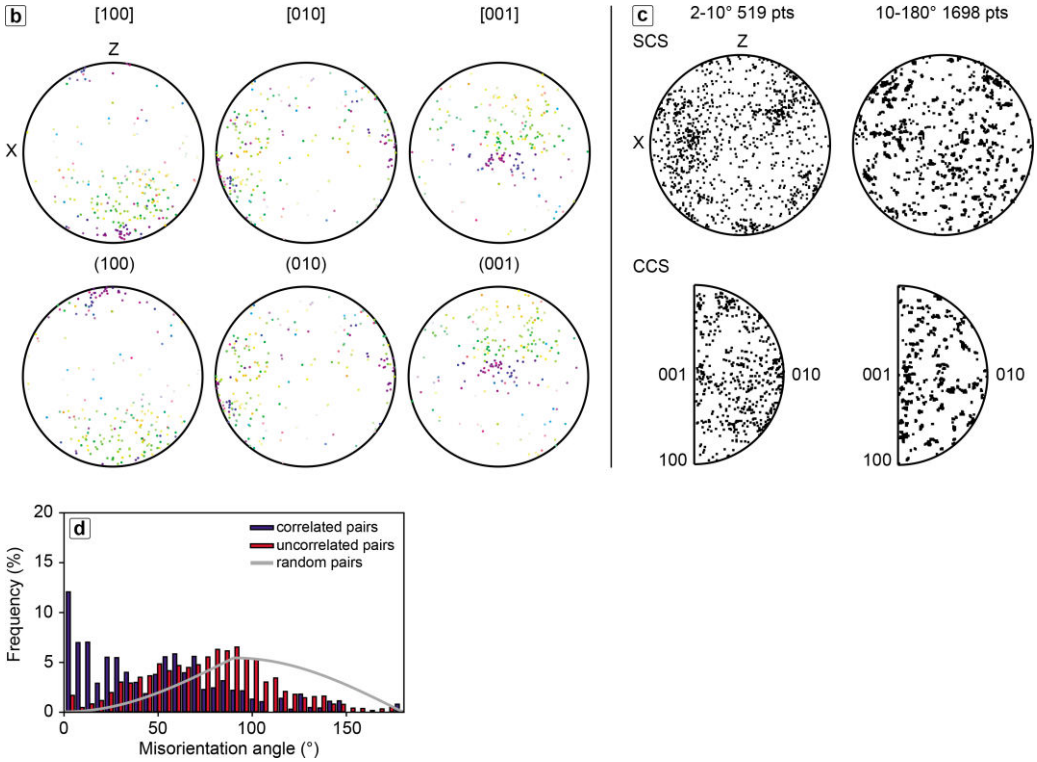

Fig. 61 EBSD map and crystallographic orientation data of neoblastic amphibole in garnet clinopyroxenite of Ulten Zone (UT23). (a) EBSD-derived inverse pole figure map with respect to X sample direction. Grain boundaries are coloured in black. Subgrain boundaries are coloured in white. (b) Pole figures of amphibole (OPPG). (c) Misorientation axis distributions for amphibole in SCS (upper row) and CCS (lower row). (d) Misorientation angle distribution for amphibole.

7.2 Discussion

7.2.1 Crystal plasticity versus fracturing in olivine of garnet peridotites from Monte Duria

Olivine porphyroclasts in the Mt. Duria garnet peridotites record plastic deformation via dislocation creep as indicated by undulatory extinction, deformation bands and the presence of subgrains (Figs. 15c, 43a). Few olivine porphyroclasts also show a clear CPO with the [100] axes oriented subparallel to the lineation and the (010) planes oriented subparallel to the foliation. This CPO is consistent with the A-type slip system of olivine which is suggested to be active in the dislocation creep regime at high temperature (> 1000 °C), low-stress regime and variable water contents (Carter and Ave'Lallemant, 1970; Jung et al., 2006; Jung and Karato, 2001; Ohuchi and Irifune, 2013). The (010) [100] is the most common activated slip system for olivine in the upper mantle (Drury et al., 2011; Hidas et al., 2019; Ismail and Mainprice, 1998; Kaczmarek et al., 2015; Matysiak and Trepmann, 2012; Michibayashi et al., 2006; Michibayashi and Mainprice, 2004; Skemer et al., 2008) and, along with the (010) [001] B-type and (001) [100] E-type, is also the easiest slip system documented to be active at subduction zones ambient conditions (Kaczmarek et al., 2015 and reference therein).

The local subgrains development in olivine porphyroclasts is documented in Figure 43a, where few low-angle boundaries define polygonal regions with a homogeneous grain size (250-300 μm) of the recrystallised olivine. Random CPO and the lack of any internal distortion (Fig. 44b, d) suggests that olivine, after an initial stage of dynamic recrystallisation, records deformation by grain-size sensitive (GSS) creep which promotes the complete obliteration of the pre-existing CPO. The reduction of the grain size by dynamic recrystallization may had promoted the transition from dislocation creep to GSS creep (Twiss, 1976; Rutter and Brodie, 1988; de Bresser et al., 1998, 2001) which results in the progressive weakening of the material and disruption of the pre-existing CPO (Karato et al., 1995; Fliervoet et al., 1999; Warren and Hirth, 2006). Similar processes have been documented in mantle xenoliths from the Jagersfontein kimberlite Skemer et al., (2008) who observed a gradual weakening of minerals fabric moving away from porphyroclasts towards more recrystallised domains. In the Mt. Duria garnet peridotites, despite the local presence of substructures in olivine porphyroclasts, the adjacent recrystallised grains are highly misoriented and display a random CPO (subset 1 in Fig. 44a, b). This indicates that crystallographic orientation of recrystallised olivine is not controlled by

porphyroclasts CPO, contrary to what expected by olivine recording transition from dislocation to diffusion creep. All together, these observations suggest that probably fine-grained olivine nucleates and grows from fractured fragments (e.g. Menegon et al., 2013; Stünitz et al., 2003; Trepmann et al., 2007). The misorientation angle distribution for correlated pairs of olivine lend further support to this interpretation, since it follows the random theoretical distribution (Fig. 44e).

7.2.2 GSS creep in olivine of garnet + amphibole peridotites from Ulten Zone

Recrystallised olivine grains show a random CPO indicating that GSS creep was the dominant deformation mechanism. Despite the absence of a CPO the recrystallised olivine crystals display a strong SPO (Fig. 45a, b). Similar features in supra-subduction peridotites have been described by Prigent et al., (2018) who observed in mylonites and ultramylonites of Semail ophiolite (Oman, Turkey) contrasting CPO and SPO in olivine recording dynamic recrystallisation during GSS-driven deformation.

7.2.3 Subgrain rotation recrystallisation in pyroxene porphyroclasts of garnet clinopyroxenites from Ulten Zone

Porphyroclastic clinopyroxene in garnet clinopyroxenites from the Ulten Zone is interpreted to deform by dislocation creep as evidenced by the undulatory extinction and the high density of subgrains (Fig. 46a). Clinopyroxene displays a strong CPO with the [010] axes oriented subparallel to the lineation and the (100) planes oriented subparallel to the foliation (Fig. 46b) indicating dislocation glide on the (100) [010] slip system. This is further supported by the low-angle misorientation angle distribution in crystal coordinates, that it shows a clear clustering close to the [001] axis (Fig. 46c). The easiest slip systems in clinopyroxene are the (100) [010], along with (100) [001] and (010) [100] (Doukhan et al., 1986; Van Duysen and Doukhan, 1984). TEM observations on experimentally deformed diopside crystal indicate that the above slip systems are activated as a function of temperature with the three slip systems active at low temperature and/or high strain rates (Doukhan et al., 1986; Van Duysen and Doukhan, 1984). The (100) [001] and (010) [100] slip systems have been frequently reported in naturally deformed clinopyroxene (e.g. Brenker et al., 2002; Frets et al., 2012; Godard et al., 1995), whereas only one case for the (100) [010] slip system has been reported in literature. This slip system has been observed by Skrotzki (1994) in deformed augite from a websterite dyke intruding

spinel peridotites of the Balmuccia massif (Ivrea-Verbano Zone, NW Italy). Porphyroclastic augite shows here significant internal deformation together with exsolution of enstatite, amphibole and pigeonite lamellae. The plastic deformation is testified by undulose extinction and bending of the exsolution lamellae. Deformation of websterite dykes have been supposed to occur at 650°C and 0.3 GPa (Skrotzki, 1994) with the exsolution of enstatite lamellae supposed to be syn-tectonic (Skrotzki et al., 1991).

Orthopyroxene porphyroclasts have a CPO identical to that of porphyroclastic clinopyroxene showing the [010] axes nearly parallel to the lineation and the (100) planes oriented subparallel to the foliation (Fig. 50b and 55b). Similarly to clinopyroxene, the CPO and the low-angle misorientation axes distribution of orthopyroxene indicate the activation of the (100) [010] glide system (Figs. 50c, 55c). The (100) [010], along with (100) [001] and (010) [001], is the easiest slip system in orthopyroxene at temperature around 800 °C (Nazè et al., 1987; Passchier and Trouw, 2005; Raimbourg et al., 2008; Skrotzki et al., 1990; 1994; Van Duysen et al., 1985). Deformation of orthopyroxene by dislocation creep is also indicated by the widespread undulatory extinction, crystal bending, presence of subgrains and "core-and-mantle" microstructures, in which the central core of the porphyroclast grades outward into subgrains and newly recrystallized small and equant grains lacking internal deformation. The development of subgrains in orthopyroxene is documented in Figure 50a, where the occurrence of low-angle boundaries is mostly restricted close to the rim of the porphyroclast. The newly recrystallised grains in the proximity of the porphyroclast display a grain-size similar to the size of subgrains and a CPO strongly controlled by the hosting porphyroclast (c.f. Fig.50b and Fig. 51b). These observations clearly indicate that orthopyroxene initially deforms by dislocation creep and later by subgrain rotation recrystallization.

7.2.4 GSS creep in the polyphase recrystallised matrix of garnet clinopyroxenites from Ulten Zone

The mineralogical phases in the recrystallised matrix in the Ulten Zone garnet clinopyroxenites are interpreted to deform by GSS creep as indicated by the small grain size (< 500 μm) and the absence of intracrystalline distortion. Both recrystallised clino- and orthopyroxene display a weak CPO, very similar to that of the parent porphyroclasts and a correlated-pair misorientation angle distribution which deviates from the theoretical random curve at low angle misorientations (Fig. 58, 59). This indicate that the CPO of the neoblasts is inherited and the deformation subsequent to recrystallisation was accommodated

by GSS creep. Similar processes in websterites recording spinel- to plagioclase-facies transition during deformation in the Ronda Massif have been reported by Hidas et al., (2013) who demonstrated that ortho- and clinopyroxene, after an initial stage of dynamic recrystallization, deformed by a GSS mechanism that randomized the pre-existing CPO.

Garnet does not display any clear CPO but the misorientation angle distribution of correlated pairs slightly deviates from the random theoretical curve likely because of the presence of few low-angle boundaries (Fig. 60e). Misorientation analyses highlight that misorientations are sharp and that subgrains are slightly misoriented with respect to each other, likely suggesting garnet fracturing (Fig. 60b).

Fine-grained amphibole in the recrystallised matrix displays similar features of neoblastic ortho- and clinopyroxene (c.f. Fig. 58, 59 and Fig. 61) indicating that amphibole growth is crystallographic controlled by porphyroclasts during GSS creep.

The above discussed evidence suggest that the recrystallised matrix deforms primarily by GSS creep. Phase mixing in a fine-grained aggregate plays a key role on GSS creep mechanism. The pinning of second phases, in this case garnet and amphibole, prevents grain growth of ortho- and clinopyroxene and stabilizes the fine aggregate microstructure, resulting in a bulk weakening of the rock (Evans et al., 2001).

7.2.5 Evidence of dislocation creep in exsolved phases within ortho- and clinopyroxene in the garnet clinopyroxenites from Ulten Zone

The exsolutions of pyroxenes and amphibole in ortho- and clinopyroxene porphyroclasts are interpreted to deform by dislocation creep. They all display the (100) planes parallel to the (100) planes of host ortho- and clinopyroxene, which is in turn parallel to the foliation, and the [010] axes nearly parallel to the lineation direction (Figs. 48, 49, 53, 54). This indicates that exsolutions deform by dislocation creep concomitantly with the deformation in host pyroxene porphyroclasts.

Garnet exsolutions show the (110) planes nearly parallel to the (100) planes of host pyroxene porphyroclasts. In Figure 57 garnet exsolutions in orthopyroxene are strongly bent. Misorientation analyses on profiles parallel to the long axis of garnet exsolutions (profile AA’ in Fig. 57) highlight a distortion of the crystalline lattice as large as 18° accommodated by rotation dominantly around <111> and <110>. Moreover, the misorientation angle distribution of correlated pairs deviates from the random theoretical distribution at low-angle

misorientation. These features are similar to those interpreted as evidence for dislocation creep in almandine-rich garnets of eclogites from HP/UHP metamorphic terranes (Bascou et al., 2001; Chen et al., 1996; Main price et al., 2004).) and pyrope-rich garnets of HP mantle rocks (e.g. websterites from Beni Bousera peridotite massif; Frets et al., 2012).On these basis we can conclude that similarly to exsolved amphibole, ortho- and clinopyroxene, also garnet exsolutions deform by dislocation creep during the deformation of the host porphyroclasts.

Microstructural observations highlight that garnet exsolution lamellae within ortho- and clinopyroxene are parallel to garnet foliation in the pyroxenite (Fig. 20e). This suggests that exsolution process is syn-tectonic and occurs concomitantly with the development of garnet foliation in the clinopyroxenite and surrounding peridotite.

Chapter 8

Extended conclusions

Pyroxenites are important constituents of the upper mantle and represent key lithologies for mantle deformation since mantle compositional heterogeneities play a major role in the strain localisation and softening (e.g. Toy et al., 2010; Treagus & Sokoutis, 1992). The origin of pyroxenites has been related to a variety of magmatic and metamorphic processes, including: i) recycling of crustal material during subduction (Allègre & Turcotte, 1986; Kornprobst et al., 1990; Morishita and Arai, 2001; Morishita et al., 2003; Yu et al., 2010); ii) moderate- to high-pressure crystal segregation from magmas rising from asthenospheric mantle sources (Bodinier et al., 1987a, 1987b; Dantas et al., 2007; Gysi et al., 2011; Kempton & Stephens, 1997; Keshav et al., 2007; Mukasa & Shervais, 1999; Rivalenti et al., 1995; Takazawa et al., 1999; Vannucci et al., 1993; Warren et al., 2009); iii) refertilisation of 'depleted' upper mantle trough melt-peridotite reactions during asthenospheric upwelling (Bodinier et al., 2008; Dantas et al., 2009; Garrido & Bodinier, 1999; Van Acken et al., 2010); and iv) reaction between peridotites and melts derived by high-pressure melting of the subducted crust (Malaspina et al., 2006; Wang et al., 2008).

Clino and orthopyroxenites occur ubiquitously in most of oceanic and orogenic peridotite massifs, such as Lherz in the Pyrenees, Beni Bousera and Ronda in the Betic-Rif belt, Lanzo, Erro-Tobbio and Ulten Zone in the Alps (Bodinier et al., 2008; Dickey, 1970; Garrido and Bodinier, 1999; Gysi et al., 2011; Kornprobst, 1969, 1970; Morten and Obata, 1983; Rampone and Borghini, 2008). Concerning our study locations, pyroxenites occurring in the Ulten Zone are an example of crystal segregation from a basaltic melt rising from the deeper portions of the mantle wedge (Nimis and Morten, 2000). These pyroxenites record a mineral phase transformation from coarse spinel websterites to fine-grained garnet clinopyroxenites (Morten and Obata, 1983; Nimis and Morten, 2000). Host peridotites record a similar evolution from

coarse protogranular spinel-lherzolites to fine-grained mylonitic garnet-amphibole peridotites (Obata and Morten, 1987). This coupled evolution has been interpreted to reflect pressure increase and cooling of pyroxenites and host peridotites from spinel- (1200 °C, 1.3-1.6 Gpa) to garnet-facies (850 °C and 2.8 Gpa) conditions induced by mantle corner flow (Nimis and Morten, 2000). As a consequence, garnet exsolved from porphyroclastic, high-T pyroxenes, and crystallised along the pyroxenite foliation during deformation.

Textural evidences (Fig. 20; chapter 4) and crystallographic orientation data (Figs. from 46 to 57; chapter 7) indicate that the transition from spinel- to garnet-facies conditions was assisted by intense shearing and deformation. Pyroxene porphyroclasts in garnet clinopyroxenites show well-developed CPOs, high frequencies of low-angle misorientations, and non-random distribution of the low-angle misorientation axes (Figs. 46, 50 55; chapter 7), indicating that pyroxene porphyroclasts deform by dislocation creep. Dislocation creep is also accompanied by subgrain rotation recrystallisation, which promotes the formation of new, smaller and equant pyroxene grains around porphyroclasts. The reduction of the grain size by dynamic recrystallisation induces a switch in the deformation mechanism from grain-size insensitive creep (i.e. dislocation creep) in the porphyroclasts to grain-size sensitive (GSS) creep in the small recrystallised grains (chapter 7). This results in a dramatic rheological weakening of pyroxenites because, GSS creep requires lower differential stresses to deform at a given strain rate compared to dislocation creep. This mechanism promotes a strain localisation and softening of pyroxenites (e.g. Pearce and Wheeler, 2011; Rutter and Brodie, 1988). The switch from dislocation creep to GSS creep is accompanied not only by a sudden decrease of the grain size but also by the formation of garnet exsolutions in pyroxenes and garnet crystallisation along foliation, in response to the spinel to garnet phase transition. Syn-tectonic metamorphic reactions produce garnet that becomes the so-called “second phase” triggering the pinning of the recrystallised matrix. Pinning is the mechanism the prevent grain growth of ortho and clinopyroxene, therefore stabilising the fine-grained microtexture for GSS creep process and significantly contributing to the weakening and strain localisation of pyroxenites (Herwegh et al., 2011; Evans et al., 2001).

The schematic illustration of Figure 62 reports a conceptual model for strain localisation and weakening of pyroxenites during shearing and deformation induced by mantle corner flow. At high-temperature and low-pressure (1 in Fig. 62), spinel lherzolites are intruded by melts rising from deeper portions of the wedge (black arrows in Fig. 62), leading the formation of

coarse spinel websterites (Nimis and Morten, 2000). Mantle convection (dashed grey bold lines in Fig. 62) induced by the subducting plate causes the movement of pyroxenites and host peridotites to greater depth close to the slab-mantle interface (2; black bold line in Fig. 62). Cooling and pressure increase promote the formation of garnet as exsolutions in porphyroclastic pyroxenes and along the pyroxenite foliation. At this stage, pyroxene porphyroclasts record crystal plasticity by dislocation creep, accompanied by syn-kinematic subgrain rotation recrystallisation (Fig. 62b). This produces a sudden reduction of the grain size triggering a transition in deformation mechanism from dislocation creep to GSS creep. The activation of the GSS creep induces a strong rheological weakening of pyroxenites creating favourable conditions for the incorporation of pyroxenites and host peridotites into the subducting crust.

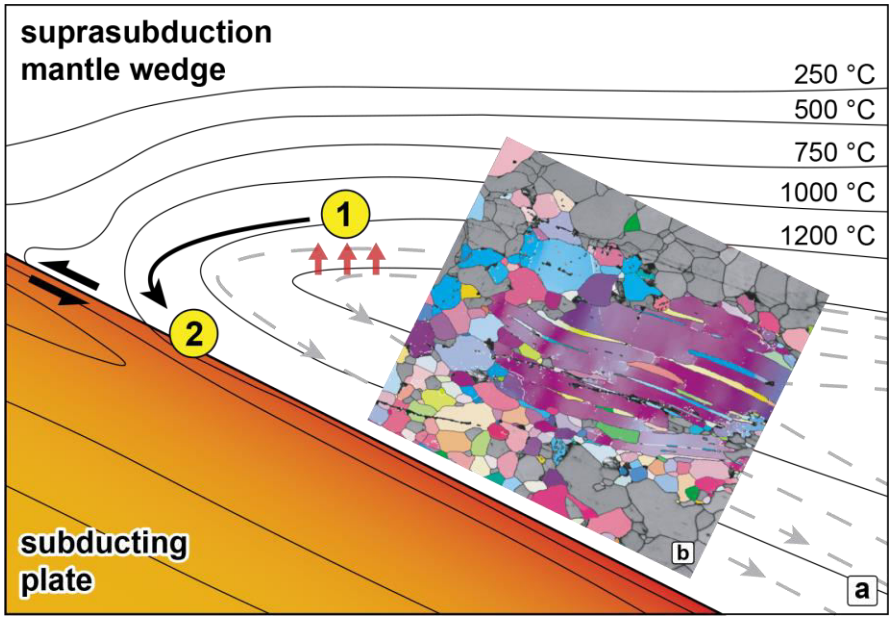

Fig. 62 Conceptual model for mantle weakening induced by corner flow (not to scale). See text for explanation. Model thermal configuration after Honda (1985). *Red lines:* rising melts. *Black bold line:* path of peridotites and pyroxenites. *Dashed grey lines:* .mantle corner flow.

Pyroxenites can also represent metasomatic products of reaction between mantle and infiltrating melts, which may be derived by melting of the subducted crust. Field-based, petrological and geochemical studies have described the interaction between peridotites and felsic continental crust via melts and supercritical liquids released at HP and UHP conditions. They all

have documented the formation of orthopyroxenite bands by reaction between peridotites and silica-saturated liquids, which dissolve olivine and precipitate new orthopyroxene (e.g. Malaspina et al., 2006; Wang et al., 2008). On the other hand, the direct interaction between peridotites and eclogite-derived melts at HP has never been clearly observed in nature. The interaction between mantle and eclogite-derived melts at high pressure was experimentally studied by Wang et al. (2016) at 1 GPa and 1200 °C and Perchuk et al. (2018) at 2.9 GPa and 750-900 °C. In these studies the reaction with mafic melts produces harzburgite and then orthopyroxenite layers. Interestingly, experiments performed at P-T conditions closed to the peak recorded by eclogites and garnet peridotites of Monte Duria (3 GPa and 750 °C) show reaction zones at the eclogite-peridotite interface with formation of orthopyroxene ± magnesite ± garnet and layers of newly-formed omphacite ± garnet ± phlogopite + orthopyroxene + magnesite by focused flow (Perchuk et al., 2018). Similar mineral associations occur at the contact between Borgo peridotite and inner tremolitite layers (Fig. 16c, d) along with the modelled mineral assemblage of tremolitites before the later hydration (Fig. 42; chapter 6).

The interaction between mafic melts and peridotite in a deformation regime (i.e. during the formation of extensional shear zones) has been widely studied in natural case studies, and experimentally and theoretically modelled, in lithospheric and sub-oceanic mantle (e.g. Garrido and Bodinier, 1999; Gysi et al., 2011; Liu, 2005; Zanetti et al., 1999; Borghini et al. 2016; Liang et al., 2010; Baltzell et al. 2015). Regardless of the composition of the melts, experiments and numerical modelling evidenced the role of shear rates in the "compaction-decompaction" porosity bands in the peridotite, favouring melt migration and solubility gradients at increasing deformation (Liang et al., 2010; Baltzell et al. 2015). Following a similar mechanism, the development of alternating pyroxenite (l.s.) bands in the peridotite of Borgo (Fig. 2, 8, 9 and 10) may have been favoured by melt-peridotite interaction during shearing. This interpretation is reported in Figure 63, which portrays a conceptual model of the interaction of eclogite-derived melt and overlying peridotite during the shearing induced by slab subduction and/or mantle corner flow. Evidence of sin-deformation melt-rock interaction is given by the occurrence of boudinage of our metasomatic layers, parallel to and wrapped by the garnet foliation of the host peridotite, indicating a shearing induced weakening of the garnet peridotite. Such mechanism has been reported by a recent work of Tommasi et al. (2017), who demonstrated that the occurrence of hydrous melts during shearing strongly changes the deformation processes in mantle peridotites. Following these authors (Tommasi et al., 2017), accomodation of deformation

by peridotite results from stress-controlled dissolution and precipitation and advective transport of chemical components by the melts. Moreover, the presence of hydrous melts also favours fast grain boundary migration producing a strong rheological weakening of the garnet peridotite. The focussed flow of slab melts into the mantle, instead of porous flow, may therefore occur when the overlying mantle peridotite undergoes shearing and weakening.

In conclusion, the Monte Duria area is a unique case study where we can observe eclogite-derived melts interacting with garnet peridotites at HP. The interaction between peridotites and eclogite-derived melts promotes the formation of websterites. Development of websterites, and clinopyroxenites in general, results in the formation of compositional and rheological anisotropies where deformation can be localised. Strain localisation and weakening can also occur when such anisotropies are already present in the mantle, as observed in the case of pyroxenites of Ulten zone which accommodate most of deformation during shearing and mineral phase transformations induced by mantle corner flow. In both cases strain softening of the mantle tends to reduce the rheological contrast between the subducted crust and the overlying mantle creating favourable condition for the emplacement of peridotites into the slab.

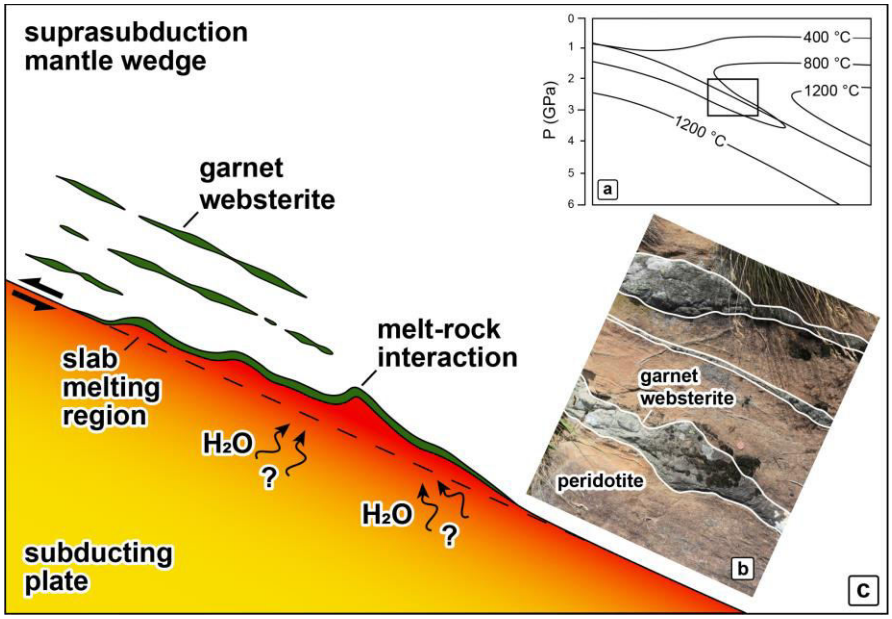

Fig. 63 Conceptual model for garnet websterite formation at the slab-mantle interface in a deformation regime during subduction (not to scale). See text for explanation. Isotherms in the inset are relative to warm subduction environments (Peacock and Wang, 1999).

References

Agard, P., Yamato, P., Soret, M., Prigent, C., Guillot, S., Plunder, A., Dubacq, B., Chauvet, A. & Monié, P. (2016). Plate interface rheological switches during subduction infancy: Control on slab penetration and metamorphic sole formation. Earth and Planetary Science Letters. Elsevier B.V. 451, 208–220.

Allègre, C. J. & Turcotte, D. L. (1986). Implications of a two-component marble-cake mantle. Nature 323, 123–127.

Andreatta, C. (1948). La" linea di Peio" nel massiccio dell'Ortler e le sue miloniti. Società tip. Mareggiani.

Arai, S., Shimizu, Y., Gervilla, F., 2003. Quartz diorite veins in a peridotite xenolith from Tallante, Spain: implications for reaction and survival of slab-derived SiO2- oversaturated melt in the upper mantle. Proceedings of the Japan Academy, Series B, 79, 146-150.

Arcay, D., Tric, E., Doin, M.P., 2007. Slab surface temperature in subduction zones: Influence of the interplate decoupling depth and upper plate thinning processes. Earth Planet. Sci. Lett. 255, 324-338

Bachmann, F., Hielscher, R., & Schaeben, H. (2010). Texture analysis with MTEX-free and open source software toolbox. In Solid State Phenomena (Vol. 160, pp. 63-68). Trans Tech Publications.

Baltzell, C., Parementier, E.M., Liang, Y., Tirupathi, S., 2015. Geochemistry, Geophysics, Geosystems. Geochem. Geophys. Geosyst. 18, 1541-1576.

Bargossi, G., Bove, G., Cucato, M., Gregnanin, A., Morelli, C., Moretti, A., & Zanchi, A. (2010). Note Illustrative della carta Geologica d'Italia in scala 1: 50.000, foglio 013" Merano".

Bascou, J., Tommasi, A. & Mainprice, D. (2002). Plastic deformation and development of clinopyroxene lattice preferred orientations in eclogites. Journal of Structural Geology 24, 1357–1368.

Becker, H. (1993). Garnet peridotite and eclogite Sm-Nd mineral ages from the Lepontine dome (Swiss Alps): new evidence for Eocene high-pressure metamorphism in the central Alps. Geology 21, 599–602.

Benciolini, N., & Poli, S. (1993). The lower continental crust in the Tonale nappe (Upper Austroalpine, Ultental): new petrological constraints. Terra Nova, 5(1), 98.

Berger, A. & Bousquet, R. (2008). Subduction-related metamorphism in the Alps: review of isotopic ages based on petrology and their geodynamic consequences. Geological Society, London, Special Publications 298, 117–144.

Biino, G.G., Marquer, D., Nussbaum, C., 1997. Alpine and pre-Alpine subduction events in polycyclic basements of the Swiss Alps. Geology 25, 751.

Bodinier, J. L., Fabriès, J., Lorand, J. P., Dostal, J., & Dupuy, C. (1987). Geochemistry of amphibole pyroxenite veins from the Lherz and Freychinede ultramafic bodies (Ariege, French Pyrenees). Bulletin de minéralogie, 110(4), 345-358.

Bodinier, J.-L., Garrido, C. J., Chanefo, I., Bruguier, O. & Gervilla, F. (2008). Origin of pyroxenite-peridotite veined mantle by refertilisation reactions: Evidence from the Ronda peridotite (Southern Spain). Journal of Petrology 49, 999-1025.

Bodinier, J.-L., Guiraud, M., Fabries, J., Dostal, J. & Dupuy, C. (1987b). Petrogenesis of layered pyroxenites from the Lherz, Freychinede and Prades ultramafic bodies (Ariege, French Pyrenees). Geochimica et Cosmochimica Acta 51, 279-290.

Borghini, A., Ferrero, S., Wunder, B., Laurent, O., Brien, P.J.O., Ziemann, M.A., 2018. Granitoid melt inclusions in orogenic peridotite and the origin of garnet clinopyroxenite. Geology 46, 1-4.

Bozhilov, K. N., Green, H. W. & Dobrzhinetskaya, L. (1999). Clinoenstatite in Alpe Arami peridotite: Additional evidence of very high pressure. Science 284, 128–132.

Brace, W. F. & Kohlstedt, D. L. (1980). Limits on lithospheric stress imposed by laboratory experiments. Journal of Geophysical Research: Solid Earth 85, 6248–6252.

Brenker, F. E., Prior, D. J. & Müller, W. F. (2002). Cation ordering in omphacite and effect on deformation mechanism and lattice preferred orientation (LPO). Journal of Structural Geology 24, 1991–2005.

Brenker, F.E., Brey, G.P., 1997. Reconstruction of the exhumation path of the Alpe Arami garnet-peridotite body from depths exceeding 160 km. J. Metamorph. Geol., 15(5), 581-592.

Brodie, K. H. (1980). Variations in mineral chemistry across a phlogopite shear zone. Journal of Structural Geology 2, 265–272.

Brouwer, F. M., Burri, T., Engi, M. & Berger, a (2005). Eclogite relics in the Central Alps: PT-evolution, Lu-Hf ages and implications for formation of tectonic melange zones. Schweizerische Mineralogische Und Petrographische Mitteilungen 85, 147–174.

Brueckner, H.K., Medaris, G., 2000. A general model for the intrusion and evolution of 'mantle' garnet peridotites in high-pressure and ultra-high-pressure metamorphic terranes. J. Metamorph. Geol. 18, 123-133.

Brueckner, J. K. (1998). Testing for strategic interaction among local governments: The case of growth controls. Journal of urban economics, 44(3), 438-467.

Burri, T., Berger, A., Engi, M., 2005. Tertiary migmatites in the Central Alps: regional distribution, field relations, conditions of formation, and tectonic implication. Schweiz. Mineral. Petrogr. Mitt. 85, 215-232.

Bystricky, M. & Mackwell, S. (2001). Creep of dry clinopyroxene aggregates. Journal of Geophysical Research 106, 13443.

Campione M, Tumiati S, Malaspina N, 2017. Primary spinel + chlorite inclusions in mantle garnet formed at ultrahigh-pressure. Geochemical Perspective Letters 4, 19-23.

Carter, N. L., & Ave'Lallemant, H. G. (1970). High temperature flow of dunite and peridotite. Geological Society of America Bulletin, 81(8), 2181-2202.

Chen, J., Wang, Q.C., Zhai, M.G., Ye, K., 1996. Plastic deformation of garnet in eclogite. Science China Series D 39 (1), 18-25

Ciancaleoni, L. & Marquer, D. (2006). Syn-extension leucogranite deformation during convergence in the Eastern Central Alps: Example of the Novate intrusion. Terra Nova 18, 170–180.

Connolly, J.A.D., 2005. Computation of phase equilibria by linear programming: A tool for geodynamic modelling and its application to subduction zone decarbonation. Earth Planet. Sci. Lett. 236, 524–541.

Dal Piaz G.V. (1993) - Evolution of Austro-Alpine and Upper Penninic basement in the northwestern Alps from Variscan convergence to post-Variscan extension. In Von Raumer J. & Neubauer F. (Eds): Pre-Mesozoic geology in the Alps. Springer-Verlag, 327-344

Dale, J., Holland, T. J. B., Powell, R., 2000. Hornblende–garnet–plagioclase thermobarometry: a nat- ural assemblage calibration of the thermodynamics of horn- blende. Contrib. Mineral. Petrol. 140, 353–362.

Dale, J., Holland, T.J.B., 2003. Geothermobarometry, P-T paths and metamorphic field gradients of high-pressure rocks from the Adula nappe, Central Alps. J. Metamorph. Geol. 21, 813-829.

Dantas, C., Ceuleneer, G., Gregoire, M., Python, M., Freydier, R., Warren, J., & Dick, H. J. B. (2007). Pyroxenites from the Southwest Indian Ridge, 9-16 E: cumulates from incremental melt fractions produced at the top of a cold melting regime. Journal of Petrology, 48(4), 647-660.

Dantas, C., Gregoire, M., Koester, E., Conceicao, R. D. & Rieck, N., Jr (2009). The lherzolite-websterite xenolith suite from Northern Patagonia (Argentina): evidence of mantle-melt reaction processes. Lithos 107, 107-120.

Davidson, C., Rosenberg, C. & Schmid, S. M. (1996). Synmagmatic folding of the base of the Bergell pluton, Central Alps. Tectonophysics 265, 213–238.

De Bresser, J. H. P., Ter Heege, J. H. & Spiers, C. J. (2001). Grain size reduction by dynamic recrystallization: Can it result in major rheological weakening? International Journal of Earth Sciences 90, 28–45.

Degli Alessandrini G, Menegon L, Malaspina N, Dijkstra A, Anderson M, 2017. Creep of mafic dykes infiltrated by melt in the lower continental crust (Seiland Igneous Province, Norway). Lithos 274-275, 169-187.

Del Moro, A., Martin, S., & Prosser, G. (1999). Migmatites of the Ulten Zone (NE Italy), a record of melt transfer in deep crust. J. Petrol., 40(12), 1803-1826.

Dickey, J. S. (1970). Partial fusion products in Alpine peridotites: Serrania De La Ronda and other examples. Mineralogical Society of America Special Paper, 3, 33-49.

Dobrzhinetskaya, L., Green, H. W. & Wang, S. (1996). Alpe Arami: A peridotite massif from depths of more than 300 kilometers. Science 271, 1841–1845.

Doukhan, J. C., Doukhan, N., Nazé, L., & Duysen, V. (1986). Défauts de réseau et plasticité cristalline dans les pyroxènes: Une revue. Bulletin de minéralogie, 109(4), 377-394.

Drummond, M.S., Defant, M.J., Kepezhinskas, P.K., 1996. Petrogenesis of slab-derived trondhjemite-tonalite-dacite / adakite magmas. Trans. R. Soc. Edinb. Earth Sci. 87, 205-215.

Drury, M. R., Avé Lallemant, H. G., Pennock, G. M. & Palasse, L. N. (2011). Crystal preferred orientation in peridotite ultramylonites deformed by grain size sensitive creep, étang de Lers, Pyrenees, France. Journal of Structural Geology. Elsevier Ltd 33, 1776–1789.

Eberli, G. P. (1988). The evolution of the southern continental margin of the Jurassic Tethys Ocen as recorded in the Allgäu Formation of the Austroalpine Nappes of Graubünden (Switzerland). Eclogae Geologicae Helvetiae, 81(1), 175-214.

Endo, S., Mizukami, T., Wallis, S.R., Tamura, A., Arai, S., 2015. Orthopyroxene-rich Rocks from the Sanbagawa Belt (SW Japan): Fluid-Rock Interaction in the Forearc Slab-Mantle Wedge Interface. J. Petrol. 56, 1113-1137.

Engi M., R. G. T. (2001). Role of the tectonic accretion channel in collisional orogeny. Geology 29, 1143–1146.

Ernst, W. G. (1978). Petrochemical study of lherzolitic rocks from the Western Alps. J. Petrol., 19(3), 341-392.

Ernst, W. G. (1981). Petrogenesis of eclogites and peridotites from the western and Ligurian Alps. American Mineralogist 66, 443–472.

Evans, B., Renner, J. & Hirth, G. (2001). A few remarks on the kinetics of static grain growth in rocks. International Journal of Earth Sciences 90, 88–103.

Evans, B.W., Trommsdorff, V., 1978. Petrogenesis of garnet lherzolite, Cima di Gagnone, Lepontine Alps. Earth Planet. Sci. Lett. 40, 333-348.

Fliervoet, T. F., Drury, M. R. & Chopra, P. N. (1999). Crystallographic preferred orientations and misorientations in some olivine rocks deformed by diffusion or dislocation creep. Tectonophysics 303, 1–27.

Frets, E., Tommasi, A., Garrido, C. J., Padrón-Navarta, J. A., Amri, I. & Targuisti, K. (2012). Deformation processes and rheology of pyroxenites under lithospheric mantle conditions. Journal of Structural Geology. Elsevier Ltd 39, 138–157.

Fumagalli, P., Poli, S., 2005. Experimentally Determined Phase Relations in Hydrous Peridotites to 6.5 GPa and their Consequences on the Dynamics of Subduction Zones. J. Petrol. 46, 555-578.

Fumasoli, M.W., 1974. Geologie des Gebietes nördlich und südlich der Jorio-Tonale-Linie im Westen von Gravedone (Como, Italia). Dissertation, Universität Zürich.

Furusho, M. & Kanagawa, K. (1999). Transformation-induced strain localization in a lherzolite mylonite from the Hidaka metamorphic belt of central Hokkaido, Japan. Tectonophysics 313, 411–432.

Galli, A., Le Bayon, B., Schmidt, M.W., Burg, J.P., Caddick, M.J., Reusser, E., 2011. Granulites and charnockites of the Gruf Complex: Evidence for Permian ultra-high temperature metamorphism in the Central Alps. Lithos 124, 17-45.

Galster, F., Cavargna-Sani, M., Epard, J., Masson, H., 2012. New stratigraphic data from the Lower Penninic between the Adula nappe and the Gotthard massif and consequences for the tectonics and the paleogeography of the Central Alps. Tectonophysics 579, 37-55.

Garrido C J. & Bodinier J L (1999). Diversity of Mafic Rocks in the Ronda Peridotite: Evidence for Pervasive Melt–Rock Reaction during Heating of Subcontinental Lithosphere by Upwelling Asthenosphere. Journal of Petrology 40, 729–754.

Gebauer, D. (1996). A P-T-t Path for an (Ultra?-) High-pressure Ultramafic/Mafic Rock-Association and its Felsic Country-Rocks Based on SHRIMP-Dating of Magmatic and Metamorphic Zircon Domains. Example: Alpe Arami (Central Swiss Alps). Geophysical Monograph Series 95, 307–329.

Gillis, K.M., Snow, J.E., Klaus, A., Abe, N., Adrião, Á.B., Akizawa, N., Ceuleneer, G., Cheadle, M.J., Faak, K., Falloon, T.J., Friedman, S.A., Godard, M., Guerin, G., Harigane, Y., Horst, A.J., Hoshide, T., Ildefonse, B., Jean, M.M., John, B.E., Koepke, J., MacHi, S., Maeda, J., Marks, N.E., McCaig, A.M., Meyer, R., Morris, A., Nozaka, T., Python, M., Saha, A., Wintsch, R.P., 2014. Primitive layered gabbros from fast-spreading lower oceanic crust. Nature 505, 204-207.

Godard, G. & van Roermund, H. L. M. (1995). Deformation-induced clinopyroxene fabrics from eclogites. Journal of Structural Geology 17, 1425–1443.

Godard, G., & Martin, S. (2000). Petrogenesis of kelyphites in garnet peridotites: a case study from the Ulten zone, Italian Alps. Journal of Geodynamics, 30(1-2), 117-145.

Godard, G., Martin, S., Prosser, G., Kienast, J. R. & Morten, L. (1996). Variscan migmatites, eclogites and garnet-peridotites of the Ulten zone, Eastern Austroalpine system. Tectonophysics 259, 313–341.

Goetze, C. & Evans, B. (1979). Stress and temperature in the bending lithosphere as constrained by experimental rock mechanics. Geophysical Journal of the Royal Astronomical Society 59, 463–478.

Green, H. W., Dobrzhinetskaya, L. F., & Bozhilov, K. N. (2010). The Alpe Arami story: Triumph of data over prejudice. Journal of Earth Science, 21(5), 731-743.

Gudelius, D., Aulbach, S., Braga, R., Ho, H.E., Woodland, A.B., Gerdes, A., 2019. Element Transfer and Redox Conditions in Continental Subduction Zones : New Insights from Peridotites of the Ulten Zone , North Italy. J. Petrol. 60, 231-268.

Gysi, A. P., Jagoutz, O., Schmidt, M. & Targuisti, K. (2011). Petrogenesis of pyroxenites and melt infiltrations in the ultramafic complex of Beni Bousera, northern Morocco. Journal of Petrology 52, 1679–1735.

Hauzenberger, C. A., Höller, W., & Hoinkes, G. (1996). Transition from eclogite to amphibolite-facies metamorphism in the Austroalpine Ulten Zone. Mineralogy and Petrology, 58(3-4), 111-130.

Heinrich, C.A., 1986. Eclogite facies regional metamorphism of hydrous mafic rocks in the Central Alpine Adula nappe. J. Petrol. 27, 123-154.

Heitzmann, P. (1987). Calcite mylonites in the Central Alpine "root zone." Tectonophysics 135, 207–215.

Hermann, J., Rubatto, D., Trommsdorff, V., 2006. Sub-solidus Oligocene zircon formation in garnet peridotite during fast decompression and fluid infiltration (Duria, Central Alps). Mineral. Petrol. 88, 181-206.

Herwartz, D., Nagel, T.J., Münker, C., Scherer, E.E., Froitzheim, N., 2011. Tracing two orogenic cycles in one eclogite sample by Lu-Hf garnet chronometry. Nat. Geosci. 4, 178-183.

Herwegh, M., Linckens, J., Ebert, A., Berger, A., & Brodhag, S. H. (2011). The role of second phases for controlling microstructural evolution in polymineralic rocks: A review. Journal of Structural Geology, 33(12), 1728-1750.

Hidas, K., Garrido, C. J., Booth-Rea, G., Marchesi, C., Bodinier, J. L., Dautria, J. M., Louni-Hacini, A. & Azzouni-Sekkal, A. (2019). Lithosphere tearing along STEP faults and synkinematic formation of lherzolite and wehrlite in the shallow subcontinental mantle. Solid Earth 10, 1099–1121.

Hidas, K., Garrido, C. J., Tommasi, A., Padrón-Navarta, J. A., Thielmann, M., Konc, Z., Frets, E. & Marchesi, C. (2013). Strain localization in pyroxenite by reaction-enhanced softening in the shallow subcontinental lithospheric mantle. Journal of Petrology 54, 1997–2031.

Hielscher, R., & Schaeben, H. (2008). A novel pole figure inversion method: specification of the MTEX algorithm. Journal of Applied Crystallography, 41(6), 1024-1037.

Hirth, G. & Kohlstedt, D. (2003). Rheology of the upper mantle and the mantle wedge: A view from the experimentalists. 83–105.

Hofmann, A. W. (1988). Chemical differentiation of the Earth: the relationship between mantle, continental crust, and oceanic crust. Earth and Planetary Science Letters 90, 297–314.

Hoinkes, G., & Thöni, M. (1993). Evolution of the Ötztal-Stubai, Scarl-Campo and Ulten basement units. In Pre-mesozoic geology in the Alps (pp. 485-494). Springer, Berlin, Heidelberg.

Holland, T.J.B., Powell, R., 1998. An internally consistent thermodynamic data set for phases pf petrological interest. J. Metamorph. Geol. 16, 309–343.

Holland, T., Powell, R., 2003. Activity–composition relations for phases in petrological cal- culations: an asymmetric multicomponent formulation. Contrib. Mineral. Petrol. 145, 492–501.

Honda, S. (1985). Thermal structure beneath Tohoku, northeast Japan. *Tectonophysics*, *112*(1-4), 69-102.

Ismaïl, W. Ben & Mainprice, D. (1998). An olivine fabric database: An overview of upper mantle fabrics and seismic anisotropy. Tectonophysics 296, 145–157.

Jin, D., Karato, S. I. & Obata, M. (1998). Mechanisms of shear localization in the continental lithosphere: Inference from the deformation microstructures of peridotites from the Ivrea zone, northwestern Italy. Journal of Structural Geology 20, 195–209.

Jung, H. & Karato, S. I. (2001). Water-induced fabric transitions in olivine. Science 293, 1460–1463.

Jung, H., Katayama, I., Jiang, Z., Hiraga, T. & Karato, S. (2006). Effect of water and stress on the lattice-preferred orientation of olivine. Tectonophysics 421, 1–22.

Kaczmarek, M. A., & Tommasi, A. (2011). Anatomy of an extensional shear zone in the mantle, Lanzo massif, Italy. Geochemistry, Geophysics, Geosystems, 12(8).

Kaczmarek, M. A., Jonda, L. & Davies, H. L. (2015). Evidence of melting, melt percolation and deformation in a supra-subduction zone (Marum ophiolite complex, Papua New Guinea). Contributions to Mineralogy and Petrology. Springer Berlin Heidelberg 170, 1–23.

Karato, S. I. & Jung, H. (2003). Effects of pressure on high-temperature dislocation creep in olivine. Philosophical Magazine 83, 401–414.

Karato, S., 2008. Deformation of Earth Materials: An Introduction to the Rheology of Solid Earth. Cambridge University Press.

Karato, S., Zhang, S. & Wenk, H. R. (1995). Superplasticity in Earth ' s Lower Mantle : Evidence from Seismic Anisotropy and Rock Physics. Science 270, 458.

Katayama, I. & Karato, S. ichiro (2008). Low-temperature, high-stress deformation of olivine under water-saturated conditions. Physics of the Earth and Planetary Interiors 168, 125–133.

Kempton, P. D. & Stephens, C. J. (1997). Petrology and geo- chemistry of nodular websterites inclusions in harzburgite, Hole 920D. In: Karson, J. A., et al. (eds) Proceedings of the Ocean Drilling Program, Scientific Results, 153. Ocean Drilling Program, pp. 321-331

Keshav, S., Sen, G. & Presnall, D. C. (2007). Garnet-bearing xenoliths from Salt Lake Crater, Oahu, Hawaii: high-pressure fractional crystallization in the oceanic mantle. Journal ofPetrology48, 1681-1724.

Kessel, R., Schmidt, M.W., Ulmer, P., Pettke, T., 2005. Trace element signature of subduction-zone fluids, melts and supercritical liquids at 120-180 km depth. Nature 437, 724-7.

Khedr, M. Z., Arai, S., Tamura, A. & Morishita, T. (2010). Clinopyroxenes in high-P metaperidotites from Happo-O'ne, central Japan: Implications for wedge-transversal chemical change of slab-derived fluids. Lithos. Elsevier B.V. 119, 439–456.

Klimm, K., Blundy, J. D., & Green, T. H. (2008). Trace element partitioning and accessory phase saturation during H2O-saturated melting of basalt with implications for subduction zone chemical fluxes. J. Petrol. 49(3), 523–553.

Kornprobst, J. (1969). Le massif ultrabasique des Beni Bouchera (Rif Interne, Maroc): Etude des péridotites de haute température et de haute pression, et des pyroxénolites, à grenat ou sans grenat, qui leur sont associées. Contributions to Mineralogy and Petrology, 23(4), 283-322.

Kornprobst, J. (1970). Les péridotites et les pyroxénolites du massif ultrabasique des Beni Bouchera: une étude expérimentale entre 1100 et 1550 C, sous 15 à 30 kilobars de pression sèche. Contributions to Mineralogy and Petrology, 29(4), 290-309.

Kornprobst, J., Piboule, M., Roden, M. & Tabit, A. (1990). Corundum-bearing garnet clinopyroxenites at beni bousera (Morocco): Original plagioclase-rich gabbros recrystallized at depth within the mantle? Journal of Petrology 31, 717–745.

Lanari, P., Vidal, O., De Andrade, V., Dubacq, B., Lewin, E., Grosch, E.G., Schwartz, S., 2014. XMapTools: A MATLAB©-based program for electron microprobe X-ray image pro- cessing and geothermobarometry. Computers & Geosciences 62, 227–240

Lavina, B., Carbonin, S., Russo, U., Tumiati, S., 2006. The crystal structure of dissakisite-(La) and structural variations after annealing of radiation damage. Am. Mineral. 91, 104-110.

Liati, A., Gebauer, D., 2003. Geochronological constraints for the time of metamorphism in the Gruf Complex (Central Alps) and implications for the

Adula-Cima Lunga nappe system. Schweiz. Mineral. Petrogr. Mitt. 83, 159-172.

Liati, A., Gebauer, D., Fanning, C.M., 2009. Geochronological evolution of HP metamorphic rocks of the Adula nappe, Central Alps, in pre-Alpine and Alpine subduction cycles. J. Geol. Soc. London. 166, 797-810.

Liu, Q., Jin, Z., Zhang, J., 2009. An experimental study of dehydration melting of phengite-bearing eclogite at 1.5-3.0 GPa. Chinese Sci. Bull. 54, 2090-2100.

Mainprice, D., Bascou, J., Cordier, P., & Tommasi, A. (2004). Crystal preferred orientations of garnet: comparison between numerical simulations and electron back-scattered diffraction (EBSD) measurements in naturally deformed eclogites. Journal of Structural Geology, 26(11), 2089-2102.

Maitland, T. & Sitzman, S. (2007). EBSD technique and materials characterization. Scanning Microscopy for Nanotechnology. Techniques and Applications 41–76.

Malaspina N, Tumiati S, 2012. The role of C-O-H and oxygen fugacity in subduction-zone garnet peridotites. Eur. J. Mineral. 24, 607-618.

Malaspina, N., Hermann, J., Scambelluri, M., 2009. Fluid/mineral interaction in UHP garnet peridotite. Lithos 146-147, 11-17.

Malaspina, N., Hermann, J., Scambelluri, M., Compagnoni, R., 2006. Polyphase inclusions in Garnet-Orthopyroxenite (Dabie-Shan, China) as monitors for metasomatism and fluid-related trace element transfer in subduction zone peridotite. Earth Planet. Sci. Lett. 249, 173-187.

Malaspina, N., Langenhorst, F., Tumiati, S., Campione, M., Frezzotti, M.L., Poli, S., 2017. The redox budget of crust-derived fluid phases at the slab-mantle interface. Geochim. Cosmochim. Acta 209, 70-84.

Malaspina, N., Scambelluri, M., Poli, S., Van Roermund, H.L.M., Langenhorst, F., 2010. The oxidation state of mantle wedge majoritic garnet websterites metasomatised by C-bearing subduction fluids. Earth Planet. Sci. Lett. 298, 417-426.

Marocchi, M., Mair, V., Tropper, P. & Bargossi, G. M. (2009). Metasomatic reaction bands at the Mt. Hochwart gneiss-peridotite contact (Ulten Zone, Italy): Insights into fluid-rock interaction in subduction zones. Mineralogy and Petrology 95, 251–272.

Marschall, H.R., Schumacher, J.C., 2012. Arc magmas sourced from mélange diapirs in subduction zones. Nat. Geosci. 5, 862-867.

Martin, S., Godard, G., Prosser, G., Schiavo, A., Bernoulli, D., & Ranalli, G. (1998). Evolution of the deep crust at the junction Austroalpine/Southalpine: the Tonale Nappe. Mem. Sci. Geol, 50, 3-50.

Massif, V. (1991). path for the Voltri Massif eclogites (Ligurian. 93–109.

Matysiak, A. K. & Trepmann, C. A. (2012). Crystal-plastic deformation and recrystallization of peridotite controlled by the seismic cycle. Tectonophysics. Elsevier B.V. 530–531, 111–127.

McDonough, W.F., Sun, S.S., 1995. The composition of the Earth. Chem. Geol. 120, 223-253.

McLellan, E. L. (1989). Sequential formation of subsolidus and anatectic migmatites in response to thermal evolution, eastern Scotland. J. Geol. 97(2), 165-182.

Menegon, L., Stünitz, H., Nasipuri, P., Heilbronner, R., & Svahnberg, H. (2013). Transition from fracturing to viscous flow in granulite facies perthitic feldspar (Lofoten, Norway). Journal of Structural Geology, 48, 95-112.

Meyre, C. & Frey, M. (1998). Eclogite facies metamorphism and deformation of the middle Adula nappe (Central Alps, Switzerland): Excursion to Trescolmen. Schweizerische Mineralogische Und Petrographische Mitteilungen 78, 355–362.

Michibayashi, K. & Oohara, T. (2013). Olivine fabric evolution in a hydrated ductile shear zone at the Moho Transition Zone, Oman Ophiolite. Earth and Planetary Science Letters. Elsevier B.V. 377–378, 299–310.

Michibayashi, K., & Mainprice, D. (2004). The role of pre-existing mechanical anisotropy on shear zone development within oceanic mantle lithosphere: an example from the Oman ophiolite. Journal of Petrology, 45(2), 405-414.

Michibayashi, K., Ina, T. & Kanagawa, K. (2006). The effect of dynamic recrystallization on olivine fabric and seismic anisotropy: Insight from a ductile shear zone, Oman ophiolite. Earth and Planetary Science Letters 244, 695–708.

Milnes, A.G., 1974. Structure of the Pennine Zone (Central Alps): a new working hypothesis. Bulletin of the Geological Society of America. Bull. Geol. Soc. Am. 85, 1727-1732.

Morishita, T., Arai, S., Gervilla, F. & Green, D. H. (2003). Closed-sytem geochemical recycling of crustal materials in alpine-type peridotite. Geochimica et Cosmochimica Acta 67, 303–310.

Morten L, Bargossi GM, Landini Bargossi F, (1976) Notizie preliminari sulle metamorfiti della Val di Rumo, Val di Non, Trento. Miner. Petrogr. Acta, 21, 137-144.

Morten, L., & Obata, M. (1983). Possible high-temperature origin of pyroxenite lenses within garnet peridotite, northern Italy. Bulletin de minéralogie, 106(6), 775-780.

Mukasa, S. B. & Shervais, J. W. (1999). Growth of sub-continental lithosphere: Evidence from repeated injections in the Balmuccia lherzolite massif, Italian Alps. Lithos 48, 287-316.

Nagel, T., de Capitani, C., Frey, M., Froitzheim, N., Stunitz, H. & Schmid, S. M. (2002). Structural and metamorphic evolution during rapid exhumation in the Lepontine dome (southern Simano and Adula nappes, Central Alps, Switzerland). Eclogae Geologicae Helvetiae 95, 301–321.

Nagel, T.J., 2008. Tertiary subduction, collision and exhumation recorded in the Adula nappe, central Alps. Geol. Soc. London, Spec. Publ. 298, 365-392.

Nazé, L., Doukhan, N., Doukhan, J. C., & Latrous, K. (1987). A TEM study of lattice defects in naturally and experimentally deformed orthopyroxenes. Bulletin de minéralogie, 110(5), 497-512.

Neugebauer, L. (1990): The Japetus model: a plate tectonic concept for the Variscan belt of Europe. Tectonophysics, 169:229-256

Newman, J., Lamb, W. M., Drury, M. R. & Vissers, R. L. M. (1999). Deformation processes in a peridotite shear zone: Reaction-softening by an H2O-deficient, continuous net transfer reaction. Tectonophysics 303, 193–222.

Nimis, P. & Morten, L. (2000). P-T evolution of "crustal" garnet peridotites and included pyroxenites from Nonsberg area (upper Austroalpine), NE Italy: From the wedge to the slab. Journal of Geodynamics 30, 93–115.

Nimis, P., Trommsdorff, V., 2001. Revised Thermobarometry of Alpe Arami and other Garnet Peridotites from the Central Alps. J. Petrol. 42, 103-115.

Obata, M., & Morten, L. (1987). Transformation of spinel lherzolite to garnet lherzolite in ultramafic lenses of the Austridic crystalline complex, northern Italy. Journal of Petrology, 28(3), 599-623.

Ohuchi, T. & Irifune, T. (2013). Development of A-type olivine fabric in water-rich deep upper mantle. Earth and Planetary Science Letters. Elsevier 362, 20–30.

Paquin, J., Altherr, R., 2001. New Constraints on the P - T Evolution of the Alpe Arami Garnet Peridotite Body (Central Alps , Switzerland) 42, 1119-1140.

Passchier, C.W., Trouw, R.A.J., 2005. Microtectonics, 2nd ed. 2005 edition. ed. Springer, Berlin ; New York.

Pearce, M. A., Wheeler, J., & Prior, D. J. (2011). Relative strength of mafic and felsic rocks during amphibolite facies metamorphism and deformation. Journal of Structural Geology, 33(4), 662-675.

Platt, J.P., Behr, W.M., 2011. Grainsize evolution in ductile shear zones: Implications for strain localization and the strength of the lithosphere. J. Struct. Geol. 33, 537-550.

Prigent, C., Guillot, S., Agard, P., Lemarchand, D., Soret, M., & Ulrich, M. (2018). Transfer of subduction fluids into the deforming mantle wedge during nascent subduction: Evidence from trace elements and boron isotopes

(Semail ophiolite, Oman). Earth and Planetary Science Letters, 484, 213-228.

Prior, D.J., Wheeler, J., Peruzzo, L., Spiess, R., Storey, C., 2002. Some garnet microstructures: an illustration of the potential of orientation maps and misorientation analysis in microstructural studies. J. Struct. Geol., Micro structural Processes: A Special Issue in Honor of the Career Contributions of R.H. Vernon 24, 999-1011.

Raimbourg, H., Kogure, T. & Toyoshima, T. (2011). Crystal bending, subgrain boundary development, and recrystallization in orthopyroxene during granulite-facies deformation. Contributions to Mineralogy and Petrology 162, 1093–1111.

Raimbourg, H., Toyoshima, T., Harima, Y. & Kimura, G. (2008). Grain-size reduction mechanisms and rheological consequences in high-temperature gabbro mylonites of Hidaka, Japan. Earth and Planetary Science Letters 267, 637–653.

Rampone, E. & Borghini, G. (2008). Melt migration and intrusion in the Erro-Tobbio peridotites (Ligurian Alps, Italy): Insinghts on magmatic processes in extending lithospheric mantle. European Journal of Mineralogy 20, 573–585.

Rampone, E., Morten, L., 2001. Records of Crustal Metasomatism in the Garnet Peridotites of the Ulten Zone (Upper Austroalpine, Eastern Alps). J. Petrol. 42, 207-219.

Ranalli, G. & Murphy, D. C. (1987). Rheological stratification of the lithosphere. Tectonophysics 132, 281–295.

Ranalli, G., Martin, S., & Mahatsente, R. (2005). Continental subduction and exhumation: an example from the Ulten Unit, Tonale Nappe, Eastern Austroalpine. Geological Society, London, Special Publications, 243(1), 159-174.

Rivalenti, G., Mazzucchelli, M., Vannucci, R., Hofmann, A. W., Ottolini, L. & Obermiller, W. (1995). The relationship be- tween websterite and peridotite in the Balmuccia peridotite massif (NW Italy) as revealed by trace element

variations in clinopyroxene. Contributions to Mineralogy and Petrology 121, 275-288.

Rubatto, D., Hermann, J., Berger, A., Engi, M., 2009. Protracted fluid-present melting during Barrovian metamorphism in the Central Alps. Contrib. Mineral. Petrol. 158, 703-722.

Rutter, E. H. & Brodie, K. H. (1988). The role of tectonic grain size reduction in the rheological stratification of the lithosphere. Geologische Rundschau 77, 295–307.

Rutter, E. H., Holdsworth, R. E., & Knipe, R. J. (2001). The nature and tectonic significance of fault-zone weakening: an introduction. Geological Society, London, Special Publications, 186(1), 1-11.

Salters, V.J.M., Stracke, A., 2004. Composition of the depleted mantle. Geochem. Geophys. Geosyst. 5(5).

Sapienza, G.T., Scambelluri, M., Braga, R., 2009. Dolomite-bearing orogenic garnet peridotites witness fluid-mediated carbon recycling in a mantle wedge (Ulten Zone, Eastern Alps, Italy). Contrib. Mineral. Petrol. 158, 401-420.

Sawyer, E. W. (2008). Atlas of migmatites (Vol. 9). NRC Research press.

Scambelluri, M., Hermann, J., Morten, L., Rampone, E., 2006. Melt- versus fluid-induced metasomatism in spinel to garnet wedge peridotites (Ulten Zone, Eastern Italian Alps): clues from trace element and Li abundances. Contrib. Mineral. Petrol. 151, 372-394.

Scambelluri, M., Pettke, T., Rampone, E., Godard, M., Reusser, E., 2014. Petrology and Trace Element Budgets of High-pressure Peridotites Indicate Subduction Dehydration of Serpentinized Mantle (Cima di Gagnone, Central Alps, Switzerland). J. Petrol. 55, 459-498.

Scambelluri, M., Pettke, T., van Roermund, H.L.M., 2008. Majoritic garnets monitor deep subduction fluid flow and mantle dynamics. Geology 36, 59.

Schmid, S.M., O.A., P., Froitzheim, N., Schönborn, G., Kissingl, E., 1996. Geophysical-geological transect and tectonic evolution of the Swiss-Italian Alps. Tectonics 15, 1036-1064.

Schmid, S.M., Rück, P., Schreurs, G., 1990. The significance of the Schams nappe for the reconstruction of the paleotectonic and orogenic evolution of the Penninic zone along the NFP 20 East Traverse, in: Pfiffner, A., Heitzmann, P. (Ed.), Deep Structure of the Alps—Results from NFP/PNR 20. Basel: Birkhäuser AG, pp. 263-287.

Schmidt, M.W., Poli, S., 1998. Experimentally based water budgets for dehydrating slabs and consequences for arc magma generation. Earth Planet. Sci. Lett. 163, 361-379.

Schmidt, M.W., Poli, S., 2014. Devolatilization During Subduction. Treatise on Geochemistry: Second Edition. Elsevier Ltd. doi:10.1016/B978-0-08-095975-7.00321-1

Schmidt, M.W., Vielzeuf, D., Auzanneau, E., 2004. Melting and dissolution of subducting crust at high pressures: the key role of white mica. Earth Planet. Sci. Lett. 228, 65-84.

Skrotzki, W. (1994). Defect structure and deformation mechanisms in naturally deformed augite and enstatite. Tectonophysics 229, 43–68.

Skrotzki, W., Muller, W. F. & Weber, K. (1991). Exsolution phenomena in pyroxenes from the Balmuccia Massif, NW-Italy. European Journal of Mineralogy 3, 39–61.

Skrotzki, W., Wedel, A., Weber, K., & Müller, W. F. (1990). Microstructure and texture in lherzolites of the Balmuccia massif and their significance regarding the thermomechanical history. Tectonophysics, 179(3-4), 227-251.

Spandler, C., Pirard, C., 2013. Element recycling from subducting slabs to arc crust: A review. Lithos 170-171, 208-223.

Steinmann, M., Stille, P., 1999. Geochemical evidence for the nature of the crust beneath the eastern North Penninic basin of the Mesozoic Tethys ocean. Geol. Rundschau 87, 633-643.

Stucki, A., Rubatto, D., Trommsdorff, V., 2003. Mesozoic ophiolite relics in the Southern Steep Belt of the Central Alps. Schweiz. Mineral. Petrogr. Mitt. 83, 285-299.

Stünitz, H., Gerald, J. F., & Tullis, J. (2003). Dislocation generation, slip systems, and dynamic recrystallization in experimentally deformed plagioclase single crystals. Tectonophysics, 372(3-4), 215-233.

Syracuse, E.M., van Keken, P.E., Abers, G.A., Suetsugu, D., Bina, C., Inoue, T., Wiens, D., Jellinek, M., 2010. The global range of subduction zone thermal models. Phys. Earth Planet. Inter. 183, 73-90.

Takazawa, E., Frey, F. A., Shimizu, N., Saal, N. & Obata, M. (1999). Polybaric petrogenesis of mafic layers in the Horoman peridotite complex, Japan. Journal of Petrology 40, 1827-1831

Thöni, M. (1981). Degree and evolution of the Alpine metamorphism in the Austroalpine unit W of the Hohe Tauern in the light of K/Ar and Rb/Sr age determinations on micas. Jahrbuch der geologischen Bundesanstalt, 124(1), 111-174.

Tiraboschi, C., Tumiati, S., Sverjensky, D., Pettke, T., Ulmer, P., Poli, S., 2018. Experimental determination of magnesia and silica solubilities in graphite-saturated and redox-buffered high-pressure COH fluids in equilibrium with forsterite + enstatite and magnesite + enstatite. Contrib. Mineral. Petrol. 173.

Todd, C.S., Engi, M., 1997. No Title. Metamorph. F. gradients Cent. Alps. J. Metamorph. Geol. 15, 513-530.

Tollmann, A. (1987). The Alpidic Evolution of the Eastern Alps-In: FLÜGEL, HW & FAUPL, P.(Eds.): Geodynamics of the Eastern Alps, 361-378, 8 Abb., F.

Tommasi, A., Langone, A., Padrón-Navarta, J. A., Zanetti, A., Vauchez, A., 2017. Hydrous melts weaken the mantle, crystallization of pargasite and phlogopite does not: Insights from a petrostructural study of the Finero peridotites, southern Alps. Earth Planet. Sci. Lett., 477, 59-72.

Toy, V. G., Newman, J., Lamb, W. & Tikoff, B. (2009). The role of pyroxenites in formation of shear instabilities in the mantle: Evidence from an ultramafic

ultramylonite, Twin Sisters massif, Washington. Journal of Petrology 51, 55–80.

Trepmann, C. A., Stöckhert, B., Dorner, D., Moghadam, R. H., Küster, M., & Röller, K. (2007). Simulating coseismic deformation of quartz in the middle crust and fabric evolution during postseismic stress relaxation—an experimental study. Tectonophysics, 442(1-4), 83-104.

Trommsdorff, V., Hermann, J., Muntener, O., Pfiffner, M., Risold, A.C., 2000. Geodynamic cycles of subcontinental lithosphere in the Central Alps and the Arami enigma. J. Geodyn. 30, 77-92.

Tullis, J. & Yund, R. A. (1991). Diffusion creep in feldspar aggregates: experimental evidence. Journal of Structural Geology 13, 987–1000.

Tullis, J., Snoke, A. W. & Todd, V. R. (1982). Significance and petrogenesis of mylonitic rocks. Geology 10, 227.

Tumiati, S., Fumagalli, P., Tiraboschi, C., Poli, S., 2013. An Experimental Study on COH-bearing Peridotite up to 3.2 GPa and Implications for Crust-Mantle Recycling. J. Petrol. 54, 453-479.

Tumiati, S., Godard, G., Martin, S., Klötzli, U., Monticelli, D., 2007. Fluid-controlled crustal metasomatism within a high-pressure subducted mélange (Mt. Hochwart, Eastern Italian Alps). Lithos 94, 148-167.

Tumiati, S., Godard, G., Martin, S., Nimis, P., Mair, V., Boyer, B., 2005. Dissakisite-(La) from the Ulten zone peridotite (Italian Eastern Alps): A new end-member of the epidote group. Am. Mineral. 90, 1177-1185.

Tumiati, S., Thöni, M., Nimis, P., Martin, S., Mair, V., 2003. Mantle-crust interactions during Variscan subduction in the Eastern Alps (Nonsberg-Ulten zone): geochronology and new petrological constraints. Earth Planet. Sci. Lett. 210, 509-526.

Tumiati, S., Zanchetta, S., Pellegrino, L., Ferrario, C., Casartelli, S., Malaspina, N., 2018. Granulite-facies overprint in garnet peridotites and kyanite eclogites of Monte Duria (Central Alps, Italy): Clues from srilankite- and sapphirine-bearing symplectites. J. Petrol. 59.

van Acken, D., Becker, H., Walker, R. J., McDonough, W. F., Wombacher, F., Ash, R. D., & Piccoli, P. M. (2010). Formation of pyroxenite layers in the Totalp ultramafic massif (Swiss Alps)-insights from highly siderophile elements and Os isotopes. Geochimica et Cosmochimica Acta, 74(2), 661-683.

Van Duysen, J. C., Doukhan, N., & Doukhan, J. C. (1985). Transmission electron microscope study of dislocations in orthopyroxene (Mg, Fe) 2 Si 2 O 6. Physics and Chemistry of Minerals, 12(1), 39-44.

Van Roermund, H. van, Carswell, D., Drury, M.R., Heijboer, T.C., 2002. Microdiamonds in a megacrystic garnet websterite pod from Bardane on the island of Fjørtoft, western Norway: evidence for diamond formation in mantle rocks during. Geology 30, 959.

van-Duysen, J. C., & Doukhan, J. C. (1984). Room temperature microplasticity of a spodumene $LiAlSi_2O_6$. Physics and Chemistry of Minerals, 10(3), 125-132

Vannucci, R., Shimizu, N., Piccardo, G. B., Ottolini, L. & Bottazzi, P. (1993). Distribution of trace-elements during breakdown of mantle garnet: an example from Zabargad. Contributions to MineralogyandPetrology113, 437-449.

Wang, J., Hattori, K. H. & Stern, C. R. (2008). Metasomatic origin of garnet orthopyroxenites in the subcontinental lithospheric mantle underlying Pali Aike volcanic field, southern South America. Mineralogy and Petrology 94, 243–258.

Warren, J. M. & Hirth, G. (2006). Grain size sensitive deformation mechanisms in naturally deformed peridotites. Earth and Planetary Science Letters 248, 438–450.

Warren, J. M., Shimizu, N., Sakaguchi, C., Dick, H. J. B. & Nakamura, E. (2009). An assessment of upper mantle het- erogeneity based on abyssal peridotite isotopic compositions. Journal of Geophysical Research 114, B12203.

Wheeler, J., Prior, D. J., Jiang, Z., Spiess, R. & Trimby, P. W. (2001). The petrological significance of misorientations between grains. Contributions to Mineralogy and Petrology 141, 109–124.

Whitney, D. L. & Evans, B. W. (2010). Abbreviations for names of rock-forming minerals. American Mineralogist 95, 185–187.

Yu, S. Y., Xu, Y. G., Ma, J. L., Zheng, Y. F., Kuang, Y. S., Hong, L. B., ... & Tong, L. X. (2010). Remnants of oceanic lower crust in the subcontinental lithospheric mantle: trace element and Sr-Nd-O isotope evidence from aluminous garnet pyroxenite xenoliths from Jiaohe, Northeast China. Earth and Planetary Science Letters, 297(3-4), 413-422.

Ziegler, P. A. (1984). Caledonian and Hercynian crustal consolidation of Western and Central Europe; a working hypothesis. Geologie en Mijnbouw, 63(1), 93-108.

Appendix

Petrography of studied samples

Garnet peridotite A2C2

Garnet peridotite A2C2 consists olivine (more than 85 vol.%), clinopyroxene, orthopyroxene, amphibole and garnet. This rock displays a porphyroblastic microstructure with mm-sized garnet, clinopyroxene (Cpx_1) amphibole (Amp_1), olivine (Ol_1) and orthopyroxene (Opx_1) surrounded by a fine-grained equigranular matrix composed by olivine (Ol_2), clinopyroxene (Cpx_2) orthopyroxene (Opx_2), minor amphibole (Amp_2) and Cr-spinel (Sp_2). Garnet usually contains inclusions of olivine, orthopyroxene and clinopyroxene. Garnets are invariably mantled or completely replaced by (Opx_{Sym}) + clinopyroxene (Cpx_{Sym}) + spinel (Sp_{Sym}) ± amphibole (Amp_{Sym}) symplectites. Double kelyphitic coronas consisting of orthopyroxene after olivine and orthopyroxene (Opx_{Sym}) + clinopyroxene (Cpx_{Sym}) + spinel (Sp_{Sym}) ± amphibole (Amp_{Sym}) after garnet have been also observed in correspondence of the previous garnet-olivine grain boundaries. In kelyphites replacing olivine, tiny crystals of baddeleyite and srilankite also occur.

Garnet peridotite MD20

This sample is characterized by a large porphyroblast of garnet (ca. 2 cm) in paragenesis with smaller (up to 5 mm) orthopyroxene (Opx_1) and clinopyroxene (Cpx_1) porphyroblasts. This porphyroclastic assemblage is surrounded by a fine-grained recrystallized matrix composed by olivine (Ol_2), clinopyroxene (Cpx_2) and orthopyroxene (Opx_2). Both Cpx_1 and Opx_1 display deformation bands. Garnet displays mm-sized inclusions of olivine and it is mantled by a symplectitic rim consisting of orthopyroxene (Opx_{Sym}) + clinopyroxene (Cpx_{Sym}) + spinel (Sp_{Sym}) ± amphibole (Amp_{Sym}) ± sapphirine. Double kelyphitic coronas consisting of orthopyroxene after olivine and orthopyroxene (Opx_{Sym}) + clinopyroxene (Cpx_{Sym}) + spinel (Sp_{Sym}) ± amphibole (Amp_{Sym}) after garnet have

been also observed in correspondence of the previous garnet-olivine grain boundaries.

Garnet peridotite DB170

Garnet peridotite DB170 has a porphyroblastic microstructure with pluri-millimetric garnets (up to 1 cm), olivine (Ol_1), orthopyroxene (Opx_1) and clinopyroxene (Cpx_1) surrounded by fine-grained recrystallized olivine (Ol_2), orthopyroxene (Opx_2), clinopyroxene (Cpx_2) and minor amphibole (Amp_2). Sometimes Opx_1 displays deformation bands. Garnet often include olivine (Ol_1) and orthopyroxene (Opx_1). It is mantled by symplectites consisting of orthopyroxene (Opx_{Sym}) + clinopyroxene (Cpx_{Sym}) + spinel (Sp_{Sym}) ± amphibole (Amp_{Sym}) ± sapphirine. Double kelyphitic coronas consisting of orthopyroxene after olivine and orthopyroxene (Opx_{Sym}) + clinopyroxene (Cpx_{Sym}) + spinel (Sp_{Sym}) ± amphibole (Amp_{Sym}) after garnet have been also observed in correspondence of the previous garnet-olivine grain boundaries.

Garnet peridotite B3A

Garnet peridotites B3A display a porphyroblastic microstructure with large garnet (up to 1 cm), olivine (Ol_1), orthopyroxene (Opx_1), clinopyroxene (Cpx_1) and amphibole (Amp_1) surrounded by fine-grained recrystallized matrix of olivine (Ol_2), orthopyroxene (Opx_2), clinopyroxene (Cpx_2) minor amphibole (Amp_2) and Cr-spinel (Spl_2). Both coarse-grained Ol_1 and Opx_1 show intracrystalline deformation microstructures like undulatory extinction and deformation bands while neoblastic Ol_2 and Opx_2 are usually strain-free. Cpx_1 occur as large porphyroblasts (up to 7 mm) and displays numerous exsolution lamellae of edenitic to pargasitic amphibole and rare inclusions of dolomite. Clinopyroxene neoblasts are inclusions-free and contain no exsolution lamellae of Na-rich amphibole. Garnet occurs as porphyroblasts of variable size (from 3 mm to 1 cm) that commonly contain inclusions of olivine, orthopyroxene and clinopyroxene. Garnet is always bordered by orthopyroxene (Opx_{Sym}) + clinopyroxene (Cpx_{Sym}) + spinel (Sp_{Sym}) ± amphibole (Amp_{Sym}) symplectites. Composite kelyphitic coronas consisting of orthopyroxene (Opx_{Sym}) after olivine and orthopyroxene (Opx_{Sym}) + clinopyroxene (Cpx_{Sym}) + spinel (Sp_{Sym}) ± amphibole (Amp_{Sym}) after garnet have been also observed in correspondence of the previous garnet-olivine grain boundaries.

Retrogressed garnet peridotite DB165

Peridotite DB165 is characterized by coarse (up to 3 mm) olivine (Ol_1) and orthopyroxene (Opx_1) surrounded by fine-grained recrystallized olivine (Ol_2), orthopyroxene (Opx_2), clinopyroxene (Cpx_2), minor amphibole (Amp_2) and Cr-spinel (Spl_2). This sample show a foliation marked by the shape preferred orientation of Ol_1. Such foliation is also defined by the SPO of recrystallized olivine, orthopyroxene, clinopyroxene and amphibole. Few orthopyroxene (Opx_1) shows undulatory extinction and deformation bands. Garnet was not observed because it is always statically replaced by chlorite pseudomorphs. Such pseudomorphs are mantled by orthopyroxene (Opx_{Sym}) + clinopyroxene (Cpx_{Sym}) + spinel (Sp_{Sym}) ± amphibole (Amp_{Sym}) symplectites post-dating the pseudomorphic replacement of garnet.

Retrogressed garnet peridotite DB166

Sample DB166 has a porphyroblastic microstructure with olivine (Ol_1) and orthopyroxene (Opx_1) enclosed in a fine-grained recrystallized matrix made by olivine (Ol_2), orthopyroxene (Opx_2), clinopyroxene (Cpx_2), minor amphibole (Amp_2) and Cr-spinel (Spl_2). Garnet was not observed since it is always completely replaced by variably deformed chlorite pseudomorphs. Within pseudomorphs chlorite displays a strong SPO indicating that chlorite crystallised in a deformation regime. An incipient chlorite (Chl_3) foliation have been also observed in correspondence of the tails of the chlorite-bearing pseudomorphs.

Retrogressed garnet peridotite DB167

Peridotite DB167 displays porphyroblastic olivine (Ol_1) and orthopyroxene (Opx_1) surrounded by fine-grained recrystallized olivine (Ol_2), orthopyroxene (Opx_2), clinopyroxene (Cpx_2), minor amphibole (Amp_2) and Cr-spinel (Spl_2). Porphyroblastic Opx_1 rarely shows undulatory extinction and deformation bands. This sample displays a foliation defined by syn-tectonic chlorite (Chl_3) and amphibole (Amp_3) post-dating the porphyroblastic and neoblastic assemblages.

Retrogressed garnet peridotite DB168

Peridotite DB168 shows porphyroblastic olivine (Ol_1) and orthopyroxene (Opx_1) surrounded by fine-grained recrystallized olivine (Ol_2), orthopyroxene (Opx_2), clinopyroxene (Cpx_2), subordinate amphibole (Amp_2) and Cr-spinel (Spl_2). Olivine and orthopyroxene porphyroblasts displays deformation bands and

undulatory extinction. This sample displays a foliation defined by syn-tectonic chlorite (Chl_3) and minor amphibole (Amp_3) post-dating the porphyroblastic and neoblastic assemblages.

Retrogressed garnet peridotite DB169

Peridotite DB169 shows coarse (up to 3 mm) olivine (Ol_1) and orthopyroxene (Opx_1) porphyroblasts mantled by fine-grained recrystallized olivine (Ol_2), orthopyroxene (Opx_2), clinopyroxene (Cpx_2), minor amphibole (Amp_2) and Cr-spinel (Spl_2). Both Ol_1 and Opx_1 display undulatory extinction and deformation bands. Olivine porphyroblasts display a marked shape preferred orientation defining a foliation in the rock. Trails of Spl_2 crystals follow this foliation.

Retrogressed garnet peridotite DB171

Retrogressed garnet peridotite DB171 consists of coarse-grained olivine (Ol_1) (up to 2.5 mm), orthopyroxene (Opx_1) and amphibole (Amp_1) surrounded by a fine-grained recrystallized matrix consisting of polygonal olivine (Ol_2), orthopyroxene (Opx_2), clinopyroxene (Cpx_2), subordinate amphibole (Amp_2) and Cr-spinel (Spl_2). Both porphyroblastic olivine and orthopyroxene show undulatory extinctions and deformation bands. This sample displays a weak foliation marked the shape preferred orientation of porphyroblastic and neoblastic olivine and amphibole. Garnet was not observed since it is invariably replaced by orthopyroxene (Opx_{sym}) + clinopyroxene (Cpx_{sym}) + spinel (Spl_{sym}) + amphibole (Amp_{sym}) symplectites.

Retrogressed garnet peridotite DB172

Retrogressed garnet peridotite DB172 displays coarse olivine (Ol_1), orthopyroxene (Opx_1) and clinopyroxene (Cpx_1) surrounded by fine-grained recrystallized olivine (Ol_2), clinopyroxene (Cpx_2), orthopyroxene (Opx_2), minor amphibole (Amp_2) and rare spinel (Spl_2). Both Ol_1 and Opx_1 frequently show evident deformation bands. In this sample garnet was not observed because it is always statically replaced by chlorite-bearing pseudomorphs. This sample displays a foliation defined by syn-tectonic chlorite (Chl_3) and minor amphibole (Amp_3) post-dating the porphyroblastic and neoblastic assemblages.

Retrogressed garnet peridotite DB173

Retrogressed garnet peridotite DB173 displays coarse (up to 3 mm) olivine (Ol_1) and orthopyroxene (Opx_1) surrounded by fine-grained recrystallized olivine (Ol_2), orthopyroxene (Opx_2), minor clinopyroxene (Cpx_2), amphibole (Amp_2) and spinel (Spl_2). Both Ol_1 and Opx_1 show undulatory extinction and deformation bands. This sample displays a weak foliation defined by syn-tectonic chlorite (Chl_3) and minor amphibole (Amp_3) post-dating the porphyroblastic and neoblastic assemblages. Several deformed chlorite-bearing pseudomorphs after garnet occur along this foliation.

Retrogressed garnet peridotite DB174

Retrogressed garnet peridotite DB174 displays coarse (up to 2 mm) olivine (Ol_1) and orthopyroxene (Opx_1) surrounded by fine-grained recrystallized olivine (Ol_2), orthopyroxene (Opx_2), minor clinopyroxene (Cpx_2), amphibole (Amp_2) and spinel (Spl_2). Both Ol_1 and Opx_1 display evident deformation bands and undulatory extinction. This sample displays a foliation defined by syn-tectonic chlorite (Chl_3) and minor amphibole (Amp_3) post-dating the porphyroblastic and neoblastic assemblages. Few deformed chlorite-bearing pseudomorphs after garnet occur along this foliation.

Retrogressed garnet peridotite DB175

Retrogressed garnet peridotite DB175 displays coarse (up to 1.5 mm) olivine (Ol_1) and orthopyroxene (Opx_1) surrounded by fine-grained recrystallized olivine (Ol_2), orthopyroxene (Opx_2), minor clinopyroxene (Cpx_2), amphibole (Amp_2) and spinel (Spl_2). This sample displays a foliation defined by syn-tectonic chlorite (Chl_3) and minor amphibole (Amp_3) post-dating the porphyroblastic and neoblastic assemblages.

Chlorite peridotite C2A

Chlorite peridotite C2A displays coarse (up to 1.5 mm) olivine (Ol_1) and orthopyroxene (Opx_1) surrounded by fine-grained recrystallized olivine (Ol_2), orthopyroxene (Opx_2), amphibole (Amp_2), rare clinopyroxene (Cpx_2) and spinel (Spl_2). Opx_1 displays evident deformation bands. This sample displays a strong foliation defined by syn-tectonic chlorite (Chl_3) and minor amphibole (Amp_3) post-dating the porphyroblastic and neoblastic assemblages.

Chlorite peridotite DB113

Chlorite peridotite DB113 shows relict olivine and orthopyroxene extensively statically overgrown by a new generation of porphyroblastic orthopyroxene (Opx_{Porph}), Mg-hornblende ($Amph_{Porph}$) and phlogopite (Phl_{Porph}). These microstructures clearly indicate a metasomatic event pre-dating the chlorite foliation. Several dolomite crystals and round-shaped brucite + calcite pseudomorphs after dolomite also occur within the olivine matrix.

Tremolitite DB146

Tremolitites display an assemblage dominated by tremolite (more than 80 vol.%), Mg-hornblende and minor chlorite. Tremolite forms a mosaic-like texture with 120° triple junctions and straight grain boundaries. The tremolite matrix hosts older mm-sized Mg-hornblende porphyroblasts. Mg-hornblende is zoned, showing dusty cores with opaque minerals occurring along the cleavages, and clear inclusion-free rims.

Tremolitite DB148

Tremolitites display an assemblage dominated by tremolite (more than 80 vol.%), Mg-hornblende and minor chlorite. Tremolite forms a mosaic-like texture with 120° triple junctions and straight grain boundaries. The tremolite matrix hosts older mm-sized Mg-hornblende porphyroblasts. Mg-hornblende is zoned, showing dusty cores with opaque minerals occurring along the cleavages, and clear inclusion-free rims.

Tremolitite DB151

Tremolitites display an assemblage dominated by tremolite (more than 80 vol.%), Mg-hornblende and minor chlorite. Tremolite forms a mosaic-like texture with 120° triple junctions and straight grain boundaries. The tremolite matrix hosts older mm-sized Mg-hornblende porphyroblasts. Sometimes Mg-hornblende is zoned, showing dusty cores with opaque minerals occurring along the cleavages, and clear inclusion-free rims.

Tremolitite DB179

Tremolitites display an assemblage dominated by tremolite (more than 80 vol.%), Mg-hornblende and minor chlorite. Tremolite forms a mosaic-like texture with 120° triple junctions and straight grain boundaries. The tremolite matrix hosts

older mm-sized Mg-hornblende porphyroblasts. Mg-hornblende is zoned, showing dusty cores with opaque minerals occurring along the cleavages, and clear inclusion-free rims. Isolated phlogopite (Phl_3) + chlorite + talc + tremolite hexagonal pseudomorphs after garnet have been recognised in textural equilibrium with tremolite.

Mafic eclogite D4

Mafic eclogite D4 displays a porphyroblastic microstructure with garnet (up to 1 mm) and minor quartz embedded in a fine-grained matrix composed by Mg-hornblende (Amp_2), diopside-rich clinopyroxene (Cpx_2) and albitic plagioclase (Pl_2). Garnet commonly includes quartz, minor rutile and amphibole. Garnet is always surrounded or occasionally replaced by symplectites consisting of Mg-hornblende (Amp_2) and plagioclase (Pl_2). Omphacite was not observed since it is always replaced by diopside-rich clinopyroxene (Cpx_2) + albite-rich plagioclase (Pl_2) + Mg-hornblende (Amp_2) symplectites.

Mafic eclogite D6

Mafic eclogite D6 displays a porphyroblastic microstructure with mm-sized garnet (up to 3 mm), minor K-feldspar and quartz embedded in a fine-grained matrix composed by Mg-hornblende (Amp_2), diopside-rich clinopyroxene (Cpx_2) and albitic plagioclase (Pl_2). Garnet is usually zoned, showing dusty cores with inclusions of quartz, omphacite, minor rutile and amphibole, and inclusions free rims. A 30-µm inclusion of dolomite has been also observed. Garnet is always surrounded or occasionally replaced by symplectites consisting of Mg-hornblende (Amp_2) and plagioclase (Pl_2). In the fine-grained matrix of the rock several diopside-rich clinopyroxene (Cpx_2) + albite-rich plagioclase (Pl_2) + Mg-hornblende (Amp_2) symplectites likely after omphacite have been observed. K-feldspar occur as 500-700 µm-sized porphyroblasts that locally display 50-100-µm thick clinopyroxene ± Mg-hornblende coronas. Few quartz porphyroblasts have irregular shape, with locally lobate-cuspate grain boundaries surrounded by 50-µm thick coronas composed by K-feldspar (Kfs_M) and minor clinopyroxene (Cpx_M) likely representing former melt films and/or pockets crystallised at quartz grain boundaries.

Kyanite eclogite B5A

Kyanite eclogite B5A displays a porphyroblastic microstructure with abundant garnet, kyanite and quartz. Few tiny inclusions of omphacite and rutile occur

within garnet and kyanite porphyroblasts. The rock matrix is composed by Mg-hornblende (Amp_2), diopside-rich clinopyroxene (Cpx_2) and albitic plagioclase (Pl_2). Garnet and kyanite are usually replaced by symplectitic intergrowths consisting of Mg-hornblende (Amp_{Sym}) and albitic plagioclase (Pl_{Sym}), whereas symplectites around kyanite are composed by anorthitic plagioclase (Pl_{Sym}), spinel (Sp_{Sym}), orthopyroxene (Opx_{Sym}) and minor sapphirine.

Kyanite eclogite D3

Kyanite eclogite D3 displays a porphyroblastic microstructure with garnet, kyanite and quartz surrounded by a fine-grained matrix composed by Mg-hornblende (Amp_2), diopside-rich clinopyroxene (Cpx_2) and albitic plagioclase (Pl_2). Garnet commonly includes tiny inclusions of amphibole, quartz and rutile. Similarly to the mafic eclogites, garnet and kyanite are usually replaced by symplectitic intergrowths consisting of Mg-hornblende (Amp_{Sym}) and albitic plagioclase (Pl_{Sym}), whereas symplectites around kyanite are composed by anorthitic plagioclase (Pl_{Sym}), spinel (Sp_{Sym}), orthopyroxene (Opx_{Sym}) and minor sapphirine. Symplectites consisting of albite-rich and anorthite-rich plagioclase replace former millimetre-sized stubby prismatic crystals of zoisite. Few quartz porphyroblasts display irregular shape, with lobate-cuspate grain boundaries surrounded by 10-20 µm thick K-feldspar (Kfs_M) coronas likely representing former crystallised melt films.

Kyanite eclogite E1

Kyanite eclogite E1 displays a porphyroblastic microstructure with garnet, kyanite and quartz surrounded by a fine-grained matrix composed by Mg-hornblende (Amp_2), diopside-rich clinopyroxene (Cpx_2) and albitic plagioclase (Pl_2). Garnet commonly includes tiny inclusions of amphibole, quartz and rutile. Similarly to the mafic eclogites, garnet and kyanite are usually replaced by symplectitic intergrowths consisting of Mg-hornblende (Amp_{Sym}) and albitic plagioclase (Pl_{Sym}), whereas symplectites around kyanite are composed by anorthitic plagioclase (Pl_{Sym}), spinel (Sp_{Sym}), orthopyroxene (Opx_{Sym}) and minor sapphirine. Symplectites consisting of albite-rich and anorthite-rich plagioclase replace former millimetre-sized stubby prismatic crystals of zoisite. Few quartz porphyroblasts display irregular shape, with lobate-cuspate grain boundaries surrounded by 10-20 µm thick K-feldspar (Kfs_M) coronas likely representing former crystallised melt films.

High-Al2O3 eclogite D1

High-Al_2O_3 eclogite D9 displays a porphyroblastic texture with large zoisite (up to 2 cm) and kyanite surrounded by a fine-grained matrix composed by diopside-rich clinopyroxene (Cpx_2) + albite-rich plagioclase (Pl_2) + Mg-hornblende (Amp_2). Zoisite contains minor inclusions of pargasite and is commonly replaced by symplectites consisting of almost pure anorthite. Kyanite is commonly replaced by symplectitic coronas consisting of anorthite-rich plagioclase (Pl_{Sym}), spinel (Sp_{Sym}), corundum and minor sapphirine.

High-Al2O3 eclogite D8

High-Al_2O_3 eclogite D9 displays a porphyroblastic texture with abundant kyanite porphyroblasts (up to 1 mm) embedded in a fine-grained matrix consisting of diopside-rich clinopyroxene (Cpx_2) + albite-rich plagioclase (Pl_2) + Mg-hornblende (Amp_2). Kyanite is partly replaced by symplectitic coronas consisting of anorthite-rich plagioclase (Pl_{Sym}), spinel (Sp_{Sym}), corundum and minor sapphirine.

High-Al2O3 eclogite D9

High-Al_2O_3 eclogite D9 displays a strong foliation defined by syn-tectonic porphyroblastic kyanite in textural equilibrium with quartz and zoisite porphyroblasts. These minerals are embedded in a fine-grained matrix composed by diopside-rich clinopyroxene (Cpx_2) + albite-rich plagioclase (Pl_2) + Mg-hornblende (Amp_2) symplectites after omphacite. Kyanite is partly replaced by symplectitic coronas consisting of anorthite-rich plagioclase (Pl_{Sym}), spinel (Sp_{Sym}), corundum and minor sapphirine. Quartz locally displays corroded edges surrounded by fine-grained intergrowths consisting of anhedral K-feldspar (Kfs_M) and clinopyroxene (Cpx_M), representing former crystallised melts. The Cpx_M + Kfs_M intergrowths are preferentially oriented parallel to the main foliation suggesting that they formed in a deformation regime when the kyanite + omphacite + quartz HP assemblage was still stable. In all the three types of eclogites, the symplectitic domains are surrounded by coronas defined by porphyroblastic pargasitic hornblende (Amp_3) and biotite.

Amphibole-bearing migmatite D2

The amphibole-bearing migmatite D2 displays a layered microstructure, consisting of leucocratic domains composed by quartz + plagioclase ± Mg-

hornblende and melanocratic domains enriched in hornblende. Leucocratic domains display a mosaic-like equilibrium microtexture with grain boundaries triple junctions at 120°. The melanocratic domains are strongly foliated and are dominated by porphyroblastic Mg-hornblende enclosed in a fine-grained matrix consisting of clinopyroxene (Cpx_2), amphibole ($Amph_2$) and albitic plagioclase (Pl_2) replacing previous garnet and omphacite.

Amphibole-bearing migmatite D5

The amphibole-bearing migmatite D5 displays a layered microstructure, consisting of leucocratic domains composed by quartz + plagioclase ± Mg-hornblende and melanocratic domains enriched in hornblende. Leucocratic domains display a mosaic-like equilibrium microtexture with grain boundaries triple junctions at 120°. The melanocratic domains are strongly foliated and are dominated by porphyroblastic Mg-hornblende enclosed in a fine-grained matrix consisting of clinopyroxene (Cpx_2), amphibole ($Amph_2$) and albitic plagioclase (Pl_2) replacing previous garnet and omphacite.

Amphibole-bearing migmatite D7

The amphibole-bearing migmatite D7 displays a layered microstructure, consisting of leucocratic domains composed by quartz + plagioclase ± Mg-hornblende and melanocratic domains enriched in hornblende. Leucocratic domains display a mosaic-like equilibrium microtexture with grain boundaries triple junctions at 120°. The melanocratic domains are strongly foliated and are dominated by porphyroblastic Mg-hornblende enclosed in a fine-grained matrix consisting of clinopyroxene (Cpx_2), amphibole ($Amph_2$) and albitic plagioclase (Pl_2) replacing previous garnet and omphacite.

Amphibole + phlogopite boudins DB101

The amphibole + phlogopite boudins DB101 display an assemblage dominated by tremolite (more than 80 vol.%), phlogopite and minor chlorite. In all the investigated samples, tremolite and phlogopite form a mosaic-like texture with 120° triple junctions and straight grain boundaries. The tremolite + phlogopite matrix hosts older mm-sized K-feldspar porphyroblasts.

Amphibole + phlogopite boudins DB102

The amphibole + phlogopite boudins DB102 display an assemblage dominated by tremolite (more than 80 vol.%), phlogopite and minor chlorite. In all the investigated samples, tremolite and phlogopite form a mosaic-like texture with 120° triple junctions and straight grain boundaries.

Porphyroclastic garnet lherzolite UT22

Porphyroclastic garnet lherzolites display large partially retrogressed garnet porphyroclasts (Grt_1) in textural equilibrium with olivine (Ol_1), orthopyroxene (Opx_1), clinopyroxene (Cpx_1) and minor amphibole (Amp_1). This porphyroclastic assemblage is surrounded by a finer-grained recrystallised matrix made of olivine (Ol_2), orthopyroxene (Opx_2), clinopyroxene (Cpx_2), subordinate amphibole (Amp_2) and spinel (Spl_2) (Fig. 19a). Olivine is present as strongly serpentinised porphyroclasts that commonly show intracrystalline deformation microstructure like deformation lamellae and kink bands (Fig. 19b). The new olivine grains are less serpentinised and are invariably strain-free. Also clinopyroxene occurs both as porphyroclasts and as fine-grained crystals in textural equilibrium with the recrystallised peridotite matrix. Large clinopyroxenes are often pseudomorphosed by fine-grained tremolite aggregates that occasionally contain preserved exsolution lamellae of garnet and garnet grains (Fig. 19c). Garnet is almost completely replaced by symplectites consisting of orthopyroxene (Opx_{Sym}) + clinopyroxene (Cpx_{Sym}) + amphibole (Amp_{Sym}) + spinel (Spl_{Sym}) or chlorite-bearing pseudomorphs that locally contain relic, pre-garnet spinel grains (Spl_1).

Fine-grained garnet-amphibole peridotite UT24

The fine-grained garnet-amphibole peridotite UT24 displays garnet (Grt_1), olivine (Ol_1), amphibole (Amp_1) and orthopyroxene (Opx_1) porphyroblasts set in a mylonitic fine-grained (< 500 μm) matrix consisting of recrystallized olivine (Ol_2), orthopyroxene (Opx_2), amphibole (Amp_2), Cr-rich spinel (Spl_2), and rare clinopyroxene (Cpx_2). The coarse-grained orthopyroxene displays peculiar intracrystalline deformation microstructures like kink bands and undulatory extinction. Kinked orthopyroxene porphyroblasts contain numerous exsolution lamellae of garnet and clinopyroxene. Orthopyroxene neoblasts are unstrained and contain no exsolution lamellae. The coarse-grained amphibole is colourless or pale green and typically includes spinel and minor clinopyroxene. Garnet occurs porphyroblasts of variable size and commonly include olivine and relic

spinel (Spl). Garnet is invariably mantled by kelyphites made of orthopyroxene (Opx_{Sym}) + clinopyroxene (Cpx_{Sym}) + amphibole (Amp_{Sym}) + spinel (Spl_{Sym}). Sometimes garnet is completely replaced by Opx_{Sym} + Cpx_{Sym} + Amp_{Sym} + Spl_{Sym} symplectites that include relics of pre-garnet, amoeboid spinel grains.

Fine-grained garnet-amphibole peridotite UT25

The fine-grained garnet-amphibole peridotite UT25 displays garnet (Grt_1), olivine (Ol_1) and amphibole (Amp_1) porphyroblasts set in a mylonitic fine-grained (< 500 μm) matrix consisting of recrystallized olivine (Ol_2), orthopyroxene (Opx_2), amphibole (Amp_2), garnet (Grt_2), Cr-rich spinel (Spl_2), and rare clinopyroxene (Cpx_2). The coarse-grained amphibole is colourless or pale green and typically includes spinel and minor clinopyroxene. Similarly to porphyroblastic Opx_1 and Cpx_1 of garnet-amphibole peridotite UT24, also porphyroblastic amphibole of this sample displays deformation microstructures like kink bands and undulatory extinction. Neoblastic Amp_2 is unstrained and inclusions-free. Garnet occurs both as large porphyroblasts (Grt_1; 2-3 mm) and as small crystals (Grt_2; up to 500 μm) in textural equilibrium with the Ol_2 + Opx_2 + Amp_2 + Spl_2 ± Cpx_2 recrystallized peridotite matrix. The coarse garnets include olivine, orthopyroxene and relic Cr-rich spinel. Spinel inclusions were not observed in small garnets, but olivine, orthopyroxene and amphibole inclusions frequently occur. Both garnet types are invariably mantled by kelyphites made of orthopyroxene + clinopyroxene + amphibole + spinel and orthopyroxene + clinopyroxene + amphibole.

Garnet clinopyroxenite UT23

Garnet clinopyroxenites display a porphyroblastic microstructure with coarse (up to 2.5 mm) clinopyroxene (Cpx_1), orthopyroxene (Opx_1) and amphibole (Amp_1) embedded in a finer-grained recrystallised matrix consisting of clinopyroxene (Cpx_2), orthopyroxene (Opx_2) and amphibole (Amp_2) in textural equilibrium with small garnet grains. The coarse clinopyroxene shows evident exsolution lamellae of garnet, orthopyroxene and amphibole. The lamellae of orthopyroxene are 50-100 μm thick and up to 3 mm long, while garnet exsolutions are typically small with aspect ratios varying from 1:1 to 5:1. The exsolved amphibole occurs as an interstitial phase at garnet-orthopyroxene-clinopyroxene grain boundaries or triple junctions (Fig. 20b). Orthopyroxene porphyroblasts are intensely deformed and show garnet exsolutions along curved crystal planes. Both neoblastic clinopyroxene and orthopyroxene are undeformed and contain no exsolution

lamellae. Garnet occurs as small crystals (up to 600 μm) in paragenesis with the neoblastic Cpx_2 + Opx_2 + Amp_2 assemblage and defines the compositional layering of the rock. Notably, the garnet layering is parallel to the orientation of the garnet exsolution lamellae within orthopyroxene and clinopyroxene.

Tremolitite UT17

Tremolitites display an assemblage dominated by tremolite, chlorite and minor Mg-hornblende. Tremolite is the most abundant phase and hosts older mm-sized Mg-hornblende porphyroblasts and numerous Chl-bearing pseudomorphs after garnet.

Tremolitite UT21

Tremolitites display an assemblage dominated by tremolite, chlorite and minor Mg-hornblende. Tremolite is the most abundant phase and hosts older mm-sized Mg-hornblende porphyroblasts and numerous Chl-bearing pseudomorphs after garnet.

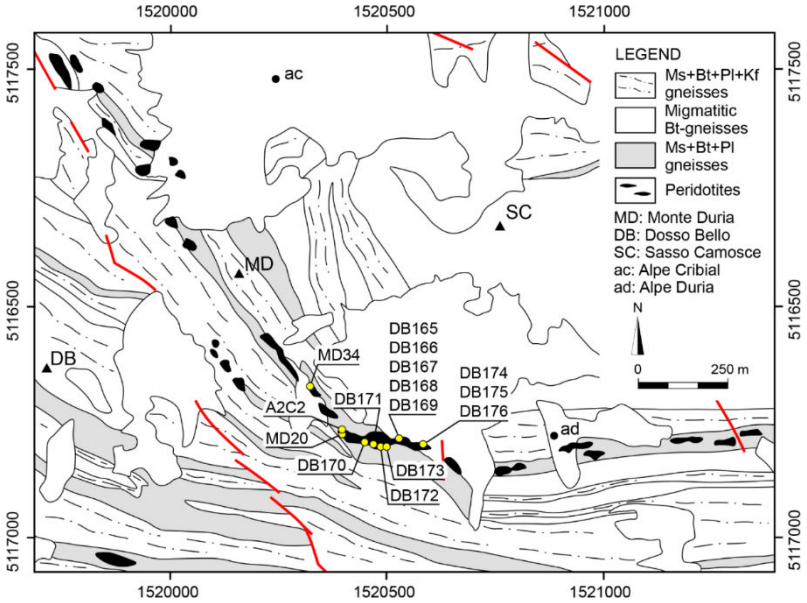

Fig. A1 Sample locations at Monte Duria. Coordinates in Gauss-Boaga (Monte Mario 1) reference system.

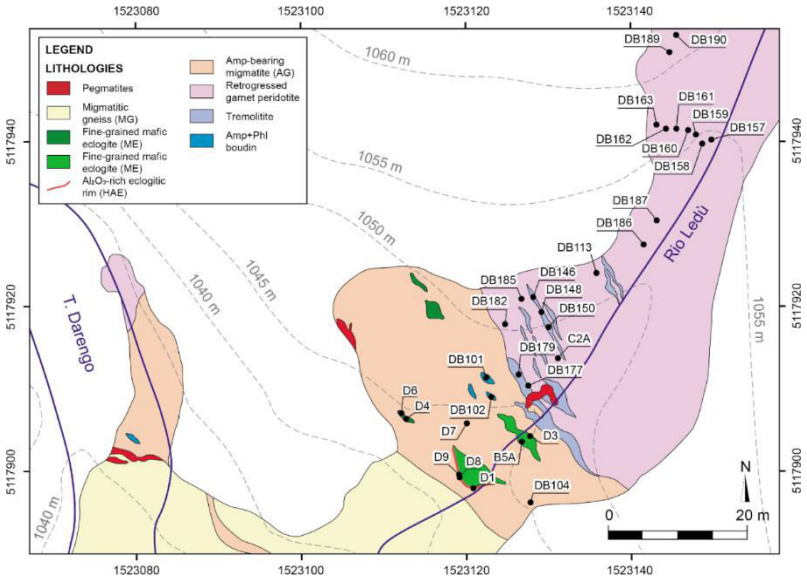

Fig. A2 Sample locations at Borgo Outcrop. Coordinates in Gauss-Boaga (Monte Mario 1) reference system.

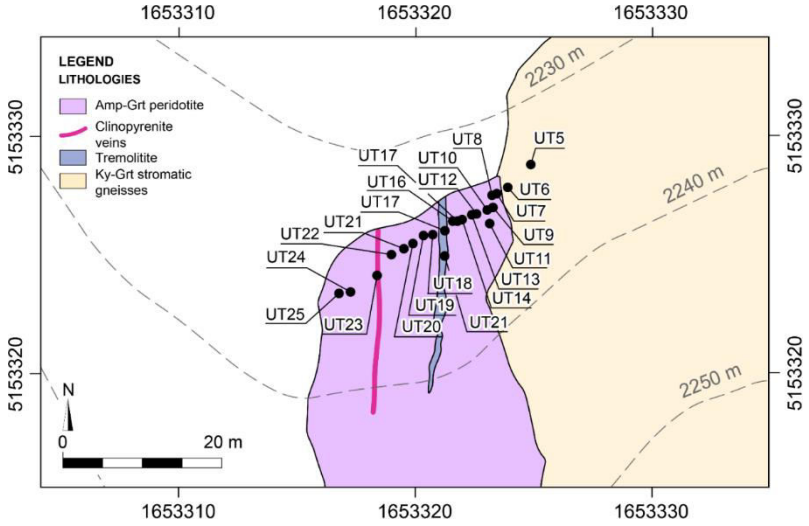

Fig. A3 Sample locations at Monte Hochwart. Coordinates in Gauss-Boaga (Monte Mario 1) reference system

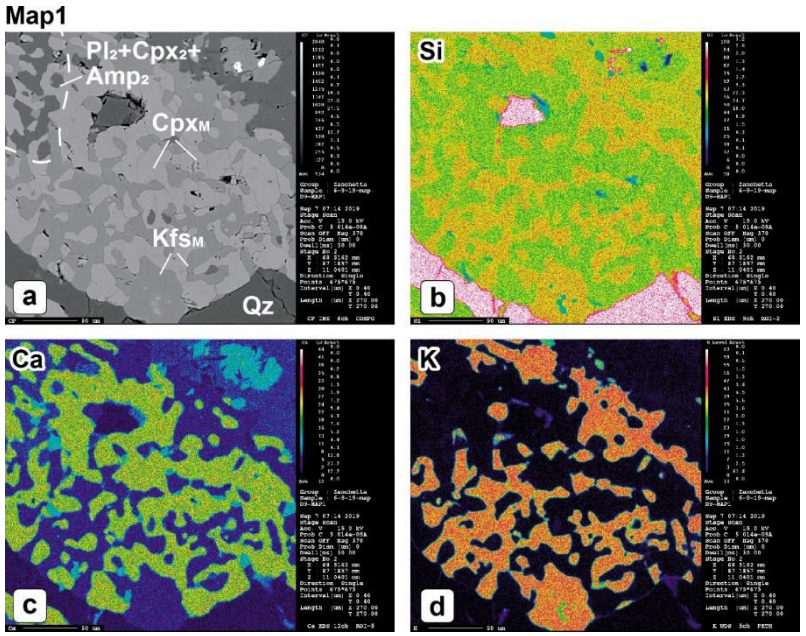

Fig. A4 Back-scattered electron (BSE) image (a) and X-ray maps of SiO_2 (b) CaO (c) and K_2O (d) concentrations of melt pocket of recrystallised Cpx_M + Kfs_M around relict quartz and Pl_2+Cpx_2+Amp_2 symplectite after omphacite in high-Al_2O_3 eclogite D9.

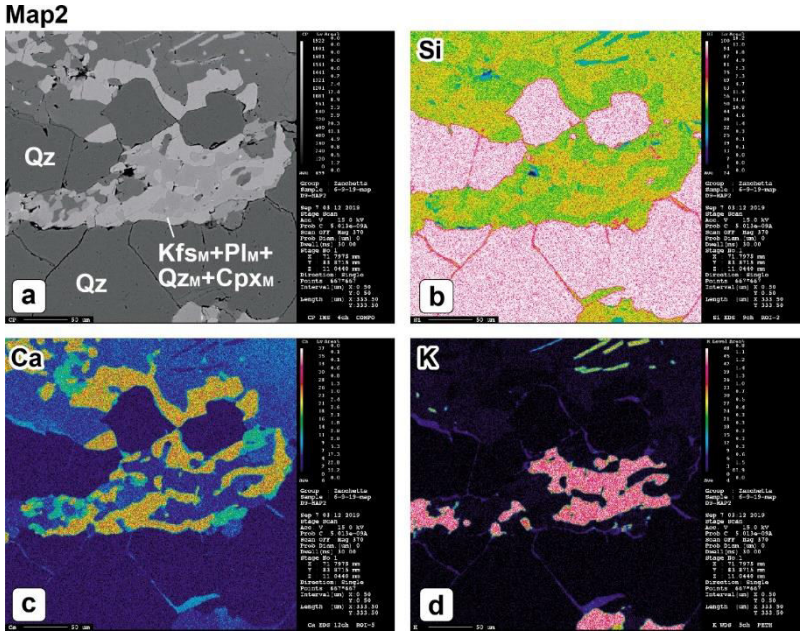

Fig. A5 BSE image (a) and X-ray maps of SiO_2 (b) CaO (c) and K_2O (d) concentrations of melt pocket of recrystallised $Kfs_M + Pl_M + Qz_M + Cpx_M$ around relict quartz in high-Al_2O_3 eclogite D9

Table A1

Lithology	Mafic eclogite										
Sample	D6										
Mineral	Zo	Zo	Zo	Zo	Zo	Aln	Aln	Aln	Aln	Aln	Aln
Comment	core	core	core	rim	rim						
SiO_2	39.04	38.19	38.47	39.00	38.38	35.41	35.34	35.39	35.30	36.05	35.52
TiO_2	0.14	0.12	0.14	0.16	0.12	0.22	0.18	0.11	0.10	0.21	0.14
Al_2O_3	29.65	28.02	28.40	29.10	28.63	21.98	22.22	22.12	22.04	22.11	22.60
Cr_2O_3	b.d.l.	b.d.l.	0.12	b.d.l.	b.d.l.	b.d.l.	b.d.l.	b.d.l.	b.d.l.	b.d.l.	b.d.l.
FeO†	4.19	4.69	4.30	4.09	4.30	8.10	7.79	7.83	7.68	7.90	7.63
MgO	0.44	0.75	0.70	0.65	0.85	1.67	1.76	1.63	1.64	1.97	1.70
MnO	0.02	0.03	0.03	0.02	0.03	0.07	0.01	0.07	0.09	0.09	0.07
CaO	22.36	20.38	21.10	21.71	20.69	13.92	14.12	14.19	14.14	14.11	14.17
SrO	0.55	0.49	0.47	0.13	0.36	b.d.l.	b.d.l.	b.d.l.	b.d.l.	b.d.l.	b.d.l.
La_2O_3	0.21	0.70	0.61	0.55	0.77	3.54	3.37	3.27	3.27	3.08	3.22
Ce_2O_3	0.78	2.15	1.73	1.57	2.16	8.45	8.20	7.99	8.21	7.76	7.95
Pr_2O_3	0.09	0.29	0.28	0.16	0.32	1.22	1.22	1.20	1.01	1.03	1.08
Nd_2O_3	0.70	1.63	1.31	1.22	1.54	4.50	4.41	4.68	4.65	4.65	4.66
Sm_2O_3	0.12	0.42	0.37	0.27	0.31	0.64	0.66	0.69	0.67	0.61	0.77
Eu_2O_3	b.d.l.	b.d.l.	b.d.l.	b.d.l.	0.02	b.d.l.	b.d.l.	b.d.l.	b.d.l.	b.d.l.	b.d.l.
Gd_2O_3	0.20	0.16	0.15	0.12	0.19	0.19	0.26	0.20	0.29	0.25	0.35
Dy_2O_3	b.d.l.	b.d.l.	b.d.l.	b.d.l.	b.d.l.	b.d.l.	b.d.l.	b.d.l.	b.d.l.	b.d.l.	b.d.l.
Y_2O_3	b.d.l.	b.d.l.	b.d.l.	b.d.l.	b.d.l.	b.d.l.	b.d.l.	b.d.l.	b.d.l.	b.d.l.	b.d.l.
PbO	0.03	b.d.l.	0.01	0.01	0.02	b.d.l.	b.d.l.	b.d.l.	b.d.l.	0.02	b.d.l.
ThO_2	0.01	0.14	0.10	0.09	0.12	0.79	0.88	0.76	0.81	0.80	0.86
UO_2	0.07	0.10	0.05	0.03	0.12	0.03	0.00	0.03	0.09	0.04	0.05
Sum	98.59	98.26	98.34	98.86	98.92	100.74	100.43	100.16	100.00	100.68	100.76
Si	4.53	4.56	4.56	4.56	4.54	4.59	4.57	4.59	4.59	4.63	4.58
Ti	0.01	0.01	0.01	0.01	0.01	0.02	0.02	0.01	0.01	0.02	0.01
Al	4.06	3.94	3.96	4.01	3.99	3.36	3.39	3.38	3.38	3.34	3.43
Cr	-	-	0.01	-	-	-	-	-	-	-	-
Fe^{3+}	0.41	0.47	0.43	0.40	0.43	0.88	0.00	0.00	0.00	0.00	0.00
Fe^{2+}	0.00	0.00	0.00	0.00	0.00	0.00	0.84	0.85	0.84	0.85	0.82
Mg	0.08	0.13	0.12	0.11	0.15	0.32	0.34	0.32	0.32	0.38	0.33
Mn	0.00	0.00	0.00	0.00	0.00	0.01	0.00	0.01	0.01	0.01	0.01
Ca	2.78	2.61	2.68	2.72	2.62	1.93	1.96	1.97	1.97	1.94	1.96
Sr	0.04	0.03	0.03	0.01	0.02	-	-	-	-	-	-
La	0.01	0.03	0.03	0.02	0.03	0.17	0.16	0.16	0.16	0.15	0.15
Ce	0.03	0.09	0.08	0.07	0.09	0.40	0.39	0.38	0.39	0.36	0.37
Pr	0.00	0.01	0.01	0.01	0.01	0.06	0.06	0.06	0.05	0.05	0.05
Nd	0.03	0.07	0.06	0.05	0.07	0.21	0.20	0.22	0.22	0.21	0.21
Sm	0.00	0.02	0.02	0.01	0.01	0.03	0.03	0.03	0.03	0.03	0.03
Eu	-	-	-	-	0.00	-	-	-	-	-	-
Gd	0.01	0.01	0.01	0.00	0.01	0.01	0.01	0.01	0.01	0.01	0.01
Dy	-	-	-	-	-	-	-	-	-	-	-
Y	-	-	-	-	-	-	-	-	-	-	-
Pb	0.00	-	0.00	0.00	0.00	-	-	-	-	0.00	-
Th	0.00	0.00	0.00	0.00	0.00	0.02	0.03	0.02	0.02	0.02	0.03
U	0.00	0.00	0.00	0.00	0.00	0.00	-	0.00	0.00	0.00	0.00
Cation Sum	12.00	12.00	12.00	12.00	12.00	12.00	12.00	12.00	12.00	12.00	12.00
X_{Mg}	0.16	0.22	0.22	0.22	0.26	0.27	0.29	0.27	0.28	0.31	0.28
$Al^{(IV)}$	-	-	-	-	-	-	-	-	-	-	-
$Al^{(VI)}$	-	-	-	-	-	-	-	-	-	-	-

Epidotes are normalised on the basis of 12 cations. † total iron as FeO. Fe^{2+} and Fe^{3+} are calculated from stoichiometry. $XMg=(Mg/Mg+Fe^{2+})$